THE UNIVERSITY *of* EDINBURGH

Non–perturbative aspects of physics beyond the Standard Model

Enrico Rinaldi

Doctor of Philosophy
The University of Edinburgh
2013

Abstract

The Large Hadron Collider (LHC) and the four major experiments set up along its 27 kilometers of circumference (ATLAS, CMS, ALICE and LHCb), have recently started to explore the high–energy frontier at $\sqrt{s} = 8$ TeV, and will move to even higher energy in just about 2 years. The aim of physics searches at LHC experiments was to complete the picture of the Standard Model (SM) of elementary particles with the discovery of the Higgs boson and to look for specific signatures of models extending the current understanding of particle interactions, at zero and non–zero temperature. In 2012, the official discovery of the Higgs boson, the only missing particle of the Standard Model, was announced by ATLAS and CMS. Other important results include the measurement of rare decay modes in heavy quarks systems, and indications of CP violation in charm decays by LHCb. Signatures of beyond the Standard Model (BSM) physics are currently being looked for in the experimental data, and this often requires the knowledge of quantities that can be computed only with non–perturbative methods.

This thesis focuses on some possible extensions of the SM and the analysis of interesting physical observables, like masses or decay rates, calculated using non–perturbative lattice methods. The approach followed for the main part of this work is to model BSM theories as effective field theories defined on a lattice. This lattice approach has a twofold advantage: it allows us to explore non–renormalizable gauge theories by imposing an explicit gauge–invariant cutoff and it allows us to go beyond perturbative results in the study of strongly interacting systems. Some of the issues of the SM that we will try to address include, for example, the hierarchy problem and the origin of dynamical electroweak symmetry breaking (DEWSB).

We investigate non–perturbatively the possibility that the lightness of the mass for an elementary scalar field in a four–dimensional quantum field theory might be due to a higher–dimensional gauge symmetry principle. This idea fits in the

Gauge–Higgs unification approach to the hierarchy problem and the results we present extend what is known from perturbative expectations. Extra dimensional models are also often used to approach DEWSB.

Another approach to DEWSB implies a new strongly interacting gauge sector that extends the SM at high energies and it is usually referred to as Technicolor. The phenomenological consequences of Technicolor can only be studied by non–perturbative methods at low energy since the theory is strongly coupled at large distances. We perform a comprehensive lattice study of fermionic and gluonic scalar bound states in one of the candidate theories for Technicolor BSM physics. We relate our findings to the nature of the newly discovered Higgs boson.

New physics is also commonly believed to be hidden in the flavour sector of the SM. In this sector, lattice calculations of non–perturbative input parameters are needed in order to make precise predictions and extract signals of possible new physics. In particular, heavy quark physics on the lattice is still in development and it is important to understand the relevant discretisation errors. We describe a preliminary study of the mixing parameter of heavy–light mesons oscillations in a partially–quenched scenario, using staggered dynamical fermions and domain wall valence fermions.

Lay summary

The Large Hadron Collider (LHC) and the four major experiments set up along its 27 kilometers of circumference (ATLAS, CMS, ALICE and LHCb), have recently started to explore the high–energy frontier of particle physics, and will move to even higher energy in just about 2 years. The aim of physics searches at LHC experiments was to complete the picture of the Standard Model (SM) of elementary particles with the discovery of the Higgs boson and to look for specific signatures of models extending the current understanding of particle interactions, at zero and non–zero temperature. In 2012, the official discovery of the Higgs boson, the only missing particle of the Standard Model, was announced by ATLAS and CMS. This is therefore an exciting time for particle physics.

Some of the questions that remain to be answered are, for example, "What is the mechanism to keep the Higgs mass as light as it turns out to be in experiments?", and "Is the Higgs boson just what we expect from the SM, or a sign of new physics?" (still well described by the theoretical framework of the SM up to the precision reached by current experiments). This thesis contains results that can shed light on possible answers to such questions. The tools used to obtain results exploit powerful computer simulations, where the elements of theories we are interested in are discretised on a space–time grid.

To try and answer the first question above, we study a theory that allows the presence of an extra spatial dimension. Although we can perceive only three dimensions and the flow of time, extra dimensions could be hidden at extremely small distances. In such a theory, we calculate the mass of a particle similar to the Higgs boson of the SM and we relate its lightness to the presence of the extra hidden dimension. Regarding the second question, instead, we describe a well–known model where the Higgs boson is not an elementary particle, as described by the SM, but actually made up by more fundamental constituents. We show how the mass of such a particle can be measured, using technically challenging

computational methods. The results help us understand the nature of the Higgs boson in some theoretical extensions beyond the SM.

The final part of this work is devoted to the study of systems composed by heavy elementary particles, where results from computer simulations are needed by experimentalists in order to make predictions from collected data. These computer simulations in the context of heavy particles have some issues that need more understanding, and in this thesis we start the development of tools specifically designed for these problems.

Declaration

I declare that this thesis was composed by myself, that the work contained herein is my own except where explicitly stated otherwise in the text. Where the work was done in collaboration with others, a significant contribution was made by the author. This work has not been submitted for any other degree or professional qualification except as specified.

(*Enrico Rinaldi, 24/09/2013*)

Acknowledgements

I wish to thank primarily my supervisor Prof. Luigi Del Debbio. I have learnt a good deal of physics in the past four years and I have had many opportunities to expand my knowledge and my collaborations. I could not have done any of these without his help and his support.

Secondly, I am very grateful to all my collaborators in the UK: Prof. Biagio Lucini, Dr. Antonio Rago and Dr. Agostino Patella, never ending sources of insights and advices, from physics to life.

A special thank to the members of the LatKMI collaboration in Nagoya, where I spent seven very fruitful months and arguably the best time of my life so far. In alphabetical order, I thank Yasumichi Aoki, Tatsumi Aoyama, Masafumi Kurachi, Toshihide Maskawa, Kohtaroh Miura, Kei-ichi Nagai, Hiroshi Ohki, Akihiro Shibata, Koichi Yamawaki, and Takeshi Yamazaki. I also thank Ritsuko Ota from the KMI office for her lifesaving support, and my officemates Akamatsu-san and Bamba-san for sharing their time with me.

In the end I want to thank all my friends in Edinburgh, my officemates in these past four years, Erick, Maria, Eoin, Oyvind, Pan, Nico, my flatmates Seb, Susanne, James, Samuel, Hari, my climbing partners Thomas, Mark and Sam and the Feynmen football team. I had a really enjoyable time in Edinburgh, despite the weather.

Contents

List of Figures

List of Tables

Chapter 1

Introduction

In this thesis we explore three of the several different ways in which Lattice Gauge Theories (LGT) can be used to enlighten non–perturbative aspects of physics beyond the Standard Model (BSM). Searches for New Physics (NP) at the LHC and at B–factories are taking advantage of the increasing precision reached in several experiments and data analysis tools. The lattice community is also advancing towards getting a more precise knowledge of non–perturbative phenomena in light of NP.

After a brief introduction of the SM as it stands now after the discovery of the Higgs boson [1] at the LHC [6, 7], we introduce some of the simplest extensions of the SM, which include extra dimensions in the Gauge–Higgs unification (GHU) scenario. Such extra dimensions can be compactified and hidden at very high energy, and they can have complicated compactification topologies. GHU is often advocated as a solution to the hierarchy problem (e.g. see Ref. [8] and references therein).

We also introduce modern Technicolor models which are, in a sense, *higgsless* since no elementary scalar field is present in the Lagrangian. These models, when they satisfy current experimental constraints from electroweak precision measurements, can explain dynamical electroweak symmetry breaking (DEWSB) and avoid fine–tuning problems [9]. Moreover, some of those models also predict

[1] The Higgs boson is the name used throughout this work to denote the scalar particle responsible for electroweak symmetry breaking and elementary particles mass, as it was introduced by Higgs [3], Englert and Brout [4] and also Guralnik, Hagen and Kibble [5]. However, the nature of the particle recently discovered at the LHC [6, 7] is a topic which is still being investigated.

NP signals to appear in the TeV region, therefore in the reach of the LHC upgrade [10].

At last, we describe how LGT can be useful in testing flavour physics processes, where non–perturbative hadronic matrix elements needs to be calculated. NP signals in flavour physics are intriguing, especially those in the heavy–quark sector involving D and B mesons [11]. Recently, signals for CP violation in the charm and bottom sectors [12] have been revealed, together with indications of rare decays which are loop–suppressed in the SM [13].

1.1 The Standard Model of particles

The Standard Model is the most successful theory of elementary particles interactions that we have. It describes three families of quarks and leptons which are fermions of spin $\frac{1}{2}$, charged under the gauge symmetry group $\mathrm{SU}(3)_c \otimes \mathrm{SU}(2)_L \otimes U(1)_Y$. The first group defines the *colour* degree of freedom of quarks and describes strong nuclear forces; as a standalone sector of the SM it is called Quantum Chromodynamics (QCD). The product of the last two groups defines the electroweak (EW) sector of the SM, where the $\mathrm{SU}(2)_L$ group defines the weak isospin quantum number and the $U(1)_Y$ defines the hypercharge. Leptons do not enter the QCD sector, while they do mix with quarks in the EW sector.

The interactions among fermions are described via a set of vector bosons related to the Lie algebras of the aforementioned gauge groups. There are in total 2 electrically charged gauge bosons $W^{\pm}$ and 2 neutral ones Z^0 and γ corresponding to the EW sector; moreover, there are 8 gauge bosons, called gluons, from the QCD sector.

Additionally there is a scalar bosonic field which is a doublet transforming under the fundamental representation of $\mathrm{SU}(2)_L$ and does not carry any colour charge. This field interacts in the Higgs sector of the SM where a *ad hoc* potential $V(\phi)$ is introduced to spontaneously break the EW symmetry. Such a breaking occurs via the generation of a non–zero vacuum expectation value for ϕ [3–5] at the minimum of the potential: $\langle\phi\rangle \equiv \frac{v}{\sqrt{2}} \sim 174$ GeV. The value of v is sometimes referred to as the EW energy scale.

At the same time, this mechanism gives masses to the EW gauge bosons $W^{\pm}$ and Z^0, while the photon γ remains massless. By coupling the Higgs sector to quarks

and leptons fields via Yukawa interactions, the Higgs mechanism produces all other elementary particles masses i.e. for the u quark $\sim y_u v(\bar{u}_L \phi u_R)$, $m_u = y_u v$.

1.1.1 QCD and confinement

Each of the gauge groups introduced above is characterised by a coupling constant which depends on the energy scale at which the theory is used, according to the renormalization principle [14]. A peculiar case is given by the QCD gauge coupling $\alpha_s(\mu) = \frac{g_s^2(\mu)}{4\pi}$ and its beta function (at one loop in perturbation theory)

$$\beta(\alpha_s) \;=\; \frac{\partial \alpha_s}{\partial(\log \mu^2)} = -\beta_0 \alpha_s^2 = -\frac{33 - 2N_f}{12\pi}\; \alpha_s^2 \;. \tag{1.1}$$

At high energies the coupling α_s decreases and it tends asymptotically to zero (for small number of flavours N_f). As a consequence, quarks and gluons behave almost freely when they are at extremely small distances and this asymptotic freedom is what allows perturbative QCD to make reliable predictions for high energy processes. On the contrary, the coupling drastically increases at low energies, of the order of the proton mass scale, meaning that perturbation theory is no longer applicable. At those energies quarks and gluons are tightly bound into hadrons and can not be observed as asymptotically free particles, a phenomenon known as confinement.

Confinement still remains unexplained from a theoretical point of view, but its phenomenology is well studied. For our purposes it is interesting to note that the spectrum of a strongly interacting theory without quark fields is composed of *glueballs*, bound states of the QCD gluons. The presence of glueballs is a purely non–perturbative effect, a consequence of confinement at large distances.

When quarks are added as extra degrees of freedom, glueballs may decay into hadrons or into lighter glueballs, but the effects of such transitions are extremely hard to detect in experiments. In fact, the existence of glueballs as resonances in QCD is not well established yet, even though lattice calculations have shown how their spectrum would look like. A complete review on this topic, both from the lattice and the experimental point of view, can be found in Ref. [15].

In this thesis, we study glueballs appearing in different models of strongly interacting physics. More details regarding specific lattice techniques and results on glueball spectroscopy can be found in Appendix B and C.

1.1.2 Problems with the Higgs sector

The Higgs sector of the SM is the only one containing an elementary scalar field. The Lagrangian describing its self–interaction can be written as

$$\begin{aligned} \mathcal{L}_{\text{Higgs}}(x) &= \big(D_\mu\phi(x)\big)^\dagger D^\mu\phi(x) - V(\phi) \\ &= \big(D_\mu\phi(x)\big)^\dagger D^\mu\phi(x) + m_H^2\phi^2(x) - \lambda_H\phi^4(x) \ , \end{aligned} \tag{1.2}$$

where there are two additional parameters of the SM, namely the Higgs mass m_H and the Higgs self–coupling λ_H. Both parameters are being thoroughly investigated at the LHC, now that the Higgs boson as been discovered.

In the following we ought to mention two issues of the SM Higgs sector that are often used to advocate new physics below the Planck scale $M_{Pl} \sim 10^{19}$ GeV. The first one is naturalness, sometimes also referred to as the hierarchy or fine–tuning problem. The second one is triviality and the related vacuum–instability issue.

The Higgs field in Eq. (1.2) has a mass which can be additively renormalized since there is no symmetry to protect it: $m_H \to m_H + \delta m_H$. This situation is remarkably different from the one regarding all other elementary particles in the SM, for which bare mass terms cannot be explicitly written without violating symmetries: quarks and leptons masses are protected by chiral symmetry, while gauge bosons masses are kept to zero by gauge invariance.

By including only one–loop perturbative contributions to the renormalization of the Higgs propagator we can write

$$\delta m_H^2 \ = \ \frac{3\Lambda_{\text{UV}}^2}{16\pi^2 v}\big(4m_t^2 - 2m_W^2 - m_Z^2 - m_H^2\big) \ , \tag{1.3}$$

where the dominant contribution comes from the top quark mass $m_t \simeq 173$ GeV and we introduced an ultraviolet cutoff Λ_{UV} which takes into account effects due to new physics at high energies.

It is clear from Eq. (1.3) that, unless the bare Higgs mass in the Lagrangian is accurately tuned (to one part in 10^{38} GeV), the SM can not account for the measured Higgs mass $m_H \simeq 125$ GeV; the Higgs boson mass should be driven to the cutoff scale by radiative corrections.

This fine–tuning problem can be ameliorated if there is new physics at $\Lambda_{\text{UV}} \ll M_{Pl}$. In fact, if there were a symmetry keeping the Higgs field massless at tree

level at higher energy scales, the currently measured m_H could be "natural".

In Chapter 2 and Chapter 3 we describe two different models which could have a naturally light Higgs since a higher–dimensional gauge symmetry in the first case, and a scale invariance symmetry in the second case, protect the Higgs mass from cutoff contributions. More details are given in Sec. 1.2 and Sec. 1.3.

The triviality issue is related to the quartic coupling λ_H. Without new physics below the Planck scale the Higgs sector becomes trivial when the energy increases: $\lambda_H(\mu) \to 0$ if $\mu \to \infty$. The most precise perturbative calculation of λ_H using renormalization group equations to evolve the couplings up to high energies suggests [16] $\lambda_H(M_{Pl}) = -0.014 \pm 0.006$ using $m_H = 125$ GeV. There are also indications that, with the current experimental results for m_H and m_t, the vacuum of the EW theory is not an absolute minimum of the effective potential: the SM is in a metastable vacuum which could decay to a different configuration. Some intriguing scenarios can be thought of in this case [16], but we do not discuss this further.

1.1.3 Flavoured fields

Interesting phenomenology in the SM arises from the flavour sector. Here we focus on the quark sector, even though the leptonic sector with neutrinos includes a rich and largely unexplored phenomenology.

Each quark $q = u, d, s, c, b, t$ has a different flavour and they can mix with each other with a pattern which is one of the most precisely studied parts in the SM. In the EW sector, quark fields appear as left–handed doublets of the weak isospin symmetry group $\mathrm{SU}(2)_L$

$$\begin{pmatrix} u \\ d' \end{pmatrix}_L \qquad \begin{pmatrix} c \\ s' \end{pmatrix}_L \qquad \begin{pmatrix} t \\ b' \end{pmatrix}_L ,$$

where the prime index is used to differentiate these weak isospin eigenstates from the usual d, s and b mass eigenstates which diagonalise the Yukawa couplings in the interactions with the Higgs field.

The rotation between flavour and mass eigenstates is given by the CKM unitary

matrix [17, 18]

$$\begin{pmatrix} d' \\ s' \\ b' \end{pmatrix} = \begin{pmatrix} V_{ud} & V_{us} & V_{ub} \\ V_{cd} & V_{cs} & V_{cb} \\ V_{td} & V_{ts} & V_{tb} \end{pmatrix} \begin{pmatrix} d \\ s \\ b \end{pmatrix} = V_{\text{CKM}} \begin{pmatrix} d \\ s \\ b \end{pmatrix} \ ,$$

which can be expressed with only 4 parameters: 3 mixing angles (θ_{12}, θ_{13}, θ_{23}) and 1 phase δ responsible for CP violation effects.

The parameters of the CKM matrix need to be measured experimentally because they are not known a priori. It turns out that there is an unexpected hierarchy in the elements of V_{CKM} such that they become smaller further away from the diagonal. This flavour hierarchy is still unexplained and it has attracted a lot of theoretical attention [19, 20].

Extracting CKM elements from experimental data of decay rates often requires the knowledge of hadronic matrix elements whose non–perturbative nature can be approached thanks to numerical lattice simulations. Moreover, processes involving heavy quarks are believed to hide NP signals [11] and, in Chapter 4, we explore how lattice QCD can help.

As a consequence of the symmetries in the flavour sector and of the diagonal nature of the mass matrix, flavour–changing currents with no net electric charge exchange (FCNC) are prohibited at tree–level [21]. This suppression of FCNC in the SM could be affected by the presence of heavy particles due to NP. BSM models wich predict new resonances can lead to enhanced FCNC, which will then appear in experiments. Therefore, it is important to study FCNC processes at higher orders (e.g. the one–loop box diagram in Fig. 1.1) and compare them to SM predictions.

1.2 Gauge–Higgs unification

We focus now on extra–dimensional theories as an attempt to solve the hierarchy problem of the Higgs sector, or rather to explain the large energy difference between the EW scale $v \sim \mathcal{O}(100 \text{ GeV})$ and the Planck scale $M_{Pl} \sim 10^{19}$ GeV. Historically, the introduction of extra dimensions dates back to 1920 [23, 24], when they were seen as a tool to unify the known forces in Nature, namely electromagnetism and gravity. In modern times the extra–dimensional approach

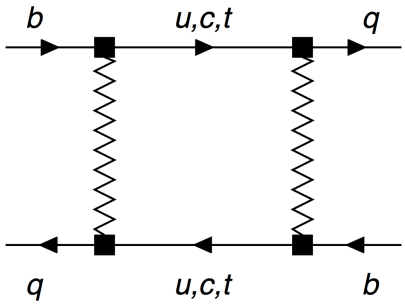

Figure 1.1 *An example of a FCNC relevant to the case of oscillations between a B_q meson and its anti–particle $\bar{B}_q$. Since this kind of diagrams are suppressed in the SM, they can hide NP signals. The picture is taken from Ref. [22].*

has been pursued aiming at the construction of a grand unified theory (GUT) [25] where all forces have a common origin at a scale $M_{\rm GUT} \sim 10^{16}$ GeV.

There is a large variety of extra–dimensional models which extend the SM. Each of them has rather clear phenomenological signatures that can be looked for at the LHC. Although no signal of the most studied models has been detected in experimental searches so far, they are valid theoretical tools which can explain the lightness of the Higgs boson and the mechanism of DEWSB [26].

In the following we introduce the Gauge–Higgs unification (GHU) scenario [27–29] in which the Higgs field is not a scalar elementary degree of freedom like in the SM, but a component of the higher–dimensional gauge field arising after compactification of an extra dimension. In this scenario the scalar field appearing in four dimensions shares the same nature as the higher–dimensional vector bosons, hence its mass is protected by the extended gauge symmetry.

The importance of extra–dimensional models in relation to the Higgs particle discovered at the LHC and the hierarchy problem is reviewed in recent papers [8, 30]. Before the Higgs discovery, however, GHU models were also able to estimate its mass $m_H \sim 125 \pm 4$ GeV [31], which is astonishingly close the the experimental value observed at the LHC.

1.2.1 Dimensional reduction

Let us introduce the basic ingredients to obtain a four–dimensional effective gauge theory, by compactifying a five–dimensional one. To simplify the treatment in this section, we start from a SU(N) Yang–Mills theory in five dimensions with

no fermions.

We can write the action generically as

$$\mathcal{S}_{5d} \;=\; \mathrm{Tr} \int \mathrm{d}^4x \int \mathrm{d}y \; -\frac{1}{2} F_{MN} F^{MN} \;, \tag{1.4}$$

where M, N are space–time indices going from 1 to 5, and we will use μ and ν for the usual four–dimensional ones. The extra spatial coordinate y has also been introduced in the equation above. The contribution of the fifth component of the field–strength tensor can be highlighted

$$\mathcal{S}_{5d} \;=\; \mathrm{Tr} \int \mathrm{d}^4x \int \mathrm{d}y \; -\frac{1}{2} F_{\mu\nu} F^{\mu\nu} - F_{\mu 5} F^{\mu 5} \;. \tag{1.5}$$

By imposing periodic boundary conditions (PBC) for the gauge fields in the extra direction, we compactify the y coordinate such that $y \to R\phi$, where R represents the radius of the compact direction and $\phi \in [-\pi, \pi]$ is now an angular coordinate. The components of the gauge fields $A_M(x, y)$ can be expanded in Fourier modes and the momenta in the extra dimension are discretised due to PBC.

For example, we have

$$A_\mu(x, \phi) \;=\; A_\mu^{(0)}(x) + \sum_{n=1}^{\infty} \left[A_\mu^{(n)}(x) e^{in\phi} + A_\mu^{(n)\star}(x) e^{-in\phi} \right] \;, \tag{1.6}$$

for the four components μ and, by going to an almost axial gauge, we obtain

$$A_5(x, \phi) \;=\; A_5^{(0)}(x) \;, \tag{1.7}$$

for the extra spatial component. The superscript denotes the mode number n, or equivalently the units of quantised momentum entering the extra dimension. We note that the static modes $A_\mu^{(0)}$ and $A_5^{(0)}$ depend only on four–dimensional coordinates and can be therefore interpreted as four–dimensional fields. They correspond to one vector gauge field and one scalar field, all transforming in the adjoint representation of the original gauge group.

By neglecting higher powers of the gauge fields (indeed all the terms coming from the commutators in F_{MN}), we can rewrite Eq. (1.4) in terms of the Fourier modes, also known as Kaluza–Klein (KK) modes in this context. We get an

effective four–dimensional action

$$\begin{aligned}\mathcal{S}_{4d} \;&= 2\pi R\ \mathrm{Tr}\ \int \mathrm{d}^4x \left\{ -\frac{1}{2}(\partial_\mu A_\nu^{(0)} - \partial_\nu A_\mu^{(0)})^2 + \frac{1}{2}(\partial_\mu A_5^{(0)})^2 \right. \\ &\left. + \sum_{n=1}^{\infty} \big[-\frac{1}{2}|\partial_\mu A_\nu^{(n)} - \partial_\nu A_\mu^{(n)}|^2 + \frac{n^2}{R^2}|A_\mu^{(n)}|^2 \big] \right\} .\end{aligned} \tag{1.8}$$

The action above can be interpreted as a four–dimensional theory where the effects of the original extra–dimensional nature are hidden in an infinite tower of particles with masses $m_{KK}^2(n) = n^2/R^2$. In other words, even though we do not see the extra dimension because it is compactified, we can infer an higher–dimensional nature of the system by attributing the mass of KK particles to the momentum flowing into the y direction.

To describe only a low–energy regime for this theory with $E \ll 1/R$, the KK masses can be integrated out, and the following effective action remains

$$\mathcal{S}_{\text{eff}} \;\sim\; 2\pi R\ \mathrm{Tr}\ \int \mathrm{d}^4x\ -\frac{1}{2}F_{\mu\nu}^{(0)}F^{(0)\mu\nu} + (D_\mu A_5^{(0)})^2 \ . \tag{1.9}$$

It is easy to see the attractive features of this dimensionally reduced action: by starting with a five–dimensional action describing only gauge fields at high energy, we end up with an action in four dimensions where ordinary gauge fields are coupled to a massless scalar field $A_5^{(0)}$. Such scalar field can not be identified with the Higgs field due to its adjoint nature in this model.

The identification of the scalar field with the Higgs boson can be made in more complicated models which have a different topology in the extra direction and also different boundary conditions. For example, by imposing an orbifold topology S^1/Z_2 where the compactified circle is reduced to an interval by the identification of $y \leftrightarrow y - \pi R$, the fifth component of the extra–dimensional gauge potential become the Higgs doublet. Moreover, the orbifold topology is suitable for defining chiral fermions, which, on the contrary, would not exist in the S^1 setup.

On the orbifold, the gauge symmetry group is broken by the boundary conditions imposed on the four–dimensional hyper-surfaces at $y = 0$ and $y = \pi R$. This feature can be used to obtain the EW symmetry breaking of the SM, for example, but we will not discuss this possibility in this thesis.

1.2.2 Radiative corrections

One then wonders about possible radiative corrections to the tree–level zero mass of the scalar field. Indeed, the original gauge invariance has been spoiled by the removal of the KK tower, at least at low energy. One–loop corrections to the scalar mass have been calculated for this simple model [32, 33] using the effective theory in Eq. (1.8). They are finite in the sense that they do not depend on the ultraviolet cutoff used to regularise the theory. This is in sharp contrast with Eq. (1.3) for example.

General arguments [34] clarify that the result obtained using the effective four–dimensional theory is unchanged even when considering an ultraviolet finite completion of the theory, e.g. a lattice regularised theory or a bosonic string theory. In fact, the relevant properties are captured by the effective description as long as locality and gauge invariance are preserved by the UV completion.

The result for the one–loop perturbative correction to the scalar mass m_5 can be written as

$$\delta m_5^2 \;=\; \frac{9 g_5^2 N}{32\pi^3 R^3}\zeta(3)\;, \tag{1.10}$$

where g_5^2 is the original five–dimensional gauge coupling and $\zeta(3)$ the Riemann function.

This relation between the mass of the scalar particle in the dimensionally reduced model and the compactification radius of the original higher–dimensional theory is the one we are after with non–perturbative methods in Chapter 2. The hierarchy between the mass of all KK modes shown before, $m_{KK}^2(n) = n^2/R^2$, and the mass of the scalar zero–mode coming from radiative corrections Eq. (1.10) is given by the smallness of the coupling constant in the perturbative calculation. It is important to check if the result of non–perturbative simulations is compatible with this expectation.

As a minor comment we underline that the mechanism to obtain a light scalar through dimensional reduction as described above, is not directly related to the Higgs boson of the SM. It is however an interesting theoretical framework where a scalar field with a mass protected from cutoff effects is present. If such a situation persists even in the non–perturbative regime, we would have even stronger interest in GHU models, which usually rely strongly on perturbative arguments.

1.3 Walking Technicolor

In Sec. 1.1.2 we have mentioned that the hierarchy problem can be solved by introducing a new symmetry protecting the Higgs mass from large radiative corrections. Leaving out supersymmetry, we consider the alternative approach of Technicolor which, in its original form, employs features already present in QCD.

Technicolor (TC) [35–37] is a BSM model involving an extra gauge group $\mathrm{SU}(N_{\mathrm{TC}})$, together with the corresponding gauge bosons and a number N_f^{TC} of fermions, called techni–quarks. The analogy with QCD is already present in the name. Other QCD–like aspects of this model are asymptotic freedom at high energies and spontaneous chiral symmetry breaking at low energies.

1.3.1 Electroweak symmetry breaking and mass generation

The idea of TC is essentially to break the EW symmetry of the SM through the techni–quark condensate which, as in QCD, makes the vacuum non–invariant under the symmetries of the Lagrangian.

In QCD, through chiral perturbation theory one can describes the interactions between the pseudo–goldstone bosons of the spontaneously broken chiral symmetry, namely the three pions, and the gauge bosons of the EW sector. The mechanism which in the Higgs sector allows three of the four degrees of freedom in the Higgs field to be rearranged to give masses to the vector gauge bosons, is reproduced analogously in this case. For QCD coupled to the EW sector, the three pions provide masses for the W and Z bosons.

Unfortunately this process does not reproduce the correct experimental masses e.g. $m_W \sim 80$ GeV, but it can only account for a $\sim 0.04\%$ fraction. This is related to the intrinsic low scale of QCD, $\Lambda_{\mathrm{QCD}} \sim 100$ MeV which translates in a small pion decay constant $f_\pi \sim 93$ MeV.

In TC the physical EW gauge boson masses can be reached through a similar mechanism by replacing quarks with techni–quarks and allowing for a higher energy scale $\Lambda_{\mathrm{TC}} \sim 100$ GeV $\gg \Lambda_{\mathrm{QCD}}$. In fact, by imposing that the decay constant of the techni–pions is of the order of the EW scale v, one can easily obtain $m_W \sim 80$ GeV.

Although TC provides an elegant way to dynamically break the EW symmetry without introducing any scalar field, it can not by itself explain the origin of fermion masses in the SM. Therefore, one introduces an extended TC (ETC) [38, 39] sector with additional particles at an even higher energy scale $\Lambda_{\mathrm{ETC}} \gg \Lambda_{\mathrm{TC}}$. The gauge symmetry of the ETC sector is somehow broken down to the TC group at the scale Λ_{TC} and the effective theory arising at lower energies contains both the TC features described above and effective four–fermions interactions which couple techni–quarks with SM quarks, providing the latter with a mass term. Such four–fermions interactions arise by integrating out the ETC gauge bosons which couples techni–quarks with SM fermions, in a similar manner as the diagram depicted in Fig. 1.1.

Since the techni–quarks form a condensate at low energy, the mass term for the SM fermions can be written as

$$m_q \sim G_{4f} \frac{\langle \bar{Q}Q \rangle}{\Lambda^2_{\mathrm{ETC}}} \sim G_{4f} \frac{N_{\mathrm{TC}} \Lambda^3_{\mathrm{TC}}}{\Lambda^2_{\mathrm{ETC}}} \ , \tag{1.11}$$

where G_{4f} is the effective coupling of four–fermions interactions, and $\langle \bar{Q}Q \rangle$ is the techni–quark condensate at the ETC scale.

To get reasonable SM quark masses e.g. $m_q = m_c \sim 1$ GeV, one requires $\Lambda_{\mathrm{ETC}} \sim 1000$ GeV (assuming a natural $G_{4f} \sim 1$). Unfortunately, it can be shown that four–fermions interactions arising from ETC but with only SM fermions allow for FCNC which do not satisfy current experimental limits. In other words, with the setup described above one either gets enhanced FCNC and experimental quark masses, or experimentally observed bounds on FCNC but too small $\lesssim 100$ MeV SM quark masses.

More details on TC and ETC phenomenology can be found in Ref. [9]. In the following we introduce a possible solution to the aforementioned problem.

1.3.2 Walking dynamics

In order to suppress FCNC coming from ETC four–fermion interactions involving SM quarks, an ETC scale $\Lambda_{\mathrm{ETC}} \sim 10^6$ GeV is needed. Since this appears in the denominator of Eq. (1.11) and $\Lambda_{\mathrm{ETC}} \gg \Lambda_{\mathrm{TC}}$, this mechanism only produces small fermion masses in the SM.

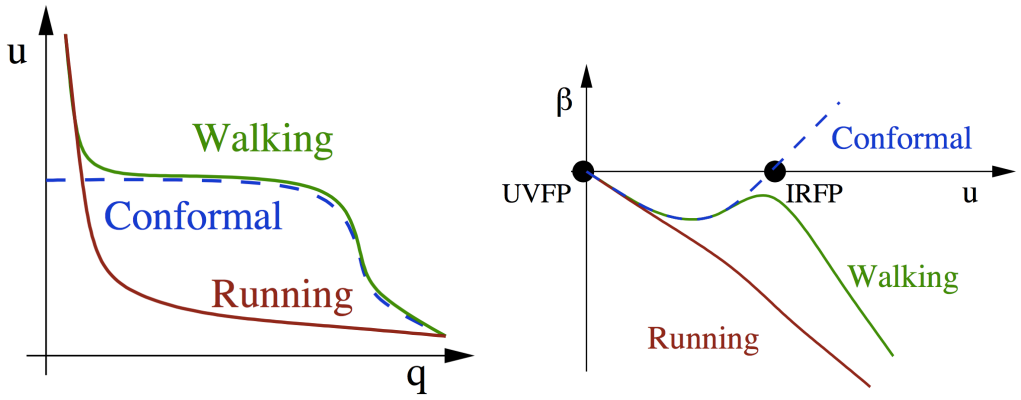

(a) *Coupling u as a function of the energy q.*

(b) *Beta function β as a function of the coupling u.*

Figure 1.2 *Running coupling and beta function in gauge theories with different infrared behaviour: running, walking and conformal. Pictures are taken from Ref. [40].*

It was suggested that a TC model with a different beta function with respect to QCD could have solved the problem. By considering TC radiative corrections to the four–fermions operators, the behaviour of the TC coupling constant $\alpha_{\rm TC}(\mu)$ between $\Lambda_{\rm TC} < \mu < \Lambda_{\rm ETC}$ strongly affects Eq. (1.11).

The techni–quark condensate acquires a renormalization factor which relates its value at the two energy scales

$$\langle \bar{Q}Q \rangle_{\rm ETC} = e^{\int_{\Lambda_{\rm TC}}^{\Lambda_{\rm ETC}} \gamma(\alpha_{\rm TC}(\mu)) \frac{d\mu}{\mu}} \langle \bar{Q}Q \rangle_{\rm TC} \ , \tag{1.12}$$

according to its anomalous dimension $\gamma(\alpha_{\rm TC}(\mu))$.

With a QCD–like beta function for the TC theory, the running of the coupling would be logarithmic and the renormalization factor would be irrelevant. However, if the TC has a conformal fixed point where a fixed coupling constant $\alpha_{\rm TC}(\mu) = \alpha^\star$ is reached in the infrared, and $\beta(\alpha^\star) = 0$, then there is a power–law enhancement of the techni–quark condensate at the ETC scale thanks to radiative corrections:

$$\langle \bar{Q}Q \rangle_{\rm ETC} = \left(\frac{\Lambda_{\rm ETC}}{\Lambda_{\rm TC}} \right)^{\gamma(\alpha^\star)} \langle \bar{Q}Q \rangle_{\rm TC} \ . \tag{1.13}$$

Even an approximately constant coupling for a large range of energies between the TC and ETC scale suffices to enhance the SM fermion masses in Eq. (1.11) and, at the same time, to keep unwanted FCNC under control. The difference between the behaviour of the beta function and the coupling in a QCD–like (running),

conformal, or approximately conformal (walking) theory is shown in Fig. 1.2. We will discuss the consequences of a walking dynamics in more details in Sec. 3.1, with an eye on the role of lattice simulations.

The realisation of TC with a walking coupling constant is called Walking Technicolor (WTC) [41]. By requiring that the techni–condensate anomalous dimension is $\mathcal{O}(1)$ in this setup, it is possible to satisfy all experimental constraints on the model [42, 43]. It is important to notice that the theory we are dealing with is a strongly–coupled one. Therefore it is advisable to treat it with non–perturbative methods if one is interested in the long–range (infrared) properties. Chapter 3 introduces a lattice study of a theory which is a candidate for WTC.

1.3.3 Compositeness

By discussing TC and WTC so far, we have not yet introduced a Higgs–like particle. The EW symmetry is broken by a mechanism that is similar to the one in place already in QCD, and there seems to be no sign of a scalar field. However, one must comply with the Higgs discovery and explain how such a particle can show up in a WTC model.

In WTC the scale invariance is broken by the presence of a dynamical fermion mass arising through spontaneous chiral symmetry breaking in the infrared. The connection between the symmetric scale invariant phase and the broken one is characterised by a continuous transition [44].

Once in the broken phase, a pseudo–goldstone boson related to the broken generators of the conformal symmetry is expected to appear at low energy, even though the scale invariance is broken explicitly as well (a more detailed discussion on this matter can be found in Ref. [44] and Ref. [45]). This boson is actually a composite scalar, formed by combining a techni–quark and anti–quark in a chirally and flavour invariant way, since it couples to the trace of the energy–momentum tensor.

This composite scalar was originally referred to as a techni–dilaton [42, 43] due to its relation with the dilatation current of the WTC. Thanks to its nature as a pseudo–goldstone boson, its mass is protected by large radiative corrections in a similar manner as the pion in QCD appears to be much lighter than other states due to approximate chiral symmetry.

By using non–perturbative analytic techniques such as Ladder equations and the holographic principle, it was shown that the discovered Higgs boson can be interpreted as a techni–dilaton arising in a WTC theory [46, 47].

It becomes of paramount importance for the lattice community to provide additional tools for the search of such a light composite scalar in candidate theories for WTC. If one could devise a WTC model which also includes a non–perturbative light scalar particle, as a bound state of techni–quarks, this may provide some evidence for BSM physics already at the LHC.

Our lattice calculation in Chapter 3 explicitly shows that such a state exists in a WTC candidate theory. Other evidence from lattice studies has been recently shown at the Lattice conference and preliminary studies with different candidate models, including different number of fermions in various representations of the gauge group, are available [48, 49].

1.4 Flavours and heavy quarks physics

In this last section we briefly introduce the phenomenology of heavy quarks, in particular focusing on neutral B meson mixing. FCNC and semileptonic decays involving heavy quarks are loop–suppressed in the SM. The contributions from BSM particles to such processes may therefore be comparable to the SM ones.

From B_d and B_s meson oscillations, which occur, at lowest order, through the box diagram in Fig. 1.1, one can extract the CKM matrix elements $|V_{td}|$ and $|V_{ts}|$. Moreover, constraints on the unitarity of the CKM matrix can be obtained by comparing the B_d and B_s oscillation frequencies.

In a similar manner to K^0–$\bar{K}^0$ mixing [50], one can study B_q meson mixing, where $q = d,\ s$. The oscillation between the particle and anti–particle is governed by an effective 2×2 Hamiltonian, defined by the hermitean mass M^q_{ij} and width Γ^q_{ij} matrices:

$$H^q_{\text{eff}} \equiv M^q_{ij} - \frac{i}{2}\Gamma^q_{ij} \ ; \qquad i\frac{\partial \left|\psi^q(t)\right\rangle}{\partial t} = H^q_{\text{eff}} \left|\psi^q(t)\right\rangle \ . \tag{1.14}$$

The off–diagonal elements M^q_{12} and Γ^q_{12} are non–zero and this allows for a B_q meson at time $t = 0$ to oscillate into a $\bar{B}_q$ at later time t, or into a superposition of the two. The usual procedure amounts to a diagonalisation of the effective Hamiltonian to get the mass and CP eigenstates, one heavier (H) than the

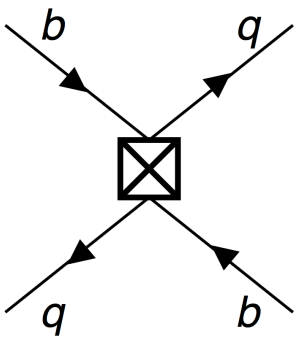

Figure 1.3 *An example of a four–quark effective operator relevant to the case of oscillations between a B_q meson and its anti–particle $\bar{B}_q$. The operator allows for a $|\Delta B| = 2$ transition and it is written on in Eq The picture is taken from Ref. [22].*

other (L). Their mass difference corresponds to the frequency of the oscillations between particle and anti–particle

$$\Delta m_q = M_H^q - M_L^q \approx 2|M_{12}^q| \ , \tag{1.15}$$

where we used the eigenvalues M_H^q and M_L^q corresponding to the heavy and light eigenstate, respectively.

In the SM, the mass difference can be calculated by replacing the box diagram in Fig. 1.1 with an effective four–quark operator as in Fig. 1.3. This operator is defined as

$$\mathcal{O}_{\Delta B=2}^{\rm SM} \ = \ \big(\bar{q}\gamma_\mu(1-\gamma_5)b\big)\big(\bar{q}\gamma_\mu(1-\gamma_5)b\big) \ , \tag{1.16}$$

and its matrix element can be expressed in terms of the B_q decay constant f_{B_q}, mass m_{B_q} and bag parameter B_{B_q}

$$\langle B_q|\, \mathcal{O}_{\Delta B=2}^{\rm SM}\, |\bar{B}_q\rangle = \frac{8}{3} f_{B_q}^2 m_{B_q}^2 B_{B_q} \ . \tag{1.17}$$

The matrix element needs to be renormalized at some energy scale μ together with bag parameter $B_{B_q}(\mu)$. A precise measurement of these quantities can be done on the lattice, as we will explain further in Chapter 4, and indeed many phenomenological predictions of mixing parameters use lattice averages [51].

When putting all the above ingredients together, and including short–distance contributions in the form of a Wilson coefficient C known perturbatively, we obtain the oscillation frequency as a function of CKM parameters and the matrix

element

$$\Delta m_q = |V_{tq}^{\star} V_{tb}|^2 C \, \langle B_q | \, \mathcal{O}_{\Delta B=2}^{\mathrm{SM}} \, | \bar{B}_q \rangle \ . \tag{1.18}$$

Experiments provide precise values for both Δm_d and Δm_s [51], while the lattice can measure the hadronic matrix element non–perturbatively. Consequently, an estimate of the CKM matrix elements is obtained.

Conversely, one could extract $|V_{tq}^{\star} V_{tb}|^2$ through other channels and unitarity fits and then compare the resulting mass differences with experiments. This last procedure shows that with nowadays lattice results for Eq. (1.17) and their theoretical error, there is still room for NP [11, 22, 52].

In Chapter 4 we will argue that more work is needed to extract heavy quarks matrix elements reliably from the lattice. A recent attempt to create a common strategy towards precise lattice calculations for B physics can be found in Chapter 8 of Ref. [53].

Chapter 2

Scalar spectrum in extra–dimensional models

The first model of BSM physics that we study in this thesis, is a five–dimensional Yang–Mills theory with non–Abelian gauge group SU(2). Although the results presented here are not phenomenologically relevant for physics at the LHC, the simple toy model investigated in the following sections provides insights on the cutoff independence of scalar particle masses in extra–dimensional theories, beyond perturbative calculations. The details of the study reported in this chapter have been published in two conference proceedings [54, 55] and two refereed journal papers [1, 56].

2.1 The five–dimensional lattice model

We are interested in describing the low–energy physics of a continuum five–dimensional SU(N_c) pure gauge theory in the regime where it is dimensionally reduced to four dimensions. It is in this regime that one can identify the appearance of a scalar field whose mass is protected from quadratic cutoff effects, thanks to a remnant of the higher–dimensional gauge symmetry. This scalar mass can be computed using perturbation theory, as explained in Sec. 1.2. The first radiative correction to the tree–level zero mass of the scalar turns out to be

$$\delta m^2 \;=\; \frac{9 g_5^2 N_c}{32\pi^3 R^3}\zeta(3)\;, \tag{2.1}$$

where g_5^2 is the gauge coupling constant of the five–dimensional theory with compactification radius R. ζ is the Riemann Zeta–function. The aim of our study is to investigate the spectrum of scalar bound states with non–perturbative methods and to shed light on the fate of Eq. (2.1) in a regime where the coupling constant is not naturally small.

2.1.1 Define an effective theory

The continuum, five–dimensional Yang–Mills theory we consider is defined by the Euclidean action

$$\mathcal{S} \;=\; \int \mathrm{d}^4x \int_0^{2\pi R} \mathrm{d}x_5 \, \frac{1}{2g_5^2} \mathrm{Tr}\; F_{MN}^2 \;. \tag{2.2}$$

The dimensionful gauge coupling g_5^2 and the radius R of the extra dimension, whose coordinate is x_5, parametrize the theory in the continuum. The field–strength tensor F_{MN} is the extra–dimensional generalization of the four–dimensional one

$$F_{MN} \;=\; \partial_M A_N - \partial_N A_M + i[A_M, A_N] \quad M, N = 1, \ldots, 5 \;, \tag{2.3}$$

where A_M is the gauge potential for the non–Abelian gauge group SU(N_c).

From dimensional analysis, we know this theory is naively non–renormalizable because $[g_5^2]^{-1} = \text{mass}$. Hence, it can not be considered as a fundamental theory valid at arbitrarily high energies. The action in Eq. (2.2) should be considered as an effective field theory in five dimensions, where only the lowest dimensional operators, allowed by gauge symmetry, have been taken into account. Operators with higher dimensionality, and their corresponding couplings, could be added in principle, but they will be suppressed by increasing powers of the cutoff energy Λ_{UV}. This ultraviolet cutoff is needed to tame divergences in the Green functions and will not be removed from the theory. On the other hand, the power of this effective field theory approach lies in the fact that physics at energies well below the cutoff scale $E \ll \Lambda_{\mathrm{UV}}$, is insensitive to the ultraviolet effects.

Low–energy physical observables for the five–dimensional theory defined by the action Eq. (2.2) can be computed. However, a suitable regularization must be defined. In the following, we adopt a gauge–invariant regulator and we define a discretised action on a five–dimensional lattice: the finite lattice spacing a determines the shortest propagating wavelength, i.e. $\Lambda_{\mathrm{UV}} \sim a^{-1}$. Since the extra

dimension plays a special role, being small and compactified on a circle, it is convenient to define two independent lattice spacings a_4 and a_5 on the lattice. The first one corresponds to the lattice spacing in the four–dimensional subspace, which has an infinite volume in the continuum, whereas the second lattice spacing is defined only in the extra fifth direction. This anisotropy $a_4 \neq a_5$ enlarges the parameter space of the model, as we will see in the following, and allows us to reach smaller compactification radii R in physical units. The inverse of the cutoff, in this case, is the bigger of the two lattice spacings, $\Lambda_{\rm UV}^{-1} \propto \max(a_4, a_5)$.

The correspondence between continuum degrees of freedom and lattice ones proceeds as follows. The continuum gauge potential $A_M(x_M)$ is replaced by gauge link variables $\mathcal{U}_M(x)$ joining the site x and the site $x + a\hat{M}$, where $a = a_4$ if $M = 1, 2, 3, 4$ and $a = a_5$ if $M = 5$. Since the fields are defined on a finite number of sites, we must impose boundary conditions. We choose periodic boundary conditions for the gauge links in all five directions, to be consistent with the compactification of the extra dimension in the continuum, where the gauge potential is defined with $2\pi R$ periodicity.

Among the possible discretisations for the action Eq. (2.2), we choose the simple Wilson plaquette action that incorporates two independent lattice spacings: the anisotropic lattice Wilson action. For a generic SU(N_c) gauge group, it is written as follows:

$$\mathcal{S}_W \;=\; \beta_4 \sum_{x;1\leq\mu<\nu\leq 4} \left[1 - \frac{1}{N_c}\mathrm{ReTr}\; P_{\mu\nu}(x)\right] + \beta_5 \sum_{x;1\leq\mu\leq 4} \left[1 - \frac{1}{N_c}\mathrm{ReTr}\; P_{\mu 5}(x)\right] \;, \tag{2.4}$$

where $P_{\mu\nu}$ is the four–dimensional plaquette (μ and ν run from 1 to 4)

$$P_{\mu\nu}(x) \;=\; \mathcal{U}_\mu(x)\mathcal{U}_\nu(x + \hat{\mu}a_4)\mathcal{U}_\mu^\dagger(x + \hat{\nu}a_4)\mathcal{U}_\nu^\dagger(x) \;, \tag{2.5}$$

$P_{\mu 5}$ is the plaquette with two extra–dimensional gauge links

$$P_{\mu 5}(x) \;=\; \mathcal{U}_\mu(x)\mathcal{U}_5(x + \hat{\mu}a_4)\mathcal{U}_\mu^\dagger(x + \hat{5}a_5)\mathcal{U}_5^\dagger(x) \;, \tag{2.6}$$

and the sum $\sum_x$ runs on all the lattice sites x of the full five–dimensional lattice volume. The two plaquette terms have different coupling constants β_4 and β_5, each controlling one of the lattice spacings via dimensional transmutation.
The anisotropic Wilson action has already been used to study this particular five–dimensional lattice model in Refs. [2, 57–61]. An equivalent and often used

parametrization of Eq. (2.4) is

$$\mathcal{S}_W \;=\; \frac{\beta}{\gamma}\sum_{x;1\leq\mu\leq\nu\leq 4}\left[1-\frac{1}{N_c}\mathrm{ReTr}\;P_{\mu\nu}(x)\right]+\beta\gamma\sum_{x;1\leq\mu\leq 4}\left[1-\frac{1}{N_c}\mathrm{ReTr}\;P_{\mu 5}(x)\right]\;, \tag{2.7}$$

where the redefined lattice coupling constant is

$$\beta \;=\; \sqrt{\beta_4\beta_5}\;, \tag{2.8}$$

and the second parameter is the so–called bare anisotropy

$$\gamma \;=\; \sqrt{\frac{\beta_5}{\beta_4}}\;. \tag{2.9}$$

The numerical results presented in the rest of this chapter have been obtained from simulations using the action Eq. (2.4). However, we use both the aforementioned parametrizations to explain our findings, in particular when comparing to existing results in the literature.

2.1.2 Lattice parameters dictionary

To summarise, we have defined a five–dimensional lattice model with the action Eq. (2.4) which is the leading order discretisation of the continuum theory Eq. (2.2). The former is a possible regularization of the non–renormalizable continuum theory, and they are both considered as effective theories. In particular, the lattice model serves as a tool to extract physical information for the dynamics of the full continuum theory in the low–energy limit, where the details of the regularization are negligible.

We want to be able to translate the parameters and observables in the lattice model, to the parameters and physical quantities of the continuum theory. Therefore, we start by analysing the relation between the lattice bare coupling constants β_4 and β_5 and the bare gauge coupling in the continuum g_5^2. The action Eq. (2.4) reduces to Eq. (2.2) at leading order when $(a_4,a_5)\to 0$, if the following relations hold:

$$\beta_4 \;=\; \frac{2N_c a_5}{g_5^2} \tag{2.10}$$

$$\beta_5 \;=\; \frac{2N_c a_4^2}{g_5^2 a_5}\;. \tag{2.11}$$

Similarly, for the action in Eq. (2.7) we have

$$\beta \;=\; \frac{2N_c}{g_5^2} a_4 \;, \tag{2.12}$$

and

$$\gamma \;=\; \frac{a_4}{a_5} \equiv \xi \;. \tag{2.13}$$

We must stress that from Eq. (2.10) to Eq. (2.13), the equal sign holds at the leading order (tree level) in the classical continuum limit. By fixing the coupling constants (β_4,β_5), or equivalently (β,γ), the two lattice spacing a_4, a_5 are defined quantum mechanically. Their ratio, defined by the renormalized anisotropy ξ, will deviate from the bare parameter γ due to quantum corrections. This deviation, as a function of β and γ itself, can be measured using suitable ratios of lattice observables and an example can be found in Ref. [2].

In the lattice model, which is defined on a finite set of points, there are two more parameters that can be adjusted. They are N_4, the number of lattice sites in each of the usual four directions, and N_5, the number of lattice sites in the extra dimension. When combined with their corresponding lattice spacings, they determine the physical size of the lattice system: $L_4 = a_4 N_4$ in four dimensions and $L_5 = 2\pi R = a_5 N_5$ in the fifth dimension. While L_4 should be always taken sufficiently large that the lattice system be considered in the infinite volume limit, L_5 is the size of the extra dimension and must be smaller than a limiting value in order to reach a dimensionally reduced phase, as explained in Sec. 2.3.2. On the other hand, if L_5 is large, a different mechanism of dimensional reduction might be in place, namely the localisation of some degrees of freedom on a four–dimensional hyper-surface (see Sec. 2.3.3).
In the following we restrict ourself to the non–Abelian gauge group SU(2), thus setting $N_c = 2$ in the above definitions.

2.1.3 Scale separations for the effective theory

We have already mentioned that the theory described by the action in Eq. (2.2) is perturbatively non–renormalizable because the five–dimensional coupling constant g_5^2 has negative mass dimension. The theory possesses another intrinsic scale when the extra dimension is compactified on the circle: the compactification scale $\Lambda_{\rm R} \sim R^{-1}$. Moreover, in order to do calculations in this effective theory, a cutoff $\Lambda_{\rm UV}$ is needed. In this section, we describe the separation between the

scales of the theory, both in the continuum and on the lattice. The main purpose is to identify the correct scale separations where we expect Eq. (2.1) to be verified. In the lattice model, this is non–trivial since the energy scales are dynamically generated.

At the classical level, the spectrum of the theory contains massless vectors, coming from the gauge field components in the four–dimensional subspace, and a massless scalar, coming from the gauge component in the extra compact direction. All the non–static Kaluza–Klein modes acquire masses proportional to Λ_{R}. In the quest for an effective description of the low–energy physics of the theory, one can integrate out the states at energies greater than the compactification scale, leaving a four–dimensional gauge field coupled to an adjoint massless scalar. This dimensionally reduced effective description is sensible only if there is a scale separation $\Lambda_{\mathrm{R}} \ll \Lambda_{\mathrm{UV}}$: the physics of the compactified theory is not affected by the details of the regularization.

If we focus on the low–energy $E \ll \Lambda_{\mathrm{R}}$ and weakly–coupled regime, we expect a perturbative spectrum, where the elementary scalar particle acquires a mass through radiative corrections, while the gauge vectors remain massless. As we explore more strongly–coupled regimes, the theory develops a non–perturbative mass gap related to confinement. The five–dimensional theory becomes difficult to study with perturbative methods and this is when we rely on the lattice model to be able to explore non–perturbative physics using numerical simulations.

The main goal of the numerical study is to understand whether the non–perturbative low–energy dynamics of the full five–dimensional theory can be described by a four–dimensional effective gauge theory coupled to a light adjoint scalar, whose mass is decoupled from the cutoff scale as suggested by the one–loop equation Eq. (2.1). Moreover, it would be interesting to find a region where the scalar mass is of the order of the mass gap in the gauge sector, so that the scalar and gauge sectors are not decoupled. It must be stressed that the simulations will be done for a theory that is five–dimensional in the ultraviolet.

The hierarchy of scales we would like to find non–perturbatively in the lattice theory is the following:

- first we need the cutoff scale of the five–dimensional theory to be well above the compactification scale, where dimensional reduction to four dimensions

take place

$$\frac{\Lambda_{\rm UV}}{\Lambda_{\rm R}} \gg 1 \ . \tag{2.14}$$

- then, low–energy physics must be separated from both the cutoff and the compactification scales. Only in this case we expect the long distance physics to be independent of the actual regularization of the theory, and not to be sensitive to contributions from higher modes. The mass gap identified by the string tension $\sqrt{\sigma}$ in four dimensions should appear as

$$\sqrt{\sigma} \ll \Lambda_{\rm UV} \ ; \qquad \sqrt{\sigma} \ll \Lambda_{\rm R} \ . \tag{2.15}$$

  In other words, since the string tension gives the inverse of the four–dimensional correlation length, when $\sqrt{\sigma}$ is small compared to the cutoff, then the characteristic length of the system is much larger than the lattice spacing, and the details of the discretisation of the theory should become insignificant.
  The same should be true for the static scalar state mass m_5

$$m_5 \lesssim \sqrt{\sigma} \ ; \qquad m_5 \ll \Lambda_{\rm UV} \ ; \qquad m_5 \ll \Lambda_{\rm R} \ . \tag{2.16}$$

- moreover, we also want to check the dependence of the scalar mass on the cutoff and the compactification radius, and see if it can be described simply by

$$m_5^2 \propto \frac{g_5^2}{R^3} \ . \tag{2.17}$$

  This would imply that scalar particles coming from higher–dimensional theories upon compactification do not suffer from quadratic cutoff effects.

In the following, we choose to express the energy scales above in units of the four–dimensional string tension $\sqrt{\sigma}$, which is the lightest one in the four–dimensional effective theory. Hence, the other three scales in the theory are characterised by three dimensionless ratios. The ultraviolet cutoff $\Lambda_{\rm UV}$, given by the inverse of the largest lattice spacing of the model, is

$$\frac{\Lambda_{\rm UV}}{\sqrt{\sigma}} \equiv \frac{1}{a_4\sqrt{\sigma}} \ , \tag{2.18}$$

because we will be dealing mostly with anisotropies $\xi = \frac{a_4}{a_5} \geq 1$. Similarly, the

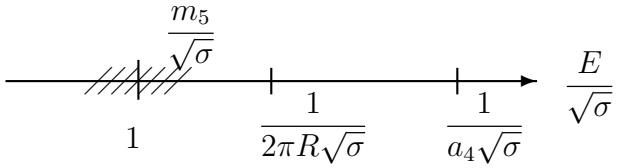

Figure 2.1 *The figure shows the desired separation of energy scales. The scales are all expressed in terms of the four–dimensional string tension that characterises the low–energy physics of the theory. The region of energies where we expect the scalar mass to lie is also highlighted.*

compactification scale $\Lambda_{\rm R}$ is

$$\frac{\Lambda_{\rm R}}{\sqrt{\sigma}} \equiv \frac{1}{2\pi R\sqrt{\sigma}} = \frac{1}{a_5 N_5\sqrt{\sigma}} \ . \tag{2.19}$$

Finally, the scalar mass m_5 can be expressed as the ratio of the scalar mass and the string tension both measured in units of the lattice spacing a_4 in our simulations:

$$\frac{m_5}{\sqrt{\sigma}} = \frac{a_4 m_5}{a_4\sqrt{\sigma}} \ . \tag{2.20}$$

In Fig. 4.1 we summarize pictorially the scale separation in the theory.

It is useful to introduce a special combination of lattice bare parameters reproducing the separation between the cutoff and the compactification scale

$$\frac{\Lambda_{\rm UV}}{\Lambda_{\rm R}} \equiv \frac{a_5 N_5}{a_4} = \frac{N_5}{\xi} \sim \frac{N_5}{\gamma} \ . \tag{2.21}$$

In the above equation, we used Eq. (2.13) which is a valid approximation only in the weak–coupling limit.

The three energy scales of the system, $\Lambda_{\rm UV}$, $\Lambda_{\rm R}$ and m_5 can be studied by adjusting the three bare parameters of the lattice model β_4, β_5 and N_5 (if N_4 is large enough for the four–dimensional subspace to be considered in the infinite volume limit). Fixing a point in the space (β_4,β_5,N_5), or equivalently (β,γ,N_5), will dynamically determine the two lattice spacings a_4 and a_5, together with the extent of the extra dimension $a_5 N_5$. Measuring the three scales with lattice simulations at different points of this bare parameter space is a powerful tool to explore the dependence of the scalar mass on a_4 and R, as we explain in Sec. 2.4: we explore a region of the phase space where R and a_4 vary independently and we try to follow, non–perturbatively, lines of constant scalar mass.

2.2 Perturbative expectations

Perturbation theory can be used as a guide to assess the behaviour of scales like the string tension and the scalar mass as functions of the parameters in the lattice model. The results in this section are expected to provide a sensible description of the numerical data only in the weak–coupling regime, because, for example, the scalar mass in Eq. (2.20) would be divergent in the perturbative regime ($\sqrt{\sigma} = 0$). Nonetheless, they are a useful to understand features of the lattice model like the possibility of defining a sensible continuum limit, as described in Sec. 2.2.3.

2.2.1 Coupling constant in the effective theory

Dimensional analysis allows us to rescale the bare dimensionful coupling constant g_5^2 of the continuum limit, and we can define a dimensionless coupling constant at the energy scale μ

$$\hat{g}_5^2(\mu) \equiv g_5^2(\mu)\mu \ . \tag{2.22}$$

At the cutoff scale $\Lambda_{\rm UV}$ we have

$$\hat{g}_5^2(\Lambda_{\rm UV}) = g_5^2(\Lambda_{\rm UV})\Lambda_{\rm UV} \ , \tag{2.23}$$

whereas at the compactification scale $\Lambda_{\rm R}$

$$\hat{g}_5^2(\Lambda_{\rm R}) = g_5^2(\Lambda_{\rm R})\Lambda_{\rm R} \ . \tag{2.24}$$

The effective four–dimensional gauge theory coupled to an adjoint scalar field that we obtain after compactification, has an effective dimensionless coupling constant g_4^2

$$\hat{g}_4^2 \equiv g_4^2 = \frac{g_5^2(\Lambda_{\rm R})}{2\pi R} \ . \tag{2.25}$$

Let us assume that the dimensionful coupling g_5^2 is independent of the scale, at least at leading order,

$$g_5^2(\Lambda_{\rm R}) = g_5^2(\Lambda_{\rm UV}) \ . \tag{2.26}$$

From this assumption it follows

$$\hat{g}_4^2 = \hat{g}_5^2(\Lambda_{\rm UV}) \left(\frac{\Lambda_{\rm R}}{\Lambda_{\rm UV}} \right) \ , \tag{2.27}$$

that shows how the effective four–dimensional coupling can be made arbitrarily small by increasing the scale separation in Eq. (2.14).

2.2.2 String tension and scalar mass in the lattice model

Let us look at the one–loop scaling relation between the gluonic scale given by the string tension in a four–dimensional SU(2) Yang–Mills theory and the gauge coupling:

$$\sigma \sim \frac{1}{(2\pi R)^2} \exp\left\{-\frac{1}{b_0 g_4^2(\Lambda_{\rm R})}\right\} , \tag{2.28}$$

where $b_0 = 11/24\pi^2$ is the first term in the perturbative β–function of the four–dimensional theory, and $g_4^2(\Lambda_{\rm R})$ is the effective dimensionless coupling constant at the compactification scale described in Sec. 2.2.1.
We aim at translating this expression in terms of the bare parameters in the lattice model. The result will be a relation between the cutoff of the model $\Lambda_{\rm UV}/\sqrt{\sigma}$ and its bare parameters valid in the weak–coupling limit. By using Eq. (2.28), together with Eq. (2.12) and Eq. (2.21), we write

$$\left(\frac{\Lambda_{\rm UV}}{\sqrt{\sigma}}\right)^{-2} = a_4^2\sigma \sim \frac{\gamma^2}{N_5^2} \exp\left\{-\frac{\beta N_5}{4 b_0 \gamma}\right\} . \tag{2.29}$$

We stress that this relation uses the tree–level relation between the lattice coupling β and the continuum gauge coupling $g_5^2(\Lambda_{\rm R})$ at the compactification scale. A successful use of this asymptotic formula has been shown in Refs. [58, 59], where the authors checked it numerically using lattice simulations with the action Eq. (2.7). This was done in a particular region of the parameter space (β,γ,N_5) of the model and in the limit $a_5 \to 0$,$N_5/\gamma = 2$ fixed. Such a study therefore indicates that there exists a specific limit of lattice parameters for which the model reproduces weak–coupling results of a dimensionally reduced five–dimensional gauge theory. In particular this means there is a scale separation between the static modes of the four–dimensional gauge fields and their higher Kaluza–Klein modes. The static scalar mode, however, has been shown to be already at the cutoff scale in that same parametric region, hence decoupled from the low–energy physics. Therefore, we should search for another set of parameters defining a low–energy theory where the static scalar mode can be thought as an effective degree of freedom.

In order to gain some insights into the behaviour of the scalar mass in the lattice

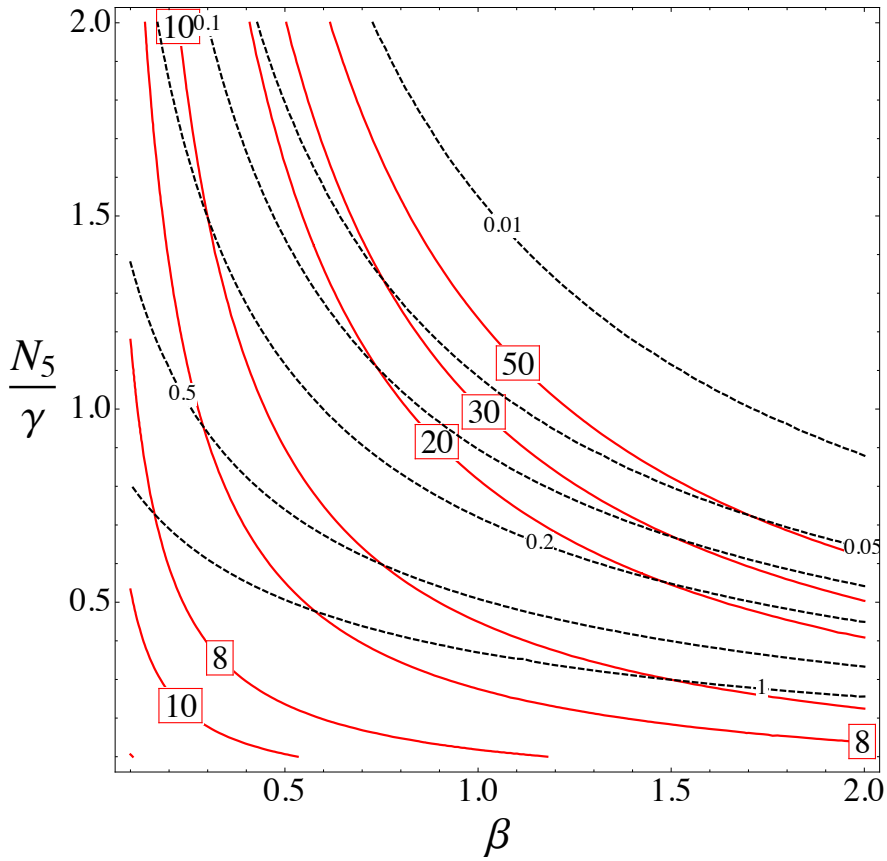

Figure 2.2 *The lines of constant lattice spacing in units of the string tension $a_4\sqrt{\sigma}$ are shown as dashed black lines in the plane $(\beta, N_5/\gamma)$. The lines of constant scalar mass in units of the string tension $m_5/\sqrt{\sigma}$ are shown with solid red lines.*

model, we are now going to assume Eq. (2.1) holds and we rewrite it in terms of β, γ, and N_5:

$$\frac{m_5}{\sqrt{\sigma}} \sim \sqrt{\frac{4\gamma}{\beta N_5}} \exp\left\{\frac{\beta N_5}{4N_c b_0 \gamma}\right\} . \tag{2.30}$$

These perturbative predictions, for the cutoff scale in units of the string tension Eq. (2.29) and for the scalar mass Eq. (2.30), can be plotted in the two–dimensional parameters plane $(\beta, N_5/\gamma)$. Lines of constant cutoff and scalar mass can be identified and some of them are shown in Fig. 2.2.

2.2.3 Removing the lattice regulator

If we assume that Fig. 2.2 represents the lines of constant physics in the bare $(\beta, N_5/\gamma)$ space, we can speculate about how to reach a continuum limit for this lattice model. By continuum limit, we mean the region where the cutoff Λ_{UV} of

the effective theory is separated enough from the low–energy physics, that the ultraviolet details of the model can be ignored and do not affect the measured observables.

Two different four–dimensional continuum theories can be described as the lattice spacing a_4 becomes smaller. The one we are interested in, a SU(2) Yang–Mills theory coupled to an adjoint scalar field, is described by the lattice model following a line of constant $m_5/\sqrt{\sigma}$ (one of the solid red lines in Fig. 2.2) towards smaller values of β and bigger values of N_5/γ. In this direction, $a_4\sqrt{\sigma}$ becomes smaller and smaller, while the scalar mass is kept fixed, and the effects of the regularization disappear.

It is interesting to note that this approach to the continuum limit happens by going towards higher values of N_5/γ, the scale separation $\Lambda_{\mathrm{UV}}/\Lambda_{\mathrm{R}}$ at tree-level. This means that the size of the extra dimension $2\pi R$ increases in units of the lattice spacing a_4, while the theory dimensionally reduces to four dimensions. An entirely similar scenario had already been suggested by the D–theory non–perturbative approach to quantum field theories [62, 63], and it would be interesting to study it from the numerical point of view.

A different four–dimensional continuum theory would appear when moving parallel to the coordinates axes in Fig. 2.2. It is easy to see that by going to larger β or, orthogonally, to larger N_5/γ, the lattice spacing vanishes. However, without fine tuning the parameters in such a way that the physical scalar mass remains constant, the scalar sector would be decoupled from the low–energy pure gauge dynamics. In this continuum limit, the four–dimensional theory would be Yang–Mills. This is the limit explored numerically by the authors of Ref. [59], where the scalar mass turns out to be at the cutoff scale.

A final remark. Let us stress again that Eq. (2.29) to Eq. (2.30) are found using one–loop continuum perturbative results and tree–level relations between the lattice parameters and the continuum ones. The lines of constant values for the cutoff $1/a_4\sqrt{\sigma}$ and for the scalar mass $m_5/\sqrt{\sigma}$ must be determined non–perturbatively using numerical simulations, and we shall see if and how they deviate from the perturbative expectations.

2.3 Investigate the phase diagram

A further issue arising in the study of the lattice model, is the possibility of having lines of phase transitions separating different phases of the lattice theory. Indeed, the perturbative predictions we referred to in Sec. 2.2 do not take into account the rich phase structure of the lattice theory. In this section, we discuss the current understanding of the phase diagram of the SU(2) pure gauge theory in five dimensions described by the action in Eq. (2.4). A cartoon of the known phase structure is shown in Fig. 2.3.

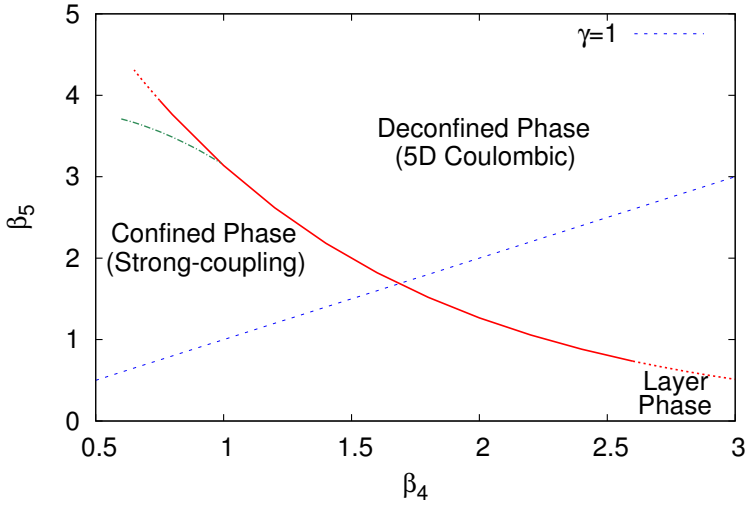

Figure 2.3 *Cartoon of the phase diagram for the lattice model described by the action Eq.* (2.4).

2.3.1 Isotropic model

We start the description of the phase diagram from the simplified model with a single parameter $\beta = \beta_4 = \beta_5$, or equivalently $\gamma = 1$ (cfr. the blue dotted line in Fig. 2.3). This isotropic model has a single lattice spacing $a = a_4 = a_5$, governed by the coupling constant, and it was studied in the pioneering work of Ref. [64]. Since then, more precise results on the phase diagram of this model were obtained by Ref. [61], which was published while the study presented in this Chapter was being completed.

The lattice observables we choose to monitor on this system are the following:

- plaquette

$$\langle P \rangle \;=\; \left\langle 1 - \frac{\sum_{M=1}^{5}\sum_{N=1}^{5}\sum_{x=1}^{N_4^4 N_5} \mathrm{ReTr}\; P_{MN}(x)}{80 N_4^4 N_5} \right\rangle \tag{2.31}$$

  whose discontinuity indicates a first order transition;

- temporal Polyakov loop

$$\langle L_t \rangle \;=\; \left\langle \frac{1}{2N_4^3} \left| \sum_{x=1}^{N_4^3} \mathrm{Tr}\; \prod_{i=1}^{N_4} \mathcal{U}_4(x + \hat{4} i a) \right| \right\rangle \tag{2.32}$$

  that monitors the centre symmetry in the temporal direction which, when compactified, plays the role of a temperature. It is defined at the origin of the extra dimension $x_5 = 0$, averaged over the three dimensional volume and normalized;

- extra dimensional Polyakov loop

$$\langle L_5 \rangle \;=\; \left\langle \frac{1}{2N_4^3} \left| \sum_{x=1}^{N_4^3} \mathrm{Tr}\; \prod_{i=1}^{N_5} \mathcal{U}_5(x + \hat{5} i a) \right| \right\rangle \tag{2.33}$$

  that monitors the centre symmetry in the extra 5^{th} direction. It is defined at the temporal origin $t = 0$, averaged over the three dimensional volume and normalized;

- and the corresponding susceptibilities

$$\chi_P \;=\; N_4^5 \left(\langle P^2 \rangle - \langle P \rangle^2 \right) \tag{2.34}$$

$$\chi_4 \;=\; N_4^3 \left(\langle L_t^2 \rangle - \langle L_t \rangle^2 \right) \tag{2.35}$$

$$\chi_5 \;=\; N_4^3 \left(\langle L_5^2 \rangle - \langle L_5 \rangle^2 \right) \tag{2.36}$$

When the geometry of the system is chosen such that $N_4 = N_5$, there is a phase transition for a particular value of $\beta = \beta_c \approx 1.64$, which correspond to a sudden jump of the plaquette expectation values and a hysteresis cycle. Moreover, by changing the dimensions of the lattice, β_c does not change. The aforementioned features are characteristic of a first order bulk phase transition. The bulk transition line separates a confined phase $\beta < \beta_c$, that is connected to the strong coupling regime, from a Coulomb–like phase $\beta > \beta_c$, connected to weak coupling. In Fig. 2.4, we plot an example of the discontinuities found for

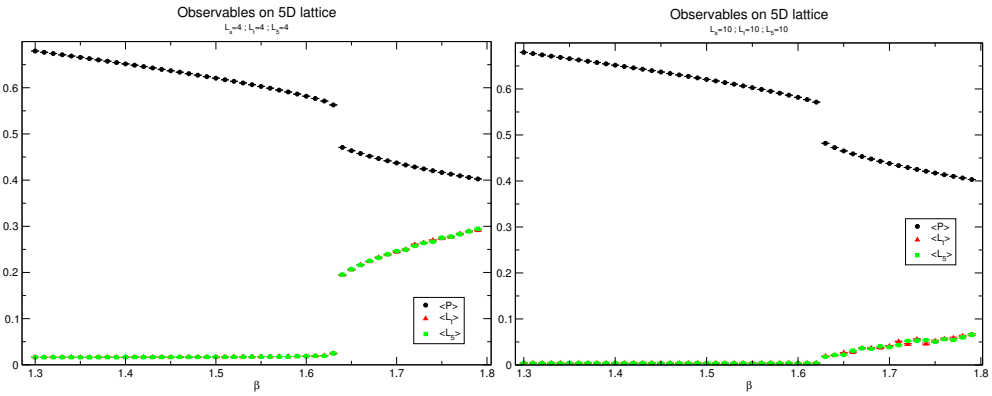

(a) *Lattice:* $N_4 = N_5 = 4$ **(b)** *Lattice:* $N_4 = N_5 = 10$

Figure 2.4 *The plots show the discontinuity found in* $\langle P \rangle$, $\langle L_t \rangle$ *and* $\langle L_5 \rangle$. *Two volumes are shown and the location of transition point is consistent between the two. The expectation value of the Polyakov loops converges to zero in the infinite volume limit as expected, but the discontinuity remains, due to the bulk nature of the transition.*

the observables at the bulk transition, for the case of a small symmetric lattice $N_4 = N_5 = 4$ and a large one $N_4 = N_5 = 10$. Local (plaquette) and non–local (Polyakov loops) observables suffer from a discontinuity at the same value of the coupling constant, suggesting, once again, the unphysical nature of the transition.

On the other hand, a physical phase transition exists in this model when the lattice size in any one dimension is decreased below a critical size, $L^{(\mathrm{crit})}$, which is the critical length of the Polyakov loop in that direction. In four dimensions, this is the analogue of a finite–temperature transition. Moreover, the bulk transition does not appear in such a case, leaving only a crossover that is smooth in β; this seems to be related to the new "compactified" geometry of the system, as we explain in the following.

Below the critical size $L^{(\mathrm{crit})}$, centre symmetry is broken and the corresponding Polyakov loop acquires a non–zero vacuum expectation value. Therefore, it can be used as an order parameter to study the phase transition. In Fig. 2.5 we show the measured observables on a lattice with a small extra dimension $N_5 = 2$. All the other dimensions are taken to be large ($N_4 = 10$). No discontinuity is present in the observables at $\beta \sim 1.64$, and the extra dimensional Polyakov loop has $\langle L_5 \rangle > 0$ for $\beta > 1.5$.

The location of the phase transition in this compactified geometry can be studied by looking for the maximum value of the susceptibility of the extra dimensional Polyakov loop, $\chi_5^{(\mathrm{max})}$. An example of the peak is shown in Fig. 2.5(b).

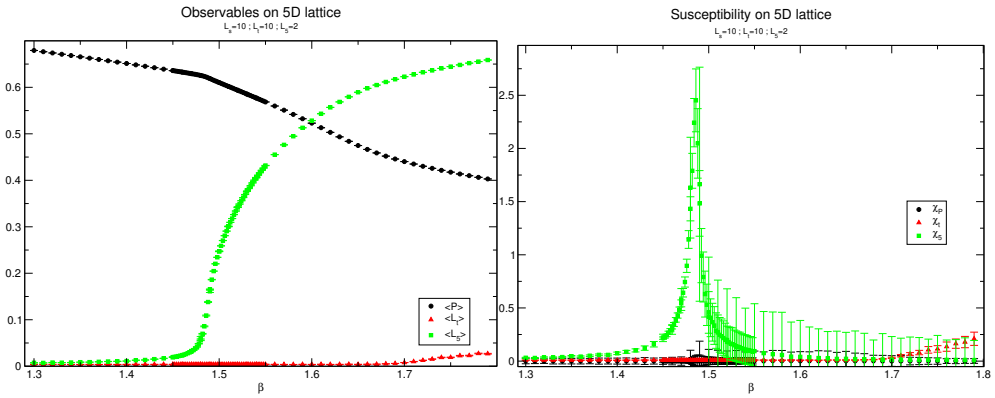

(a) *Expectation values* **(b)** *Susceptibilities*

Figure 2.5 *Scan in β for an isotropic lattice $N_4 = 10$, $N_5 = 4$. (a) Average values for $\langle P \rangle$, $\langle L_t \rangle$ and $\langle L_5 \rangle$. The statistical errors are smaller than the symbol's size. (b) Susceptibilities χ_P, χ_t and χ_5.*

Precise results for the location of the peak can be obtained by reweighting techniques, without the need of performing additional Monte Carlo simulations. We implement a multi–histogram reweighting method [65] and study χ_5 for a large range of couplings β and volumes N_4.

The peak of the susceptibility goes to infinity in the thermodynamic limit, and its position approaches a critical value $\beta_c(N_4 = \infty, N_5)$ following

$$\chi_5^{(\max)}(\beta_c(N_4, N_5)) \sim N_4^{\gamma/\nu} \tag{2.37}$$

$$|\beta_c(N_4, N_5) - \beta_c(N_4 = \infty, N_5)| \sim N_4^{-1/\nu} , \tag{2.38}$$

where γ and ν are the critical exponents of the universality class the system belongs to. An example of the scaling with $N_4 = 4$-10, at fixed $N_5 = 2$, is shown in Fig. 2.6. The critical exponents in Eq. (2.37) have been computed rather precisely in Ref. [59] and Ref. [61]: the results are entirely compatible with a second order phase transition in the universality class of the four–dimensional Ising model ($\gamma = 1$, $\nu = 1/2$). Such a result is also consistent with the conjecture of Ref. [66]. Our study is compatible with the results in the literature, but our volumes were not large enough to obtain a robust determination of the critical exponents. Indeed, measuring the critical exponents for the system defined at this transition line is not the aim of our study. A summary of the locations for $\chi_5^{(\max)}$ and its corresponding values is reported in Tab. 2.1. Note that we use a different definition for $\langle L_5 \rangle$ and χ_5 with respect to Ref. [61]. The errors are obtained by measuring the spread of the values β_c and $\chi_5^{(\max)}$ across 200 bootstrap samples.

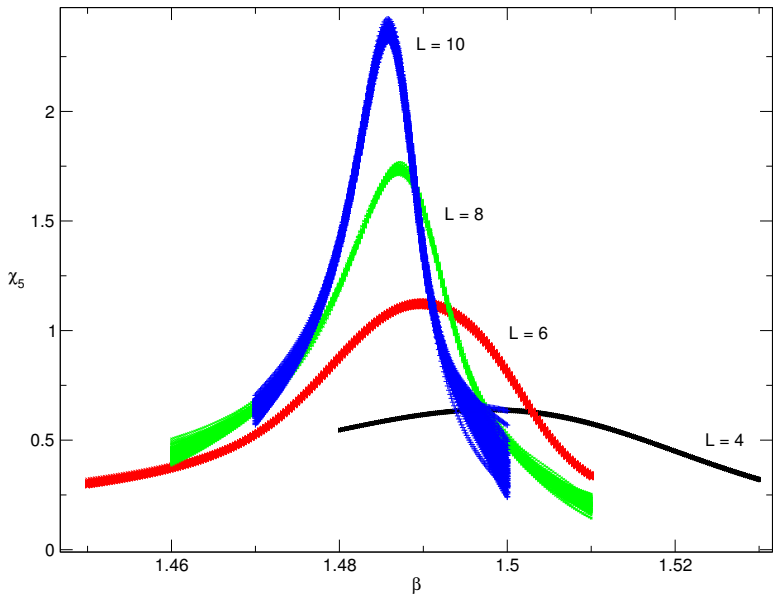

Figure 2.6 *Scaling of the extra dimensional Polyakov loop susceptibility χ_5 with the volume N_4 (L in the plot), at fixed $N_5 = 2$. The curves are obtained from different bootstrap samples in a multi–histogram reweighting technique.*

N_4	β_c	$\chi_5^{(\max)}$
4	1.49796(75)	0.6391(26)
6	1.4898(6)	1.1219(62)
8	1.48713(51)	1.739(11)
10	1.48583(3)	2.362(18)

Table 2.1 *Summary of the extracted maxima of the extra dimensional Polyakov loop susceptibility on lattices with $N_4 = 4$-10 and $N_5 = 2$.*

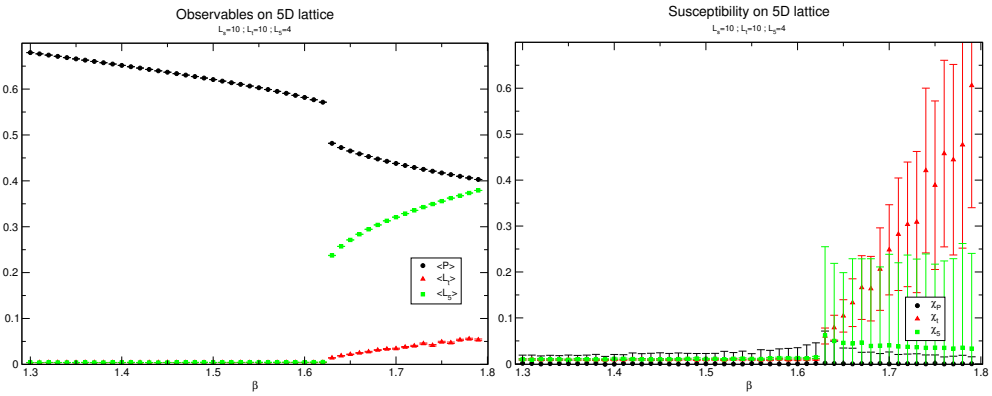

(a) *Expectation values* **(b)** *Susceptibilities*

Figure 2.7 *Scan in β for an isotropic lattice $N_4 = 10$, $N_5 = 4$. (a) Average values for $\langle P \rangle$, $\langle L_t \rangle$ and $\langle L_5 \rangle$. The statistical errors are smaller than the symbol's size. (b) Susceptibilities χ_P, χ_t and χ_5. The data show a bulk first order phase transition on this lattice.*

When the number of points in the compact fifth dimension is increased from $N_5 = 2$ to $N_5 = 4$, the second order phase transition can not be located. In its place, the bulk transition reappears, suggesting that, if any one of the dimensions becomes larger than a minimal lattice size $L^{(\mathrm{min})}$, no sign of the second order phase transition can be detected. Since we relate the bulk transition to the five dimensional nature of the system, we consider the second order phase transition as a sign of dimensional reduction to a compactified geometry. This $L^{(\mathrm{min})}$ seems to be between 2 and 6, according to Ref. [61]. We plot the observables and the relative susceptibilites on a $N_4 = 10$, $N_5 = 4$ lattice in Fig. 2.7.

2.3.2 Compact model

After investigating the simple isotropic model, we allow both couplings β_4 and β_5 to vary independently, and we study the structure of the phase diagram using the same methods presented in the previous section. Let us first focus on the region of the parameter space where $\gamma > 1$. From Eq. (2.13) we know that $a_4 > a_5$, and hence the extra dimension can be easily made small enough to obtain dimensional reduction, in the sense described above.

The phase diagram in this region has been studied for $N_5 = 4$ and $N_5 = 6$ by the authors of Ref. [2]. On the other hand, Ref. [59] also studies the same region of parameters, but with a different approach where N_5/γ is kept constant while $N_5 \to \infty$. In that case, one can study the phase structure in the limit $a_5 \to 0$.

We performed a study on the lines of Ref. [2], but on slightly bigger four–dimensional lattices. This serves as a cross–check of the validity of our simulation code in the anisotropic case $\gamma \neq 1$. Our aim is not to study the details of the phase transitions, but to locate the phase where dimensional reduction takes place. In Fig. 2.8 we compare our results with the ones presented in the literature in the two–dimensional plane of couplings (β_4,β_5). In the following we comment on the features of this phase diagram.

For fixed N_5, there is a line of second order phase transition, which is the continuation of the one found in Sec. 2.3.1 (cfr. points on the purple dashed line $\gamma = 1$ in Fig. 2.8). This second order line merges into the bulk one as the anisotropy is decreased below a critical value $\gamma_c(N_5)$, which depends on N_5. For $\gamma > \gamma_c(N_5)$, at fixed N_5, the transition line separates a phase where the centre symmetry on the extra compact direction is not broken (at smaller β_5)

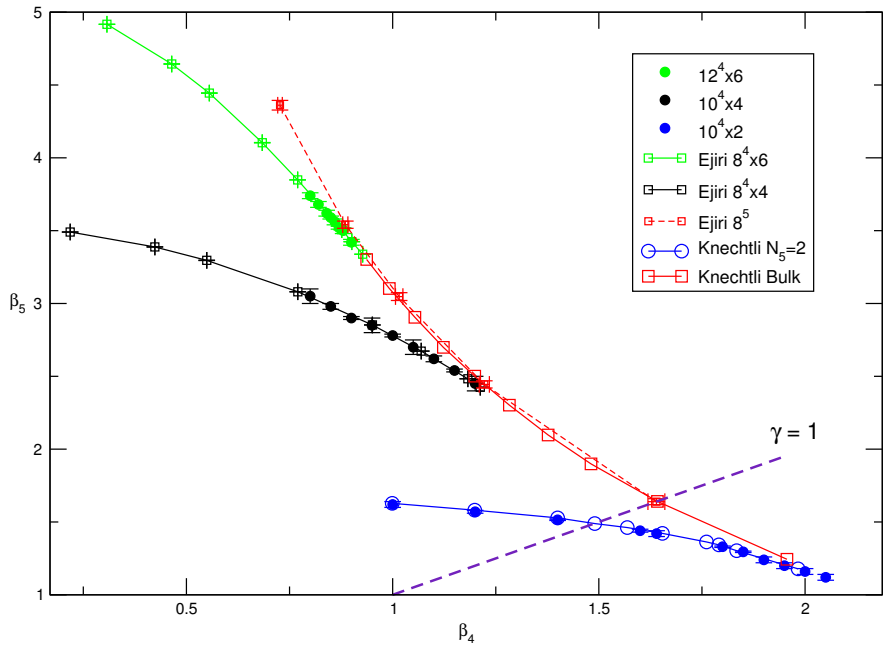

Figure 2.8 *Phase diagram of the five–dimensional SU(2) pure gauge lattice model. Results from Ref. [2] (Ejiri), and from Ref. [61] (Knechtli), are shown. The latter are extrapolated to the thermodynamic limit. Both the bulk transition and the second order ones are shown. Our results are plotted with filled circles and come from simulations on the lattices shown in the legend of the plot. They are compatible with the ones in the literature.*

from the phase where the symmetry is broken and the compact Polyakov loop acquires a non–zero expectation value (at larger β_5). We refer to this phase as the dimensionally reduced one, extending the reasonings of Sec. 2.3.1. However, for $\gamma < \gamma_c(N_5)$ the bulk phase transition line separates a confined phase (at smaller β_4) from a Coulomb–like phase extending to the weak–coupling regime, exactly as for the isotropic case.

This pattern of phase transitions is shown, for fixed N_5, in Fig. 2.9. Since the second order phase transition is physical, its location changes as we change N_5. Note also that, at fixed N_5, there is no sign of a bulk phase transition for $\gamma > \gamma_c$. This is consistent with the emerging physical picture that the disappearance of the bulk phase transition happens when the five–dimensional system compactifies; in other words, γ_c defines a critical lattice spacing in the extra dimension a_{5c} that makes $2\pi R = a_5 N_5$ smaller than the critical $L_{5c} = a_{5c} N_5$. The interesting region for our purposes, is at $\gamma > \gamma_c$ and above the line of second order phase transition, where the extra dimension is smaller than its critical value $L_5 < L_{5c}$.

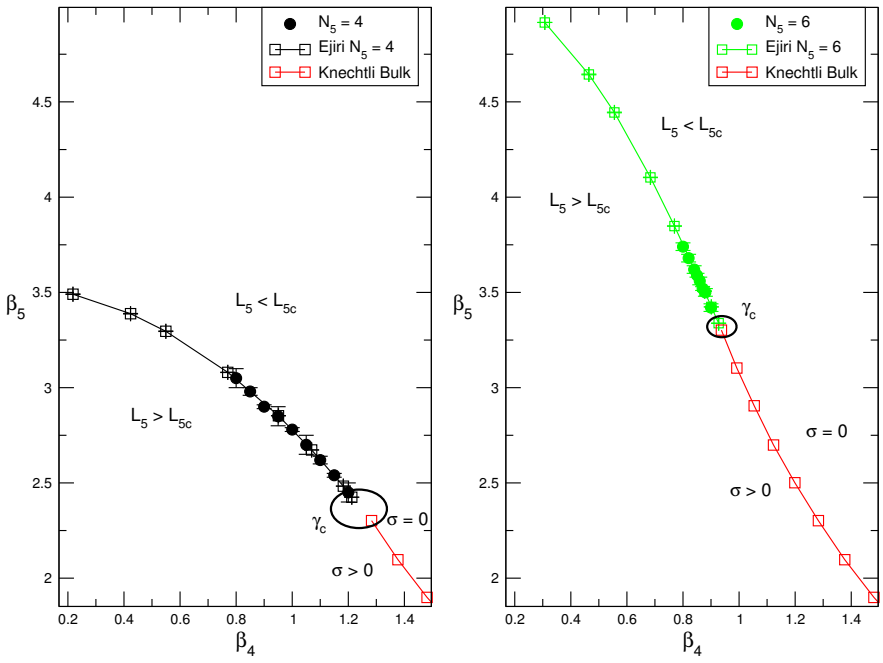

Figure 2.9 *Phase diagram of the five–dimensional SU(2) pure gauge lattice model in the (β_4, β_5) plane for different values of N_5. Note that the location of this transition changes with N_5. The region we are interested in studying is the one labelled by $L_5 < L_{5c}$. We also show compatibility with existent results.*

2.3.3 Layer model

Finally, let us describe the phase diagram of the anisotropic model where $\gamma < 1$. This region of parameters, the lattice spacing in the extra dimension is larger than the four–dimensional one $a_5 > a_4$. With this relation between the lattice spacings, it is very difficult to recover the dimensionally reduced phase from compactification, as in the previous section. However, it is suggested that a different type of dimensional reduction might take place when the extra dimension is very large. In such a case, one could recover a four–dimensional theory that is defined on a layer due to a localisation mechanism: the fields and particles of the theory are confined on a single layer and can not propagate in the extra dimension.

Numerical observations for a so–called layer phase in the model we are studying have been presented in Ref. [67] and Ref. [61]. In particular, it is claimed that the line of bulk first order transition present on large symmetric lattices ends on a critical point for finite values of the couplings β_4 and β_5. The appealing feature of such a critical point is to allow for a non–perturbative quantum continuum limit of the full five–dimensional theory to be taken.

We study the fate of the bulk transition line in the region where Ref. [67] finds some evidence for a critical point. The presence of such a point is estimated by looking at the scaling of the difference between the expectation value of the five dimensional plaquette Eq. (2.6) in the two phases separated by the transition. When such a difference vanishes, the energy gap between the two vacua of the system goes to zero and the first order transition ends. To define the nature of the critical point, and the continuum theory that could eventually be defined, requires additional studies. However, a vanishing energy gap in the thermodynamic limit is required as a necessary condition.

In the following we measure the plaquette abutting in the extra dimension and defined as

$$\langle P_5 \rangle = \left\langle \frac{1}{8N_4^4 N_5} \sum_x \sum_\mu \mathrm{Tr}\ (U_{\mu 5}(x)) \right\rangle \ . \tag{2.39}$$

This expectation value can be measured on the two vacua separated by a potential barrier at the bulk transition line. One can simulate separately on each vacuum by creating Markov chains starting from unit gauge configurations (cold) or random gauge configurations (hot).

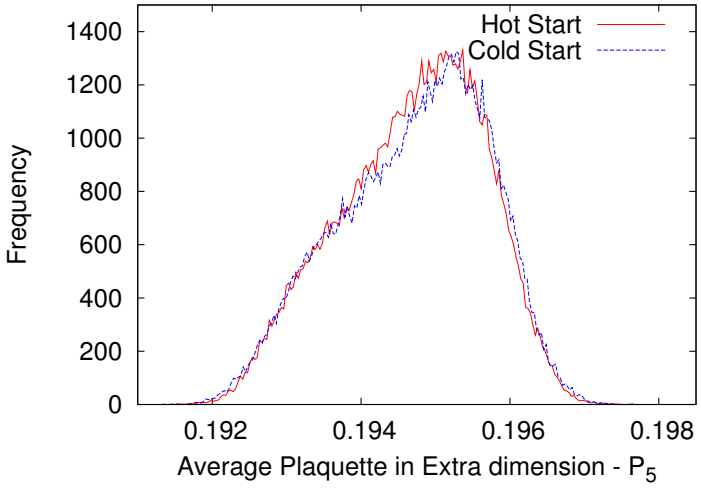

Figure 2.10 *Histograms of the average plaquette in the extra dimension, $\langle P_5 \rangle$ starting from both cold and hot configurations for $N_4 = 20$ and $N_5 = 8$ at $\beta_4 = 2.60$ and $\beta_5 = 0.8435$. At these couplings, we are in the bulk transition region, but the volume is still small enough to have a non–zero tunnelling probability: the plaquette fluctuates between the two vacua.*

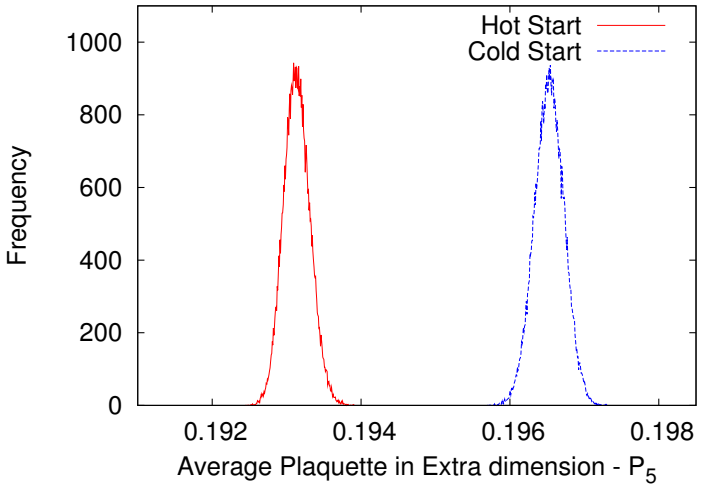

Figure 2.11 *Histograms of the average plaquette in the extra dimension, $\langle P_5 \rangle$ starting from both cold and hot configurations for $N_4 = 32$ and $N_5 = 8$ at $\beta_4 = 2.60$ and $\beta_5 = 0.844$. On this large volume, the system equilibrates in different states and no tunnelling event occurs.*

Due to the large lattice spacing in the extra dimension, centre symmetry is preserved even when N_5 is smaller than N_4 in the region of parameters we explore. Therefore, we simulate lattices with $N_4 = 16$, 20, 24 and 32 sites in the usual four directions, and $N_5 = 8$ in the extra dimension. We measure $\langle P_5 \rangle$ at the

coupling $\beta_4 = 2.6$ and for a range of $\beta_5 \in [0.8430, \ldots, 0.8445]$ that is known to be in the bulk transition region [67]. However, the study of Ref. [67] does not explore volumes larger than $N_4 = 16$ in the same region of couplings. This can be a source of concern, especially in light of the fact that a_4 can be really small at large β_4 and the thermodynamic limit is reached for increasingly larger number of points N_4.

The histograms of $\langle P_5 \rangle$ on a large $N_4 = 20$ lattice at $\beta_4 = 2.60$ and $\beta_5 = 0.8435$ are shown in Fig. 2.10. The plot seems to indicate a null energy gap between the two vacua in which the plaquette fluctuates when starting from opposite gauge configurations. However, a longer simulation on a even larger volume $N_4 = 32$ confirms the presence of the bulk first order transition in the thermodynamic limit. In Fig. 2.11, a small but non–vanishing energy gap is clearly visible.

We exclude the presence of a critical point, at least up to the explored coupling $\beta_4 = 2.6$ on the bulk transition line, thanks to our large volume simulation. Such a critical point might exist at larger values $\beta_4 > 2.60$, but larger volumes will be needed for a correct estimate of the thermodynamic limit. We have shown that it will become prohibitively expensive to check whether or not the bulk transition line ends at finite couplings. Therefore, the attempt of defining a continuum five–dimensional theory on a non–perturbative critical point with Monte Carlo simulations might not be worth investigating further.

2.4 Strategy of the lattice simulations

Our main goal is to study whether a light scalar particle does exist in the low–energy spectrum of the five–dimensional theory. So far we have described the features of the lattice model used to regularize the five–dimensional theory. In the following we describe the strategy of the numerical simulations and the details of the measured observables to set the energy scales in a non–perturbative way.

2.4.1 Setting the scale

The lattice model we described in Sec. 2.1 has four tuneable parameters: the two coupling constants β_4 and β_5, and the number of sites N_4 and N_5. In the thermodynamic limit ($N_4 \to \infty$), we are left with three parameters. Fixing the

bare coupling constants dynamically determines the two lattice spacings, whereas fixing N_5 determines the length of the extra dimension. In other words, we choose a point in a three–dimensional bare parameter space (β_4,β_5,N_5) which determines a system with a given separation of scales ($\Lambda_{\rm UV}$,$\Lambda_{\rm R}$,m_5). These three energy scales can only be determined by measuring physical observables with numerical Monte Carlo simulations. As explained in Sec. 2.1.3, we express the energy scales in units of the string tension $\sqrt{\sigma}$.

First, we determine the cutoff scale $\Lambda_{\rm UV}$ from Eq. (2.18). A measure of the four–dimensional string tension in units of the lattice spacing yields a good estimate for the separation between the low-energy scale and the cutoff. Moreover, the string tension $\sqrt{\sigma}$ is a well defined observable to be measured in numerical simulations of pure gauge systems. An estimate of $a_4\sqrt{\sigma}$ can be extracted from correlation functions of suitable operators. We choose to measure correlation functions of Polyakov loops winding around the three spatial dimensions of length $L_4 = a_4 N_4$. The asymptotic large–time behaviour of these correlators is governed by the lightest torelon state. Assuming that a flux tube with massless modes is generated, the torelon mass can be used to obtain the string tension as we explain in details in Sec. 2.4.2.

The second scale that can be easily determined non–perturbatively, is the scalar mass in Eq. (2.20). Having obtained the string tension $a_4\sqrt{\sigma}$, we measure $a_4 m_5$ and take their ratio. The scalar mass is obtained from the lightest scalar state propagating in correlation functions of scalar operators. These are operators that only project on the 0^{++} representation of the symmetry group of the cube (with positive parity and charge), following standard spectroscopic notation.

It is important to notice a peculiar feature of scalar 0^{++} operators in the five–dimensional lattice model. Due to the presence of the extra dimension, we distinguish scalar operators built using Polyakov loops wrapping around the compact fifth dimension, from those created using Wilson loops embedded in the three large spatial dimensions. To make things clear in the following, we generically refer to the first kind of operators as the scalar ones. Operators of the second type are referred to as glueball operators. In Sec. 2.4.2 we detail the construction of each kind of operator.

The last scale we need to measure is the compactification scale $\Lambda_{\rm R}$. For this we need a measure of the extra dimensional lattice spacing a_5. From Eq. (2.21), the separation between the cutoff and the compactification scale is determined,

$\xi = a\gamma^2 + b\gamma + c$

a	b	c	$\tilde{\chi}^2$
–	1.600(15)	-0.446(37)	0.61
-0.03(1)	1.767(62)	-0.641(76)	0.32
-0.06(1)	1.950(45)	$1 - a - b$	0.77

Table 2.2 *Parameters of the fitted function $\xi = \xi(\gamma)$. We fit data from $\gamma \sim 1.224$ to $\gamma = 4$.*

at leading order, by the bare parameters of the lattice model. At a fixed point (β_4,β_5,N_5), N_5/γ can be used to approximately estimate $\Lambda_{\rm R}$, once $\Lambda_{\rm UV}$ is known. However, we already mentioned that this is only valid in the weak–coupling limit. We measure the systematic deviation of $\frac{\Lambda_{\rm UV}}{\Lambda_{\rm R}}$ from its tree–level value $\frac{N_5}{\gamma}$, since our simulated points are at not so large β. Due to quantum fluctuations, we expect corrections to Eq. (2.13). Such radiative corrections to the bare parameter γ have been studied in Ref. [2] for a limited region of parameter space, and a non–perturbative map $\xi = \xi(\gamma, \beta)$ can be inferred. In order to do this, we interpolate the available data. This allows us to estimate the ratio $\frac{\Lambda_{\rm UV}}{\Lambda_{\rm R}}$ for the points we simulated. In the region where ξ was initially measured non–perturbatively, the value of ξ is shown to be fairly insensitive to the values of β (cfr. Fig. 1 in Ref. [2]), in particular for the values that we need, namely $1.7 \leq \xi \leq 3.0$. The relation $\xi = \xi(\gamma)$ is shown in Fig. 2.12.

We perform three different fits of the data: a linear fit, a quadratic one, and a quadratic fit imposing $\xi(1) = 1$. The details of the fits are summarised in Tab. 2.2. In practice, to obtain ξ for the points in our simulations, we use a cubic polynomial interpolation, nested inside a bootstrap procedure to obtain statistical errors. For each point (γ,ξ) taken from Ref. [2], we generate a gaussian distribution whose mean and standard deviation are given by ξ and its estimated statistical error. Then we choose ξ randomly from those distributions at each γ and interpolate the resulting set of points. We do this for 1000 different random choices of ξ, effectively obtaining a new distribution of ξ at each interpolated γ value from whose standard deviation we estimate the errors on the interpolated points. These errors are such that all the lower order fits are compatible with the interpolation, as shown in Fig. 2.12.

We have described how to measure the three energy scales of the system using numerical non–perturbative simulations. Here we summarise the steps we follow in our simulations:

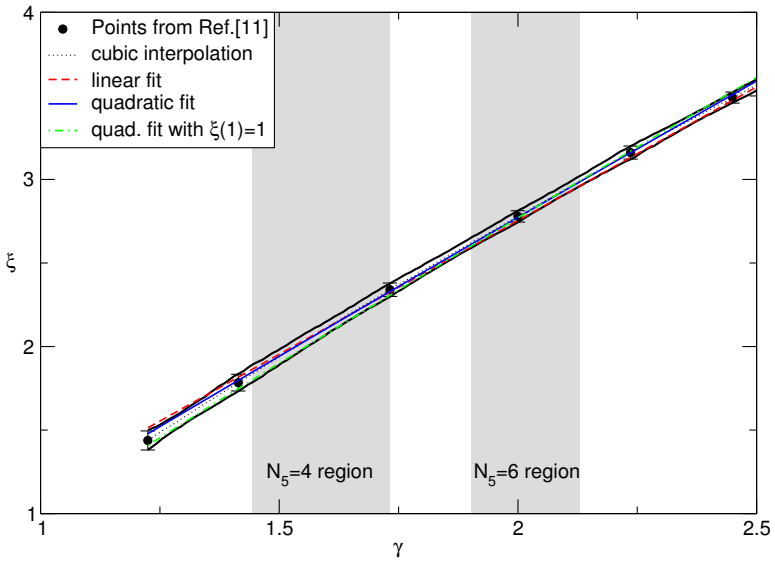

Figure 2.12 *The relation $\gamma \sim \xi$ is corrected by quantum fluctuations. We interpolated data for ξ taken from Ref. [2]. All the data are in phase where $\sqrt{\sigma} \neq 0$. In the plot we show fits from Tab. 2.2 and a cubic polynomial interpolation. We perform simulations with parameters corresponding to γs in the grey shaded regions. The fits and interpolation compare well with data, and are hardly distinguishable.*

1. we fix a point in the three–dimensional parameter space (β_4,β_5,N_5), making sure that belongs to the dimensionally reduced phase;

2. on this point we measure $a_4\sqrt{\sigma}$ and $a_4 m_5$ from correlation functions of suitable operators;

3. the measured observables determine the cutoff scale and the scalar mass through Eq. (2.18) and Eq. (2.20);

4. we use the available data of ξ to estimate the compactification scale using Eq. (2.21) and the measured cutoff scale;

5. we then move to a different point (β_4,β_5,N_5) and repeat steps 2-4;

6. this allows us to map the dependence of the energy scales on the bare parameters and to determine lines of constant physics;

7. more importantly, this allows us to study the behaviour of m_5 as a function of $\Lambda_{\rm UV}$ or $\Lambda_{\rm R}$ and to disentangle cutoff effects from compactification effects.

2.4.2 Lattice observables

String tension

To extract the string tension we use Polyakov loop operators L_i winding around the three spatial dimensions ($i \in \{1, 2, 3\}$). These operators have a non–zero overlap with torelon states. Such non–local states are characterised by a mass which grows linearly with the size of the lattice, $L_4 = a_4 N_4$ in this case. The string tension is the coefficient of this linear dependence. More specifically, the mass of the torelon state is related to the string tension by the leading order formula [68]

$$a_4 m_{\mathrm{tor}}(N_4) \;=\; a_4^2 \sigma N_4 - \frac{\pi(D-2)}{6N_4} \;, \tag{2.40}$$

where D is the number of space–time dimensions.

We can invert Eq. (2.40) and can extract the string tension as

$$a_4^2 \sigma \;=\; \frac{a_4 m_{\mathrm{tor}}(N_4)}{N_4} + \frac{\pi(D-2)}{6N_4^2} \;, \tag{2.41}$$

and we set $D = 4$ in our analysis, since we are measuring the string tension of the low–energy dimensionally reduced system, which is effectively four dimensional.

Significant finite–size systematics is known to be small for long Polyakov loops, i.e. loops yielding $N_4 a_4 \sqrt{\sigma} > 3$. We explicitly check the absence of finite–size effects in Sec. 2.4.2.

Measures of Polyakov loop operators are difficult because of the signal–to–noise ratio of such observables is very poor. The quality of the signal for the two–point correlator degrades very quickly with the time separation; specific techniques are usually needed in order to enhance the signal, and obtain statistically accurate results.

In this work, we use an improved diagonal spatial smearing with a further step of blocking as first described in Ref. [69]. The set of parameters used here is the same as in Ref. [69], namely $(p_a, p_d) = (0.40, 0.16)$ (cfr. Fig. B.2). The choice of the optimal parameters depends on the physical scale of the lattice simulation. As we will show in Sec. 2.5, the scale $a_4\sqrt{\sigma}$ changes rapidly in the bare parameter space. Therefore, it turns out that the chosen smearing parameters are very efficient only for a limited number of simulated points. Nonetheless, having differently smeared

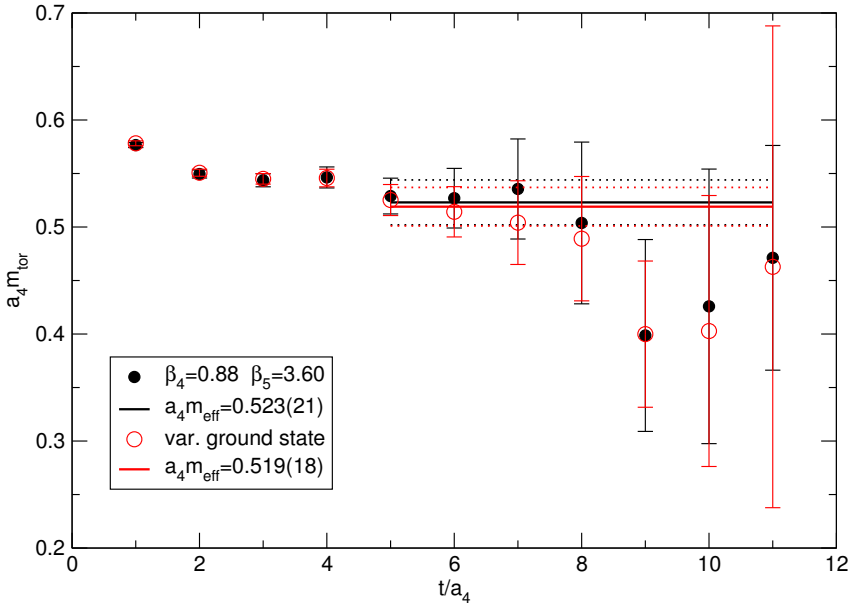

Figure 2.13 *Comparison between the ground state effective mass extracted from the diagonal correlator of the highest blocking level (black points) and the one extracted from the variational procedure (red circles). The operators are $L_4 = 12a_4$ spatial Polyakov loops at 4 different blocking levels, and their correlator was measured along a $L_t = 2L_4 = 24a_4$ temporal distance. The correlator was averaged over the $N_5 = 6$ extra dimension slices.*

and blocked operators allows for a better signal to be extracted, thanks to the increased overlap with the torelon ground state.

Different iterations of the smearing and blocking procedure give rise to different operators which can be cross correlated with each other to form a matrix of correlators. The effective torelon mass can be extracted using a single–state hyperbolic cosine ansatz for the diagonal element in the correlator matrix. A different estimate comes from a variational analysis of the correlator matrix. A comparison between the two estimates is shown in Fig. 2.13. The comparison was done on a lattice with a longer temporal direction $L_t = 2L_4$ and using the same fitting window for the effective mass plateaux in both cases. We confirm that the best projection onto the ground state is obtained using operators at the maximum blocking level available on a given volume.

In Fig. 2.14 we show two examples of torelon effective masses. The first one represents a case where the overlap of the operator is not optimal and the effective mass plateaux is reached at larger time separations. The second one, on the other hand, is a case where the plateaux is reached already at $t/a_4 = 2$, thanks to a good overlap of the operator on the ground state.

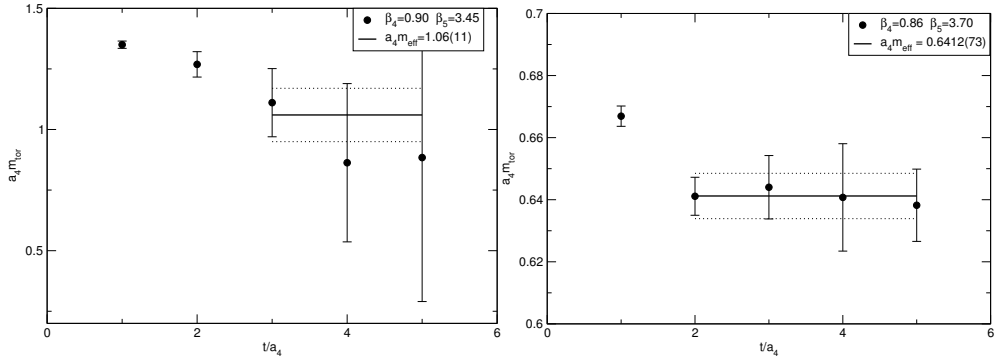

(a) $\beta_4 = 0.90, \beta_5 = 3.45$ **(b)** $\beta_4 = 0.86, \beta_5 = 3.70$

Figure 2.14 *Example of plateaux of torelon effective masses. (a) The final mass comes from a weighted fit of the points in the plateaux that is reached only at $t/a_4 = 3$ due to the small overlap of the operator onto the ground state. (b) At lower masses the plateaux is longer and the signal is extracted more reliably.*

A summary of all the torelon masses and their corresponding string tensions is reported in Tab. A.5, and Tab. A.6. The fitting range for the effective mass plateaux is also shown in the tables. We also report the physical size $L_4\sqrt{\sigma}$ in the same tables. As mentioned above, finite–size effects can be kept under control when $L_4\sqrt{\sigma}$ is large; in other words we would like our physical lattice volume to be much larger than the typical correlation length of the system, given by the inverse of the string tension.

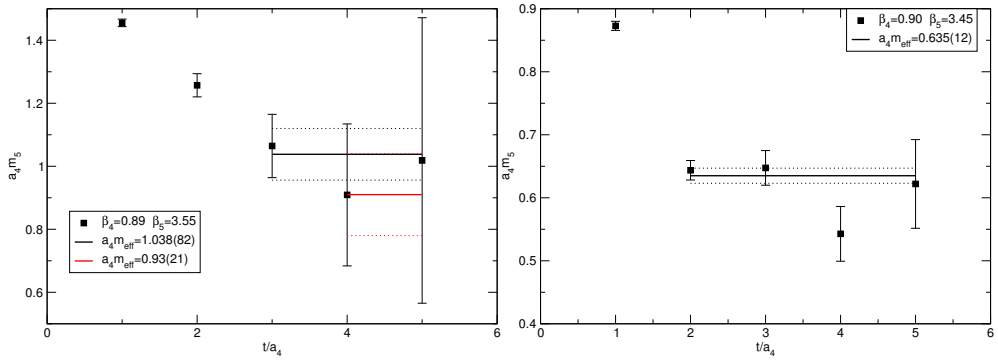

(a) $\beta_4 = 0.89, \beta_5 = 3.55$ **(b)** $\beta_4 = 0.90, \beta_5 = 3.45$

Figure 2.15 *Example of plateaux for one of the highest scalar masses (a) and one of the lowest (b). (a) The operator overlaps poorly on the ground state and the plateaux is reached at large temporal distances. In this case we tried to estimate the systematic error on the fitting range, by choosing two different fitting windows. (b) The plateaux is reached already at $t/a_4 = 2$.*

Scalar mass

The second observable we want to measure is the mass of the static scalar mode. For this purpose we need an operator with scalar quantum numbers in three dimensions, e.g. that transforms in the A_1 irreducible representation of the cubic symmetry group with positive parity and charge (more details about lattice symmetry channels are given in Appendix B). As mentioned in Sec. 2.4.1, we use gauge–invariant operators built using Polyakov loops winding around the extra compact dimension. In particular, we choose combinations transforming as scalars under the cubic symmetry group, which only carry a site index in the four–dimensional subspace:

$$\mathcal{O}_1(t) \;=\; \sum_x \mathrm{Tr}\,\left[L_5(x,t)\right]\,; \qquad L_5(x,t) = \prod_{j=1}^{N_5} \mathcal{U}_5(x + j a_5 \hat{5}, t)\;, \tag{2.42}$$

and

$$\mathcal{O}_2(t) \;=\; \sum_x \mathrm{Tr}\,\left[\phi(x,t)\phi^\dagger(x,t)\right]\,; \qquad \phi(x,t) = \frac{L_5 - L_5^\dagger}{2}\;. \tag{2.43}$$

The sum $\sum_x$ is an average over the spatial volume in order to obtain zero–momentum operators on a fixed timeslice t. When computing the correlators

$$C_1(t) \;=\; \frac{1}{N_t}\sum_{\tau=1}^{N_t} \langle 0|\, \mathcal{O}_1^\dagger(\tau)\mathcal{O}_1(\tau+t)\,|0\rangle \;\;, \tag{2.44}$$

and

$$C_2(t) \;=\; \frac{1}{N_t}\sum_{\tau=1}^{N_t} \langle 0|\, \mathcal{O}_2^\dagger(\tau)\mathcal{O}_2(\tau+t)\,|0\rangle \;\;, \tag{2.45}$$

we average over the extra–dimensional coordinate, as we did in the case of the string tension.

The first operator $\mathcal{O}_1$ is the same one used in Ref. [59]. For the operator in Eq. (2.43) it is possible to apply a smearing procedure following the one introduced in Ref. [70] for a scalar Higgs field. The operator ϕ is replaced by a smeared version that consists of a gauge–invariant combination of parallel transporters in the three–dimensional spatial subspace. In this case, the smearing procedure depends on a set of parameters that can be adjusted and optimised. We have tested several combinations of parameters and chose the optimal one in a certain region of the parameter space.

We found the lowest smearing level of $\mathcal{O}_2$ to have the largest projection onto the

	$a_4\sqrt{\sigma}$		$a_4 m_5$	
N_4	12	16	12	16
(0.845,3.80)	0.2358(11)	0.2364(25)	1.05(31)	1.44(9)
(0.870,3.65)	0.2358(11)	0.2359(27)	0.998(93)	1.08(26)
(0.870,3.65)	0.2383(12)	0.2392(25)	0.777(78)	0.956(99)

Table 2.3 *Comparison between the observables on two different four–dimensional volumes and fixed $N_5 = 6$. The string tensions are independent of N_4 and the scalar masses are compatible within one standard deviation.*

ground state. Moreover, the effective masses extracted from $\mathcal{O}_1$ and the lowest smearing level of $\mathcal{O}_2$ are always compatible. When $a_4 m_5$ is small, the smeared operators show better plateaux than the unsmeared ones, but we have not studied their projection onto the ground state with a systematic variational procedure.

We obtain plateaux of effective masses similar to the ones shown in Fig. 2.15, where operator $\mathcal{O}_1$ is used. Similarly to Fig. 2.14, we have a region of parameters where effective masses are heavy and the operators used overlap poorly on the ground state. On the other hand, longer and better behaved effective masses can also be found. In the former case, we estimate a systematic error inherent to the choice of the plateaux region. This systematic error is reported in the tables of results and propagated to the final results described in Sec. 2.5.

Finite volume effects

An attempt to estimate the effects of a finite four–dimensional volume has been made. Both the observables $a_4\sqrt{\sigma}$ and $a_4 m_5$ have been measured for different values of N_4 on a specific set of points at $N_5 = 6$. This study excludes significant effects due to the finite volume for the above observables

For three different points in the bare parameter space (β_4,β_5), we simulate two different four–dimensional lattice sizes, $N_4 = 12$ and $N_4 = 16$. The three points have a very similar string tension at $N_4 = 12$, but on that volume $L_4\sqrt{\sigma}$ turns out to be slightly smaller than 3, our rule of thumb for trusting Eq. (2.41). In Fig. 2.16 the volume dependence is shown for $a_4\sqrt{\sigma}$ and $a_4 m_5$, while the results are summarised in Tab. 2.3. We note that the larger statistical error for $a_4\sqrt{\sigma}$ on the largest volume is due to a larger torelon mass (the number of configurations is the same for both volumes).

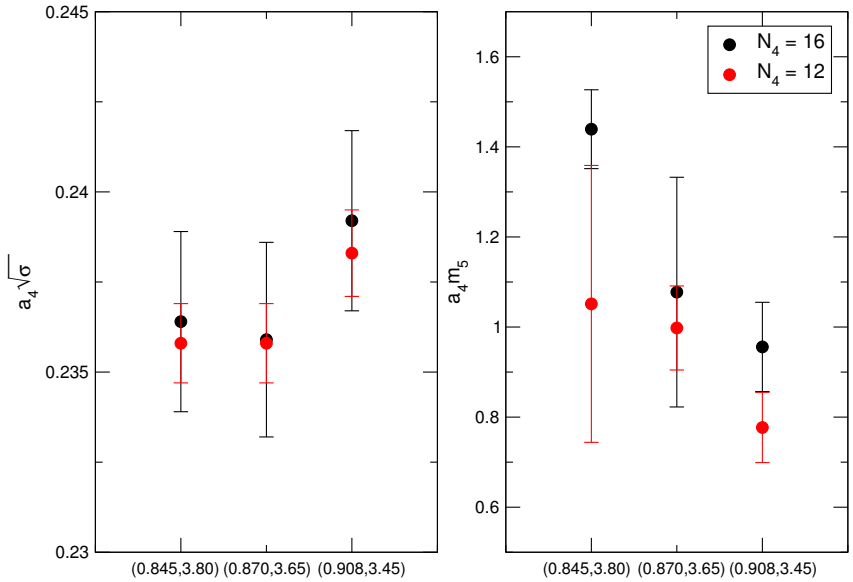

Figure 2.16 *For three different points reported on the x axis, we show the string tension and the scalar mass in units of the cutoff length. Two volumes are compared and sizable finite–size effects can be ruled out. The results are summarised in Tab. 2.3.*

Glueball mass

A different estimate for the scalar mass, that we refer to as glueball mass, is obtained using a symmetrized combination of spatial Wilson loops. Glueball operators are important to understand if the ground state in the scalar channel can be considered as the static mode whose mass is perturbatively described by Eq. (2.1). We expect the operators $\mathcal{O}_1$ and $\mathcal{O}_2$ to couple mainly with a scalar state whose nature is extra dimensional. On the other hand, we know that the low–energy spectrum of four–dimensional confining gauge theories contains glueball states, and the scalar one is the lightest of such states. We want to study how different operators mix with the scalar state. This mixing can be used as a guide to identify a region of parameters where the scalar state can be considered as the static scalar Kaluza–Klein mode, from a region where glueballs dominate the large distance physics and all Kaluza–Klein modes decouple.

To obtain an accurate estimate of the glueball mass from correlation functions, we use a combination of the improved diagonal smearing described in Fig. B.2 and a variational ansatz. In particular, we choose three different spatially shaped Wilson loops in order to construct glueball operators. This procedure has been very successful in extracting highly accurate glueball masses in three and four–dimensional SU(N) gauge theories [69, 71, 72] and also in lattice QCD [73]. A

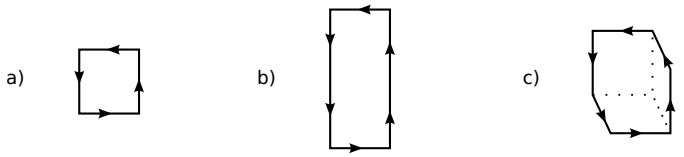

Figure 2.17 *Wilson loops used in the construction of glueball operators in the scalar channel. Each of these three operators is smeared according to Fig. B.2 in order to construct a larger variational ansatz.*

detailed explanation of the techniques used in extracting glueball masses from the lattice is given in Appendix B and we also refer to Ref. [71] where our measurement setup was first implemented.

To create operators coupling to glueball states in four dimensions, we use the four–links plaquette, the six–links rectangular plaquette and the six–links chair shown in Fig. 2.17. Symmetrized combinations of these operators projecting only onto the scalar representation of the three–dimensional cubic symmetry group are referred to in the following as $\mathcal{O}_a$, $\mathcal{O}_b$ and $\mathcal{O}_c$, built starting respectively from the path a), b) and c) in Fig. 2.17. They are also zero–momentum projections.

To estimate the mixing in the scalar spectrum of the lattice theory, we used the following procedure:

- compute the full correlation matrix $C_{\alpha\beta}(t)$, where the lower indices run over the scalar operators of the following type: $\mathcal{O}_2$, $\mathcal{O}_a$, $\mathcal{O}_b$, $\mathcal{O}_c$
- employ a variational procedure to find a linear combination of the correlated operators such that the propagating state is the lightest, or even the excited ones
- decompose the approximate mass eigenstates obtained from the previous step into their projections onto the basis operators $\mathcal{O}_2$, $\mathcal{O}_a$, $\mathcal{O}_b$, $\mathcal{O}_c$.

The last step of this variational analysis gives us informations about the nature of the propagating state. If the main projection is onto glueball operators $\mathcal{O}_a$, $\mathcal{O}_b$ and $\mathcal{O}_c$, the mass extracted is likely to be associated to a glueball state rather than a scalar of extra–dimensional origin. At the same time, a significant projection onto $\mathcal{O}_2$ indicates that the state investigated is probably a scalar coming from the compactification mechanism.

This variational procedure is carried on only for a limited region of parameters, due to the large computational cost of measuring the full correlation matrix

$C_{\alpha\beta}(t)$. We choose points at fixed $\gamma \approx 1.54$ and we investigate how the mixing of the extracted states changes as we increase β, moving away from the line of second order phase transition. An example of the effective mass plateaux for the ground state and its low–energy excitations is also shown in Fig. 2.18 for two values of β; we compare the results of the variational procedure, with the results obtained from diagonal correlators of pure scalar operators. More results are reported in Sec. 2.5.1.

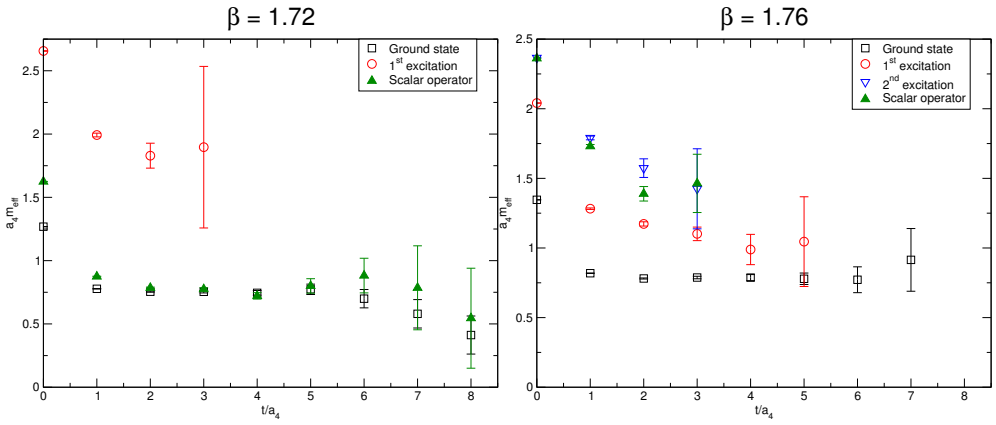

(a) $\beta = 1.72, \gamma \approx 1.54$ **(b)** $\beta = 1.76, \gamma \approx 1.54$

Figure 2.18 *Example of effective mass plateaux for two different values of β. (a) At $\beta = 1.72$ the mass of the low–lying scalar state obtained from the variational ansatz is compatible with the one we measured using only scalar operators. (b) At $\beta = 1.76$ the scalar operator yields a mass which is compatible with the second excitations of the scalar spectrum.*

2.4.3 Simulation details

We perform simulations at two different values of N_5 and two different four–dimensional volumes $(a_4 N_4)^4$. The simulations use a heatbath update algorithm [74], whose steps are combined with overrelaxation to reduce autocorrelations between successive gauge configurations.

The smaller lattice has $N_4 = 10$ and $N_5 = 4$. On this lattice, we generate $\mathcal{O}(800000)$ configurations and measure correlators of the interesting observables. Correlators are binned over 20 configurations after thermalization and the statistical errors comes from a jack-knife procedure. We select a wide range of values for the couplings β_4 and β_5, starting very close to the line of second order phase transition. In this region we expect a light scalar in units of the

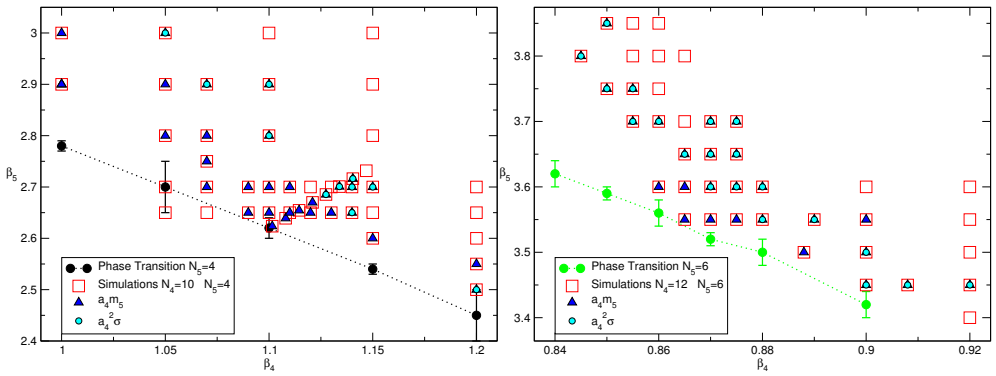

(a) $N_4 = 10,\ N_5 = 4$ **(b)** $N_4 = 12,\ N_5 = 6$

Figure 2.19 *The plots show the region of the phase diagram that we explored with numerical simulations, both for $N_5 = 4$ (a) and $N_5 = 6$ (b). The location of the second order phase transition is also shown. The blue triangles are points where the scalar mass $a_4 m_5$ was reliably extracted, whereas the cyan circles represent points where we were able to measure the string tension $a_4\sqrt{\sigma}$.*

lattice spacing because the scalar mass is the inverse of the correlation length, and the latter diverges at the critical line. From the phase structure discussed in Sec. 2.3.2, we also expect to find a finite string tension.

Similarly, we simulate a lattice with $N_4 = 12$ and $N_5 = 6$, generating $\mathcal{O}(600000)$ configurations and binning the observables over 20 configurations. In the tables of Appendix A, we show both the bare parameters fixing the location of the point in the phase diagram, and the values of ξ (cfr. Sec. 2.4.2) used to set the scale separation $\Lambda_{\rm UV}/\Lambda_{\rm R}$. Therefore, we can compare the separation of scales in Eq. (2.21) to the naive estimate at tree level, i.e. $\frac{N_5}{\gamma}$. The naive expectation turns out to be systematically larger than what is obtained by measuring the anisotropy non–perturbatively. As a result, we are able to explore the following scale separation range between the cutoff and the compactification radius

$$1.7 \lesssim \frac{N_5}{\xi} = \frac{\Lambda_{\rm UV}}{\Lambda_{\rm R}} = \frac{2\pi R}{a_4} \lesssim 2.3\ . \tag{2.46}$$

Since this is the first time that this particular region of the phase space is explored with lattice simulations, we performed a broad scan, aiming primarily at identifying the interesting region.

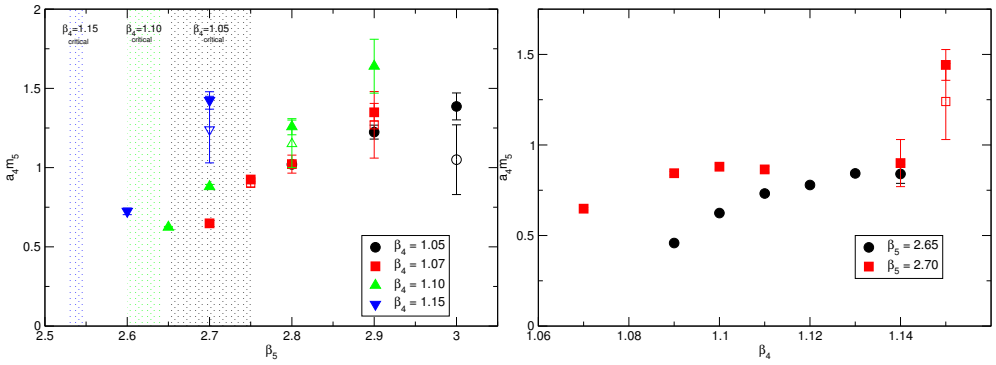

(a) *Fixed β_4 values* **(b)** *Fixed β_5 values*

Figure 2.20 *(a) The scalar mass in units of the lattice spacing $a_4 m_5$ as a function of β_5 and for four different values of β_4 at $N_5 = 4$. The approximate location of the critical region is shown by the shaded regions for the different values of β. (b) At fixed β_5, we show the behaviour of $a_4 m_5$. Smaller values of β_4 are closer to the phase transition line, but we do not have an estimate of its location in this direction. Open symbols correspond to alternative fitting ranges in the effective mass plateaux for the scalar state. When not shown, errors are smaller than symbols.*

2.5 Results for the scale separations

2.5.1 Lines of constant physics

In this section we first look at the measured observables as functions of the bare parameters. For example, our data allow us to study the behaviour of $a_4\sqrt{\sigma}$ at fixed value of β_4 as we change β_5, and vice versa. The same can be done with the measured $a_4 m_5$ and therefore with the ratio $m_5/\sqrt{\sigma}$. In Fig. 2.20(a) we select four different values of β_4 and we plot the mass $a_4 m_5$ obtained from scalar operators as a function of β_5. Fig. 2.20(b) shows the dependence of the scalar mass as a function of β_4 for fixed β_5. The values of $a_4 m_5$ are taken from Tab. A.3 and Tab. A.4.

We notice that the scalar mass approaches the cutoff scale $a_4 m_5 \gtrsim 1$ as we move away from the line of second order phase transition. This happens both in the β_4 and β_5 directions. Similarly if we move in the parameter space along a line of fixed γ, while changing β. In this last case, we perform a study of the scalar mass and of the glueball mass.

We choose $\gamma \approx 1.54$ in order to obtain a separation of scales $\Lambda_{\rm UV}/\Lambda_{\rm R} \approx 2$ when

taking into account the renormalized anisotropy ξ. In the interval $\beta \in [1.71,\ 1.77]$, we accurately study the low–lying spectrum of scalar particles employing our larger set of operators with the inclusion of glueballs, introduced in Sec. 2.4.2. We study the operator content of the different mass eigenstates in the scalar channel. In particular, we extract the mass of the scalar ground state and its first excitation, shown in Fig. 2.21. In the plot we compare the non–perturbative scalar masses calculated via the variational ansatz with the masses obtained solely from effective mass plateaux of scalar operators $\mathcal{O}_1$. From the results in the plot, we see that a variational analysis is crucial to identify the lightest scalar state as β is increased.

For the same set of points, we measure the normalized projection of the mass eigenstates onto each operator used in the correlation matrix. The projection of the extracted ground state is shown in Fig. 2.22. The plot clearly shows how the contribution of the scalar operators to the ground state decreases as β increases. At higher values of β, glueball operators have a larger overlap onto the ground state. On the other hand, we see that at lower values of β, which are closer to the line of second order phase transition, the scalar state has a dominant contribution from the *extra–dimensional* operators. A similar plot concerning the first excited state is shown in Fig. 2.23. Up to $\beta = 1.75$, the first excited state is dominated by a projection onto the scalar operators, suggesting an extra–dimensional nature for this particle.

We conclude that the scalar mass becomes heavy in units of the cutoff scale while moving away from the critical line, as shown in Fig. 2.21. This suggests that at $\beta \gtrsim 1.77$ for $N_5 = 4$ the scalar particle becomes heavy. This result compare well with data from Ref. [59]. In fact, data taken at $1.83 \leq \beta \leq 1.91$ and $N_5 = 4$, $\gamma = 2$, correspond to a scalar mass $m_5 \gtrsim 2\Lambda_{\mathrm{UV}}$. This is a region of parameter space where the scalar particle cannot be considered a low–energy degree of freedom of the theory.

While the scalar mass becomes smaller as we approach the critical line, the opposite happens to the string tension. Its behaviour in bare parameter space is best illustrated by the data at $N_5 = 6$. All the points where we were able to extract the string tension $a_4\sqrt{\sigma}$ are summarised in Tab. A.5 for $N_5 = 4$, and Tab. A.6 for $N_5 = 6$. In Fig. 2.24(a) the string tension is shown at three different values of β_4: the common feature of the data is that the string tension suddenly increases as the critical line is approached. We interpret this behaviour as an increase of the lattice spacing a_4 in units of the physical string tension

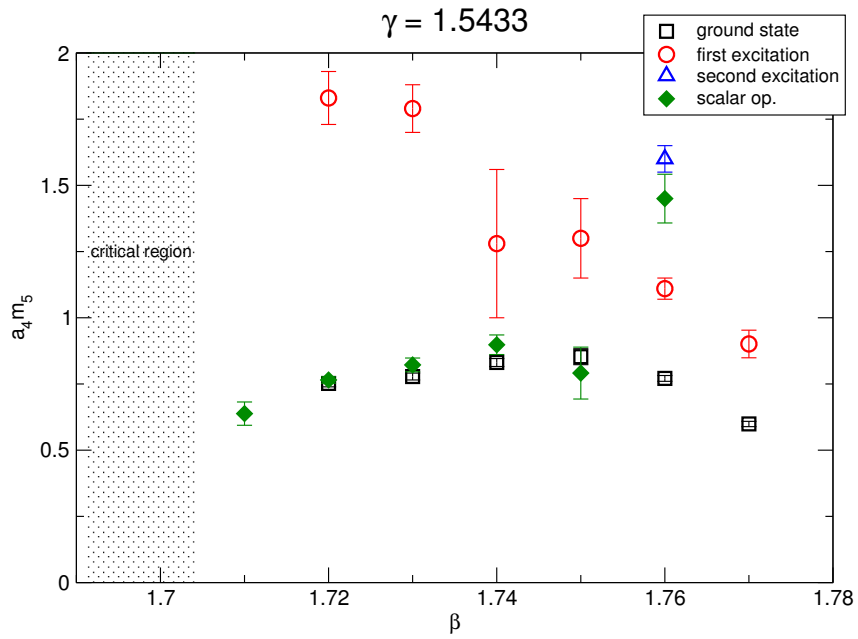

Figure 2.21 *The scalar mass in units of the lattice spacing $a_4 m_5$ as a function of β for a fixed value of $\gamma = 1.5433$. The shaded area is the approximate location of the second order phase transition. Open symbols refer to masses obtained from a variational procedure. Filled symbols are masses extracted from diagonal correlators of scalar operators.*

$\sqrt{\sigma}$, following Sec. 2.1.3. A similar functional dependence of $a_4\sqrt{\sigma}$ is shown in Fig. 2.24(b), where β_5 is fixed. At lower values of β_4, closer to the line of phase transition, the string tension grows and it becomes very difficult to extract a signal from our numerical simulations. We can easily infer from the data that the string tension will decrease with increasing β at fixed γ, as already reported in Ref. [59]. This behaviour is expected since $\beta \to \infty$ is the weak–coupling limit of the theory, and accordingly the string tension should vanish.

By combining the results just shown, we can identify lines of constant physics in the phase diagram at fixed $N_5 = 4$, and similar features exist at $N_5 = 6$. The lines of constant cutoff $\Lambda_{\rm UV}$ are represented by contour lines of $a_4\sqrt{\sigma}$ and are shown in Fig. 2.25 by interpolating the numerical data. These lines start close to the line of second order phase transition for $\gamma \sim \gamma_c$, but then move away from it as γ is increased. To summarize, at fixed γ, the lowest β corresponds to the lowest $\Lambda_{\rm UV}$; a larger separation between the low–energy physics and the cutoff is found at bigger values of β, and this is the region where the lattice discretisation starts to become irrelevant and we can safely extract the low–energy physics from numerical simulations (cfr. Eq. (2.15)).

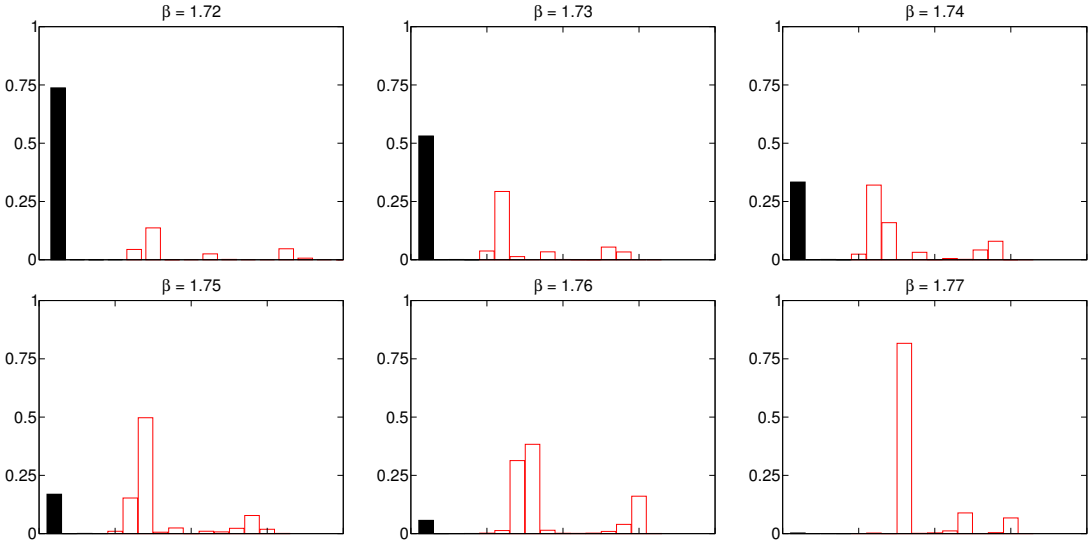

Figure 2.22 *Relative projection of the ground state onto each of the operators in the variational set. Filled bars correspond to the set of smeared scalar operators, whereas the empty bars refer to the smeared versions of glueball operators*

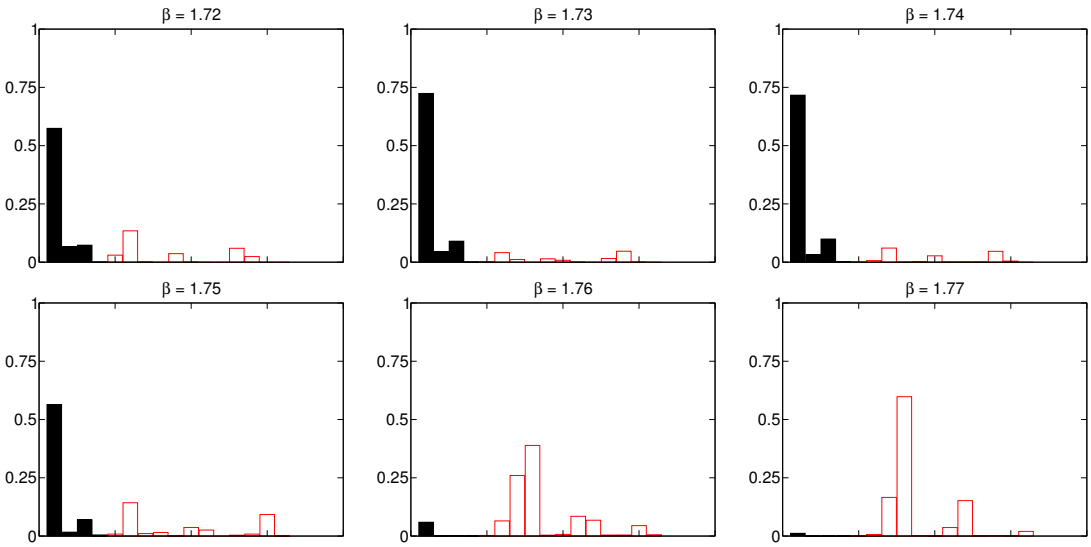

Figure 2.23 *Relative projection of the first excited state onto each of the operators in the variational set. Filled bars correspond to the set of smeared scalar operators, whereas the empty bars refer to the smeared versions of glueball operators.*

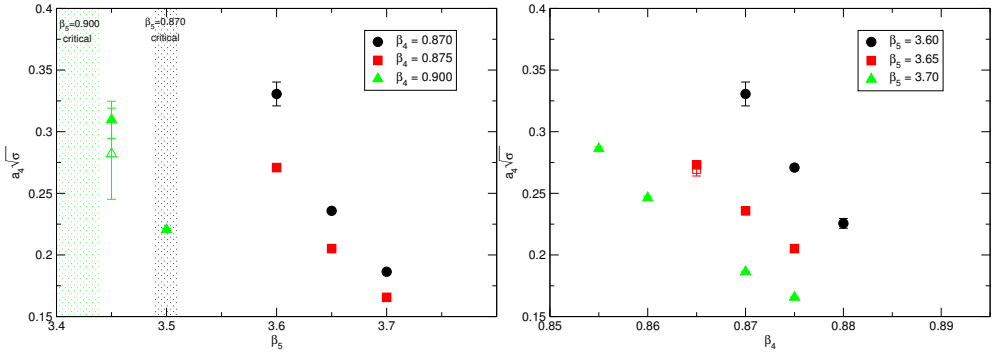

(a) *Fixed β_4 values* **(b)** *Fixed β_5 values*

Figure 2.24 *(a) The string tension in units of the lattice spacing $a_4\sqrt{\sigma}$ as a function of β_5 and for three different values of β_4 at $N_5 = 6$. The approximate location of the critical region is shown for the different β_4. (b) At fixed β_5, we show the behaviour of $a_4\sqrt{\sigma}$. Smaller values of β_4 are closer to the phase transition line, but we do not have an estimate of its location in this direction. Open symbols correspond to alternative fitting ranges in the effective mass plateaux for the torelon state. When not shown, errors are smaller than symbols.*

What we are really interested in is the behaviour of the scalar mass m_5 in units of the string tension $\sqrt{\sigma}$. By looking at the ratio of $a_4 m_5$ over $a_4\sqrt{\sigma}$, we can deduce the lines of constant scalar mass. They are shown in Fig. 2.26 for $N_5 = 4$. Unfortunately, we cannot use all the measured values of $a_4 m_5$, because we also need a measure of $a_4\sqrt{\sigma}$ on the same point. The general pattern of these lines is again quite clear: the lightest scalar is found closer to the second order critical line, but it soon starts decoupling from the low–energy physics as we move away from it. There is only a small patch of the phase space we explored where Eq. (2.14), Eq. (2.15) and Eq. (2.16) hold simultaneously. The lightest mass m_5 we measured is of order $2\sqrt{\sigma}$.

Using the non–perturbative lines of constant physics, we can try to discuss the different types of continuum limit. Our findings can be compared to the perturbative picture reported in Ref. [59], bearing in mind that our results are obtained for fixed values of N_5 and N_4 and therefore could be affected by finite–volume effects. At any fixed value for β_4 in the dimensionally reduced phase, there is a lower bound for β_5, given by the location of the critical point. By increasing β_5, we cross lines of decreasing lattice spacing a_4, therefore moving towards a continuum limit, meaning that the lattice discretisation effects vanish. At the same time we cross lines of increasing scalar mass m_5, which inevitably decouples from the low–energy spectrum: the low–energy effective theory described in this

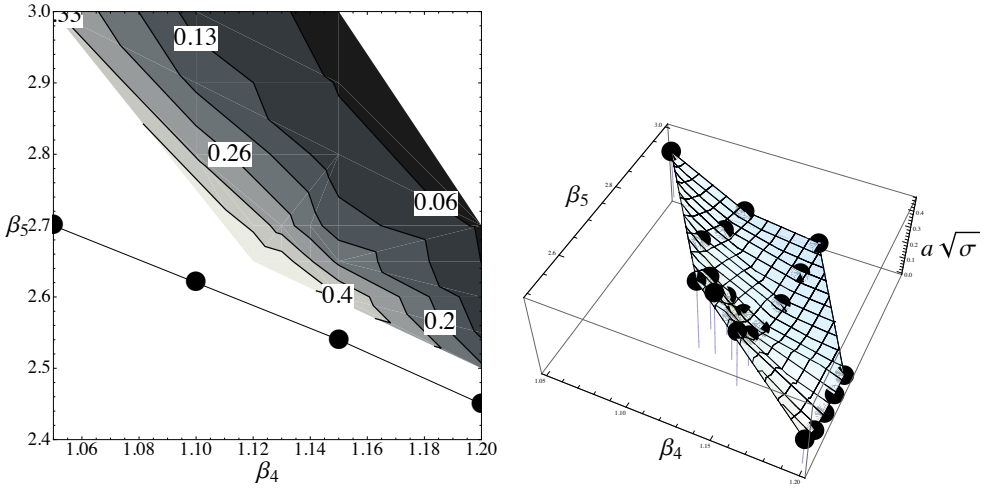

(a) *Lines of constant* $a_4\sqrt{\sigma}$ **(b)** *Three dimensional surface*

Figure 2.25 *Lines of constant string tension* $a_4\sqrt{\sigma}$ *at* $N_5 = 4$ *in the bare parameter plane. The lines are obtained interpolating the data with a two–dimensional surface.*

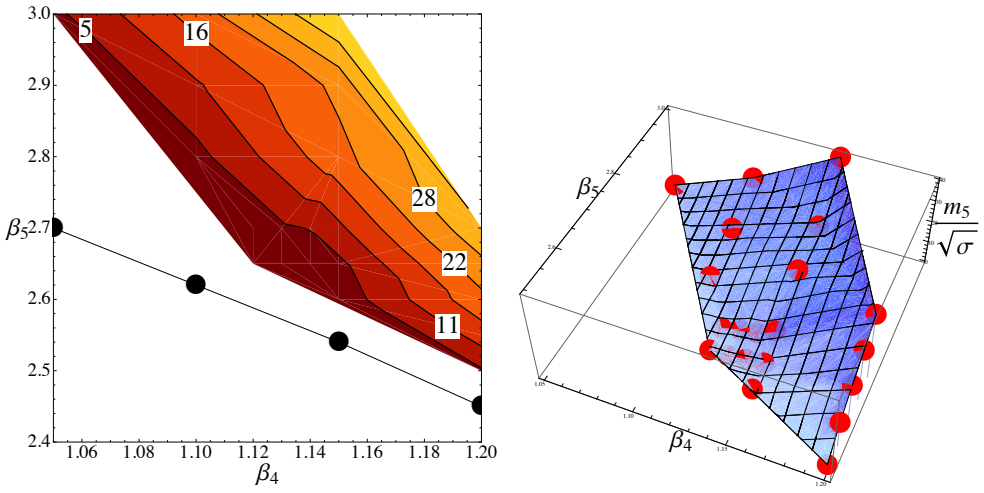

(a) *Lines of constant* $m_5/\sqrt{\sigma}$ **(b)** *Three dimensional surface*

Figure 2.26 *Lines of constant scalar mass* $m_5/\sqrt{\sigma}$ *at* $N_5 = 4$ *in the bare parameter plane. The lines are obtained interpolating the data with a two–dimensional surface.*

region is four–dimensional, and contains only gauge degrees of freedom. A similar limit occurs at fixed β_5 and increasing β_4. However, by following a line of constant scalar mass in the phase diagram, we cross lines of different fixed lattice spacing. In particular, moving towards smaller β_4 and bigger β_5 the lattice spacing decreases, allowing us to reach the desired separation between the cutoff and the low–energy physics with a constant value of the scalar mass.

The low–energy dynamics is then described by an effective four–dimensional theory with a light adjoint scalar in the low–energy spectrum, having started with a five–dimensional theory with only gauge degrees of freedom. This being an effective description, it is expected to hold only up to the energy scales given by the compactification radius, as we already mentioned in Sec. 2.1.3. What we have learned from our non–perturbative map of the energy scales in the phase diagram of the lattice model is that it requires a certain amount of fine tuning to pin down the location of a line of constant mass and to follow it. Moreover, the behaviour of the cutoff scale near the line of second order phase transition (cfr. Fig. 2.24) makes it very difficult to determine $\frac{m_5}{\sqrt{\sigma}}$ non–perturbatively, thereby limiting our ability to reach values of the scalar mass that are smaller than the square root of the string tension.

This is an important result for future studies in this context, and it was not anticipated using perturbative arguments. For example, looking at the perturbative results in Fig. 2.2, or equivalently at Fig. 7 in Ref. [59], where the line of phase transitions in the $a_5 \to 0$ is taken into account, we note that the lines of fixed $a_4\sqrt{\sigma}$ go straight into the critical line. This behaviour is not supported by our non–perturbative results: those lines cannot cross the point where the phase transition occurs, because $a_4\sqrt{\sigma}$ increases as we approach that point. Any attempt to follow a line of constant scalar mass would have to deal with this problem.

2.5.2 Compactification effects on the scalar mass

So far we have only explored the behaviour of energy scales in the bare parameter space. However, each point we have simulated on the phase diagram corresponds to a precise location in the space given by the three energy scales we are interested in, that are $\Lambda_{\rm UV}$, $\Lambda_{\rm R}$ and m_5. We can therefore translate our results at $N_5 = 4$ and $N_5 = 6$ into a common set of points $(\Lambda_{\rm UV}, \Lambda_{\rm R}, m_5)$. This approach allows us to study m_5 as a function of the other two energy scales, instead of the bare

parameters. From now on we express the energies $\Lambda_{\rm UV}$ and $\Lambda_{\rm R}$ using their length counterpart, $a_4\sqrt{\sigma}$ and $R\sqrt{\sigma}$ respectively. These two length scales are related to each other by Eq. (2.21) and they are both measured non–perturbatively: the first is directly measured, whereas the second relies on the interpolated data of ξ from Ref. [2].

The range of values of $a_4\sqrt{\sigma}$ and $R\sqrt{\sigma}$ spanned in our simulations is shown in Fig. 2.27, and the data we used are summarised in Tab. A.7 and Tab. A.8. In the following plots, we report results from $N_5 = 4$ together with the ones from $N_5 = 6$. When more than one value for $a_4\sqrt{\sigma}$ or $a_4 m_5$ is extracted for the same (β_4, β_5) point (cfr. Tab. A.3 to Tab. A.6), we apply the following procedure: if the values are compatible within one standard deviation, we plot the weighted average as central value, and the weighted error as the statistical error; we also use the spread of the results to estimate the systematic error due to the choice of the effective mass plateaux. If the values are not compatible, we use the average for the central value, whereas the systematic error is chosen to comprise both the lowest and the highest values.

With our available data, we can explore the behaviour of the scalar mass m_5 in the following region of lattice spacing a_4

$$0.15 \;<\; a_4\sqrt{\sigma} \;<\; 0.40 \;, \tag{2.47}$$

and compactification radius R

$$0.05 \;<\; R\sqrt{\sigma} \;<\; 0.12 \;. \tag{2.48}$$

The major advantage of interpreting the data in this new physical space is that we can disentangle compactification effects from cutoff effects. It is clear from Fig. 2.27 that we have points at different values of the lattice spacing, but at the same value of the compactification radius. The scalar mass on those particular points can therefore be studied at fixed compactification scale and different cutoff scale. On the other hand, we also have points at the same value of the lattice spacing, but at different radii, which can be used to study the behaviour of the scalar mass at fixed cutoff scale. From Fig. 2.27 we can also infer that increasing N_5 would allow us to explore a wider range of cutoff values for fixed compactification scale.

Our main goal is to clarify the validity of the result in Eq. (2.1) where the

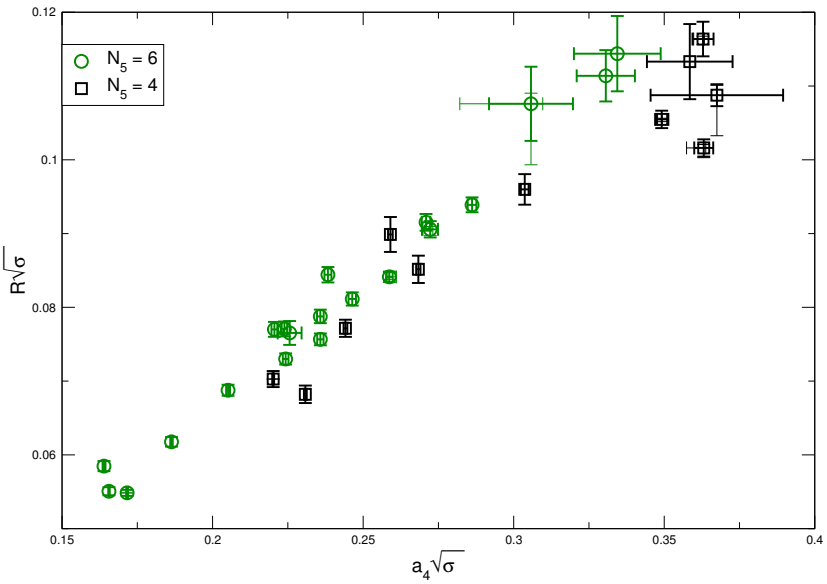

Figure 2.27 *The points in the phase space are mapped into the physical space of the energy scales of the system. In the plot we report the length scale corresponding to the ultraviolet cutoff, and the one corresponding to the compactification energy. Using both data from $N_5 = 4$ and $N_5 = 6$, we can span a larger region of this space. Some points have two different type of error bars described in the text: the thicker one is statistical, whereas the thinner is systematic as.*

perturbative scalar mass is expected to depend strongly on the compactification scale. In our lattice model we would like to see if there are leading cutoff corrections to this expected behaviour when we look at the non–perturbatively measured scalar mass. The simplest way of looking for these corrections is to study the dependence of the scalar mass on the lattice spacing. However, our values for the lattice spacing usually correspond to different values of the compactification radius. It is clear from this discussion that the study in Ref. [59] cannot give any hints about Eq. (2.1): the lattice spacing always changes together with the compactification radius, because their ratio is forced to be constant. Nothing can be said about the dependence of m_5 at fixed compactification scale nor at fixed cutoff scale from the results of these earlier studies. Using our data, we can plot m_5 as a function of a_4 and separately as a function of R. The plots are shown in Fig. 2.28: Fig. 2.28(a) shows the scalar mass dependence on the lattice spacing in the range defined in Eq. (2.47), whereas Fig. 2.28(b) shows its behaviour as a function of the compactification radius in the range of Eq. (2.48). The observed range for the scalar mass in units of the string tension is

$$2 \; < \; \frac{m_5}{\sqrt{\sigma}} \; < \; 10 \; . \tag{2.49}$$

The important thing to notice in this analysis is how the scalar mass changes between the two plots. While some of the points are insensitive to the two different choices of variables, it is striking to see points with the same mass but far away in Fig. 2.28(a) fall on top of each other once expressed in terms of the compactification radius in Fig. 2.28(b). If Eq. (2.1) holds, then the combination $m_5 R$ should be independent of R at leading order, while retaining any dependence on the cutoff a_4. In order to separate the scalar particle from the Kaluza–Klein modes, this variable should be less than one as we stated in Eq. (2.16). In Fig. 2.29 we plot $m_5 R$ as a function of $a_4\sqrt{\sigma}$. The data show a scalar mass in units of the compactification radius in the range

$$0.2 \; < \; m_5 R \; < \; 0.5 \; . \tag{2.50}$$

Such range is smaller than the one spanned by $m_5/\sqrt{\sigma}$ by almost one order of magnitude for the same interval of lattice spacings. This evidence supports the observation that the dependence on $a_4\sqrt{\sigma}$ is milder than the one shown in Fig. 2.28(a) and it is compatible with the perturbative expectation in Eq. (2.1), giving a coupling constant of order $\mathcal{O}(3)$. The product $m_5 R$ does not show any sign of quadratic divergences as the lattice spacing is reduced. However, we must recall that all the simulations were performed on a fixed value of N_4, therefore the points at the smallest values of $a_4\sqrt{\sigma}$ are the ones on the smallest physical volumes and finite–size effects could be present. On the other hand, large values of $a_4\sqrt{\sigma}$ point in the direction of larger discretisation effects.

2.6 Conclusions and future prospects

In this Chapter we presented a non–perturbative study of a SU(2) pure gauge theory in five dimensions. The system, discretised on anisotropic lattices, was investigated in the so–called dimensionally reduced phase, where a light scalar particle is expected, in perturbation theory, due to compactification of the extra dimension. The lattice discretisation provides a gauge–invariant regulator for a non–renormalizable effective theory and allows numerical simulations of the low-energy non–perturbative physics.

If the scales of the theory are properly separated, one–loop perturbative calculations suggest the low–energy dynamics of this theory to be described by a four–dimensional gauge theory coupled to a massive scalar field. We have

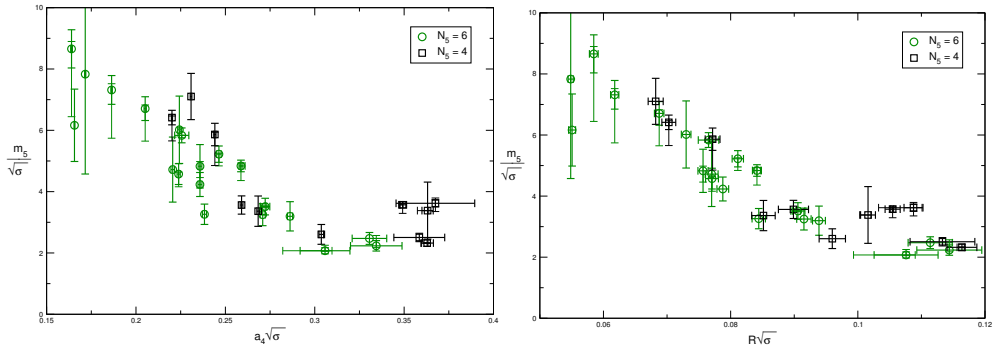

(a) $m_5/\sqrt{\sigma}$ *vs.* $a_4\sqrt{\sigma}$ **(b)** $m_5/\sqrt{\sigma}$ *vs.* $R\sqrt{\sigma}$

Figure 2.28 *(a) The scalar mass as a function of the lattice spacing for* $N_5 = 4$ *and* $N_5 = 6$*; (b) The same scalar mass is also shown as a function of the compactification radius. Points at the same value of the radius have the same mass within the statistical error. Each of the point in (a) corresponds to a point in (b). Systematic errors due to the choice of the effective mass plateaux are reported for some points using thinner error bars.*

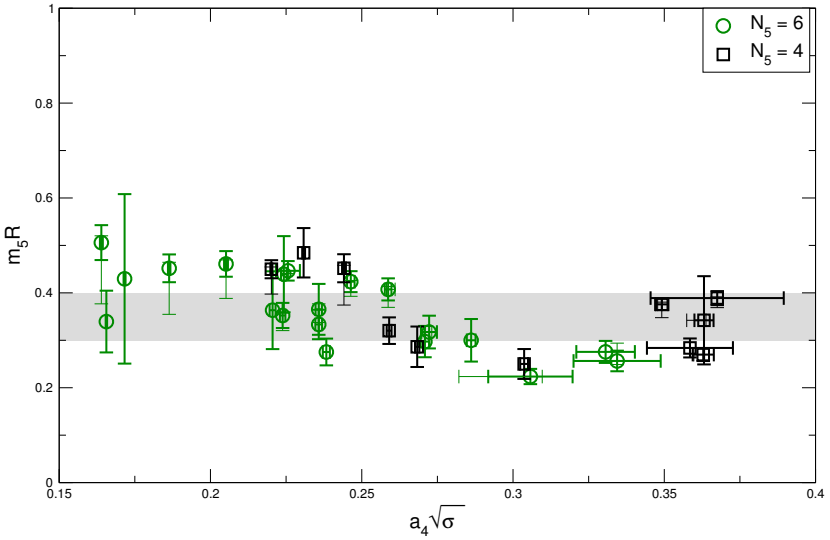

Figure 2.29 *The scalar mass in units of the compactification radius* m_5R *is shown to be mildly dependent on the lattice spacing* $a_4\sqrt{\sigma}$*. The grey band* $0.3 \leq m_5R \leq 0.4$ *includes all points within two standard deviations and it is drawn to guide the eye. Also in this case, systematic errors are shown with thinner error bars, whereas the thicker ones represent statistical standard deviations.*

measured the mass of the non–perturbative scalar states in a specific region of the bare parameter space, where we expect to find the desired separation between physical scales. We have also determined numerically the four–dimensional lattice spacing in units of the string tension. This allowed us to describe the lines of constant scalar mass and constant ultraviolet cutoff as they arise non–perturbatively.

The final non–perturbative picture given in Sec. 2.5.2 seems to confirm the observation in Ref. [59] about the possibility of effectively describing a four–dimensional Yang–Mills theory with a scalar adjoint particle in the continuum limit. Although that observation was based entirely on perturbative results explained in Sec. 2.2, our numerical simulations show how this continuum limit could be actually reached by following lines of constant scalar mass in the parameter space of the model. As we described in Sec. 2.5.1, this is not a straightforward procedure and it definitely requires some sort of fine tuning. Moreover, we were not able to find a trajectory where the scalar mass was lighter than the string tension, at least in the region of the phase space we explored.

Even though the search for a light scalar requires fine tuning in this simple model, we have shown that its mass is only very mildly affected by the ultraviolet cutoff, whereas it strongly depends on the radius of the compactified extra dimension. This is entirely compatible with the perturbative result of Eq. (2.1) and it is the first non–perturbative evidence that the mass of scalar particles coming from a compactification mechanism does not have a quadratic dependence on the cutoff. We need to bear in mind that our results are obtained at finite lattice spacings, both a_4 and a_5, and at finite volume. Exploring regions of parameter space where the lattice spacings are smaller will improve the scale separations, reducing the effects of the discretisation chosen to represent the continuum effective theory. Moreover, larger lattices will be needed to keep the physical volume close enough to the thermodynamic limit of the system.

Chapter 3

Scalar spectrum in Technicolor models

The study of strongly-interacting models often resorts to lattice gauge theory methods. In this chapter we show how such methods can be applied to explore the spectrum of (quasi–)conformal theories. We describe a detailed investigation of a SU(3) gauge theory with 12 massless Dirac fermions in the fundamental representation of the gauge group. We refer to such theory in the following as twelve–flavour QCD, even though it shares only little with QCD, as we will explain. In fact, this theory is asymptotically free in the ultraviolet, but its infrared dynamics is believed to be governed by a fixed point in the renormalization group flow. Thanks to these features, it might serve as a model for BSM physics explaining DEWSB, being one possible candidate for Walking Technicolor (cfr. Sec. 1.3).

We focus our attention on gluonic observables like the string tension and the glueball spectrum. There are two main reasons why we are interested in such observables. First, they provide an additional tool to investigate the suspected infrared conformal nature of the theory when their spectrum is compared to the one of mesonic states [75–78]. The second reason is that the scalar glueball state carries no (techni-)flavour charge and therefore has the same quantum numbers as the Higgs boson which, in a walking technicolor theory, would be naturally light since it appears as the Nambu-Goldstone boson of the spontaneously broken conformal symmetry [42, 43]. The mixing of such composite Higgs boson with glueballs is an important issue that could be resolved in a lattice study.

The results in this chapter have been presented in a proceeding paper [79] and submitted for publication [80]. They are an important part of the LatKMI collaboration's project of investigating gauge theories with a large number of fundamental flavours using non–perturbative lattice simulations, in the quest for a candidate BSM theory to explain DEWSB through strong dynamics.

3.1 Lattice studies of Technicolor

When (quasi–)conformal theories are discretised on the lattice, and simulated on a computer, effects due to infrared scales like the lattice volume and the fermion mass are introduced, spoiling the characteristic symmetries of the theories. As a consequence, it is impossible to simulate a conformal theory on a lattice without explicitly breaking its scale symmetry. However, since we know how this breaking occurs, we can exploit this fact to identify conformality in a lattice gauge theory.

A gauge theory with an infrared fixed point (IRFP) on its massless critical surface can be studied, in the limit of infinite volume $L \to \infty$, by looking at the scaling laws introduced due to a small mass deformation m_f. Such a theory is termed mass–deformed conformal gauge theory (mCGT) and a series of recent papers [78, 81–83] has carefully established a full set of scaling relations for its spectrum, matrix elements and correlators. Moreover, the effects of a finite lattice size L can also be accounted for [77, 84, 85].

We recall here that a massless gauge theory which is infrared conformal does not display confinement, it is chirally symmetric and its spectrum is made of unparticles. On the contrary, a massless gauge theory with chiral symmetry breaking has a well defined non–vanishing string tension due to confinement and has a spectrum containing Goldstone boson which are massless and hadrons with a characteristic non–zero mass. Chiral symmetry breaking and confinement are not necessarily related. Let us assume here that they are. For the following discussion it is important to highlight how these two scenarios are modified when a small fermion mass m_f is introduced.

3.1.1 Hyperscaling near the fixed point vs. chiral perturbation theory

The infrared conformal gauge theory becomes a mCGT where m_f is the relevant coupling which sets the scale of the departure from the critical point on the massless surface. In this case, the infrared dynamics is characterised by a string tension and a massive spectrum of bound states (fermionic and gluonic). The mass m_f is a relevant parameter in the sense of the renormalization group. As a result, the mass M_X of every state X features a power–law dependence

$$M_X \;=\; A_X m_f^{\frac{1}{1+\gamma_\star}} \;. \tag{3.1}$$

The above relation is characteristic of the scaling of length scales in the study of critical phenomena [75, 76, 81, 82, 84] and it is usually referred to as the *hyperscaling* relation. $\gamma_\star$ is the value of the mass anomalous dimension at the fixed point and, while the coefficient A_X is different for different states of the spectrum, $\gamma_\star$ is universal, being an intrinsic feature of the IRFP.

The hyperscaling relation implies that all mass scales in the spectrum will go to zero in the massless (chiral) limit with the same rate. Therefore, ratios of mass observables should be constant as the fermion mass m_f is lowered. It is important to remind that this behaviour is expected to hold sufficiently close to the critical massless surface, where the linearised form of renormalization group equations, from which Eq. (3.1) is obtained, is a good approximation.

In contrast to the hyperscaling relation, a gauge theory whose infrared physics is characterised by chiral symmetry breaking features a different scaling, dictated by the explicit breaking of chiral symmetry due to the fermion mass m_f. When a small m_f is introduced, the Goldstone bosons associated to the spontaneous breaking of chiral symmetry (the would-be pion states in QCD) acquire a mass which scales like

$$M_\pi \;=\; A_\pi \sqrt{m_f} \;, \tag{3.2}$$

while other hadronic states remain massive also in the chiral limit

$$M_X \;=\; A_X m_f + B_X \;, \tag{3.3}$$

where B_X is of the order of the strong dynamics scale (e.g. $\Lambda_{\rm QCD}$). The above relations are a consequence of Chiral Perturbation Theory (ChPT) [86], which

describes the low–energy dynamics of theories with broken chiral symmetry.

The relations Eq. (3.1)-(3.3), are derived for a fermion mass deformation m_f which is much smaller than the characteristic dynamical scale of the gauge theory Λ. In the opposite case $m_f \gg \Lambda$, both the infrared conformal theory and the chirally broken one have the same spectrum [75, 78] characterised by fermionic bound states of n quarks with mass

$$M_F^{(n)} \sim n\, m_f \,, \tag{3.4}$$

and gluonic bound states

$$M_G \sim \Lambda \,. \tag{3.5}$$

In fact, this heavy–mass regime can be described, in both theories, by the same low–energy effective action, which is the Yang–Mills action. Therefore, as first suggested in Ref. [76, 78] it is possible to mistake a chiral symmetry broken theory with heavy fermions, and a theory with a IRFP. For example, when looking at the masses of the vector (ρ) over the pseudoscalar (π) state one would observe a constant ratio

$$\frac{m_\rho}{m_\pi} \approx 1 \tag{3.6}$$

for both theories.

A possible solution to this problem is to compare the fermionic spectrum to the gluonic one. In particular, the gluonic spectrum i.e. string tension and glueball masses, of a chiral symmetry breaking theory with heavy fermions would be independent of the fermion mass and reflects only the dynamically–generated scale Λ. Observing a constant ratio between, for example, the pseudoscalar mass m_π and the string tension $\sqrt{\sigma}$ for a certain range of fermion masses m_f would be a hint that the theory is infrared conformal.

3.1.2 Renormalization flow studies on the lattice

In the discussion about conformal gauge theory on the lattice, we have focused so far in the analysis of the spectrum and its comparison with the one in a chirally broken theory. This is not the only way to distinguish such different theories using methods of lattice gauge theories. With the purpose of identifying the presence of a IRFP in a continuum massless gauge theory using lattice methods, one can turn to study directly the running of the gauge coupling $g(\mu)$. As we have

seen in Sec. 1.3, the gauge coupling $g(\mu)$ of a (quasi–)conformal theory behaves like the one of an asymptotically free theory when $\mu \gg \Lambda$, but for low energies $\mu \ll \Lambda$ remains approximately constant and reaches the fixed point value $g_\star$ (or eventually blows up if conformality is spontaneously broken in the infrared e.g. by a fermionic dynamical mass).

Frameworks to compute the running coupling of asymptotically free theories defined on the lattice exist, like the Schroedinger functional (SF) [87] or Monte Carlo renormalization group (MCRG) methods [88]. They have been successfully applied to Yang–Mills theories and QCD first, but are now starting to give results for theories with (approximate) conformality. A short list of works exploiting the SF method for candidate Technicolor theories [89–95] or the MCRG method [96–99] is given for reference, but it is not meant to be complete as this is a very active research field. A nice (and almost up to date) summary of lattice studies for (Walking) Technicolor candidate theories can be found in Ref. [100].

Recently a new scheme, called Wilson Flow (WF), has been proposed [101] to study the renormalization flow of gauge theories. This scheme is very well suited for lattice gauge theories. It could be applied to the kind of strongly–interacting theories that we are interested in, as candidates for BSM physics. The WF method has been used to precisely set the scale in lattice QCD simulations [102, 103], but only few applications interesting to BSM physics exist so far [104, 105]. We will probably see more studies of (Walking) Technicolor candidate theories using the WF method in the future [106].

3.2 Twelve–flavour QCD

In the rest of this chapter, we focus only on one of the possible gauge theories that are being considered as Walking Technicolor candidates. It is a SU(3) gauge theory with 12 massless fermions in the fundamental representation of the gauge group. We briefly recall what lattice studies have been performed so far by different groups and what is the common lore about the existence of a IRFP in this theory. Then we describe the setup of the lattice simulations used to perform the study in this thesis and the results obtained for the spectrum of the theory, focusing in particular on flavour–singlet scalar states and the string tension.

Twelve–flavour QCD has received a lot of interest in the last few years because

its number of flavours $N_f = 12$ is very close to the perturbative critical value $N_f^\star = 11.5$ [1]. The first lattice studies of this theory provided evidences in favor of a IRFP [90] using the SF method to study the running of the coupling constant. However, shortly after, a detailed study of the mesonic spectrum and the chiral condensate on large volumes showed that twelve–flavour QCD features confinement and chiral symmetry breaking [85, 108]. Such conclusions were based on a scaling analysis of the spectrum following what has been described in Sec. 3.1. As we have already mentioned, such scaling laws are modified by corrections due to a large fermion mass m_f and a finite lattice size L. It is difficult to account for scaling corrections and, for example, an alternative analysis [109] of the data in Ref. [108] indicates the infrared dynamics of the theory near the chiral limit is conformal. Moreover, there are results about the study of thermal transition lines [110] in twelve–flavour QCD which provide results difficult to interpret in a conclusive manner.

Further studies started looking for different ways of keeping the systematic errors of the lattice simulations under control. For example, using MCRG methods, an IRFP has been found [97, 99], and this result has been confirmed using a different renormalization scheme [111, 112]. Moreover, additional support for the IRFP scenario comes from the study of the Dirac operator eigenvalues and their distribution [113]. Given that compatible results have been obtained with methods having different sources of systematic errors, the possibility of twelve–flavour QCD being an infrared conformal theory seems promising.

It is important to mention that often lattice results from various groups are obtained using different discretisations of the gauge and fermionic action, leading to different systematic effects in the resulting numerical simulations. When the discretisation of the continuum theory action is changed, the phase structure of the lattice model described by such an action changes and phase transitions related to the ultraviolet properties of the model can appear. The physics we are interested in studying from the discretised model is in the infrared regime, but bulk phase transitions can prevent us to reach the relevant region of the parameter space. While the issue of lattice artefact transitions is quite well known for different discretisation of QCD with light and strange quarks, large–N_f QCD and, specifically, twelve–flavour QCD have only recently started to be investigated from this point of view. Results from different groups point out a very interesting

[1] The critical number of flavours below which conformality is lost and chiral symmetry breaking sets in. It has been calculated based on Schwinger–Dyson equation and the 2–loop beta function for gauge groups SU(N_c) with arbitrary N_f fermions in several representations [107].

phase structure [114–116], that we will not discuss further. Suffices to say that the set of parameters and the lattice action used in our simulations appear to be in the correct phase, smoothly connected to the large volume and weak coupling limit of the continuum theory.

The LatKMI collaboration has studied SU(3) gauge theories with $N_f = 4$, 8, 12 and 16 using a common setup of lattice simulations that will be described in the following. The goal of the study is to be able to compare the observables for each different theory in a common framework which is subject to the same systematic effects. This way one can expect a better controlled comparison between the theories with different number of flavours.

Results have been presented in Ref. [117] for the mesonic spectrum of $N_f = 12$ and Ref. [49] for the chiral properties of $N_f = 8$. The properties of the $N_f = 4$ and $N_f = 16$ theories are also discussed [118–120]. The current understanding of the LatKMI collaboration is that the $N_f = 4$ theory is chirally broken and confining with a m_ρ/m_π ratio growing to infinity as $m_f \to 0$. The $N_f = 8$ theory features a small but non–zero chiral condensate in the chiral limit, hinting at spontaneously broken chiral symmetry. However, its spectrum satisfies the hyperscaling relation Eq. (3.1) for values of m_f not too close to the chiral limit. The coexistence of both the above phenomena is interpreted as a signal of "walking": there exists a region of scales with a slowly running coupling, triggering conformal–like behaviour in the spectrum. To conclude, the spectrum of the $N_f = 12$ theory seems to accomodate the presence of a IRFP and additional evidence is provided by looking at gluonic observables in the following sections.

3.3 Details of the lattice simulations

The numerical simulations of the continuum SU(3) gauge theory with 12 degenerate fermions are carried out by the LatKMI collaboration using the staggered formulation to discretise the fermionic action and the Symanzik approach to the gauge action. In particular, the 12 degenerate massless fermions in the continuum are represented using 3 degenerate staggered fermion species, each coming in 4 tastes (3 species $\times$ 4 tastes = 12 flavours) on the lattice. Appendix D gives a brief overview of the properties of staggered fermions. Since

Monte Carlo simulations can not deal with massless fermions [2], each fermion species has a bare mass am_f, which is one of the input parameters of the lattice model.

At finite lattice spacing, where the simulations take place, the continuum flavour symmetry does not hold exactly, due to ultraviolet artefacts which give rise to interactions between different tastes. One of the consequences of this flavour symmetry breaking is that, in a given symmetry channel of the mesonic and baryonic spectrum, multiplets appear corresponding to different taste structures of the corresponding interpolating operator enhancing the state from the vacuum. These multiplets would be degenerate if flavour symmetry were exact. The mass splitting within the states of a multiplet is referred to as taste splitting and is commonly used as a reference measure for good flavour symmetry: the smallest taste splitting, the better the lattice realisation of flavour symmetry.

Different staggered fermion actions exist which try to reduce taste splitting. We use the Highly Improved Staggered Quark (HISQ) action, firstly introduced in Ref. [121] and widely used for lattice QCD simulations thanks to the highly suppressed taste splitting and excellent continuum scaling among the different staggered formulations [122]. We will comment more about taste splitting in our simulations (see Sec. 3.3.1).

In contrast to the originally defined HISQ [121], we drop some of the improvements used to get a better scaling of physical properties to the continuum limit. For example, we used the Symanzik tree–level discretisation of the gauge action, therefore dropping the tadpole improved term, and we neglected the mass correction in the Naik term [122] for the fermions. The inclusion of these terms is expected to reduce lattice artefacts, but they are known to increase the overall cost of the simulations. Therefore, for a theory such as the one we are interested in, where the level of understanding of the continuum physics is not at all comparable with what is found for lattice QCD, we decide to sacrifice some of the improvements to obtain results from more efficient simulations.

We generate gauge configurations with the standard hybrid Monte–Carlo (HMC) algorithm, using the MILC code (version 7 [123]) with a few modifications. For

[2]Massless fermions can be incorporated in lattice simulations with currently available algorithms only if zero modes of the Dirac operator are removed. The reason for this resides in the practical need to invert the Dirac operator matrix many times during the simulation. The most popular way to avoid fermionic zero modes and simulate massless quarks is to employ twisted boundary conditions.

example, the Hasenbusch mass preconditioning [124] has been added to reduce the large computational cost required to invert the Dirac operator at the small fermion masses am_f.

The bare gauge coupling constant is set to $\beta = 6/g^2 = 4.0$, which is the value closer to weak coupling in Ref. [117]. This is the only gauge coupling at which the gluonic spectrum is investigated for twelve–flavour QCD. Therefore the main results of this chapter are obtained at fixed lattice spacing. In the following, we try to estimate the effects of this finite lattice spacing on our observables.

We simulate four physical volumes $(aL)^3$ with $L = 18, 24, 30, 36$ and aspect ratio $T/L = 4/3$, where T is the number of points in the temporal direction (e.g. the one used to calculate correlation functions). The larger than unity aspect ratio provides smaller finite–temperature effects. We select different bare quark masses on each volume, from $am_f = 0.05$ on the largest $L = 36$ volume, to $am_f = 0.16$ on the smallest $L = 18$. Using a larger volume at smaller bare fermion mass is important to keep finite–size effects under control, as we describe in the following. This set of parameters, summarised in Tab. 3.1, allows us to check for finite–size systematics at fixed quark mass and to test hyperscaling in the infinite volume limit. The simulated pseudoscalar masses belong to the interval $0.32 < am_\pi < 0.74$.

The most important features of our simulations, that are worth mentioning, are the excellent flavour symmetry realisation of the HISQ action and the large number of configurations, obtained after $\mathcal{O}(1000)$ thermalisation trajectories, from uninterrupted Markov chains. For ensembles labeled with A in Tab. 3.1, we saved configurations every 5 Monte Carlo trajectories (with Molecular Dynamics length $\tau = 1$), while for the rest of the ensembles we saved configurations every 2 trajectories. Therefore, we generate between approximately 10000 and 30000 trajectories to perform a large statistics analysis of the gluonic and fermionic spectrum.

3.3.1 Mesonic spectrum

Before describing the main results of our study, we recall the most suggestive features of the results obtained in Ref. [117]. The mesonic spectrum of twelve–flavour QCD, comprising the pseudoscalar mass m_π, the vector mass m_ρ and the pseudoscalar decay constant F_π, has been studied on a subset of the parameters

Tag	N_f	$L^3 \times T$	β	am_f	$N^{\mathrm{G}}_{\mathrm{cfgs}}$	$N^{\mathrm{S}}_{\mathrm{cfgs}}$
A1	12	$18^3 \times 24$	4.0	0.06	3090	5000
A2	12	$18^3 \times 24$	4.0	0.08	5250	5000
A3	12	$18^3 \times 24$	4.0	0.10	5190	5000
A4	12	$18^3 \times 24$	4.0	0.12	5200	5000
A5	12	$18^3 \times 24$	4.0	0.16	4200	5000
B0	12	$24^3 \times 32$	4.0	0.05	9440	7200
B1	12	$24^3 \times 32$	4.0	0.06	14000	14000
B2	12	$24^3 \times 32$	4.0	0.08	15340	15000
B3	12	$24^3 \times 32$	4.0	0.10	9480	9000
C0	12	$30^3 \times 40$	4.0	0.05	7500	4500
C1	12	$30^3 \times 40$	4.0	0.06	14000	12000
C2	12	$30^3 \times 40$	4.0	0.08	11450	13000
C3	12	$30^3 \times 40$	4.0	0.10	5000	4000
D0	12	$36^3 \times 48$	4.0	0.05	5100	5000
D1	12	$36^3 \times 48$	4.0	0.06	6000	4100

Table 3.1 *Parameters of lattice simulations for $N_f = 12$ QCD by the LatKMI collaboration. $N^{\mathrm{G}}_{\mathrm{cfgs}}$ is the number of saved gauge configurations used for the measurement of the gluonic observables, while $N^{\mathrm{S}}_{\mathrm{cfgs}}$ are used for the fermionic flavour–singlet scalar state measurement. The Tag column identifies each ensemble.*

and configurations in Tab. 3.1, but also for an additional gauge coupling value $\beta = 6/g^2 = 3.7$.

First of all, the results for the pseudoscalar and vector spectrum at both lattice spacings show a negligible dependence on the (taste) flavour structure of the interpolating operators used in the two–point functions. To obtain the pseudoscalar mass, for example, one can use two different interpolating operators with the correct quantum numbers 0^-, but different spin–taste structure (see Ref. [125] for a detailed explanation and Appendix D for an overview). In the continuum limit, these two different operators will couple to the same state and their correlation function would decay exponentially with time according to the mass of the pion (π). However, as already mentioned, the lattice discretisation used breaks flavour symmetry and different *pions* can be created.

The pseudoscalar operator with (spin $\otimes$ taste) structure ($\gamma_5 \otimes \xi_5$) (called PS in the following) couples with the Goldstone boson of chiral symmetry breaking hence the lightest, while a different pseudoscalar ($\gamma_5\gamma_4 \otimes \xi_5\xi_4$) (SC) couples to a heavier state. These states would be degenerate in the continuum and their mass difference measures the taste splitting. For a reference, the PS operator correspond to combination II in Table 1 of Ref. [125], while SC to combination I.

A similar case holds for the vector state, for which the operator $(\gamma_i\gamma_4 \otimes \xi_i\xi_4)$ (PV) and $(\gamma_i \otimes \xi_i)$ (VT) can be used (respectively combination III and IV in Table 1 of Ref. [125]).

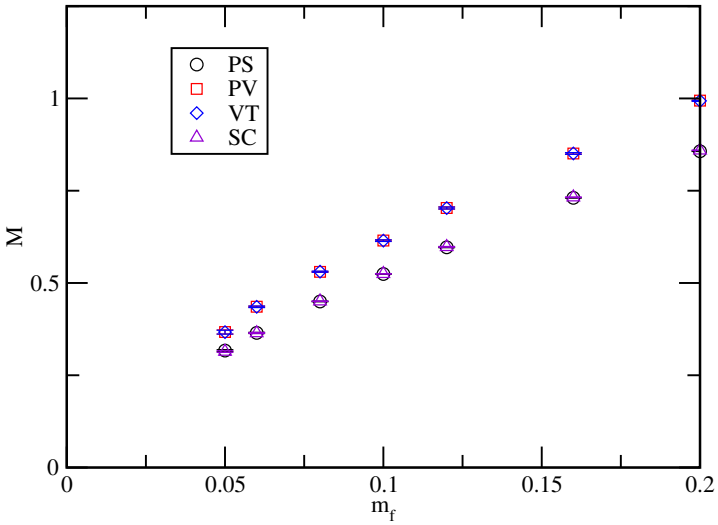

Figure 3.1 *An example of the small taste splitting in the spectrum of $N_f = 12$ QCD with HISQ fermions at $\beta = 4.0$ on the volume $L = 30$ $T = 40$. The figure is taken from Ref. [117]. M and m_f are the meson mass and the bare quark mass respectively, both in units of the common fixed lattice spacing a. PS and SC refer to pseudoscalar mesons coming from operators with different internal taste structure, whereas PV and VT refer to vector mesons.*

In Fig. 3.1 we show the taste splitting in the pseudoscalar and vector channels for the weaker gauge coupling $\beta = 4.0$ (hence the smaller lattice spacing) on a $L = 30$ lattice. The mass difference between PS and SC is negligible for all the fermion masses shown. The same is true for PV and VT. This should be kept in mind when comparing the results of the LatKMI collaboration with other twelve–flavour QCD results.

The second feature we want to underline here is the hyperscaling analysis of m_π, m_ρ and F_π using Eq. (3.1). A modified version of Eq. (3.1) has been used, to keep into account the finite volume of the lattice and the possibility of having sub–leading corrections due to a somewhat large m_f. The addition of such corrections was used to estimate a systematic error on the measured $\gamma_\star$. The results favour a common value of $\gamma_\star$ for the three channels explored and at both lattice spacings, summarised in Figure 14 of Ref. [117], between $0.4 < \gamma_\star < 0.5$.

For the analysis in the following, we mention the value $\gamma = 0.414(6)$ characteristic of the m_π scaling at $\beta = 4.0$ (for our current purposes, the systematic errors on

γ have been neglected).

3.4 Fermionic scalar spectrum

In this section, we present the results of the flavour–singlet scalar spectrum obtained using correlators of fermionic operators. We compare our calculation to what is known from lattice simulations of QCD, in order to gain some insights on the problems which arise. The details of this measurement have been described in Ref. [80], which we follow. A disclaimer: the measurements in this section have not been performed by the author himself, but by other members of the LatKMI collaboration. They are included in this work due to the relevance to the topic discussed and because the author has personally contributed to Ref. [80].

In QCD, the lightest flavour–singlet scalar state is the $f_0(500)(\sigma)$ meson. Its light mass in QCD is quoted between 400 and 550 MeV and several studies suggest a non–$q\bar{q}$ nature for this state. The σ meson of real world QCD has been reviewed in the latest Particle Data Group [126] and several studies were carried out using lattice simulations, both with and without the inclusion of dynamical quarks [127–130].

Another example of a flavour–singlet scalar particle is the 0^{++} glueball, a state generated by the strong–interacting nature of the gluon field. The experimental evidence of glueballs as resonances in QCD has yet to be proven, but the physics program of newly designed facilities like the PANDA experiment [131, 132] has started to address this issue. A recent detailed review on glueballs and their importance in experimental studies can be found in Ref. [15], where results from lattice simulations are also included.

Since the pion is very light in QCD, due to its Goldstone boson role for chiral symmetry breaking, a two–pions s–wave scattering states could also be a relevant source of mixing to this channel. A recent lattice calculation [133] tries to address and quantify this source of mixing, albeit with non–physical pion masses. Moreover, in QCD, we expect mixing between gluonic and fermionic degrees of freedom, so that some of the states in the light mesonic nonet could contain gauge field excitations as relevant degrees of freedom.

This mixing could also happen in the large–N_f versions of QCD. However, we should note that the candidate for a composite Higgs of dilatonic nature must be

predominantly a fermionic bound state and not a glueball state. This is needed in order to couple the Higgs with the electro–weak sector, since the gluons do not carry SU(2) $\times$ U(1) charges.

From the lattice QCD studies done so far, we take the message that it is rather difficult to obtain a clear signal for flavour–singlet quantities. In general, we can ascribe the difficulty to the intrinsic large statistical fluctuations of such quantities. Moreover, due to the vacuum–like quantum numbers of flavour–singlet scalar states, the computation of disconnected diagrams is a mandatory element of any lattice computation, if a correct estimate of the mass is needed. This requires computationally expensive measurements and high statistics in order to give results with relatively small errors, which is the reason of the high number of configurations described in Tab. 3.1.

Previous studies of the scalar spectrum using fermionic operators in $N_f = 12$ QCD either did not include the computation of disconnected diagrams [108], or were restricted to an unphysical region of the parameter space that is not related to the continuum limit physics of the asymptotically free theory [134]. Our study is the first one incorporating the explicit computation of disconnected diagrams for a model relevant to BSM physics.

We summarise the ensembles used for the calculation of the σ meson mass of our twelve–flavour QCD theory in Tab. 3.2. We also report the corresponding pseudoscalar mass am_π for a comparison and the ration between the two, m_σ/m_π. In QCD, we know that $m_\sigma/m_\pi \approx 3.5$, given the experimental values of m_σ and m_π. Moreover, since the pion becomes exactly massless in the chiral limit of QCD, such ratio would go to infinity. However, it is clear that a different situation takes place when twelve flavours of dynamical quarks are included, because $m_\sigma/m_\pi < 1$ in the range of masses we explored.

3.4.1 The flavour–singlet scalar correlator

In our staggered fermionic calculation, we employ the local scalar fermionic bilinear operator

$$\mathcal{O}_{\mathrm{S}}(t) \;=\; \sum_{i=1}^{3} \sum_{\vec{x}} \overline{\chi}_i(\vec{x},t)\chi_i(\vec{x},t) \;, \tag{3.7}$$

$L^3 \times T$	am_f	N_{cfgs}	am_σ	am_π	m_σ/m_π
$24^3 \times 32$	0.05	11000	$0.240(12)\binom{00}{02}$	$0.3273(19)^*$	$0.73(4)\binom{0}{0}$
$24^3 \times 32$	0.06	14000	$0.283(16)\binom{04}{01}$	$0.3646(16)^*$	$0.78(4)\binom{1}{0}$
$24^3 \times 32$	0.08	15000	$0.363(21)\binom{02}{22}$	0.4459(11)	$0.81(5)\binom{0}{5}$
$24^3 \times 32$	0.10	9000	$0.458(41)\binom{32}{06}$	0.5210(7)	$0.88(8)\binom{6}{1}$
$30^3 \times 40$	0.05	10000	$0.277(13)\binom{19}{07}$	$0.3192(14)^*$	$0.87(4)\binom{6}{2}$
$30^3 \times 40$	0.06	15000	$0.331(14)\binom{45}{10}$	$0.3648(9)^*$	$0.91(4)\binom{12}{3}$
$30^3 \times 40$	0.08	15000	$0.386(21)\binom{00}{20}$	0.4499(8)	$0.86(5)\binom{0}{4}$
$30^3 \times 40$	0.10	4000	$0.437(50)\binom{07}{09}$	0.5243(7)	$0.83(9)\binom{1}{2}$
$36^3 \times 48$	0.05	5000	$0.285(22)\binom{00}{03}$	$0.3204(7)^*$	$0.89(7)\binom{0}{1}$
$36^3 \times 48$	0.06	6000	$0.307(21)\binom{23}{04}$	$0.3636(9)^*$	$0.84(6)\binom{6}{1}$

Table 3.2 *Parameters of lattice simulations for $N_f = 12$ QCD at fixed $\beta = 4.0$. N_{cfgs} is the number of saved gauge configurations. The second error of am_σ is a systematic error coming from the fit range. The values of am_π are from Ref. [117], but the ones with (*) have been updated using configurations reported in Tab. 3.1. The error on m_σ/m_π comes only from am_σ.*

where the index i runs through the 3 different staggered fermion species. The explicit staggered spin–taste structure of the bilinear operator can be written as

$$\overline{\chi}_i(y + A)(\mathbf{1} \otimes \mathbf{1})_{AB}\chi_i(y + B) \ , \tag{3.8}$$

in contrast to the pseudoscalar (PS) one

$$\overline{\chi}_i(y + A)(\gamma_5 \otimes \xi_5)_{AB}\chi_i(y + B) \ . \tag{3.9}$$

Here, y is the origin point of the lattice hypercube, and A, B are vectors belonging to that same hypercube.

We can see that a part of the full flavour symmetry is exact, the one corresponding to the 3 fermion species under which the operator in Eq. (3.7) is symmetric. Moreover, since taste splitting is very small in our simulations (see Fig. 3.1), the rest is only broken by a negligible amount.

From $\mathcal{O}_{\text{S}}(t)$ we calculate the two–point correlator. This correlator contains two contractions: the so–called connected term $C(t)$ and the disconnected term $D(t)$, which includes a subtraction of its vacuum expectation value to remove the vacuum contribution from the two–point function. In formulae, we can write

$$\langle \mathcal{O}_{\text{S}}(t)\mathcal{O}^\dagger_{\text{S}}(0)\rangle \ = \ 3D(t) - C(t) \ , \tag{3.10}$$

where the factor in front of $D(t)$ comes from the number of species. Therefore, the contribution of the disconnected term $D(t)$, with respect to the connected one $C(t)$, increases with N_f. It turns out such contribution can not be neglected in our case, and it actually dominates at large temporal distances t. A typical result for $-C(t)$ and $3D(t)$ is shown in Fig. 3.2.

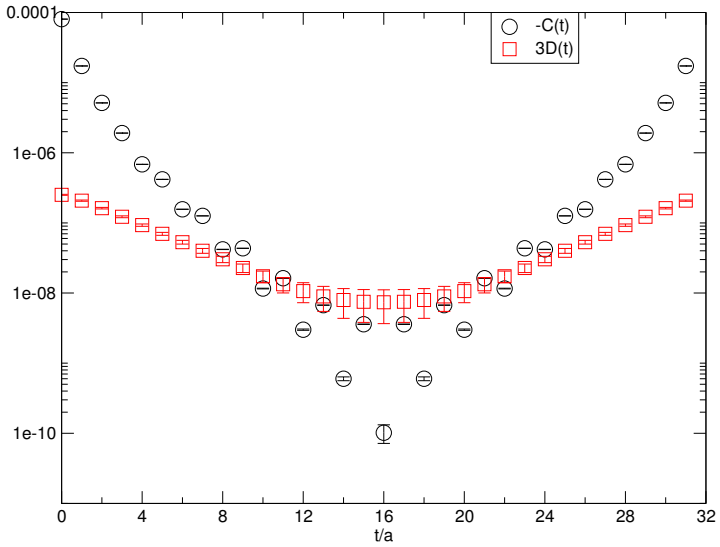

Figure 3.2 *Connected $-C(t)$ and disconnected $3D(t)$ correlators for $L = 24$ and $am_f = 0.06$.*

The operator $\mathcal{O}_{\rm S}$ overlaps with the flavour–singlet scalar state, but also with a flavour non–singlet pseudoscalar state ($\pi_{\overline{\rm SC}}$). This is the staggered parity partner of σ and it is due to the taste structure of the staggered fermions. In the large–time limit, the correlator in Eq. (3.10) behaves as

$$3D(t) - C(t) \;=\; A_\sigma(t) + (-1)^t A_{\pi_{\overline{\rm SC}}}(t) \;, \tag{3.11}$$

where

$$A_H(t) \;=\; A_H(e^{-m_H t} + e^{-m_H (T-t)}) \tag{3.12}$$

is the exponential decay of the correlator on a finite temporal lattice, and the pseudoscalar state has a $(\gamma_5\gamma_4 \otimes \xi_5\xi_4)$ spin–taste structure (hence the SC subscript), but is symmetric under change of fermionic species. The appearance of the oscillating factor $(-1)^t$ is due to the hypercubic non–local definition of staggered fermions on the lattice.

As is often the case $C(t)$ can also be regarded as a flavour non–singlet scalar correlator because the disconnected contraction does not contribute to such state. Therefore, it is expected to have a contribution from the lightest non–singlet

scalar state (a_0) (e.g. $a_0(980)$ in QCD [126]), and its staggered parity partner ($\pi_{\rm SC}$). When t is large, we can write

$$-C(t) \;=\; A_{a_0}(t) + (-1)^t A_{\pi_{\rm SC}}(t)\;, \tag{3.13}$$

where both a_0 and $\pi_{\rm SC}$ are species non-singlet and have the same taste structure as σ and $\pi_{\overline{\rm SC}}$, respectively.

The $\pi_{\rm SC}$ state is degenerate with the $(\gamma_5\otimes\xi_5)$ (PS) pseudoscalar and also with $\pi_{\overline{\rm SC}}$. As already mentioned before, $m_{\pi_{\rm SC}} = m_\pi = m_{\pi_{\overline{\rm SC}}}$ when the taste symmetry, thus the full flavour symmetry, is recovered. This degeneracy of masses is expected to hold almost exactly in our simulations.

From Eq. (3.11) and Eq. (3.13), the large–time asymptotic form of $3D(t)$ can be written as

$$3D(t) \;=\; A_\sigma(t) - A_{a_0}(t) + (-1)^t (A_{\pi_{\rm SC}}(t) - A_{\pi_{\overline{\rm SC}}}(t))\;. \tag{3.14}$$

In the large–time region, $3D(t)$ behaves as a smooth function of t in contrast to $-C(t)$, which has a clear oscillating behavior depicted already in Fig. 3.2. This means that the taste–symmetry breaking between $A_{\pi_{\rm SC}}(t)$ and $A_{\pi_{\overline{\rm SC}}}(t)$ in Eq. (3.14) is small, as expected from the discussion in Sec. 3.3.1.

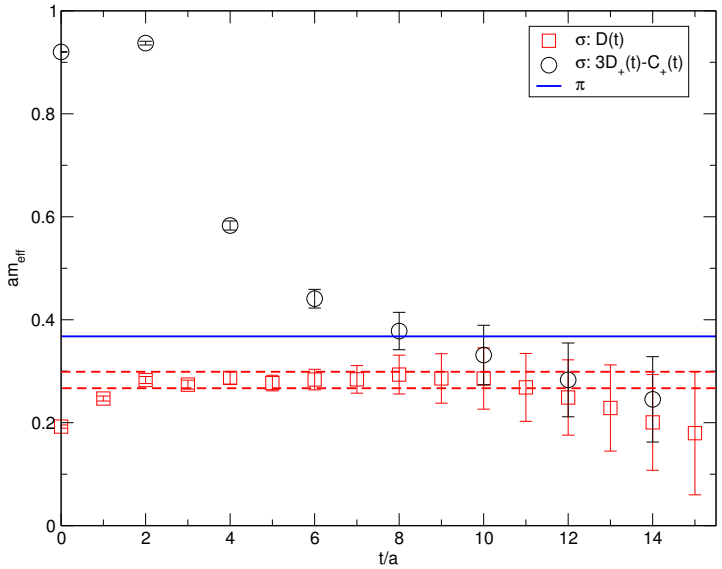

Figure 3.3 *Effective scalar mass am_σ from correlators in Eq.* (3.11)*, with the projection explained in the text, and in Eq.* (3.14) *for $L = 24$ and $am_f = 0.06$. The dashed and solid lines highlight the fit result for am_σ with statistical error band and am_π, respectively.*

In order to minimize $A_{\pi_{\overline{\rm SC}}}(t)$ in $3D(t) - C(t)$, we adopt a projection, $C_+(t) = 2C(t) + C(t+1) + C(t-1)$, at even t. Fig. 3.3 shows that the effective mass of $3D_+(t) - C_+(t)$ at large t is smaller than am_π, while the error is large. As an alternative method, we also employ $D(t)$ to extract am_σ, and its effective mass is also shown in the figure. The effective mass plateau of $D(t)$ is consistent with the one of $3D_+(t) - C_+(t)$ in the large–time region. Furthermore the plot clarifies the importance of using $D(t)$ to extract am_σ, because it performs better in identifying the lightest scalar state, even at small temporal separations. This might be caused by a reasonable cancellation among contributions from excited scalar states and the a_0 state in $D(t)$. It should be noted that, because am_σ is so small, the exponential damping of $D(t)$ is slow; this helps preventing the rapid degradation of the signal–to–noise ratio.

The disconnected correlator $D(t)$, which is essential to obtain the σ mass, can be calculated by inverting the staggered Dirac operator at each space–time point $(\vec{x}, t)$. However, this all–to–all propagator is very expensive due to the large number of points in the lattice. It is known that the computational cost of this inversion can be reduced by a factor of 10 if a stochastic noise method is used [135].

Large statistical fluctuations from the random noise in the method are dealt with by using a variance reduction method already employed for the flavour–singlet pseudoscalar [135, 136] and chiral condensate [137] in usual lattice QCD. Also, the same method was used to calculate the flavour–singlet scalar meson in $N_f = 12$ QCD [134].

The noise reduction method employs a number N_r of random sources and the results depend on this number until convergence is reached. The dependence of $D(t)$ on N_r has been studied and we selected $N_r = 64$ as the number for which our results converged.

3.4.2 A scalar lighter than the pion

We fit $D(t)$ between $t = 4$ and $t = 8$, assuming a single light state propagating in this region, to obtain am_σ for all the parameters. A systematic error coming from the fitting range choice is estimated by the difference of central values obtained with several fit ranges. The results of am_σ and m_π are reported in Tab. 3.2. We find that $am_\sigma < am_\pi < am_{a_0}$ for all the investigated fermion masses. The difference of am_σ and am_π is more than one standard deviation when the statistic

and systematic errors are combined in quadrature, except for $am_f = 0.06$ on $L = 30$, where there is a sizable systematic error.

The flavor–singlet scalar spectrum as function of am_f and for three different volumes is summarised in Fig. 3.4. We note that finite–size effects are under control since, at each am_f, the two largest simulated volumes agree within one standard deviation.

For a check of consistency with the hyperscaling of am_π, which was described briefly in Sec. 3.3.1, we fit am_σ on the largest volume data at each am_f. Using the hyperscaling form $m_\sigma = C(m_f)^{1/1+\gamma}$ with a fixed $\gamma = 0.414$ estimated from m_π, we obtain a good value of $\chi^2/\mathrm{dof} = 0.12$. This fit is also shown in Fig. 3.4.

In Sec. 3.1.1, we noted that the consistency with the hyperscaling relation can also be tested by looking at the ratio of mass scales. Therefore, we estimate the ratio m_σ/m_π (cfr. Tab. 3.2). All the ratios are plotted in Fig. 3.5 . They are smaller than unity by more than one standard deviation, except the one at $am_f = 0.06$ on $L = 30$, which has a large systematic error. A constant fit with the largest volume data at each am_f gives

$$\frac{m_\sigma}{m_\pi} \;=\; 0.86(3)\ . \tag{3.15}$$

The results presented in this section are all consistent with the theory being infrared conformal in the chiral limit. However, it is clear that we have only explored a limited mass region: even though hyperscaling seems to describe the large volume data very well, simulations with smaller fermion masses should be explored. In fact, one could spot a slight tendency of growing m_σ/m_π in Fig. 3.5, which will result in a pion lighter than the scalar in the chiral limit of the theory. On the other hand, the presence of a scalar state which is lighter than the pseudoscalar one, is in contrast with QCD and with chiral symmetry breaking, even at large fermion masses am_f. We can gather more evidence on the conformal nature of the theory by studying its gluonic observables in the next section.

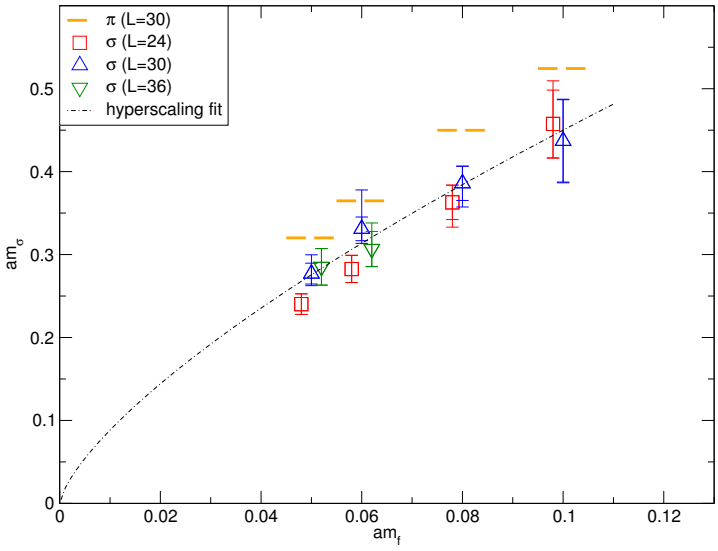

Figure 3.4 *The spectrum obtained from the effective mass of $D(t)$ in Eq.* (3.14) *is plotted for several fermion masses* $0.05 \leq am_f \leq 0.10$ *and volumes, as summarised in Tab. 3.2. The fermionic flavour–singlet scalar spectrum is compared to the pseudoscalar (π) one. A state lighter than the pion is found and, in the large–volume limit, its scaling is consistent with Eq.* (3.1).

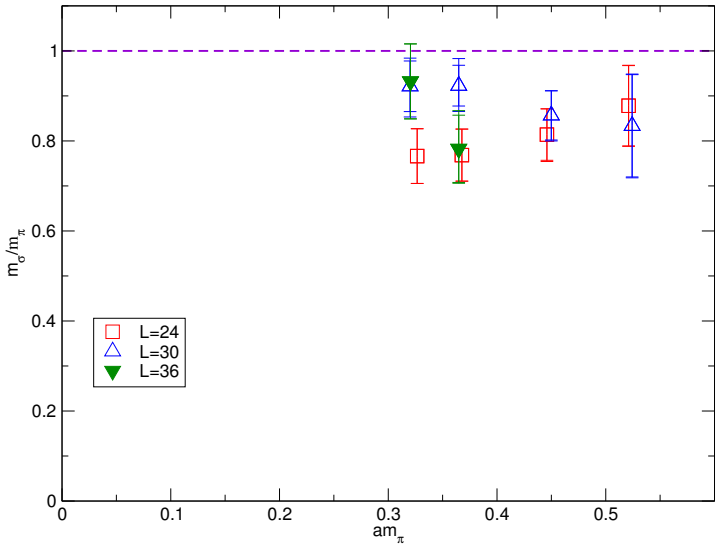

Figure 3.5 *The mass ratio between the fermionic flavour–singlet scalar state and the pseudoscalar one m_σ/m_π as a function of the pseudoscalar mass. The plotted ratio aligns at a constant value which is fitted on the largest volumes in Eq.* (3.15). *Although the statistical errors are large, the ratios are smaller that one within the error.*

3.5 Gluonic observables

In this section we describe the effort done to extract the mass of the lightest glueball masses, the scalar 0^{++} and the tensor 2^{++} one, together with the

string tension $a\sqrt{\sigma}$ on the ensembles in Tab. 3.1. The results are obtained by the author using a powerful and versatile code described for the first time in Ref. [71]. The same code was used to measure glueball masses in lattice QCD with $N_f = 2+1$ dynamical flavours [73], the string tension in finite temperature gauge theories [138] and the full spectrum of a pure gauge theory in four dimensions near a critical point [139]. We refer to the original paper [71] and Appendix B for the detailed description of the algorithm. The results presented in this section are summarised in Tab. 3.3 to Tab. 3.6.

We first look at simple gluonic observables like the Polyakov loops along the four dimensions

$$P_i = \frac{1}{3N_j^3} \sum_x \mathrm{Tr} \left(\prod_{n=0}^{N_i-1} U_i(x + n\hat{i}) \right) , \tag{3.16}$$

where i is the direction of winding and $j \neq i$ are the three orthogonal directions in which the sum over x is performed. When i is a spatial dimension, $N_i = L$, while for the temporal direction we have $N_i = T$. In SU(3) this is a complex quantity and it is often useful to consider its absolute value $|P_i|$.

In a pure gauge theory, $\langle P_i \rangle$ is the order parameter for the deconfinement transition, related to the breaking of centre symmetry in the temporal direction of the lattice. When i is different from the temporal direction, a value $\langle P_i \rangle \neq 0$ can be regarded as indicating a spatial deconfinement phase, which is a finite volume artefact. If dynamical fundamental fermions are added to the gauge theory, $\langle P_i \rangle$ ceases to be an order parameter, because centre symmetry is not an exact symmetry of the fermionic part of the action. However, it can be used to identify phases of the lattice model which are connected to the thermodynamic limit, where $\langle P_i \rangle = 0$ necessarily [140].

In the infinite volume limit of a lattice gauge theory with fundamental fermions we expect the Polyakov loops in all directions to be distributed around zero. Typical values for P_i and its absolute value are shown in Fig. 3.6 for fixed $am_f = 0.08$. An entirely similar situation is present for all the other quark masses, and it suggests the simulations are performed in a phase smoothly connected to the one in the thermodynamic limit of the lattice model. Of course, this does not prevent us to be affected by finite–size effects and indeed we will discuss them for all our physical observables in the following.

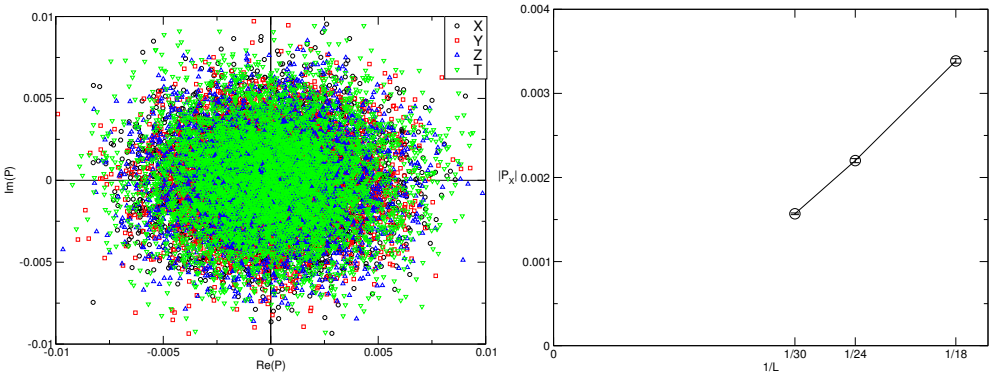

(a) $L = 18$ *and* $am_f = 0.08$ **(b)** $am_f = 0.08$ *and* $L = 18,\ 24,\ 30$

Figure 3.6 *The plot (a) shows the scatter plot of real and imaginary part of* P_i *for* $L = 18$ *and* $am_f = 0.08$*. For all directions, the distribution in centred around the origin. In panel (b)* $\langle |P_X| \rangle$ *is plotted as a function of* $1/L$ *for* $am_f = 0.08$*. This plot suggests the explored phase is smoothly connected to the infinite volume one. Similar plots hold for all the masses.*

3.5.1 String tension

The string tension is measured using the same approach described in Sec. 2.4.2. To extract the physical observable $a\sqrt{\sigma}$, from the ground state mass of the torelon state, we use

$$am_{\rm tor}(L) = a^2\sigma L - \frac{\pi}{3L} - \frac{\pi^2}{18L^3}\frac{1}{a^2\sigma}\ , \tag{3.17}$$

which also includes the next–to–leading order universal correction [141].

The quantity $am_{\rm tor}(L)$ is obtained by fitting the correlator of smeared and blocked spatial Polyakov loops at large temporal distances. In this case, the smearing algorithm depicted in Fig. B.2 is chosen with $(p_a, p_d) = (0.40, 0.25)$. This set of parameters for the smearing procedure results from an optimisation analysis of the signal for the ground state.

A variational analysis which considers each level of smearing/blocking as a different basis operator is employed. We find that, for all the sets of parameters in Tab. 3.1, the ground state of Polyakov loop correlators has a $\mathcal{O}(1)$ contribution from the basis operator at the maximum level of blocking and smearing. The signal in the correlators is very good and allows us to obtain $a\sqrt{\sigma}$ with a relative statistical error of the 1%-5% level.

Thanks to our extended range of parameters, we are able to study both the quark

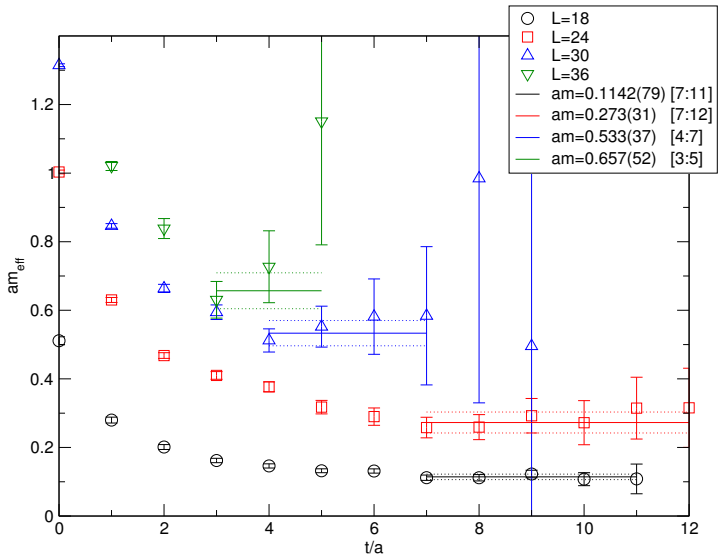

Figure 3.7 *The ground state effective mass extracted from correlators of spatial Polyakov loops with a variational approach. Results for different spatial volumes $L = 18$, 24, 30 and 36 are shown at fixed bare quark mass $am_f = 0.06$. A good plateau is always found, but for the largest volume, and the fitted mass is plotted, together with the one standard deviation error, in the temporal range where the fit has been performed.*

mass dependence of the string tension and also its finite volume dependence. First, we focus on the finite volume dependence. In particular, we check that Eq. (3.17) is correctly representing the measured torelon masses. For a range of spatial sizes $18 \leq L \leq 36$, we measure the effective mass of the ground state from Polyakov operators at fixed fermion mass $am_f = 0.06$. Fig. 3.7 shows both the effective masses and the fit results. Although heavier masses at larger L have a degraded signal due to the strong exponential decrease of the correlators, we see a reasonable effective mass plateau from which $am_{\rm tor}$ is obtained. The mass for $L = 30$ and $L = 36$ give the same string tension, indicating Eq. (3.17) can be trusted and the extracted $a\sqrt{\sigma}$ has negligible finite–size systematics.

We then move to check the fermion mass dependence of our observable. On a fixed volume $L = 24$, thus using Polyakov operators of equal length, we measure $am_{\rm tor}$ for $0.05 \leq am_f \leq 0.10$. The effective masses are plotted in Fig. 3.8. Due to the fixed value of L, the plot implies an increasing string tension with the fermion mass. However, in this plot we know that the lightest masses have not reached their infinite volume values.

When the volume and mass dependence are put together we obtain $a\sqrt{\sigma}$ plotted in Fig. 3.9. The results is very promising as it shows finite–size effects are under

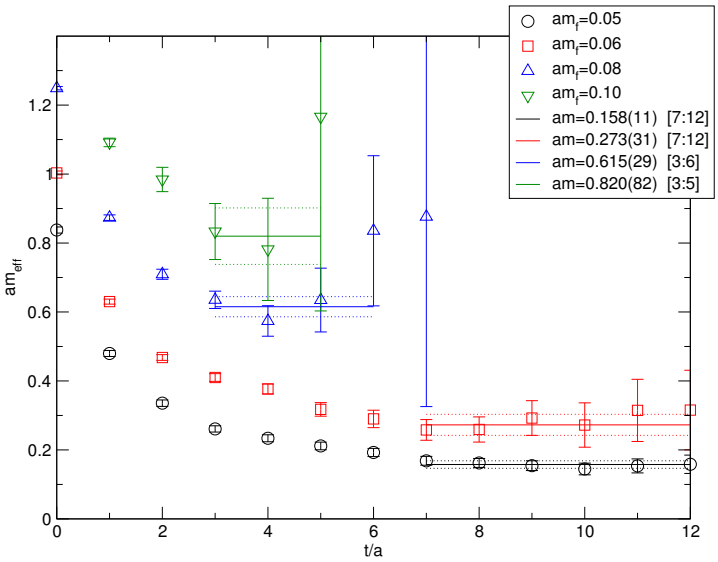

Figure 3.8 *The ground state effective mass extracted from correlators of spatial Polyakov loops with a variational approach. Results for different bare quark masses $am_f \leq 0.10$ at fixed lattice volume $L = 24$ are shown. A good plateau is always found, but for the largest quark mass, and the fitted mass is plotted, together with the one standard deviation error, in the temporal range where the fit has been performed.*

control in the whole region of simulated masses. Note that we only have results on the smallest volume $L = 18$ for $am_f > 0.10$. We believe the corresponding fermion masses are too far from the chiral limit [117].

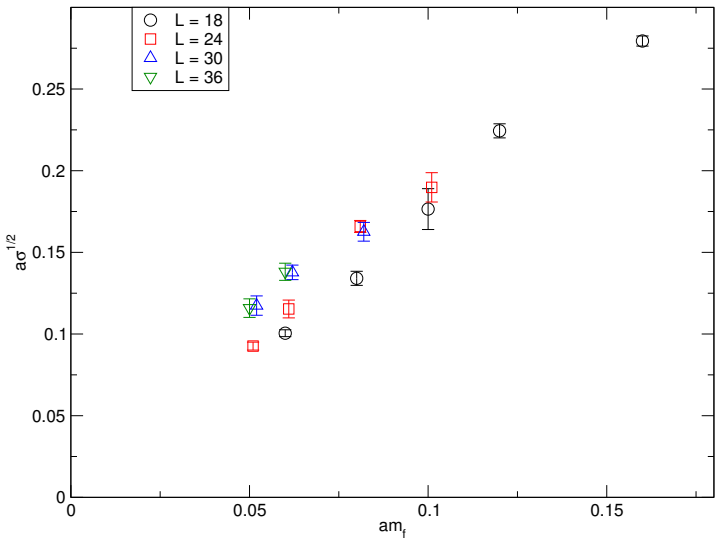

Figure 3.9 *The string tension in units of the lattice spacing $a\sqrt{\sigma}$ is plotted as a function of the bare quark mass am_f. Estimates from different volumes from $L = 18$ to $L = 36$ are plotted, showing that finite–size effects are well under control if larger volumes are used at smaller fermion masses. Some points are shifted horizontally for clarity.*

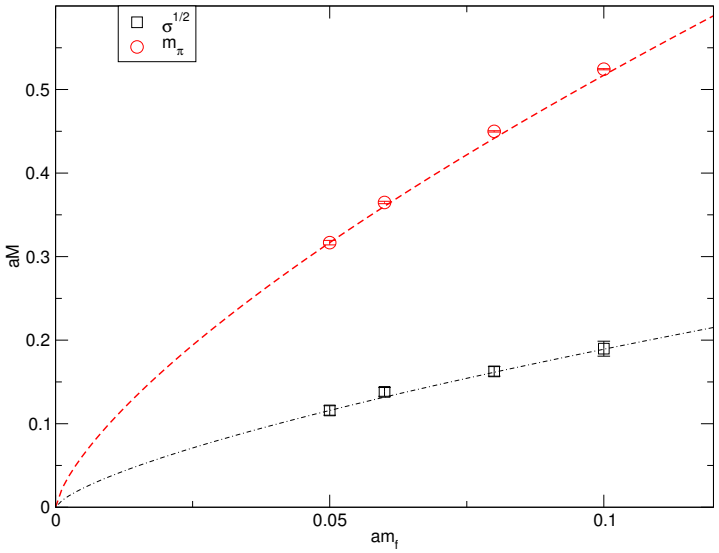

Figure 3.10 *The string tension and the pseudoscalar mass plotted as a function of am_f using their infinite volume estimates. The curves are functions of the form $A_X m_f^{1/(1+\gamma)}$, where A_X depends on the observable and γ is fixed to 0.414, which is the value found for the scaling of $X = \pi$. The curves represent the data of $X = \sqrt{\sigma}$ quite well.*

Another conclusion we infer from Fig. 3.9 is the clear fermion mass dependence of the string tension. Such dependence on am_f can not be accommodated in a theory with heavy fermions [78]: in the same range of quark masses, the pseudoscalar mass and the string tension change by the same factor ($\simeq 2$). Moreover, if data on the largest volumes is considered at each fermion mass, the scaling of the string tension is well described by Eq. (3.1). In Fig. 3.10 we compare the scaling of am_π and $a\sqrt{\sigma}$. If the same anomalous dimension $\gamma = 0.414$ is used for both observables, the data are well represented by the hyperscaling relation.

Alternatively, one can look at the ratio $m_\pi/\sqrt{\sigma}$, which is plotted in Fig. 3.11. Again, if finite–size effects are accounted for by selecting the larger volumes at smaller quark masses, the ratio plateaus at a constant value, signalling a common scaling of am_π and $a\sqrt{\sigma}$ with am_f.

It is also very interesting to consider the ratio between the flavour–singlet scalar state, described in Sec. 3.4.2, and the string tension, $m_\sigma/\sqrt{\sigma}$. This ratio would approach a constant value ≈ 3.55 in the continuum limit of a SU(3) pure gauge theory [69], where the scalar state is represented by the 0^{++} glueball. If the quark masses explored in this study were too heavy, and consequently twelve–flavour QCD were effectively described by a pure gauge theory, we would expect a similar

value for this ratio [78]. However, this is not the case, as we find

$$2.0 \lesssim \frac{m_\sigma}{\sqrt{\sigma}} \lesssim 2.7 \ , \tag{3.18}$$

when considering all the volumes and masses in Tab. 3.2. Fig. 3.12 shows $m_\sigma/\sqrt{\sigma}$ and the comparison with the pure gauge SU(3) value.

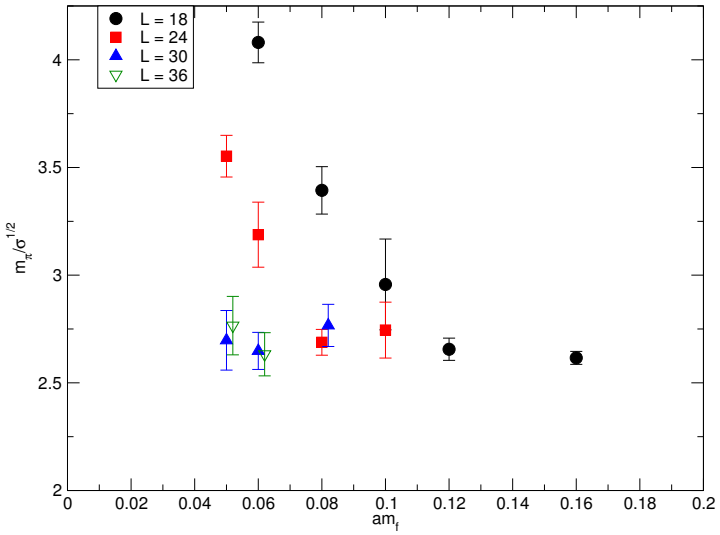

Figure 3.11 *At different bare quark masses, we estimate the mass ratio between the pseudoscalar state and the string tension $m_\pi/\sqrt{\sigma}$. Data on different volumes are shown (slightly displaced for clarity).*

3.5.2 Glueball masses

In this section we focus on the ground state mass extracted from correlators of spatial closed Wilson loops with scalar (0^{++}) quantum numbers. We refer to this state as the scalar glueball because such operators create a gluonic bound state from the vacuum of a Yang–Mills theory on the lattice. In twelve–flavour QCD, where dynamical fermions are affecting the dynamics of the vacuum, the fermionic bound state of Sec. 3.4.2 can in principle have a non–zero overlap on the gluonic operators we describe in the following. Formally, any state which is a flavour–singlet scalar couples with the operators we used, unless there are selection rules which forbid it. However, as we discuss in Sec. 3.5.3, the coupling strength of gluonic operators with the lightest 0^{++} state is not know a priori, but can be estimated by our numerical simulations.

Since we refer to Appendix B for the details of the measurements, we only mention here what is relevant for the discussion of the results. In particular,

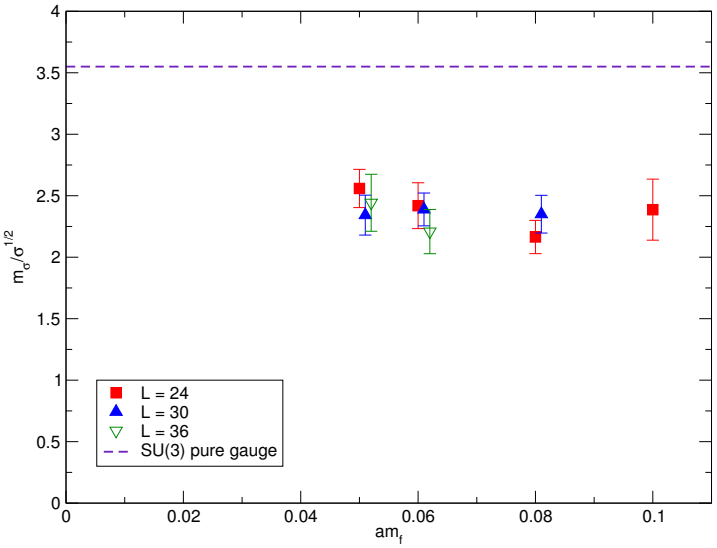

Figure 3.12 *At different bare quark masses, we estimate the mass ratio between the fermionic flavour–singlet scalar state and the string tension $m_\sigma/\sqrt{\sigma}$. Data on different volumes are shown (slightly displaced for clarity). As a comparison, the ratio between the lightest scalar state and the string tension of a SU(3) pure gauge theory in the continuum is shown.*

it is worth pointing out that we use a large number of different shapes for the spatial Wilson loops in order to enlarge the variational operatorial basis. For each set of parameters in Tab. 3.1, we measure 32 different Wilson loop shapes, from the four–links plaquette to some ten–links loop. All the shapes are then transformed under the symmetry group of the three–dimensional lattice in such a way that an invariant combination is constructed.

As for the string tension, we include operators with different levels of smearing and blocking: before building each interpolating operator, the gauge links are replaced by their smeared version. This way we obtain an even larger variational basis of gauge–invariant interpolating operators $\mathcal{O}_\alpha(x,t)$ with well–defined rotational quantum number.

For every configuration, we measure a matrix of correlation functions, whose elements are

$$\tilde{C}_{\alpha\beta}(t) \;=\; \sum_\tau \langle 0|\, \mathcal{O}^\dagger_\alpha(t+\tau)\mathcal{O}_\beta(\tau)\,|0\rangle \quad . \tag{3.19}$$

By solving the generalised eigenvalue problem for the matrix above, optimal operators (i.e. those that create almost pure states $|i\rangle$) can be found that are

a linear sum of the basis vectors

$$\tilde{\mathcal{O}}_i(t) \;=\; \sum_\alpha v^i_\alpha \mathcal{O}_\alpha(t)\,; \qquad \tilde{\mathcal{O}}_i(t)\,|0\rangle \approx |i\rangle \;\;, \tag{3.20}$$

where v^i_α are the components of the i^{th} eigenvector. Different eigenvectors v^i correspond to different states.

The mass am_i of the i^{th} state is extracted by fitting correlators of optimal operators using

$$\bar{C}_{ii}(t) = |c_i|^2 \left(e^{-am_i t} + e^{-am_i(T-t)}\right) \;\;, \tag{3.21}$$

where T is the length of the lattice in the time direction and the functional form is a consequence of the usual exponential decay in a lattice with periodic boundary condition in the time direction.

In general, glueball correlators are very noisy and this limits the usefulness of numerical correlators Eq. (3.21) to short time separations. However, although Eq. (3.21) is only valid at large t, if the overlap with an Hamiltonian state is almost perfect, it is possible to extract a reliable value for the mass at short time separation, since the decay is largely dominated by a single state. For this to be true, a careful construction of the variational basis is paramount. Whether the state created by an optimal operator $\tilde{\mathcal{O}}_i(t)$ is a good approximation of the Hamiltonian eigenstates can be checked by looking at the value of the overlap $|c_i|^2$: the closer this number is to one, the better is the variational calculation.

For each set of simulated parameters, we perform the variational analysis briefly described above and we obtain the correlator corresponding to the optimal operator that projects on the ground state ($i = 1$). We calculate the effective mass and we look for a plateau where Eq. (3.21) can be applied. Moreover, we also look at the relative projection of the i^{th} eigenstate onto each operator α in the variational basis, in a similar way to what has been described in Sec. 2.4.2

$$\text{proj}_\alpha \;=\; \frac{|v^i_\alpha|^2}{\sum_\alpha |v^i_\alpha|^2} \;. \tag{3.22}$$

A typical correlator $\bar{C}_{ii}(t)$ (normalised to unity at $t = 0$) corresponding to the ground state of the scalar glueball is shown in Fig. 3.13. In this plot, the logarithmic scale helps identifying a temporal region where Eq. (3.21) is satisfied. We choose the fitting range by looking at the effective mass. For example,

Fig. 3.14 shows that a reasonable plateau is found and that the fitted mass is compatible across different volumes.

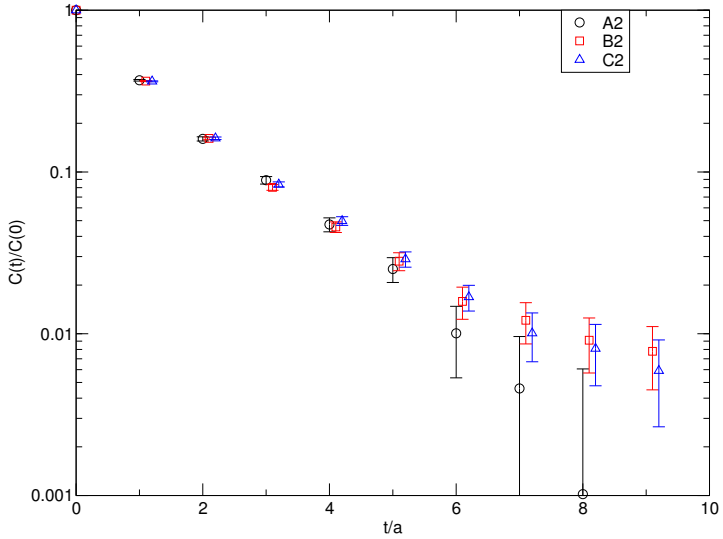

Figure 3.13 *Normalised correlator for the ground state of the scalar glueball at* $am_f = 0.08$ *and different volumes, corresponding to ensembles A2, B2 and C2 of Tab. 3.1. Points are slightly displaced for clarity.*

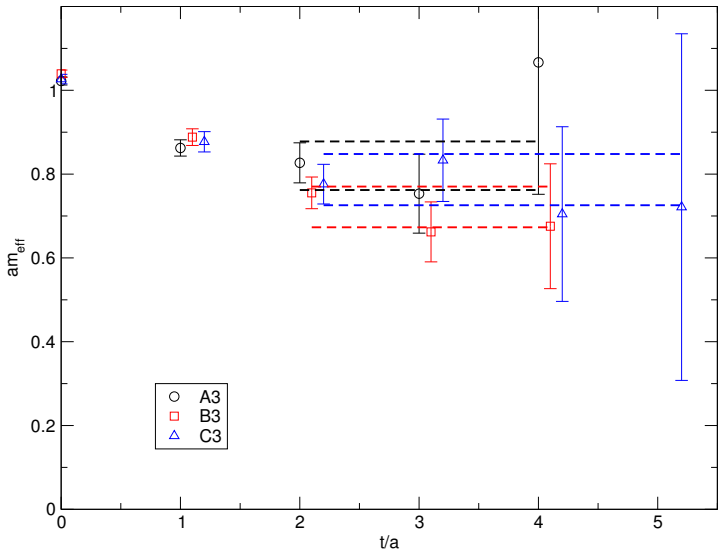

Figure 3.14 *Effective mass for the ground state of the scalar glueball at* $am_f = 0.10$ *and different volumes, corresponding to ensembles A3, B3 and C3 of Tab. 3.1. Points are slightly displaced for clarity, and the fitted values are shown with their one standard deviation contour.*

At large fermion masses $am_f \geq 0.10$, the overlap $|c_i|^2$ for the ground state is of the order 80%-90%, which seems to indicate the variational procedure is effective and contamination from excited states is negligible. Moreover, in the same mass

region, finite–size effects seems under control because correlators on different volumes give mass estimates compatible within the statistical error (cfr. Fig. 3.14 for a clear example).

The situation is less optimal at lighter fermion masses. For example, at $am_f = 0.06$ the ground state correlator shows a dependence on the spatial size of the lattice L which is reported in Fig. 3.15(a). Moreover, the corresponding effective mass in Fig. 3.15(b) indicates the plateau kicks in at different temporal distances, starting at later times for smaller volumes. We believe such behaviour is related to the mixing with the light fermionic state with the same quantum numbers described in Sec. 3.4.2. Further discussions on the issue are reported in the next section.

A summary plot of the results in Tab. 3.3 to Tab. 3.6 is shown in Fig. 3.16. In the plot the scalar glueball is compared to the pseudoscalar state.

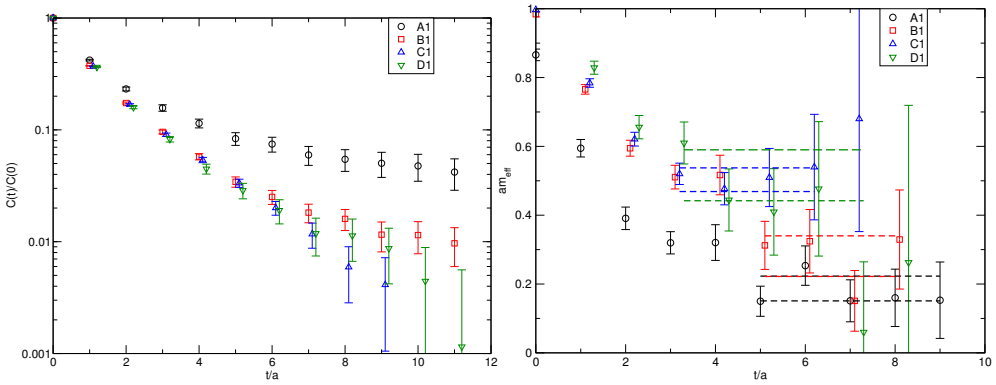

(a) $C(t)/C(0)$ **(b)** $am_{\text{eff}}(t)$

Figure 3.15 *Comparison between correlators and the corresponding effective masses obtained for different volumes at* $am_f = 0.06$.

3.5.3 Mixing with fermions

We have constructed two different kind of operators with the same symmetry properties: both the gluonic operators and the fermionic one couple to the lightest flavour–singlet scalar state albeit with possibly different strengths. It is possible to study the strength of the coupling of each operator with the ground state by including them all into a variational analysis. Then the relative projection in Eq. (3.22) would provide a sensible definition of the mixing of the lightest mass eigenstate with gluonic or fermionic operators.

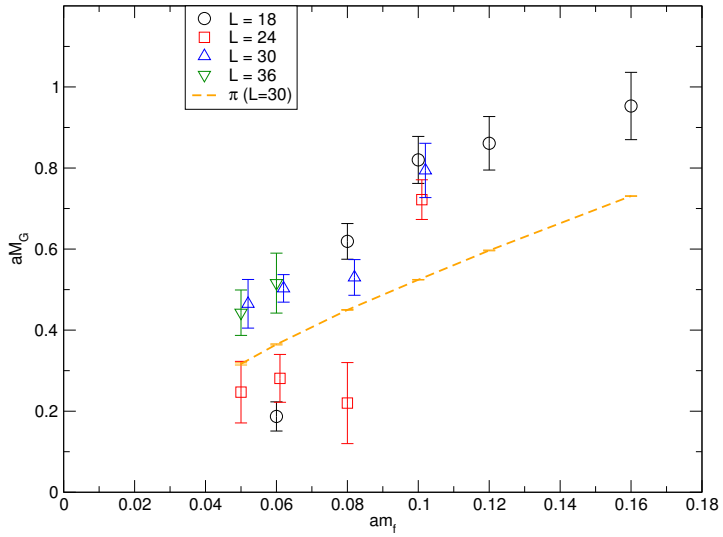

Figure 3.16 *The scalar glueball mass in units of the lattice spacing aM_G is plotted as a function of the bare quark mass am_f. Estimates from different volumes from $L = 18$ to $L = 36$ are plotted. The location of the pseudoscalar (π) state mass is also highlighted. Some points are shifted horizontally for clarity.*

At the moment a full variational analysis that takes into account the cross correlation of gluonic and fermionic operators has not been finalised, due to increased computational time needed. However, by comparing the scalar spectrum of Fig. 3.4, obtained with fermionic operators, to the scalar glueball spectrum of Fig. 3.16 we note that some of the masses are similar.

Therefore, we compare the ground state effective mass calculated from correlators of gluonic and fermionic interpolating operators separately. At light fermion masses $am_f < 0.10$, and generally on small volumes $L < 30$, the behaviour of the effective masses indicates both kind of interpolating operators couple to the same light state at large temporal separation. For example, this is shown for $am_f = 0.06$ and two volumes in Fig. 3.17.

When the volume is increased, the overlap between the effective masses gets worse. However the situation is complicated by somewhat larger statistical errors. In Fig. 3.18 we plot the gluonic and fermionic effective masses on a $L = 30$ volume for two light fermion masses.

A state lighter than the pseudoscalar in correlators of gluonic interpolating operators is absent also when the fermion mass is increased $am_f > 0.08$. We do not have a final explanation for this phenomenon, but the data might be explained in two ways. First, it could be that the overlap of gluonic operators

on the lightest state actually decreases when the fermion mass (or the volume) increases and that this is encoded in the non–perturbative dynamics of the twelve–flavour theory. A second explanation is that, since all the scalar states become heavier for larger am_f, the signal quality for the gluonic correlators gets worse to the point that we can not distinguish a light state from the noise at large time separations.

The masses extracted from correlators of gluonic and fermionic operators might indicate the presence of two separate flavour–singlet scalar states, although this is not shown convincingly enough in our data. A possible interpretation would be that the lighter of the two is a fermionic bound state, identified with the technidilaton, the Goldstone boson of broken conformal symmetry, while the heavier is a glueball state whose origin is to be found in the strongly–interacting nature of the theory.

Our results are not conclusive yet, and a more detailed analysis is needed to resolve this issue. In particular we are working towards a full variational analysis which will measure directly the overlap of each operator onto the lightest scalar state. This approach has been shown to be very effective for lattice QCD in channels where mixing between the single–hadron spectrum and the two–hadron spectrum is not negligible [133].

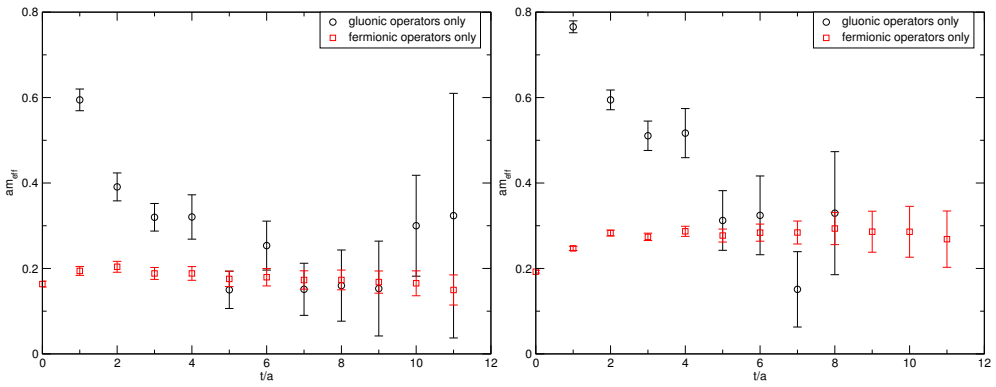

(a) $L = 18\ T = 24$ **(b)** $L = 24\ T = 32$

Figure 3.17 *Comparison between the effective mass of the ground state in the scalar channel obtained using fermionic or gluonic operators. Two volumes at* $am_f = 0.06$ *are shown.*

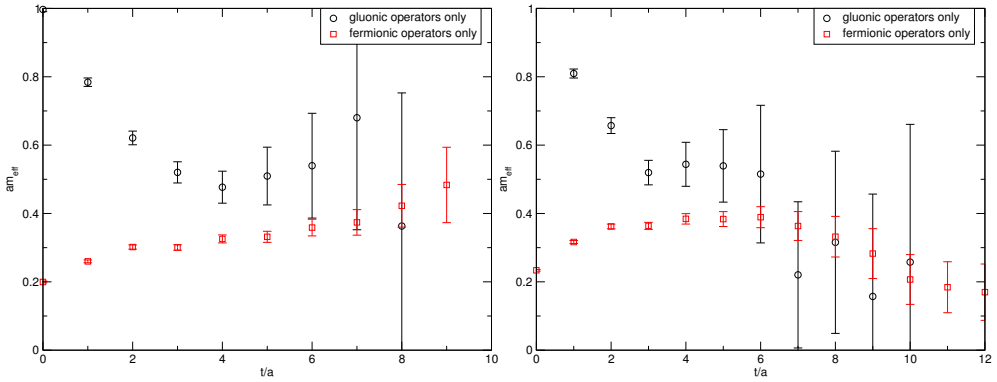

(a) $am_f = 0.06$ **(b)** $am_f = 0.08$

Figure 3.18 *Comparison between the effective mass of the ground state in the scalar channel obtained using fermionic or gluonic operators. Two bare quark masses* $am_f = 0.06$ *and* 0.08 *on the same volume* $L = 30$ *are shown.*

3.5.4 Discretisation errors

Thanks to the analysis of glueball masses in different symmetry channels of the spectrum, we have a way of estimating possible sources of discretisation errors. In particular, we can investigate if the continuum rotational symmetry of the system is approximately realised on the lattice at the parameters of our simulations.

At finite lattice spacing the states with continuum spin J are decomposed into irreducible representations of the discrete symmetry group of the lattice. For example, a spin $J = 2$ state in the continuum is split into two different lattice irreducible representations, the dimension 2 E representation and the dimension 3 T_2 representation.

Operators which transform solely under the E and T_2 representations can be constructed with the same algorithm used for the scalar representation. In principle, since they are two different symmetry channels of the discretised Hamiltonian, their ground states will have different masses. However, they correspond to the same state in the continuum and we expect a degeneracy of their masses when the continuum rotational symmetry is restored.

For a subset of our simulations parameters we explicitly check that the glueball masses in the E^{++} and T_2^{++} symmetry channel, corresponding to the continuum 2^{++} glueball state, are degenerate within our statistical accuracy. This indicates discretisation effects on the continuum rotational symmetry are small. An

example of the effective mass plot for the 2^{++} glueball state at $am_f = 0.06$ and $L = 24$ is shown in Fig. 3.19.

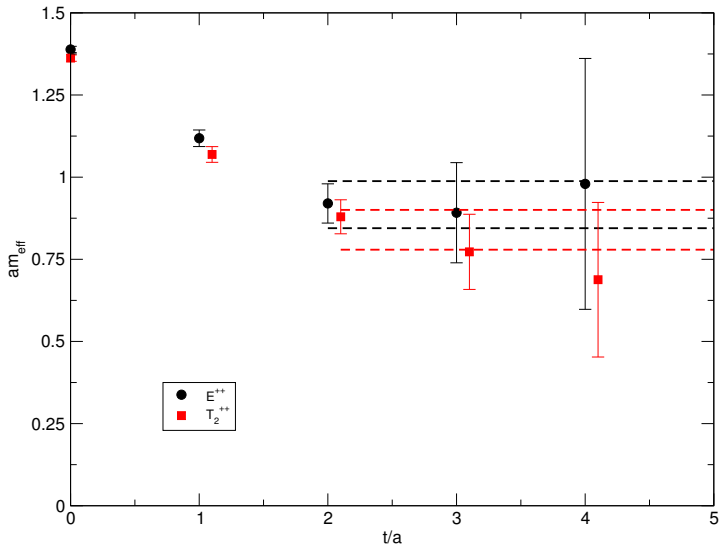

Figure 3.19 *The 2^{++} glueball effective mass extracted using E^{++} operators and T_2^{++} operators. The extracted mass is compatible in the two symmetry channels, as shown by the dashed lines. Points are shifted horizontally for clarity.*

3.6 Summary

Twelve–flavour QCD has received a lot of attention as a possible candidate theory for Walking Technicolor and therefore explaining DEWSB thanks to its strong dynamics and quasi–conformal nature. In this Chapter we have studied the low–energy spectrum of the theory using lattice gauge theory simulations. The results presented above greatly improve upon previous studies by including, for the first time, flavour–singlet scalar states and gluonic observables.

Our simulations with the HISQ staggered action suggest the existence of a flavour–singlet scalar state lighter than the pseudoscalar pion state. Thanks to the introduction of gluonic operators, we discover this light state has a non–negligible mixing with a scalar glueball state, that seems to decrease at large volume. We interpret this as a hint towards the purely fermionic nature of the light scalar. If this is true, such a state would be the lattice realisation of a technidilaton, the (pseudo–)Goldstone boson of broken dilatation symmetry.

Even though our lattice simulations are carried out at finite fermion mass, hence

at explicitly broken conformal symmetry, the appearance of this mass hierarchy between the scalar and pseudoscalar state can be due to the conformal nature of the twelve–flavour theory in the chiral limit.

In support of this observation, we show that ratios of mesonic masses with the string tension are constant, indicating a common scaling law in the form of Eq. (3.1). The addition of a gluonic quantity like the string tension $a\sqrt{\sigma}$ to the measured spectral observables allows us to consolidate the expectations of Ref. [117] about the conformal nature of twelve–flavour QCD in the massless fermion limit.

Moreover, we conclude that our simulated fermion masses are not in the heavy mass region, but are close to the chiral limit. The data are not consistent with the simulated theory being described by a pure gauge theory, where the effects of fermions are neglected.

Although we show how we control finite–size effects and some sources of discretisation errors, this study could be extended to lighter fermion masses and larger volumes. However, we intend to use the experience gathered in this study to investigate eight–flavour QCD. The reason for this comes from the larger anomalous dimension of the latter theory with respect to twelve–flavour QCD. A $\gamma \sim 1$ value is needed for a Walking Technicolor candidate theory to satisfy some electroweak precision tests and this is not featured by twelve–flavour QCD. A recent study [49] suggests such a large γ value is a characteristic of the $N_f = 8$ SU(3) gauge theory.

Tag	$a\sqrt{\sigma}$	$am_{0^{++}}$
A1	0.1005(21)	0.187(36)
		0.362(30)
A2	0.1341(43)	0.619(44)
A3	0.177(13)	0.820(58)
A4	0.2244(43)	0.861(66)
A5	0.2794(31)	0.953(83)

Table 3.3 *The string tension and scalar glueball masses measured for the configuration ensembles A in Tab. 3.1. When alternative fitted masses for $am_{0^{++}}$ are shown, they come from different fitting ranges of the corresponding effective masses.*

Tag	$a\sqrt{\sigma}$	$am_{0^{++}}$
B0	0.0926(24)	0.247(76)
		0.394(37)
B1	0.1153(55)	0.281(59)
		0.555(24)
B2	0.1659(37)	0.22(10)
		0.540(49)
B3	0.1898(90)	0.722(49)

Table 3.4 *The string tension and scalar glueball masses measured for the configuration ensembles B in Tab. 3.1. When alternative fitted masses for $am_{0^{++}}$ are shown, they come from different fitting ranges of the corresponding effective masses.*

Tag	$a\sqrt{\sigma}$	$am_{0^{++}}$
C0	0.1174(59)	0.465(60)
C1	0.1378(45)	0.503(34)
C2	0.1626(57)	0.530(44)
C3	0.2189(21)	0.794(67)

Table 3.5 *The string tension and scalar glueball masses measured for the configuration ensembles C in Tab. 3.1. When alternative fitted masses for $am_{0^{++}}$ are shown, they come from different fitting ranges of the corresponding effective masses.*

Tag	$a\sqrt{\sigma}$	$am_{0^{++}}$
D0	0.1159(57)	0.443(56)
D1	0.1381(53)	0.516(74)

Table 3.6 *The string tension and scalar glueball masses measured for the configuration ensembles D in Tab. 3.1. When alternative fitted masses for $am_{0^{++}}$ are shown, they come from different fitting ranges of the corresponding effective masses.*

Chapter 4

Heavy fermions phenomenology from the lattice

Signals of New Physics (NP) in the flavour sector of the SM could emerge due to the high precision measurements of the CKM matrix elements. Several tensions at the 2σ to 3σ level with the SM predictions are present in the unitarity triangle [142, 143]: they could be explained by the presence of NP or by a lack of theoretically precise predictions. To extract elements of the CKM matrix from experimental data of semileptonic decays or neutral mesons oscillations, it is often required to estimate non–perturbative contributions which can only be provided by lattice calculations (e.g. see Ref. [53] for an up-to-date review of lattice results).

Lattice QCD calculations of physical quantities up to the charm mass scale can be easily done on today's computing resources with reasonably small errors (of order 1% or less [144, 145]). However, the b-quark sector, and the top one as well, are still out of the reach of modern lattice computations due to their much higher energy scale: the lattice cutoff, given by the inverse of the lattice spacing, can not be made larger than the bottom quark mass while, at the same time, retaining a large physical volume in the simulation. Therefore, approaches based on Heavy–Quark Effective Theories [146] (HQET) are usually implemented to, loosely speaking, *extrapolate* charm physics results to the energy scale of bottom physics.

In this chapter we introduce some of the HQET–inspired methods used to deal

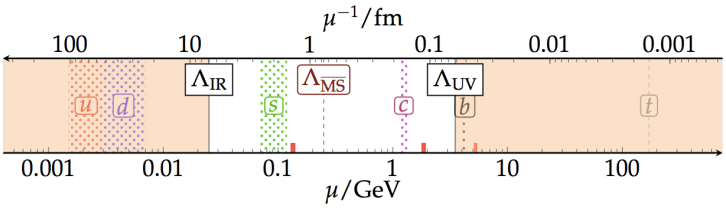

Figure 4.1 *Picture taken from Ref. [147]. It shows the different energy scales entering a lattice QCD calculation. Both length and energy units are shown. The lattice simulation necessarily have and infrared* $\Lambda_{\rm IR} \sim 1/L$ *and an ultraviolet* $\Lambda_{\rm UV} \sim 1/a$ *cutoff. Heavy quarks do not fit a typical lattice QCD calculation.*

with heavy quarks on the lattice. Most of them require using partially–quenched, or mixed–action, calculations where the dynamical fermions are treated differently from the valence fermions. We describe our tentative calculation to approach the B meson system using Domain Wall valence fermions to measure hadron masses and mixing parameters on top of configurations generated with $N_f = 2{+}1$ flavours of dynamical asqtad staggered fermions provided by the MILC collaboration.

The results presented in the following are preliminary and will not cover the full spectrum of observables we plan to measure. Moreover, the chiral and continuum limits, together with the renormalization, of the measured quantities is still under development and will not be described.

4.1 Lattice strategies for heavy fermions

Heavy quarks, like the b and t quarks, have a mass $m_q \gtrsim 4$ GeV which is beyond the ultraviolet cutoff of current lattice QCD calculations with dynamical flavours.

Let us forget about the top quark and focus on the bottom one with $m_b(\mu = m_b^{\overline{\rm MS}}) = 4.18 \pm 0.03$ GeV [126]. This mass can be translated in lattice units as $am_b \approx 1.31$ by using a typical fine lattice with $a = 0.06$ fm or, in other words, a cutoff of $a^{-1} = 3.2$ GeV.

Given the vicinity of this value to the cutoff, $m_b \sim a^{-1}$, a lattice QCD simulation including b quarks would be highly affected by uncontrolled discretisation effects $\mathcal{O}(am_b)^n$. A much finer lattice spacing would be required to treat the b quark on the same footing of the other light quarks, but at the same time the number of lattice points should be increased to keep the physical volume fixed: to do this would require a prohibitively large $L = 120$ lattice in order to have a 2 fm

box and $am_b \lesssim 0.5$. A pictorial example of the different energy scales entering a lattice QCD calculation is shown in Fig. 4.1.

The most recent lattice calculations of B physics quantities use highly improved lattice actions (following the Symanzik improvement program [148]) to reduce discretisation errors for light, strange and charm quarks. For example, the HISQ staggered action (or its less improved version, asqtad) [149] and the twisted–mass Wilson–Clover action [150, 151] can easily reach $am_c \sim 0.4$ with $N_f = 2 + 1 + 1$ dynamical flavours.

The bottom quark can be introduced in different ways. We briefly mention two approaches in the following and leave out the non–relativistic QCD (NRQCD) approach [152, 153] and the relativistic heavy quarks (RHQ) approach [154, 155] for sake of brevity. The references provided should be checked for a detailed description of the frameworks not covered in this work.

The first approach employs simulations of heavy quarks in the static limit $m_h = \infty$ and includes terms proportional to powers of the inverse heavy quark mass in a systematic way. One important ingredient of this HQET–inspired approach is the non–perturbative matching of quantities between the effective heavy quark description and QCD which renders the theory renormalizable: it has a well defined continuum limit.

The second approach we describe in the following is the one which is more relevant to our calculation. In fact, it does not require a simulation at the static point since it uses ratios of quantities with an exactly known value at the $m_h = \infty$ point. By knowing carefully constructed combinations of correlation functions involving heavy and light quarks and their behaviour with respect to m_h down to the charm region, phenomenologically relevant B physics quantities can be estimated precisely.

4.1.1 HQET lattice action

The ALPHA collaboration calculates heavy quark physics by discretising on the lattice the effective Lagrangian describing a static heavy quark in QCD [146]. The effective Lagrangian in the continuum can be obtained by expanding the QCD action in inverse powers of the heavy mass m_h.

On a discrete Euclidean lattice, the action for a static heavy quark field, up to

$1/m_h^k$ order, can be written [156] as

$$\mathcal{S}_{\rm HQET} = a^4 \sum_n \left\{ \mathcal{L}_{\rm stat}(n) + \sum_j^k \mathcal{L}^{(j)}(n) \right\} \tag{4.1}$$

$$\mathcal{L}_{\rm stat}(n) = \bar{\psi}_h(n) \big[D_0 + \delta m \big] \psi_h(n) \tag{4.2}$$

$$\mathcal{L}^{(j)}(n) = \sum_i \omega_i^{(j)} \mathcal{O}_i^{(j)}(n) \ , \tag{4.3}$$

where ψ_h is the static heavy quark satisfying $\frac{1+\gamma_0}{2}\psi_h = \psi_h$, D_0 is the backward lattice derivative and the local composite operators $\mathcal{O}_i^{(j)}$ have dimension $d = 4+j$. At first order in $1/m_h$ there are two dimension–5 operators to be added:

$$\mathcal{O}_1^{(1)} = \bar{\psi}_h(n) \big[\sigma \mathbf{B} \big] \psi_h(n) \tag{4.4}$$

$$\mathcal{O}_2^{(1)} = \bar{\psi}_h(n) \big[\mathbf{D}^2 \big] \psi_h(n) \ , \tag{4.5}$$

with coefficients $\omega_i^{(1)} = -1/2m_h$ at tree level. In the above equation $\mathcal{O}_1^{(1)}$ describes the spin interaction of the heavy particle, while $\mathcal{O}_2^{(1)}$ describes its kinetic motion ($\mathbf{B}$ is the chromomagnetic field strength and $\mathbf{D}$ is the three–dimensional covariant derivative appropriately discretised).

When inserting the $\mathcal{S}_{\rm HQET}$ in a path integral formulation to compute correlation functions, the $1/m_h$ terms only appear as local insertions into correlators evaluated with the static action only. A typical correlation function at order $1/m_h$ can be written as

$$\langle \mathcal{O} \rangle = \langle \mathcal{O} \rangle_{\rm stat} - a^4 \sum_n \left\{ \omega_1 \left\langle \mathcal{O} \mathcal{O}_1^{(1)}(n) \right\rangle_{\rm stat} + \omega_2 \left\langle \mathcal{O} \mathcal{O}_2^{(1)}(n) \right\rangle_{\rm stat} \right\} \ , \tag{4.6}$$

where $\langle \cdots \rangle_{\rm stat}$ denotes the expectation value evaluated with the static action.

When added to the light quarks QCD action, $\mathcal{S}_{\rm HQET}$ brings in new parameters (couplings) which need to be tuned in order for the full theory to end on the renormalized trajectory and reach the continuum limit. At order $1/m_h$, there are 3 new couplings: the additive mass renormalization δm, the spin coefficient ω_1 and the kinetic coefficient ω_2. More parameters need to be tuned when the effective description of light–heavy currents is also implemented as an expansion in $1/m_h$. This tuning is just a reflection that the theory has to be renormalized, since mixing among operators with different dimensions can occur if not forbidden by the lattice symmetries.

The non–perturbative matching of the coefficients at order $1/m_h$ has been carried forward using a Schroedinger functional type of setup [157]. The underlying idea is that one can simulate relativistic heavy quarks reliably on the lattice with $am_h < 1$ only on a small volume (fractions of fermi per side). The results for selected correlation functions involving the couplings to match on such small volumes are compared to the ones obtained with the HQET lattice action and then scaled up to large ~ 2 fm volumes with finite–size step scaling functions.

The fermion discretisation mainly adopted to apply this method is one of the cheapest, namely $\mathcal{O}(a)$–improved Wilson fermions. Among the technical methods used in the simulations, extra care is usually taken to reduce the noise–to–signal ratio of light-heavy correlators thanks to the inclusion of an operator basis for each channel explored and the use of a variational ansatz (cfr. Appendix B.3 for an example with gluonic observables).

4.1.2 The ratio method

The ETM collaboration has defined a very simple and clever approach to heavy quark physics. The proposal fully exploits HQET as a means to extrapolate relativistic results in the c–quark region up to the b–quark energy in a controlled manner. The extra handle to control the extrapolation to the 4 GeV region is given by the static point $m_h = \infty$, where the heavy quark mass is sent to infinity: $m_b \sim 4$ GeV becomes an interpolated point, rather than an extrapolated one, with much better control over systematic effects.

The method, which uses a combination of ratios and interpolations, was first defined in Ref. [158] and then successfully used to evaluate with great precision the b quark mass, the B and B_s decay constants [159] and, very recently, the B mesons mixing parameters [160].

Instead of simulating at the static point, or in its vicinity as it is done in the method of Sec. 4.1.1, the ETMC method defines appropriate quantities with a well known and exact $1/m_h \to 0$ limit, inspired by HQET formulae. Such quantities are usually different depending on the observable, e.g. the renormalized b quark mass, or the B decay constant f_B.

By taking the values of those quantities at several different successive values of m_h and constructing appropriate ratios, one sees that the static limit is equal to

unity, exactly. Moreover, many systematics cancel in the ratios which are built usually around, and just above, the charm region. For example, in the ratios of light-heavy pseudoscalar meson masses at two different heavy quark masses, the discretisation effects are small, even if $am_h \sim 1$. Chiral and continuum limits of such ratios are very well controlled and yield very small systematic errors (1%-2% level).

In the following we give an example of how the ratio method works for the bottom quark mass measurement. In HQET one can write the following asymptotic behaviour for the light-heavy pseudoscalar mass M_{lh} in the static limit

$$\frac{M_{lh}}{m_h^{\rm pole}} = \text{constant} \ , \tag{4.7}$$

where we used the heavy quark pole mass [161].

If one considers renormalized quark masses at some reference energy $\bar{m}_h$ and takes a sequence of them, with fixed ratio $\bar{m}_h^{(n+1)} = \lambda \bar{m}_h^{(n)}$, it is possible to construct the following ratios

$$y(\bar{m}_h^{(n)}) \equiv \frac{M_{lh}(\bar{m}_h^{(n)})}{\rho(\bar{m}_h^{(n)},\mu)\bar{m}_h^{(n)}} \cdot \frac{\rho(\bar{m}_h^{(n-1)},\mu)\bar{m}_h^{(n-1)}}{M_{lh}(\bar{m}_h^{(n-1)})} \ . \tag{4.8}$$

In the above equation we have introduced the factors $\rho(\bar{m}_h^{(n)},\mu)$, known at N^{3}LO in perturbation theory, to relate the renormalized mass at scale μ to the pole mass of Eq. (4.7). This relation $m_h^{\rm pole} = \rho(\bar{m}_h,\mu)\bar{m}_h(\mu)$ which is used with $\mu =$ 3 GeV needs renormalized masses $\bar{m}_h$ which are obtained by starting from bare masses around the charm ~ 1 GeV. The applicability of perturbative factors like $\rho(\bar{m}_h^{(n)},\mu)$ down to such low energies is arguable. This step could be improved using a non–perturbative renormalization scheme for example.

The quantities in Eq. (4.8) are defined at fixed lattice spacing a and renormalized light quark mass $\bar{m}_l$. A well controlled chiral $\bar{m}_l \to m_d^{\rm phys}$ and continuum $a \to 0$ limit exists for $y(\bar{m}_h^{(n)})$ at every step n.

Thanks to HQET we can relate the chiral and continuum results $y(\bar{m}_h^{(n)})$ at different heavy quark masses, knowing that the value at $1/\bar{m}_h = 0$ is unity

$$y(\bar{m}_h) = 1 + \frac{a}{\bar{m}_h} + \frac{b}{\bar{m}_h^2} \ . \tag{4.9}$$

The b-quark mass is extracted by subsequent steps of λ starting from a triggering mass $\bar{m}_h^{(1)}$: $\bar{m}_b = \lambda^{K_b}\bar{m}_h^{(1)}$. Here the number of steps K_b is determined from the chain

$$y(\bar{m}_h^{(2)})y(\bar{m}_h^{(3)})\cdots y(\bar{m}_h^{(K+1)}) = \frac{1}{\lambda^K}\frac{M_{dh}(\bar{m}_h^{(K+1)})}{M_{dh}(\bar{m}_h^{(1)})}\cdot \rho \text{ factors} , \tag{4.10}$$

where the arrival point $M_{dh}(\bar{m}_h^{(K+1)})$ coincides with the physical B meson mass.

A similar strategy, but employing different ratios than the ones in Eq. (4.8), is used for f_B, f_{B_s} and B_d/B_s bag parameters. HQET is very important since it guides the construction of ratios and it helps in defining improved quantities with smaller systematics.

4.2 Domain Wall valence fermions and staggered sea fermions

The important ingredients we look for to start a lattice measurements of hadronic matrix elements in the B system are the following:

1. good chiral symmetry properties of the fermion discretisation (both for the dynamical and valence sectors) in order to suppress mixing of operators protected by the corresponding Ward–Takahashi identity;

2. improved fermion discretisation to remove leading lattice artefacts and reduce discretisation errors;

3. lattice ultraviolet cutoff as large as possible, possibly in the 3 to 4 GeV range.

We choose our fermionic dynamical sector to be described by the staggered formalism, improved by link smearing (asqtad version) [162] to remove $\mathcal{O}(a)$ taste–breaking effects. The configurations used for the measurements are generated including 2 degenerate light flavours plus a heavier strange quark by the MILC collaboration and they are publicly available [163]. Ref. [162] contains results obtained on the configurations by the collaboration itself but they are mainly focused on physics of light quarks.

The most interesting feature of the configurations used, among good chiral properties and $\mathcal{O}(a)$ improvement, is the relatively high ultraviolet cutoff. In fact we are able to select two publicly available MILC ensembles with $a^{-1} \sim 3.2$ GeV and $a^{-1} \sim 4.3$ GeV. The scale of the cutoff goes from almost three times the charm quark mass to the bottom quark mass and allows us to get an extra handle for controlling discretisation effects in the B sector. Details of the ensembles are summarised in Tab. 4.1 for reference. The same configurations have been used before to explore B physics with very promising results [164].

We would like to mention here a common problem of gauge configurations at small lattice spacing. It is known that the currently used algorithm (RHMC) in lattice QCD simulations has poor scaling properties [165] and finer lattices are affected by a slow update of long–range modes such as the topological charge density [166]. If the topological charge does not evolve during the RHMC history, this may cast doubts on the realisation of the path integral since the configuration space is not sampled properly. The topological charge and its susceptibility on the SF1 and UF1 ensembles have been studied in Ref. [167] and the authors show a decent evolution of such quantities.

We proceed with a partially–quenched (or mixed–action) calculation. The systematic errors concerning the extrapolation of physical quantities to the b–quark mass region are expected to be dominant over the ones coming from a non–unitarity in the fermionic sector. In Sec. 4.2.2 we describe how to control the effects of different quark mass renormalizations between the sea and valence sector. In practice, since we are using two different actions in our work, it is important to match them such that a sensible continuum limit can be reached [168]. Mixed–action simulations have been studied using effective theories [169] for the setup we use in the following.

We choose valence fermions described by the Domain Wall formalism (DWF) to ensure a higher degree of chiral symmetry, protecting our valence lattice currents. By increasing the amount of chiral symmetry in the system we expect to alleviate systematic errors in the non–perturbative renormalization procedure of hadronic matrix elements. Moreover, it is believed that this in general gives a better scaling in the lattice spacing [170]. The same mixed–action setup is one of the most popular due to the availability of staggered gauge configurations for a wide set of parameters and has been used before for several applications (e.g. Ref. [171]).

SF1: $a \approx 0.06$ fm $\rightarrow a^{-1} \sim 3.2$ GeV

am_l/am_s	β	$L \times T$	am_π	am_{η_s}	$m_\pi L$	r_0/a
0.0036/0.018	7.47	$48^3 \times 144$	0.09353(7)	0.20731(6)	4.5	7.732

UF1: $a \approx 0.045$ fm $\rightarrow a^{-1} \sim 4.3$ GeV

am_l/am_s	β	$L \times T$	am_π	am_{η_s}	$m_\pi L$	r_0/a
0.0028/0.014	7.81	$64^3 \times 192$	0.0712(1)	0.1583(1)	4.5	10.388

Table 4.1 *Parameters of the MILC $N_f = 2 + 1$ asqtad staggered fermions ensembles used in this calculation. The data are taken from Ref. [167]. Additionally we know the Kaon mass value $am_K =$ 0.16034(8) in the SF1 ensemble. The UF1 (ultrafine) ensemble has not yet been used in measurements, but it is included to check the scaling of physical observables towards the continuum limit.*

4.2.1 Observables

The set of observables we measure includes pseudoscalar isotriplet meson masses and the bag parameter of neutral meson oscillations. We also measure pseudoscalar decay constants, but the results are not shown in this work because the analysis is still in progress.

Meson masses are obtained by fitting the large–time asymptotic behaviour of two–point correlation functions $C_2^\Gamma(t)$ between zero–momentum mesonic interpolating operators $\mathcal{O}_{fg}^\Gamma(t)$:

$$C_2^\Gamma(t) = \sum_\tau \left\langle \mathcal{O}_{fg}^{\Gamma\dagger}(t+\tau)\mathcal{O}_{fg}^\Gamma(\tau) \right\rangle \tag{4.11}$$

$$\mathcal{O}_{fg}^\Gamma(t) = \sum_x \bar{\psi}_f(x,t)\Gamma\psi_g(x,t) \ , \tag{4.12}$$

with Dirac structure given by the Γ representative of gamma matrices and flavour content identified by labels f and g.

When focusing on pseudoscalar masses obtained from purely connected correlators (isotriplet) we choose $\Gamma = \gamma_5$ and several combinations of (f, g) pairs; our light-light (ll) meson corresponding to the pion has $f = g = u = d$ degenerate light quarks, the kaon which is our light-strange (ls) meson has $f = u = d$ and $g = s$, the strange-strange (ss) combination is a fictitious particle we call η_s and has $f = g = s$ flavour content. Mesons with heavy quarks are identified with charmed meson names: the D meson is our light-heavy (lh) combination with $f = u = d$ and $g = c$, while the D_s (strange-heavy (sh)) has $f = s$. Finally the

heavy-heavy (hh) meson is identified with the η_c particle having $f = g = c$.

The bag parameter is measured on the lattice using a ratio of a three–point function over two–point functions. The three–point function contains the insertion of the four–quark operator that is used to effectively describe at low energy the flavour–changing box diagrams of the SM for heavy quarks [172]

$$\mathcal{O}^{\mathrm{SM}}_{\Delta H=-2} \;=\; \big(\bar{h}\gamma_\mu(1-\gamma_5)q\big)\big(\bar{h}\gamma_\mu(1-\gamma_5)q\big)\;, \tag{4.13}$$

where the quark q can be chosen to be a light (l) or a strange (s) one in our computation and H is the flavour quantum number corresponding to the heavy quark (h). This is analogous to the $\Delta S = -2$ operator in the effective Hamiltonian describing K^0–$\overline{K}^0$ oscillations, where q is a down quark and h is replaced by the strange quark.

For example, the D meson bag parameter is defined as

$$B_D = \frac{\left\langle \bar{D}^0 \right| \mathcal{O}^{\mathrm{SM}}_{\Delta H=-2} \left| D^0 \right\rangle}{\frac{8}{3}\left\langle \bar{D}^0 \right| \bar{h}\gamma_\mu\gamma_5 l \left|0\right\rangle \left\langle 0\right| \bar{h}\gamma_\mu\gamma_5 l \left| D^0 \right\rangle}\;, \tag{4.14}$$

where the numerator is the three–point function defining the matrix element of the four–quark operator relevant to neutral meson oscillations, while the denominator includes two–point functions related to the D meson decay constant, f_D, measured in experiments. As a ratio it is dimensionless and defined in such a way that statistical and systematic effects partially cancel between numerator and denominator.

The ratio B_D can be defined analogously for the D_s meson by replacing $l \to s$ quarks and $D \to D_s$ mesons. The results obtained for the D and D_s mesons can be used together with an extrapolation prescription to the b–quark mass region (cfr. Sec. 4.1.2) for extracting the corresponding quantities related to B mesons. Ultimately this is the goal of our calculation. However, we stick to the above naming convention in the following since the lattice results are obtained around the charm quark mass region.

In the construction of the mesonic interpolating operators we use both local (point) sources and extended (wall) source to invert the Dirac operator and compute the fermion propagators. We follow the methods and the terminology introduced in Ref. [173] by the RBC & UKQCD collaboration for two and three–point correlation functions. In particular, our preferred choice for the source

function is the Z2PSWall which has been shown to decrease the statistical error when extracting effective plateau for light quantities [173].

We use the UKHadron code and the highly optimised BAGEL kernels [174] to perform the DWF Dirac operator inversion with different kernels (cfr. Appendix D.3.5) and to perform the contractions used to generate two and three–point functions.

4.2.2 Tuning

As a first step of the calculation, we choose the light and strange DWF valence quark masses in order to reduce the systematic effects coming from the mixed–action nature of the simulation. We measure the π mass, the K mass and the η_s mass with several choices of am_l^{DWF} and am_s^{DWF}. We aim at reproducing, in units of the lattice spacing, the unitary masses in Tab. 4.1 obtained with valence quarks equal to sea quarks. The scanned values of am_l^{DWF} and am_s^{DWF} are reported in Tab. 4.2.

We also select a range of heavy valence quark masses am_h^{DWF} to lie near the energy region of the physical η_c mass. In the SF1 ensemble, using $a^{-1} = 3.2$ GeV, we obtain $am_{\eta_c} = 0.9324$ by using the central value of the PDG [126] estimate $\eta_c = 2983.7 \pm 0.7$ MeV.

During this tuning procedure we use local point sources at the origin to construct our interpolating operators. Moreover, the Domain Wall action is implemented with the Shamir kernel, an extra dimension of size $L_s = 16$ and domain wall height $M_5 = 1.6$. This choice is motivated by previous studies, but a wider range of parameters (L_s,M_5) is explored in Sec. 4.2.3.

The results of the scan in the light region are shown in Fig. 4.2. For the kaon region we plot the results in Fig. 4.3, while for the heavy quark they are shown in Fig. 4.4. We end up by choosing one light fermion mass, two very close strange quark masses and six different heavy masses around the charm quark mass. They are summarised in Tab. 4.3 and are used in the following. A similar strategy will be applied to the UF1 ensemble in the future.

$am_l^{\rm DWF}$	$N_{\rm conf}$	$am_l^{\rm DWF}$	$N_{\rm conf}$	$am_h^{\rm DWF}$	$N_{\rm conf}$
0.05	40	0.003 - 0.017	78	0.35	80
0.025	40	0.003 - 0.018	78	0.25	80
0.01	40	0.0032 - 0.017	78	0.23	80
0.005	79	0.0032 - 0.018	78	0.22	80
0.0032	78	–		0.21	80
0.003175	80	–		0.219	80
0.00316	80	–		0.2199	80
0.00315	80	–		0.2198	80
0.003	79	–		0.2195	80
0.002	79	–		0.218	80
0.0015	40	–		0.2175	80
0.001	40	–		0.217	80

Table 4.2 *Bare valence masses used to measure light-light, light-strange, and heavy-heavy mesons on $N_{\rm conf}$ configurations in ensemble SF1. The simulations used the Shamir kernel with $L_s = 16$ and $M_5 = 1.6$. The correlators used point sources at the origin.*

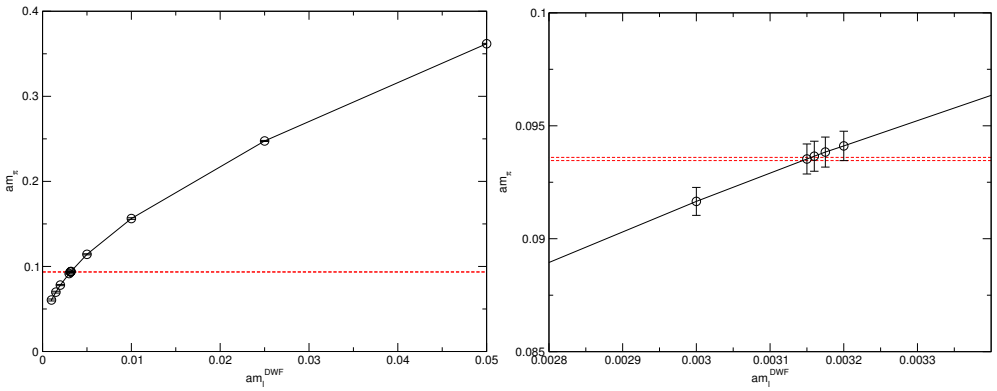

(a) *Scanned range* **(b)** *Zoom*

Figure 4.2 *Tuning of the light valence quark mass $am_l^{\rm DWF}$ on the SF1 ensemble. The unitary pion mass on this ensemble is shown with a dashed red line.*

4.2.3 Test of chiral symmetry

Before describing the results obtained for the meson masses and for the bag parameters, we turn our attention to the chiral properties of our DWF formulation. In particular we monitor the so–called residual mass $m_{\rm res}$ which can be interpreted as the mass a DWF fermion would dynamically acquire in the chiral limit due to finite–L_s violations to the chiral Ward–Takahashi identity (cfr. Appendix D.3.4 for more details).

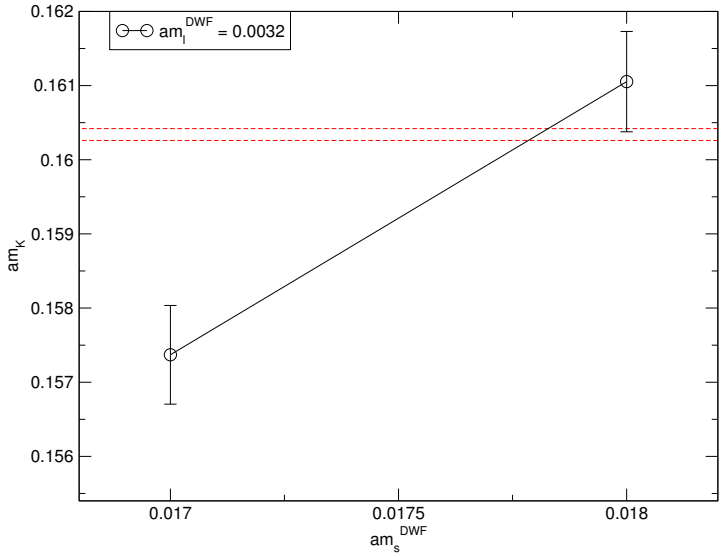

Figure 4.3 *Tuning of the strange valence quark mass am_s^{DWF} on the SF1 ensemble. The unitary kaon mass on this ensemble is shown with a dashed red line.*

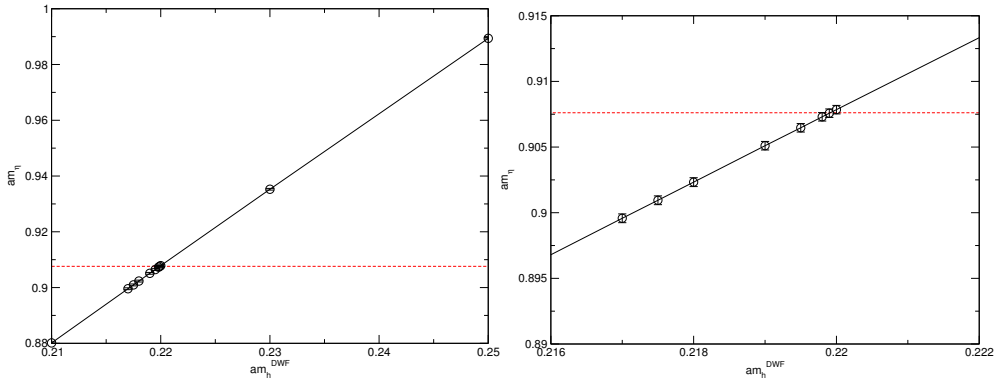

(a) *Scanned range* **(b)** *Zoom*

Figure 4.4 *Tuning of the heavy valence quark mass am_h^{DWF} on the SF1 ensemble. The physical η_c mass in units of the lattice spacing for this ensemble is shown with a dashed red line.*

It is know that the residual mass depends strongly on L_s and M_5, but also on the choice of the DWF kernel at fixed bare quark mass. Moreover, it is important to study the dependence of m_{res} on the quark mass, while keeping other parameters fixed. In particular, the DWF formulation is known to have problems at large bare fermion masses [175, 176].

Without entering into the details, there exists an upper bound for the bare input quark mass above which the DWF framework breaks down: the low–lying eigenmodes in the spectrum are not bounded to the boundaries any more and unphysical contributions from the bulk start dominating the dynamics.

am_l^{DWF}	am_s^{DWF}	am_h^{DWF}
0.0032	0.017, 0.018	0.11, 0.16, 0.22, 0.30, 0.37, 0.44

Table 4.3 *Selected set of valence bare quark masses used in the measurements. They are obtained by tuning the resulting pseudoscalar meson masses to their unitary values in the SF1 row of Tab. 4.1.*

Such unphysical behaviour of the lattice theory is clearly exposed when looking at the quantity $R(t)$ defined in Eq. (D.36). This ratio is expected to become constant in an intermediate region of times t in order to define an effective residual mass. When such a plateau can not be identified, we have reached the unphysical phase of the lattice theory.

In the following plots, we show $R(t)$ (labelled as $m_{\mathrm{res}}(t)$) for 6 different quark masses corresponding to am_h^{DWF} defined in Tab. 4.3. We select alternatively the Shamir kernel, used in the tuning Sec. 4.2.2, and the Möbius kernel used in the measurements Sec. 4.3. A range of different sizes L_s is used to check the scaling of m_{res}, and several values of M_5 are also implemented.

For Shamir fermions with small $L_s = 6$, the residual mass decreases with increasing M_5 at each quark mass am_h^{DWF} as can be seen in Fig. 4.5. However, it remains of the order ~ 0.01 giving almost a 10% correction to am_h^{DWF}. Increasing L_s should decrease m_{res} further. On the contrary, m_{res} increases with increasing am_h^{DWF} using Möbius fermions at fixed $L_s = 6$ and fixed M_5, even though it is smaller by a factor of ~ 5 with respect to the Shamir case.

Increasing M_5 corresponds to larger residual mass and therefore poorer chiral behaviour of the fermions. This becomes worse for larger am_h^{DWF}, and the extreme case is at $am_h^{\mathrm{DWF}} = 0.44$ and $M_5 = 1.8$, where $m_{res}(t)$ does not have a plateau but a cusp. This behaviour is reported in Fig. 4.6.

In our simulations of Sec. 4.3 we use Möbius fermions with $L_s = 8$ and $M_5 = 1.6$. The residual mass for this choice of domain wall parameters is plotted in Fig. 4.7. The figure shows that the residual mass can always be defined and it is ~ 0.001 for all am_h^{DWF} values.

In Fig. 4.8 we show that Möbius fermions with $L_s = 8$ perform better than Shamir fermions with $L_s = 12$ for a quark mass $am_h^{\mathrm{DWF}} = 0.11$ therefore having a smaller residual mass. The situation is the same also for $am_h^{\mathrm{DWF}} = 0.44$ as shown in Fig. 4.9. The plots have been obtained by measuring the ratio $R(t)$ on the same gauge configuration for all set of parameters shown.

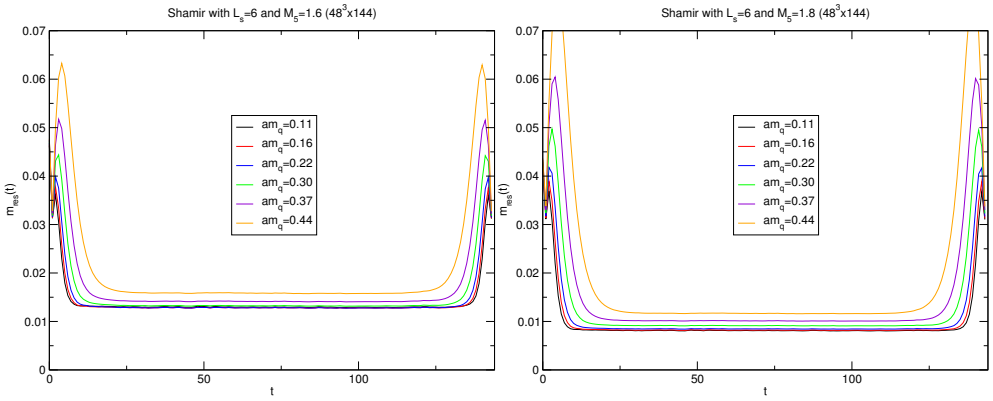

(a) $L_s = 6$ *and* $M_5 = 1.6$ **(b)** $L_s = 6$ *and* $M_5 = 1.8$

Figure 4.5 *Ratio for* $m_{res}(t)$ *measured with Shamir fermions for* $L_s = 6$ *and two different domain wall height* $M_5 = 1.6$ *and* 1.8*. The residual mass decreases with increasing* M_5 *for each quark mass* am_q*.*

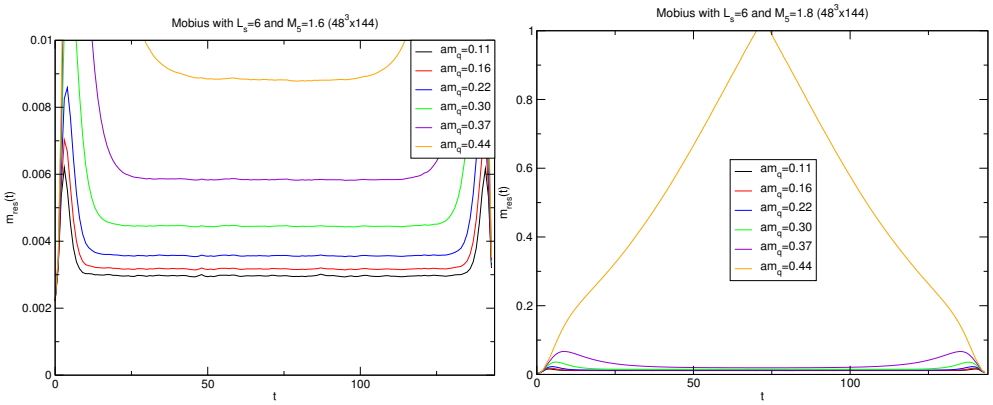

(a) $L_s = 6$ *and* $M_5 = 1.6$ **(b)** $L_s = 6$ *and* $M_5 = 1.8$

Figure 4.6 *Ratio for* $m_{res}(t)$ *measured with Möbius fermions for* $L_s = 6$ *and two different domain wall height* $M_5 = 1.6$ *and* 1.8*. The residual mass increases with increasing* M_5 *for each quark mass* am_q*. At* $M_5 = 1.8$*, the heaviest quark mass* $am_q = 0.44$ *does not have a well defined residual mass.*

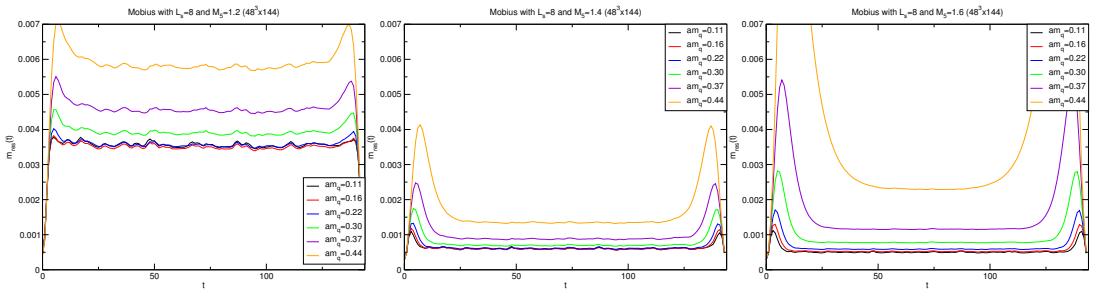

(a) $M_5 = 1.2$ **(b)** $M_5 = 1.4$ **(c)** $M_5 = 1.6$

Figure 4.7 *Ratio for $m_{res}(t)$ measured with Mobius fermions for $L_s = 8$ and three different domain wall height $M_5 = 1.2$, 1.4 and 1.6. The residual mass is lower than the one seen in Fig. 4.6 and decreases by going from $M_5 = 1.2$ to $M_5 = 1.4$. However, at large quark masses the $m_{res}(t)$ behaviour is worse when using $M_5 = 1.6$. (The vertical axis scale is the same for all plots).*

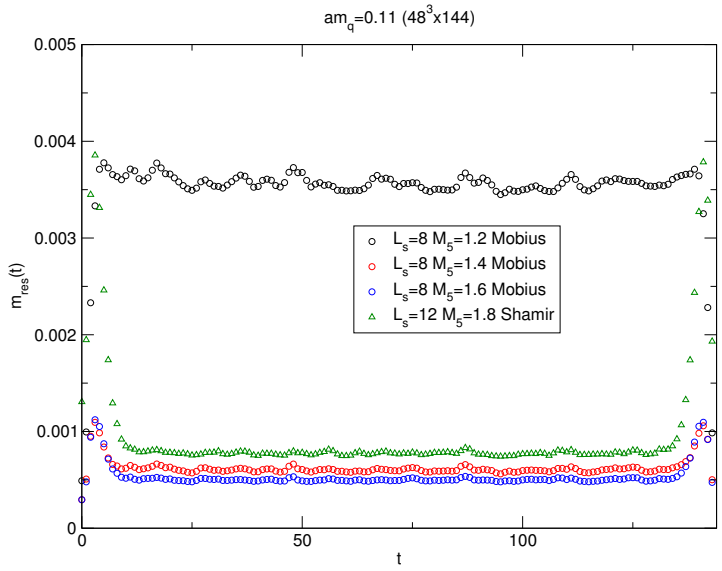

Figure 4.8 *Comparison of $m_{res}(t)$ for a fixed quark mass $am_h^{\mathrm{DWF}} = 0.11$ (our lowest one) with both Shamir and Mobius fermions.*

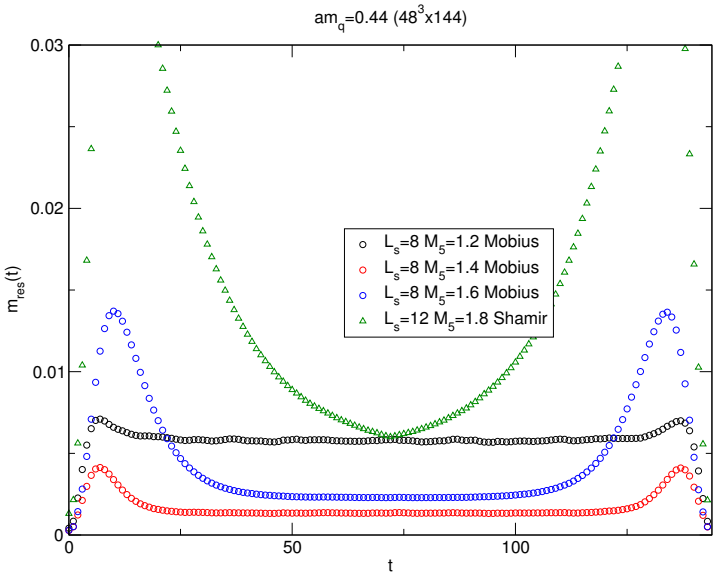

Figure 4.9 *Comparison of $m_{res}(t)$ for a fixed quark mass $am_h^{\mathrm{DWF}} = 0.44$ (our largest one) with both Shamir and Mobius fermions.*

4.2.4 Renormalization strategy

Bag parameters measured on the lattice needs to be renormalized before a result at the physical point can be reached. In our setup it renormalizes multiplicatively. However, the inclusion of heavy quarks and HQET–inspired methods require a careful treatment of the renormalization procedure.

As long as the bare observables are calculated with relativistic quarks and are not extrapolated to the b–quark mass region, usual non–perturbative renormalization (NPR) schemes can be applied. The NPR schemes are used to evolve lattice results to the energy scale where continuum perturbation theory can be applied. After this intermediate step one can convert the results to a more convenient continuum scheme like $\overline{\text{MS}}$ to compare with experiments.

In this work we intend to employ the step–scaling analysis with off–shell renormalization [177, 178] which is widely used in RBC/UKQCD calculations [179].

When trying to interpret our results at the b–quark mass scale, an additional ingredient needs to be taken into account. This depends on the actual method used to extrapolate the lattice results to such high energy. If we resort to the ratio method of the ETM collaboration described in Sec. 4.1.2 applied to decay constants and bag parameters [160], the matching between QCD and HQET has to be introduced.

In particular, the ratios one constructs in order to have a fixed static limit come from HQET, whereas the calculated observables are obtained in QCD through lattice simulations and then fixed by NPR at a reference scale. A simple way of looking at this problem for the case of the bottom mass referred to in Sec. 4.1.2 is the relation between the renormalized mass $\bar{m}_h$ coming from QCD and the pole mass used in the HQET formula Eq. (4.7). For decay constants and bag parameters there are complicated factors to be introduced. A detailed treatment of them by the ETM collaboration is described in the appendix of Ref. [160].

4.3 Results

We extract observables defined in Sec. 4.2.1 using 50 configurations, each taken every 20 HMC trajectories, from the SF1 ensemble of Tab. 4.1. This helps reducing autocorrelations between measurements. The statistical errors on the

effective masses or effective bag parameters are obtained from 500 bootstrap samples. The fits use a full covariance matrix analysis of the errors.

From the set of DWF parameters studied in Sec. 4.2.3 we select the Möbius kernel with $L_s = 8$ and $M_5 = 1.6$. This choice has been shown to give good chiral properties up to our larger bare fermion mass and it is computationally cheap. The total computational cost is still large due to the large volume of the configurations ~ 3 fm.

The interpolating mesonic operators in Eq. (4.11) are computed using stochastic wall sources (Z2PSWall [173]) on two different well–separated timeslices, $t = 0$ and $t = 40$. The time separation $T_{\text{sep}} = 40$ is preferred to the more conventional choice $T_{\text{sep}} = T/2 = 72$ which is used to evaluate the bag parameter Eq. (4.14). A shorter time separation increases the statistical precision but our choice is still large enough to suppress contributions of excited states and reach a plateau value. A similar approach for the bag parameter has been used in Ref. [180] and Ref. [160] to produce very good results for the study of BSM contributions to B_K and B_B.

4.3.1 Hadron masses

The measured pseudoscalar meson masses with the naming convention introduced in Sec. 4.2.1 are reported in Tab. 4.4. The same table also indicates the time window used to fit the two–point function Eq. (4.11). Excited state contaminations seem to be absent in the fitting range used as can be seen from the several effective mass plots at the end of this Chapter, Fig. 4.17 to Fig. 4.19.

Since we have two stochastic wall sources, we double the statistics and reduce the error by combining propagators from each of the sources when constructing the two–point functions.

Let us now briefly review the different meson masses, from the fictitious η_s particle to the heavy η_c meson. In Tab. 4.1 we have an estimate for am_{η_s} measured in a unitary simulation. Thanks to the tuning in Sec. 4.2.2 we expect our valence strange quark masses am_s^{DWF} to reproduce nearly the same value. This is indeed verified in Fig. 4.11 where both am_s^{DWF} can be interpolated to reach the unitary value.

For all the mesons including a heavy quark we do not have unitary values. In

order to compare our results to physical ones we took the D and D_s mass from corresponding the PDG world averages [126] and translated them in lattice units as already mentioned in Sec. 4.2.2 for the case of the η_c meson. Hence we get

$$am_D \simeq 0.5828 \tag{4.15}$$

$$am_{D_s} \simeq 0.6152 \ . \tag{4.16}$$

The D meson contains a light quark and a heavy quark. In our computation the heavy quark is in the charm region. At fixed light quark mass $am_l^{\mathrm{DWF}} = 0.0032$ we have six different am_D estimates, one from each am_h^{DWF} value. The result is reported in Fig. 4.11. The heavy mass $am_h^{\mathrm{DWF}} = 0.22$ is the one that gives the closer physical D mass, as expected from the tuning procedure (cfr. Fig. 4.4).

When we exchange the light quark with the strange one, we obtain the D_s meson whose mass is shown in Fig. 4.12 for a fixed value of $am_s^{\mathrm{DWF}} = 0.018$. Finally the η_c mass is reported in Fig. 4.13. This differs from Fig. 4.4 mainly because in the measurements we use a better fermionic kernel and improved sources for our operators.

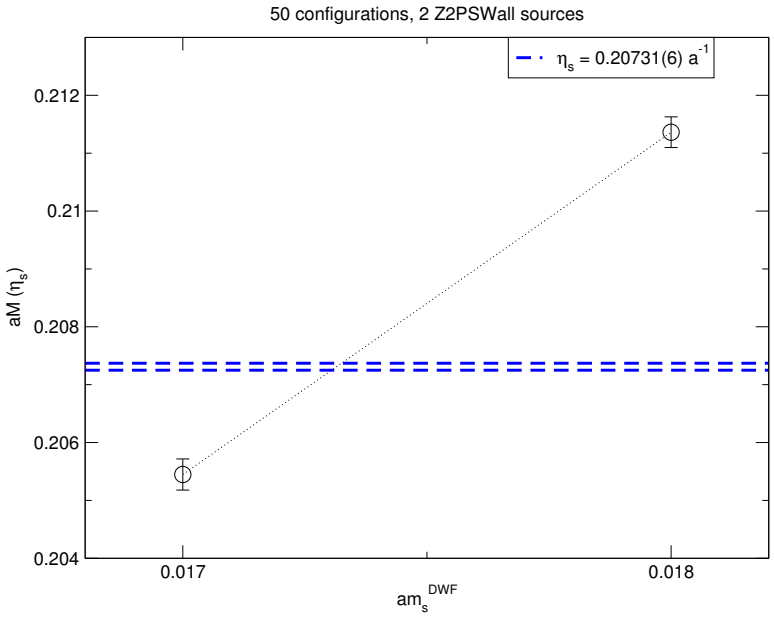

Figure 4.10 *The strange-strange pseudoscalar isotriplet meson (η_s) as a function of the strange quark mass am_s^{DWF}. This fictitious isotriplet meson η_s has been measured in a unitary simulations and its value in lattice units, also reported in Tab. 4.1, is shown with a dashed blue line. The dotted line joining the points is just to guide the eye towards the region of bare valence masses where the unitary meson mass is recovered.*

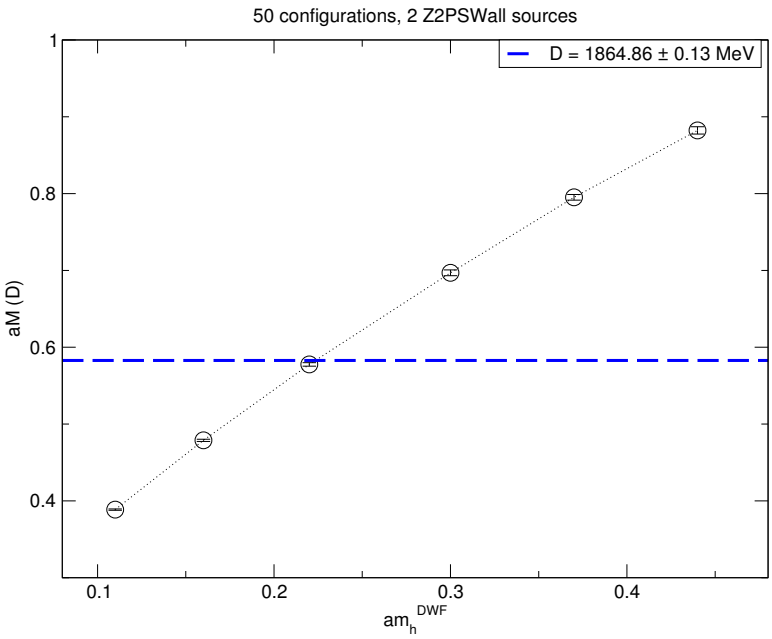

Figure 4.11 *The light-heavy pseudoscalar isotriplet meson (D) as a function of the heavy quark mass am_h^{DWF} at fixed $am_l^{\mathrm{DWF}} = 0.0032$. The PDG physical mass of the D meson in lattice units is shown with a dashed blue line. The dotted line joining the points is just to guide the eye. The charm mass region is determined by the crossing of the two lines.*

4.3.2 Bag parameters

The second observable that we analyse is the bag parameter defined in Eq. (4.14). We do the measurement for three different pair of masses corresponding to the kaon, the D and the D_s meson. They are labelled as light-strange (ls), light-heavy (lh) and strange-heavy (sh) bag parameter. A summary of the results is given in Tab. 4.5.

The fitted values are extracted from the time range where the ratio of the three–point function to the two–point functions in Eq. (4.14) reaches a plateau. The quality of such a plateau is reported in effective bag parameter plots given in Fig. 4.20 to Fig. 4.22 at the end of this Chapter.

In Fig. 4.14 we show the kaon bag parameter B_K and its dependence on the strange quark mass. A similar plot for B_D is shown in Fig. 4.15. Here the dependence on the heavy quark mass goes in the right direction, but the statistical error dominates at large fermion masses.

For the case of the D_s meson, the bag parameter's statistical error is better

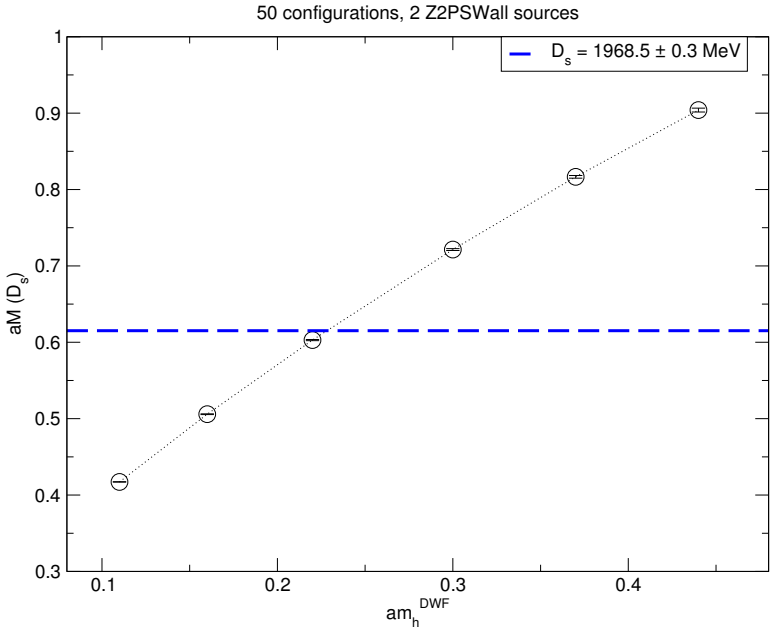

Figure 4.12 *The strange-heavy pseudoscalar isotriplet meson (D_s) as a function of the heavy quark mass am_h^{DWF} at fixed $am_s^{\mathrm{DWF}} = 0.018$. The PDG physical mass of the D_s meson in lattice units is shown with a dashed blue line. The dotted line joining the points is just to guide the eye. The charm mass region is determined by the crossing of the two lines.*

under control. The resulting dependence on am_h^{DWF} at fixed strange quark mass $am_s^{\mathrm{DWF}} = 0.018$ is shown in Fig. 4.16. Once properly renormalized, these results can be extrapolated to the b–quark mass region and give an estimate of the B_s-$\bar{B}_s$ meson mixing by using, for example, the ratio method in Sec. 4.1.2.

4.4 Conclusions and outlooks

At the current level we are not in a position to extract physically relevant quantities from our data. However, we have tested some of the methods we plan on using to extract B physics from DWF chiral fermions on very fine MILC staggered configurations.

The good chiral properties of DWF fermions help in simplifying the renormalization analysis of the matrix elements. The fine lattice spacings of the gauge ensembles reduce the discretisation errors at large bare quark mass, allowing us to explore the regime where $am_b < 1$.

Chiral and continuum extrapolations can be taken once the analysis shown above

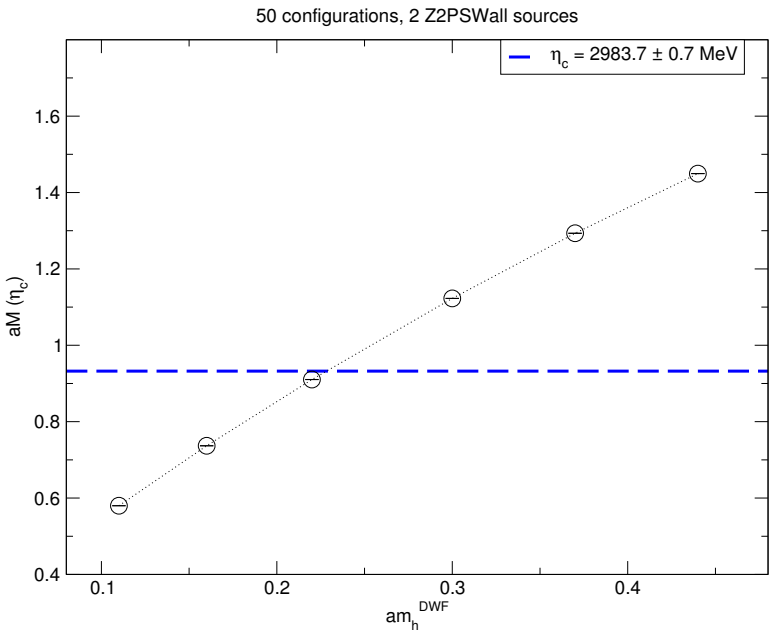

Figure 4.13 *The heavy-heavy pseudoscalar isotriplet meson (η_c) as a function of the heavy quark mass am_h^{DWF}. The PDG physical mass of the η_c meson in lattice units is shown with a dashed blue line. The dotted line joining the points is just to guide the eye. The charm mass region is determined by the crossing of the two lines.*

is repeated on the UF1 ensemble as well. Moreover, an extrapolation from the charm region to the bottom one must be used, for example following the ratio and interpolation methods described in Sec. 4.1.2. Employing the ratio method in this calculation is a step in a different direction with respect to previous DWF calculations of B physics quantities from the RBC/UKQCD collaboration [181].

This work is expected to contribute to the already quite large collection of flavour physics results from the lattice [53]. It is of paramount importance for the search of NP signals in current precision experiments that the lattice community starts providing phenomenologically relevant results, completed with an accurate error budget. Using different techniques and methodologies will help to achieve a better understanding of systematic errors in heavy quark physics from the lattice. Crosscheck calculations from different groups is also a welcome addition to the field.

Tag	am_1^{DWF}-am_2^{DWF}	aM	t_{min}-t_{max}
ll (π)	0.0032-0.0032	0.09678(35)	25-60
ls1 (K)	0.0032-0.017	0.1609(5)	30-60
ls2 (K)	0.0032-0.018	0.1646(5)	30-60
lh1 (D)	0.0032-0.11	0.3886(9)	25-60
lh2 (D)	0.0032-0.16	0.4788(14)	25-60
lh3 (D)	0.0032-0.22	0.5776(23)	25-50
lh4 (D)	0.0032-0.30	0.6969(37)	25-45
lh5 (D)	0.0032-0.37	0.7952(37)	22-35
lh6 (D)	0.0032-0.44	0.8822(48)	22-35
s1s1 (η_s)	0.017-0.017	0.20545(27)	25-60
s2s2 (η_s)	0.018-0.018	0.21136(26)	25-60
s2h1 (D_s)	0.018-0.11	0.4172(3)	25-60
s2h2 (D_s)	0.018-0.16	0.5059(5)	30-60
s2h3 (D_s)	0.018-0.22	0.6029(7)	30-60
s2h4 (D_s)	0.018-0.30	0.7214(12)	30-60
s2h5 (D_s)	0.018-0.37	0.8166(17)	30-60
s2h6 (D_s)	0.018-0.44	0.9040(25)	30-60
h1h1 (η_c)	0.11-0.11	0.5799(2)	30-60
h2h2 (η_c)	0.16-0.16	0.7369(2)	30-55
h3h3 (η_c)	0.22-0.22	0.9103(2)	30-50
h4h4 (η_c)	0.30-0.30	1.1227(1)	30-60
h5h5 (η_c)	0.37-0.37	1.2933(1)	30-60
h6h6 (η_c)	0.44-0.44	1.4495(1)	30-60

Table 4.4 *Results for light-light, light-strange, light-heavy, strange-strange, strange-heavy and heavy-heavy pseudoscalar meson masses on 50 configurations of ensemble SF1 (the results are obtained by using 2 wall sources). The tag column also reports the corresponding physical meson in brakets.*

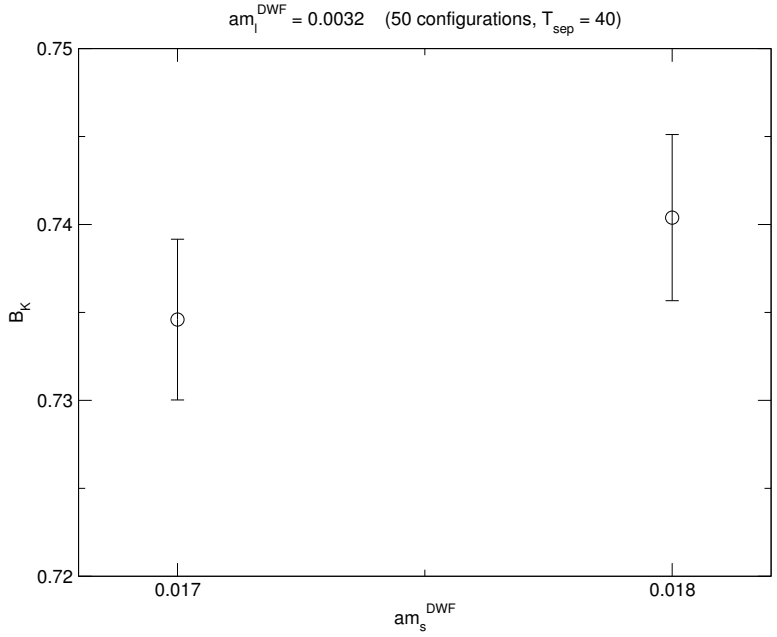

Figure 4.14 *The light-strange pseudoscalar meson (K) bag parameter as a function of the strange quark mass am_s^{DWF} at fixed $am_l^{\mathrm{DWF}} = 0.0032$.*

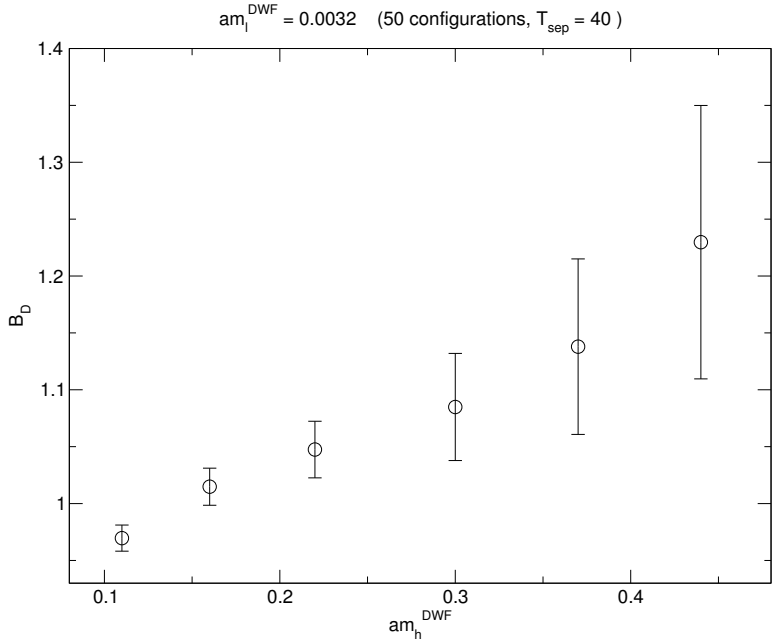

Figure 4.15 *The light-heavy pseudoscalar meson (D) bag parameter as a function of the heavy quark mass am_h^{DWF} at fixed $am_l^{\mathrm{DWF}} = 0.0032$.*

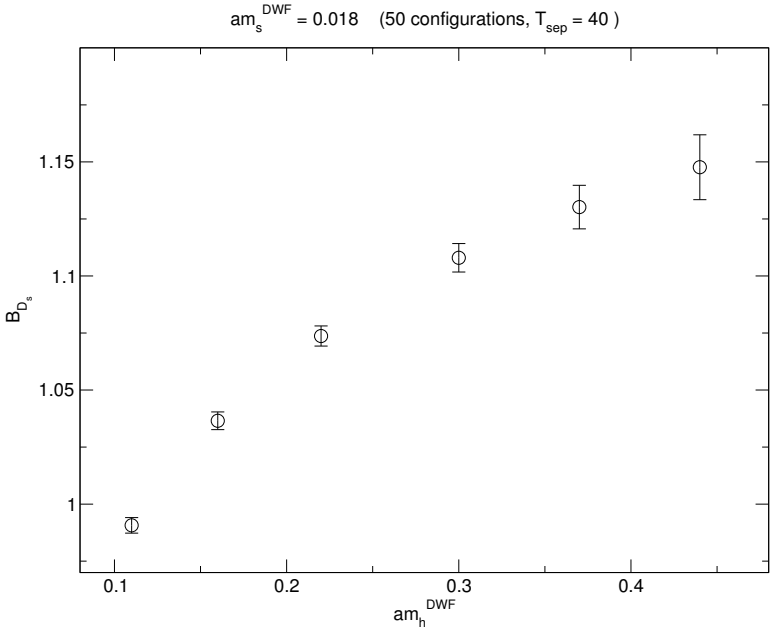

Figure 4.16 *The strange-heavy pseudoscalar meson (D_s) bag parameter as a function of the heavy quark mass $am_h^{\rm DWF}$ at fixed $am_s^{\rm DWF} = 0.018$.*

Tag	$am_1^{\rm DWF}$-$am_2^{\rm DWF}$	B	$t_{\rm min}$-$t_{\rm max}$
ls1 (K)	0.0032-0.017	0.7346(47)	10-30
ls2 (K)	0.0032-0.018	0.7404(47)	10-30
lh1 (D)	0.0032-0.11	0.970(11)	12-28
lh2 (D)	0.0032-0.16	1.015(16)	12-28
lh3 (D)	0.0032-0.22	1.047(25)	12-28
lh4 (D)	0.0032-0.30	1.085(47)	12-28
lh5 (D)	0.0032-0.37	1.138(77)	12-28
lh6 (D)	0.0032-0.44	1.23(12)	12-28
s2h1 (D_s)	0.018-0.11	0.9907(34)	12-28
s2h2 (D_s)	0.018-0.16	1.0365(39)	12-28
s2h3 (D_s)	0.018-0.22	1.0737(44)	12-28
s2h4 (D_s)	0.018-0.30	1.1080(62)	12-28
s2h5 (D_s)	0.018-0.37	1.1302(95)	12-28
s2h6 (D_s)	0.018-0.44	1.148(14)	12-28

Table 4.5 *Results for light-strange, light-heavy and strange-heavy pseudoscalar bag parameter on 50 configurations of ensemble SF1. The tag column also reports the corresponding physical meson in brakets.*

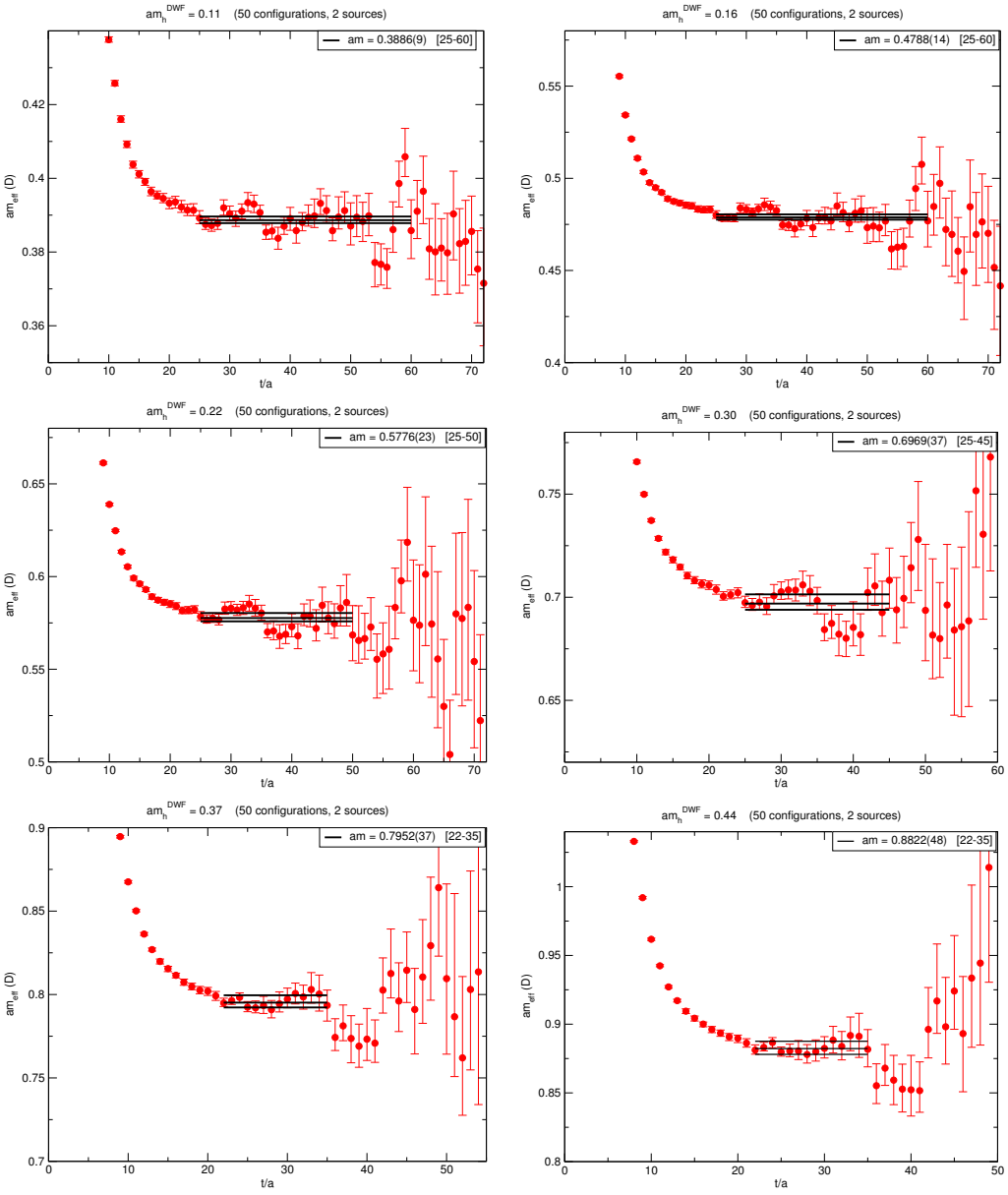

Figure 4.17 *Effective mass of the light-heavy pseudoscalar isotriplet meson (D) and the corresponding fitted masses using correlators of wall sources at the origin $t = 0$ and at $t = 40$.*

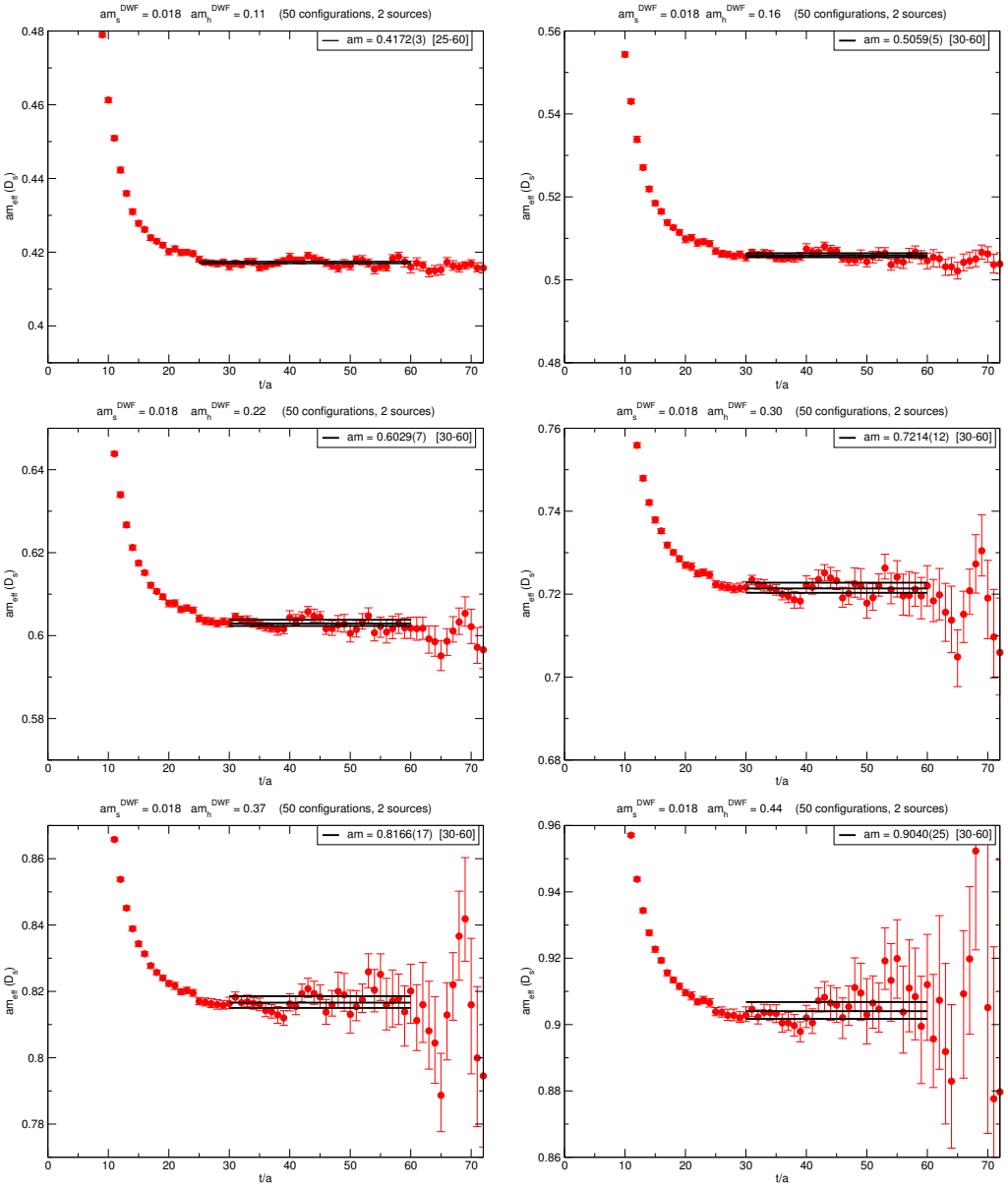

Figure 4.18 *Effective mass of the strange-heavy meson (D_s) and the corresponding fitted masses using correlators of wall sources at the origin $t = 0$ and at $t = 40$.*

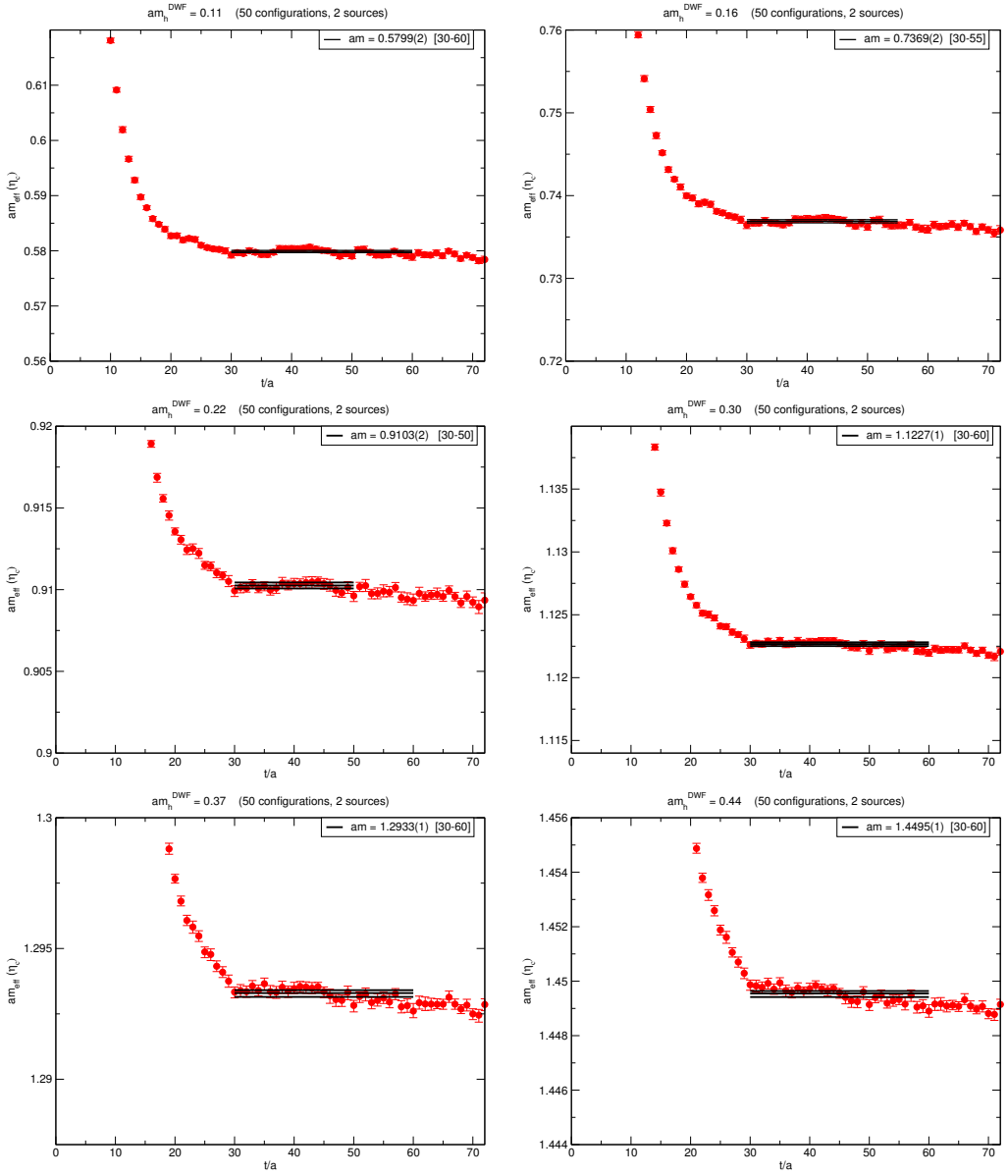

Figure 4.19 *Effective mass of the heavy-heavy pseudoscalar isotriplet meson (η_c) and the corresponding fitted masses using correlators of wall sources at the origin $t = 0$ and at $t = 40$.*

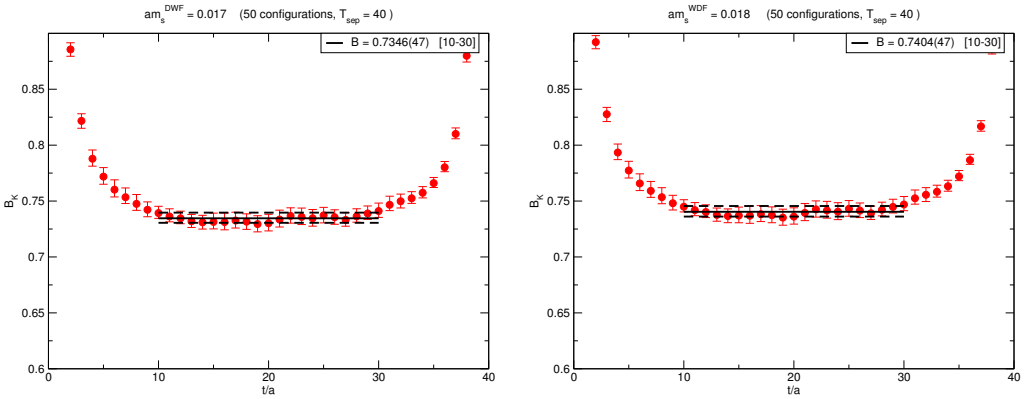

Figure 4.20 *Effective bag parameter of the light-strange pseudoscalar isotriplet meson (K) and the corresponding fitted value using wall sources at the origin $t = 0$ and at $t = 40$.*

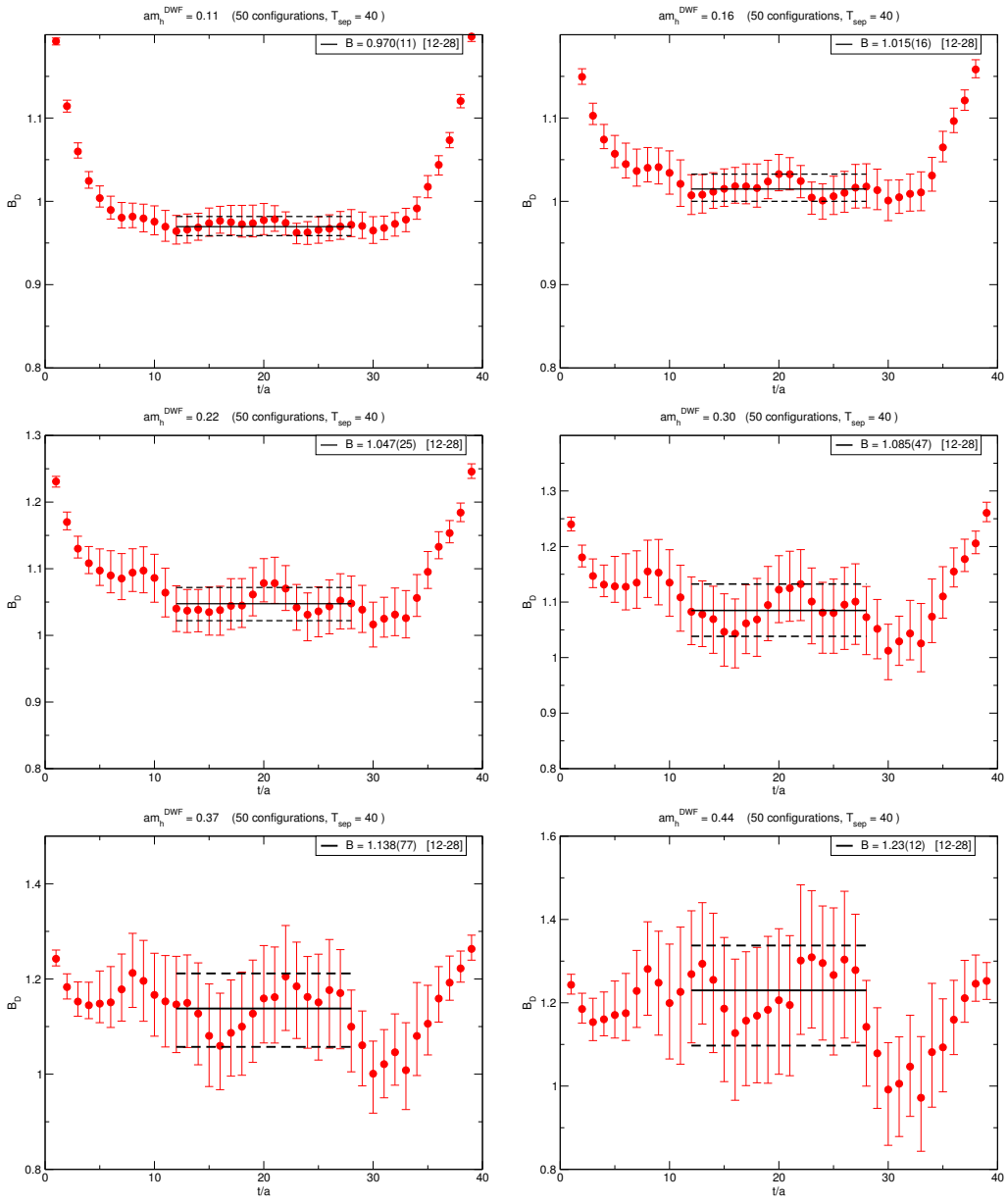

Figure 4.21 *Effective bag parameter of the light-heavy pseudoscalar isotriplet meson (D) and the corresponding fitted value using wall sources at the origin $t = 0$ and at $t = 40$.*

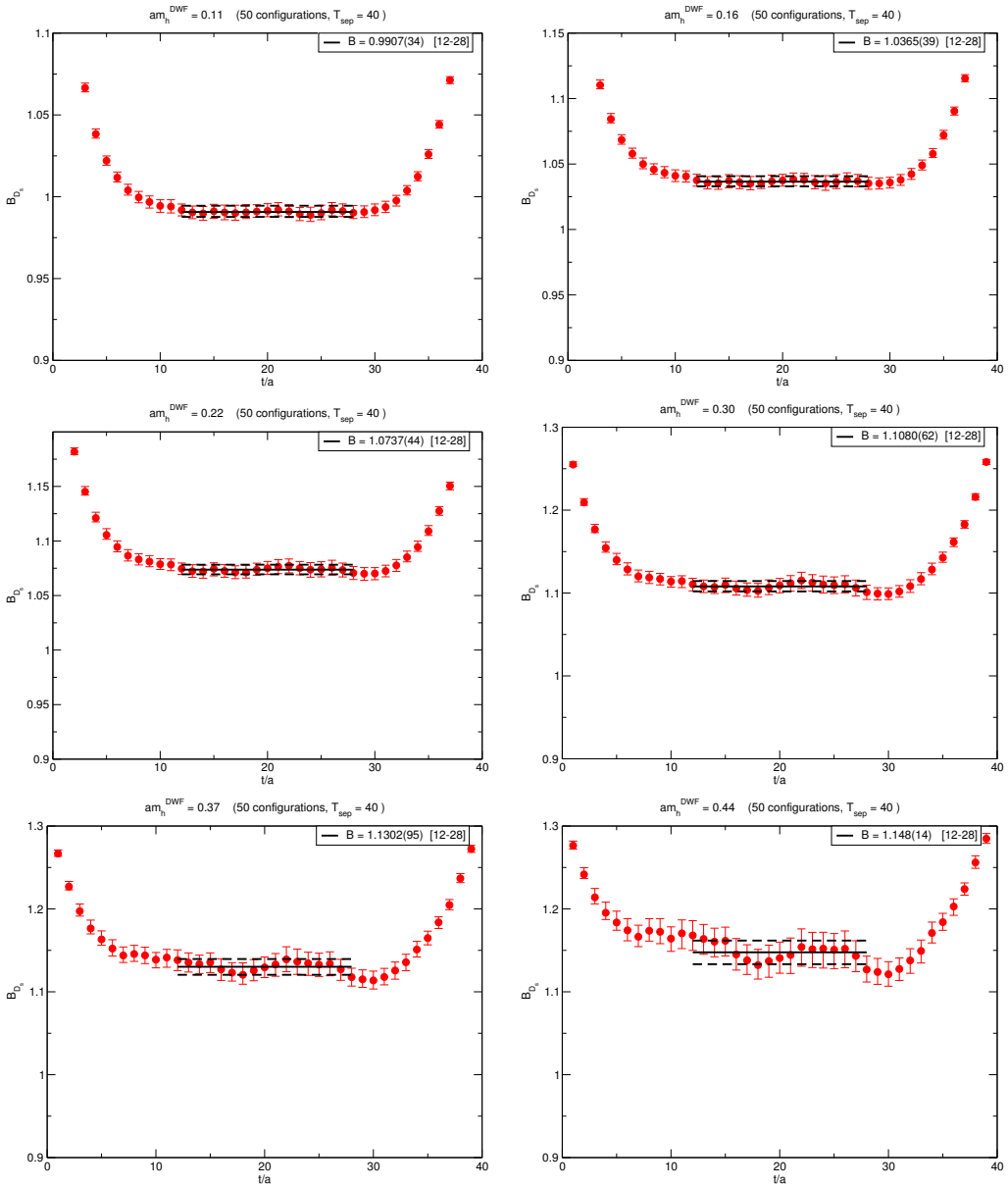

Figure 4.22 *Effective bag parameter of the strange-heavy meson (D_s) and the corresponding fitted value using wall sources at the origin $t = 0$ and at $t = 40$.*

Chapter 5

Conclusions

This thesis has been concerned with some applications of non–perturbative lattice gauge theory methods, specifically aiming at improving our theoretical understanding of Beyond the Standard Model scenarios. With experimental data at higher and higher energies becoming available thanks to the great performances of LHC and its detectors, theoretical models wishing to explain the observed Standard Model as a low–energy description of physics at the TeV scale need inputs from lattice simulations to become more predictive.

Lattice simulations of QCD have reached an astonishing level of precision, with quark masses and hadronic matrix elements measured with sub–percent accuracy, often leading the corresponding world averages in the PDG [126]. The improvements, both in simulations algorithms and analysis techniques, together with machines development in the last 30 years, has made this possible. It is now important to bring this knowledge into the new territory of BSM physics.

5.1 Extra dimensions and the lattice

Extra–dimensional models are often advocated in BSM scenarios since they ameliorate the hierarchy problem by removing the fine–tuning issue in the quadratic cutoff dependence of the Standard Model Higgs boson mass.

We explicitly defined one of these models on a five–dimensional lattice and performed numerical simulations to extract properties of its low–energy dynamics.

The model in the continuum is a naively non–renormalizable five–dimensional SU(2) Yang–Mills theory. Upon compactification of the extra dimension, a scalar degree of freedom with a finite mass appears in the low–energy effective four–dimensional theory. This mechanism sounds theoretically promising as it leads to a light scalar particle with a mass independent on the cutoff thanks to the higher dimensional gauge symmetry protecting the original vector bosons in the Lagrangian.

Although this model is not phenomenologically relevant due to the absence of chiral fermions or the adjoint nature of the resulting scalar field in four–dimensions, it works well as a toy model to study dimensional reduction and the Kaluza–Klein mechanism from five to four dimension on the lattice. We studied the phase diagram of the lattice model and its low–lying spectrum using state-of-the-art simulations to confirm if perturbative expectations remain valid in the non–perturbative regime.

In particular, one–loop calculations of the scalar mass in this specific model hint at the possibility of this mass being independent of the cutoff, while being inversely proportional to the radius of the compactified dimension. We measured the mass of a scalar bound state in our non–perturbative Monte Carlo simulations and we discovered this feature of the model is intact, even in the regime where the coupling constant is not small.

Our study of this simple five–dimensional model reveals a complex phase structure and a somewhat delicate fine tuning of the model's parameters is needed to control the dynamically generated hierarchy of scales. Such fine tuning is hard to quantify and it is difficult, and maybe inappropriate, to compare it with the one in the SM Higgs sector. Nevertheless, we have shown how to successfully apply lattice techniques to explore new models, even a non–renormalizable one, towards a better understanding of BSM physics.

Possible future directions of this lattice approach to extra–dimensional models include the study of AdS theories in the Randall–Sundrum scenario. Other groups already started investigating the Hosotani mechanism for DEWSB on the lattice [29, 182]. Moreover, it is possible to explore orbifold models with lattice techniques [183] and this opens the way to the inclusion of chiral fermions in extra–dimensional models.

5.2 Lattice Walking Technicolor

Another class of models we referred to in this work is Technicolor models and their "walking" version. Walking Technicolor models are alternative scenarios for electroweak symmetry breaking, where a new strongly–interacting gauge sector is added to the Standard Model gauge groups, together with new families of fermions. The dynamics of the new gauge sector produces a technifermion condensate which breaks the electroweak symmetry group in a similar way to the Higgs mechanism: the role of the Higgs vev is replaced by the condensate from the Technicolor sector and the Higgs boson itself arises as a product of the Technicolor dynamics.

In WTC models, there is no elementary scalar field and the hierarchy and fine–tuning problems are solved at the expenses of adding a new strongly–interacting sector, with its spectrum of new particles and symmetries. However, theoretical predictions for these strongly–interacting models can rely only on non–perturbative methods.

In this thesis we focus on one of the many gauge theories that can be used as WTC models and we apply the framework of lattice gauge theories to extract phenomenological predictions. In particular, we studied a SU(3) gauge theory with $N_f = 12$ degenerate fermions in the fundamental representation of the gauge group, by discretising its continuum action using the HISQ fermion action and the Symanzik tree–level gauge action.

Many lattice calculations have been performed in recent year concerning this particular theory. Nevertheless we have added important contributions, like the measurement of a flavour–singlet scalar particle using both fermionic and gluonic operators and a variational estimate of glueball masses and the string tension.

The analysis of the scalar and, more importantly, flavour–singlet spectrum has revealed a state lighter than the pseudoscalar one, in contrast with the dynamics of a QCD–like theory where chiral symmetry breaking implies a vanishing pion mass, always lighter than any other in the spectrum. Moreover, thanks to the addition of the string tension measurement we have shown that fermionic and gluonic scales go to zero in the chiral limit of the theory. This effect is compatible with the presence of a conformal fixed point, which is one of the necessary ingredients in candidate theories for WTC models.

Although there are several hints that twelve–flavour QCD is a conformal theory, our lattice simulations have been performed at finite fermion mass and the extrapolation to the chiral limit of the properties we showed in this work might not be straightforward. Simulations with smaller quark masses would be advisable to reach a more stringent conclusion. Unfortunately, finite–volume effects in this theory are larger than in QCD, often requiring $m_\pi L \sim 10$; this condition was satisfied in the work we presented, but much greater computational resources would be needed to get points at smaller fermion masses while remaining close to the infinite volume limit.

5.3 Heavy–quark physics on the lattice

Besides issues related to the naturalness of the SM Higgs and the origin of electroweak symmetry breaking, the flavour sector of the SM may hide signs of new physics (NP). This sector, including Yukawa couplings giving mass to the fermions and the CKM matrix parametrizing quarks flavoured interactions, has always been subject to a lot of scrutiny. Recently, flavour physics has been explored with very high precision measurements at the LHC and at B factories, especially in the heavy quarks region including, for example, D meson systems and B mesons rare decay processes. New generations of B factories like Belle II and upgrades to LHC experiments like LHCb will soon improve our experimental knowledge of these heavy fermion systems.

An advanced theoretical framework for translating those results to SM parameters and NP signals with great accuracy requires lattice QCD calculations of matrix elements including heavy quarks. As we have clearly stated in this work, fermions as heavy as the bottom quark are out of reach for current simulations. Moreover, only recently there has been a renewed interest in charm physics on the lattice due to new and fast algorithms and supercomputers which allow for large lattices with high ultraviolet cutoff.

We have focused on various possibilities, available in the literature, to advance our theoretical knowledge of non–perturbative hadronic matrix elements for B mesons using lattice QCD. As for the other topics discussed in this thesis, the lattice framework turns out to be the best tool we have. However, due to its limitations, namely the necessity of having an infinite volume limit together with a continuum limit, it is not directly applicable to B physics.

Using HQET applied to the lattice has proven to be quite successful in describing heavy quarks. Lattice QCD results for B and B_s mesons decay constants, as well as for their mixing parameters, are on the market. This field is still young and many sources of systematic errors have to be fully understood.

We have presented preliminary results of our own approach to this type of calculations using Domain Wall valence fermions and staggered asqtad gauge ensembles with dynamical quarks up to the strange flavour. DWF valence quarks have very good scaling behaviour and chiral properties. Staggered fermions with asqtad improvement yield small discretisation errors and gauge configurations are available up to very high ultraviolet cutoff ~ 4 GeV. These properties should allow us to calculate matrix elements relevant to B physics with a good control over systematics errors.

Usually such systematics errors arise in the renormalization procedure applied to the matrix elements. In this respect, it is known that the DWF formulation helps, since it has a higher degree of chiral symmetry due to the Ginsparg–Wilson relation satisfied by the DWF Dirac operator. Moreover, the amount of chiral symmetry can be systematically improved by changing the parameters of the simulations. We have shown this for the case of heavy DWF quarks by using different kernels for the Dirac operator.

To summarise, we have started a calculation that will be relevant for computing f_B, f_{B_s}, B_B, B_{B_s} and related quantities. Simple spectroscopic observables and matrix elements have been extracted from lattice simulations with somewhat small statistical uncertainties, even for bare quark masses corresponding to charm quarks. This is a promising signal towards a complete study which will include a chiral and continuum extrapolation together with the non–perturbative renormalization of the relevant operators.

Appendix A

Tables of results for the anisotropic five–dimensional lattice model

This appendix includes a list of tables, taken from Ref. [56], summarising the results obtained in Chapter 2.

We start with reporting the list of simulated points on two different geometries. First, in Tab. A.1, we give a list of points used for measurements on the $10^4 \times 4$ lattice. Then we move to the larger $12^4 \times 6$ lattice in Tab. A.2.

The results for the mass of the scalar state, obtained on a subset of the simulated points where a good signal was present, are reported in Tab. A.3 and Tab. A.4.

The same is done for the torelon mass and the corresponding string tension in Tab. A.5 and Tab. A.6.

At the end of the appendix, we give a summary of the physical scale ratios $\frac{\Lambda_{\rm UV}}{\Lambda_{\rm R}}$, $a_4\sqrt{\sigma}$, $R\sqrt{\sigma}$, $\frac{m_5}{\sqrt{\sigma}}$ and Rm_5. Results on the $N_5 = 4$ lattice are reported in Tab. A.7, while the ones for the $N_5 = 6$ lattice are shown in Tab. A.8.

$N_4 = 10$ $N_5 = 4$						
β_4	β_5	β	γ	$\frac{N_5}{\gamma}$	ξ	$\frac{N_5}{\xi}$
1.00	2.90	1.7029	1.7029	2.3488	2.291(39)	1.744(29)
1.00	3.00	1.7320	1.7320	2.3094	2.339(40)	1.709(29)
1.05	2.65	1.6680	1.5886	2.5178	2.095(39)	1.911(35)
1.05	2.70	1.6837	1.6035	2.4944	2.119(38)	1.889(35)
1.05	2.80	1.7146	1.6329	2.4494	2.169(36)	1.844(32)
1.05	2.90	1.7449	1.6619	2.4068	2.219(37)	1.801(31)
1.05	3.00	1.7748	1.6903	2.3664	2.268(38)	1.764(30)
1.07	2.65	1.6838	1.5737	2.5417	2.067(43)	1.934(37)
1.07	2.70	1.6997	1.5885	2.5180	2.092(40)	1.911(35)
1.07	2.75	1.7153	1.6031	2.4950	2.117(40)	1.889(34)
1.07	2.80	1.7309	1.6176	2.4727	2.141(38)	1.866(33)
1.07	2.90	1.7615	1.6462	2.4297	2.195(38)	1.824(30)
1.09	2.65	1.6995	1.5592	2.5653	2.040(43)	1.959(39)
1.09	2.70	1.7155	1.5738	2.5415	2.068(41)	1.934(38)
1.10	2.65	1.7073	1.5521	2.5771	2.029(42)	1.969(41)
1.10	2.70	1.7233	1.5667	2.5531	2.056(41)	1.948(39)
1.10	2.80	1.7549	1.5954	2.5071	2.105(38)	1.900(36)
1.10	2.90	1.7860	1.6236	2.4635	2.152(37)	1.858(33)
1.10	3.00	1.8165	1.6514	2.4221	2.202(38)	1.815(32)
1.11	2.65	1.7150	1.5451	2.5888	2.018(44)	1.986(43)
1.11	2.70	1.7311	1.5596	2.5647	2.042(42)	1.959(41)
1.12	2.65	1.7227	1.5382	2.6004	2.009(44)	1.998(44)
1.12	2.70	1.7389	1.5526	2.5762	2.032(42)	1.972(43)
1.13	2.65	1.7304	1.5313	2.6120	1.995(45)	2.008(47)
1.13	2.70	1.7467	1.5457	2.5877	2.019(44)	1.984(45)
1.14	2.65	1.7381	1.5246	2.6235	1.981(45)	2.019(45)
1.14	2.70	1.7544	1.5389	2.5991	2.007(45)	1.995(44)
1.15	2.60	1.7291	1.5036	2.6602	1.944(47)	2.059(58)
1.15	2.65	1.7457	1.5180	2.6350	1.969(45)	2.031(48)
1.15	2.70	1.7621	1.5322	2.6105	1.996(43)	2.006(45)
1.15	2.80	1.7944	1.5603	2.5634	2.043(40)	1.955(40)
1.15	2.90	1.8262	1.588	2.5188	2.092(37)	1.912(36)
1.15	3.00	1.8574	1.6151	2.4765	2.139(38)	1.869(34)
1.20	2.50	1.7320	1.4433	2.7712	1.839(50)	2.180(58)
1.20	2.55	1.7492	1.4577	2.7439	1.861(49)	2.151(58)
1.20	2.60	1.7663	1.4719	2.7174	1.886(50)	2.121(54)
1.20	2.65	1.7832	1.4860	2.6917	1.912(48)	2.091(51)
1.20	2.70	1.8000	1.5000	2.6666	1.939(49)	2.063(53)
1.10153	2.62363	1.70	1.54	2.59	2.014(44)	1.986(42)
1.10801	2.63906	1.71	1.54	2.59	2.014(44)	1.986(42)
1.11449	2.6545	1.72	1.54	2.59	2.014(44)	1.986(42)
1.12097	2.66993	1.73	1.54	2.59	2.014(44)	1.986(42)
1.12745	2.68536	1.74	1.54	2.59	2.014(44)	1.986(42)
1.13393	2.70079	1.75	1.54	2.59	2.014(44)	1.986(42)
1.14041	2.71623	1.76	1.54	2.59	2.014(44)	1.986(42)
1.14688	2.73166	1.77	1.54	2.59	2.014(44)	1.986(42)

Table A.1 *Simulated points on the $N_4 = 10$, $N_5 = 4$ lattice and corresponding scale separation $\frac{\Lambda_{\mathrm{UV}}}{\Lambda_{\mathrm{R}}} = \frac{N_5}{\xi}$.*

$N_4 = 12$ $N_5 = 6$						
β_4	β_5	β	γ	$\frac{N_5}{\gamma}$	ξ	$\frac{N_5}{\xi}$
0.845	3.80	1.7919	2.1206	2.8293	2.976(30)	2.016(19)
0.850	3.75	1.7853	2.1004	2.8565	2.941(30)	2.039(20)
0.850	3.85	1.8090	2.1282	2.8192	2.988(31)	2.008(20)
0.855	3.70	1.7786	2.0802	2.8842	2.909(27)	2.061(20)
0.855	3.75	1.7906	2.0942	2.8649	2.934(29)	2.045(19)
0.855	3.80	1.8025	2.1081	2.8460	2.957(29)	2.029(20)
0.855	3.85	1.8143	2.1220	2.8275	2.978(31)	2.016(20)
0.860	3.70	1.7838	2.0742	2.8926	2.902(29)	2.069(20)
0.860	3.75	1.7958	2.0881	2.8733	2.923(29)	2.053(20)
0.860	3.80	1.8077	2.1020	2.8543	2.945(28)	2.038(20)
0.860	3.85	1.8196	2.1158	2.8357	2.968(29)	2.022(20)
0.865	3.55	1.7523	2.0258	2.9617	2.823(32)	2.126(23)
0.865	3.60	1.7646	2.0400	2.9410	2.846(31)	2.109(23)
0.865	3.65	1.7768	2.0541	2.9208	2.869(29)	2.092(21)
0.865	3.70	1.7889	2.0682	2.9010	2.889(29)	2.076(21)
0.865	3.80	1.8130	2.0959	2.8626	2.936(30)	2.045(21)
0.870	3.55	1.7574	2.0200	2.9702	2.811(32)	2.133(24)
0.870	3.60	1.7697	2.0341	2.9495	2.836(32)	2.117(23)
0.870	3.65	1.7819	2.0482	2.9293	2.858(30)	2.099(23)
0.870	3.70	1.7941	2.0622	2.9094	2.880(29)	2.083(22)
0.875	3.55	1.7624	2.0142	2.9788	2.802(33)	2.140(24)
0.875	3.60	1.7748	2.0283	2.9580	2.823(31)	2.123(24)
0.875	3.65	1.7871	2.0424	2.9377	2.849(31)	2.106(22)
0.875	3.70	1.7993	2.0563	2.9177	2.872(29)	2.090(21)
0.880	3.55	1.7674	2.0085	2.9873	2.792(34)	2.149(25)
0.888	3.50	1.7629	1.9853	3.0222	2.755(34)	2.179(26)
0.890	3.55	1.7775	1.9971	3.0042	2.775(35)	2.163(27)
0.900	3.45	1.7621	1.9578	3.0645	2.711(31)	2.212(26)
0.900	3.50	1.7748	1.9720	3.0425	2.735(32)	2.194(27)
0.900	3.55	1.7874	1.9860	3.0210	2.756(33)	2.178(26)
0.908	3.45	1.7699	1.9492	3.0781	2.699(33)	2.226(25)
0.920	3.40	1.7686	1.9224	3.1210	2.653(31)	2.261(26)
0.920	3.45	1.7815	1.9364	3.0983	2.676(32)	2.241(26)
0.920	3.50	1.7944	1.9504	3.0761	2.699(30)	2.223(26)
0.860	3.60	1.7595	2.0459	2.9325	2.855(30)	2.102(22)
0.880	3.60	1.7798	2.0226	2.9664	2.816(33)	2.131(25)
0.900	3.60	1.8000	2.0000	3.0000	2.777(34)	2.159(26)
0.920	3.55	1.8072	1.9643	3.0544	2.722(33)	2.205(26)
0.920	3.60	1.8198	1.9781	3.0331	2.743(32)	2.187(27)
0.940	3.40	1.7877	1.9018	3.1548	2.619(30)	2.291(26)
0.940	3.50	1.8138	1.9296	3.1094	2.665(30)	2.251(26)
0.940	3.60	1.8395	1.9569	3.0659	2.709(31)	2.215(25)

Table A.2 *Simulated points on the $N_4 = 12$, $N_5 = 6$ lattice and corresponding scale separation $\frac{\Lambda_{\mathrm{UV}}}{\Lambda_{\mathrm{R}}} = \frac{N_5}{\xi}$.*

Scalar masses on $N_4 = 10$ $N_5 = 4$			
β_4	β_5	$a_4 m_5$	$t_{\min} - t_{\max}$
1.00	2.90	1.118(26)	2 - 4
1.00	3.00	1.406(56)	2 - 4
1.00	3.00	1.30(19)	**3 - 4**
1.05	2.80	1.020(16)	2 - 4
1.05	3.00	1.386(85)	2 - 4
1.05	3.00	1.05(22)	**3 - 4**
1.07	2.70	0.6482(69)	2 - 4
1.07	2.75	0.925(13)	2 - 4
1.07	2.75	0.904(29)	**3 - 4**
1.07	2.80	1.022(57)	3 - 4
1.07	2.90	1.349(56)	2 - 4
1.07	2.90	1.27(21)	**3 - 4**
1.09	2.65	0.4586(43)	2 - 4
1.09	2.70	0.844(10)	2 - 4
1.10	2.65	0.624(05)	2 - 4
1.10	2.70	0.880(14)	2 - 4
1.10	2.80	1.258(51)	2 - 4
1.10	2.80	1.15(15)	**3 - 4**
1.10	2.90	1.64(17)	2 - 4
1.11	2.65	0.732(11)	2 - 4
1.11	2.70	0.865(32)	3 - 4
1.12	2.65	0.779(11)	2 - 4
1.14	2.65	0.840(52)	3 - 4
1.14	2.70	0.90(13)	3 - 4
1.15	2.60	0.724(21)	3 - 4
1.15	2.70	1.424(55)	2 - 4
1.15	2.70	1.24(21)	**3 - 4**
1.20	2.50	0.923(76)	3 - 4
1.10801	2.63906	0.638(44)	3 - 4
1.11449	2.6545	0.765(12)	3 - 4
1.12097	2.66993	0.822(26)	3 - 4
1.12745	2.68536	0.898(37)	3 - 4
1.13393	2.70079	0.791(98)	3 - 4
1.14041	2.71623	1.450(92)	2 - 4
1.14041	2.71623	1.18(34)	**3 - 4**

Table A.3 *Static scalar mode masses for $N_4 = 10$, $N_5 = 4$. The fitting range for the effective mass plateaux is shown in the last column. Boldface values are alternative fitting ranges.*

Scalar masses on $N_4 = 12$ $N_5 = 6$			
β_4	β_5	$a_4 m_5$	$t_{\min} - t_{\max}$
0.845	3.80	1.05(31)	3 - 5
0.845	3.80	**1.17(20)**	3 - 5
0.850	3.75	1.273(74)	2 - 3
0.850	3.75	1.14(19)	**3 - 4**
0.850	3.85	1.65(15)	2 - 4
0.850	3.85	1.04(36)	**3 - 4**
0.855	3.70	0.91(14)	3 - 5
0.855	3.75	1.35(25)	3 - 5
*0.860	3.60	0.581(20)	4 - 7
0.860	3.70	1.294(67)	2 - 4
0.860	3.70	1.19(24)	**3 - 4**
0.865	3.55	0.3312(38)	2 - 4
0.865	3.60	0.677(25)	4 - 5
0.865	3.65	0.95(10)	3 - 5
0.870	3.55	0.4679(86)	4 - 5
0.870	3.60	0.818(58)	3 - 4
0.870	3.65	0.998(93)	3 - 5
0.870	3.70	1.401(92)	2 - 4
0.870	3.70	1.07(26)	**3 - 4**
0.875	3.55	0.532(20)	4 - 5
0.875	3.60	0.880(97)	3 - 4
0.875	3.65	1.40(8)	2 - 4
0.875	3.65	1.16(25)	**3 - 4**
0.875	3.70	1.02(20)	3 - 5
0.880	3.55	0.727(50)	3 - 5
0.880	3.55	**0.86(15)**	3 - 5
*0.880	3.60	1.318(57)	2 - 4
*0.880	3.60	1.30(21)	**3 - 4**
0.888	3.50	0.595(19)	3 - 5
0.888	3.50	0.561(34)	**4 - 5**
0.890	3.55	1.038(82)	3 - 5
0.890	3.55	0.93(21)	**4 - 5**
0.900	3.45	0.635(12)	2 - 5
0.900	3.50	1.173(72)	2 - 5
0.900	3.50	0.91(13)	**4 - 5**
0.908	3.45	0.777(78)	3 - 5
0.920	3.45	1.46(11)	2 - 4
0.920	3.45	1.06(33)	**3 - 4**

Table A.4 *Static scalar mode masses for $N_4 = 12$, $N_5 = 6$. The fitting range for the effective mass plateaux is shown in the last column. Boldface values are alternative fitting ranges. (The starred points come from a lattice with a longer temporal distance $L_t = 2L_4$)*

Torelon masses and string tensions on $N_4 = 10$ $N_5 = 4$					
β_4	β_5	$a_4 m_{\mathrm{tor}}$	$t_{\mathrm{min}} - t_{\mathrm{max}}$	$a_4\sqrt{\sigma}$	$\sim L_4\sqrt{\sigma}$
1.05	3.00	1.219(24)	2 - 4	0.3638(33)	3.6
1.05	3.00	1.173(71)	**3 - 4**	0.3574(99)	3.6
1.07	2.90	1.334(39)	2 - 4	0.3793(52)	3.8
1.07	2.90	1.16(11)	**3 - 4**	0.356(15)	3.6
1.10	2.80	1.116(16)	2 - 4	0.3493(23)	3.5
1.10	2.80	1.105(48)	**3 - 4**	0.3478(69)	3.5
1.10	2.90	0.428(2)	2 - 4	0.2308(5)	2.3
1.14	2.65	1.215(27)	2 - 4	0.3633(37)	3.6
1.14	2.65	1.190(71)	**3 - 4**	0.3598(99)	3.6
1.14	2.70	0.6153(39)	2 - 4	0.2683(7)	2.7
1.15	2.70	0.3798(14)	2 - 4	0.2201(3)	2.2
1.20	2.50	0.5663(41)	2 - 4	0.2590(8)	2.6
1.12745	2.68536	1.18(10)	3 - 4	0.358(14)	3.6
1.13393	2.70079	0.8175(78)	2 - 4	0.3037(13)	3.0
1.14041	2.71623	0.491(3)	2 - 3	0.2441(6)	2.4

Table A.5 *Torelon masses for $N_4 = 10$, $N_5 = 4$. The fitting range for the effective mass plateaux is shown together with the calculated string tension. Boldface values are alternative fitting ranges.*

Torelon masses and string tensions on $N_4 = 12$ $N_5 = 6$					
β_4	β_5	$a_4 m_{\mathrm{tor}}$	$t_{\mathrm{min}} - t_{\mathrm{max}}$	$a_4\sqrt{\sigma}$	$\sim L_4\sqrt{\sigma}$
0.845	3.80	0.5800(60)	2 - 5	0.2358(11)	2.8
0.850	3.75	0.7127(75)	2 - 5	0.2582(12)	3.1
0.850	3.75	0.730(16)	**3 - 5**	0.2610(26)	3.1
0.850	3.85	0.2665(19)	2 - 4	0.1717(4)	2.1
0.850	3.85	0.2658(18)	**3 - 4**	0.1715(4)	2.1
0.855	3.70	0.8954(99)	2 - 5	0.2862(14)	3.4
0.855	3.75	0.5162(51)	2 - 5	0.2243(9)	2.7
0.860	3.70	0.6412(73)	2 - 5	0.2464(12)	3.0
0.865	3.65	0.808(19)	3 - 5	0.2732(29)	3.3
0.865	3.65	0.784(34)	**4 - 5**	0.2694(53)	3.2
0.870	3.60	1.224(77)	3 - 5	0.3306(97)	4.0
0.870	3.65	0.5798(62)	2 - 5	0.2358(11)	2.8
0.870	3.70	0.3295(19)	2 - 5	0.1864(4)	2.2
0.875	3.60	0.7933(92)	2 - 4	0.2709(14)	3.3
0.875	3.65	0.4177(31)	2 - 5	0.2051(6)	2.5
0.875	3.70	0.2418(10)	3 - 5	0.1656(2)	2.0
0.880	3.55	1.25(12)	3 - 5	0.334(14)	4.0
*0.880	3.60	0.523(21)	5 - 11	0.2256(40)	2.7
0.890	3.55	0.5140(49)	2 - 5	0.2239(9)	2.7
0.900	3.45	1.06(11)	3 - 5	0.310(15)	3.7
0.900	3.45	0.87(25)	**4 - 5**	0.282(37)	3.4
0.900	3.50	0.4963(52)	2 - 5	0.2205(10)	2.6
0.908	3.45	0.5942(67)	2 - 5	0.2383(12)	2.9
0.920	3.45	0.2353(19)	2 - 4	0.1639(5)	2.0

Table A.6 *Torelon masses for $N_4 = 12$, $N_5 = 6$. The fitting range for the effective mass plateaux is shown together with the calculated string tension. Boldface values are alternative fitting ranges. (The starred point comes from a lattice with a longer temporal distance $L_t = 2L_4$)*

$N_4 = 10$ $N_5 = 4$				
$\frac{\Lambda_{\rm UV}}{\Lambda_{\rm R}}$	$a_4\sqrt{\sigma}$	$R\sqrt{\sigma}$	$\frac{m_5}{\sqrt{\sigma}}$	Rm_5
1.763(29)	0.3638(33)	0.1021(19)	3.81(23)	0.389(25)
1.763(29)	0.3638(33)	0.1021(19)	2.89(61)	0.295(63)
1.763(29)	0.3574(99)	0.1003(32)	3.88(26)	0.389(29)
1.763(29)	0.3574(99)	0.1003(32)	2.95(62)	0.295(63)
1.824(30)	0.3793(52)	0.1101(23)	3.56(15)	0.392(19)
1.824(30)	0.3793(52)	0.1101(23)	3.35(54)	0.369(60)
1.824(30)	0.356(15)	0.1033(48)	3.79(21)	0.392(28)
1.824(30)	0.356(15)	0.1033(48)	3.57(57)	0.369(62)
1.900(35)	0.3493(23)	0.1056(21)	3.60(14)	0.380(17)
1.900(35)	0.3493(23)	0.1056(21)	3.29(41)	0.348(44)
1.900(35)	0.3478(69)	0.1052(29)	3.62(16)	0.380(20)
1.900(35)	0.3478(69)	0.1052(29)	3.31(41)	0.348(44)
1.857(32)	0.2308(5)	0.0682(12)	7.10(75)	0.484(52)
2.019(45)	0.3633(37)	0.1168(29)	2.31(15)	0.270(18)
2.019(45)	0.3598(99)	0.1156(41)	2.33(16)	0.270(20)
1.994(43)	0.2683(7)	0.0852(19)	3.36(50)	0.286(43)
2.006(44)	0.2201(33)	0.0703(15)	6.47(24)	0.455(20)
2.006(44)	0.2201(33)	0.0703(15)	5.66(94)	0.397(67)
2.180(57)	0.2590(8)	0.0899(24)	3.56(30)	0.320(28)
1.986(42)	0.358(14)	0.1133(51)	2.51(14)	0.284(20)
1.986(42)	0.3037(13)	0.0960(21)	2.61(32)	0.250(31)
1.986(42)	0.2441(6)	0.0772(16)	5.94(38)	0.458(31)
1.986(42)	0.2441(6)	0.0772(16)	4.9(1.4)	0.37(11)

Table A.7 *The results of our numerical simulations are reported in this table for $N_5 = 4$. When more than one value is shown, they come from different fitting ranges in the plateaux of the primary observables. The spread of the values is used to estimate a systematic error that is then reported in the plots.*

$N_4 = 12\ N_5 = 6$				
$\frac{\Lambda_{\rm UV}}{\Lambda_{\rm R}}$	$a_4\sqrt{\sigma}$	$R\sqrt{\sigma}$	$\frac{m_5}{\sqrt{\sigma}}$	Rm_5
2.016(19)	0.2358(11)	0.0757(8)	4.5(1.3)	0.337(99)
2.016(19)	0.2358(11)	0.0757(8)	4.98(84)	0.377(64)
2.039(20)	0.2582(12)	0.0838(9)	4.93(29)	0.413(25)
2.039(20)	0.2610(26)	0.0847(12)	4.88(29)	0.413(25)
2.039(20)	0.2582(12)	0.0838(9)	4.41(75)	0.369(63)
2.039(20)	0.2610(26)	0.0847(12)	4.36(74)	0.369(63)
2.008(20)	0.1717(5)	0.0549(6)	9.59(88)	0.526(49)
2.008(20)	0.1715(4)	0.0548(6)	9.60(88)	0.526(49)
2.008(20)	0.1717(5)	0.0549(6)	6.1(2.1)	0.33(12)
2.008(20)	0.1715(4)	0.0548(6)	6.1(2.1)	0.33(12)
2.061(19)	0.2862(14)	0.0939(10)	3.20(48)	0.300(45)
2.045(19)	0.2243(9)	0.0730(8)	6.0(1.1)	0.439(80)
2.069(20)	0.2464(12)	0.0811(9)	5.25(28)	0.426(23)
2.069(20)	0.2464(12)	0.0811(9)	4.84(98)	0.393(79)
2.092(21)	0.2732(29)	0.0910(13)	3.49(38)	0.317(35)
2.092(21)	0.2694(53)	0.0897(20)	3.54(39)	0.317(35)
2.117(23)	0.3306(97)	0.1114(35)	2.47(19)	0.276(23)
2.099(23)	0.2358(11)	0.0788(9)	4.23(39)	0.333(31)
2.083(22)	0.1864(41)	0.0618(7)	7.52(50)	0.464(31)
2.083(22)	0.1864(41)	0.0618(7)	5.7(1.4)	0.355(86)
2.123(24)	0.2709(14)	0.0915(11)	3.25(36)	0.297(33)
2.106(22)	0.2051(64)	0.0688(7)	6.83(41)	0.469(29)
2.106(22)	0.2051(64)	0.0688(7)	5.6(1.2)	0.388(84)
2.090(21)	0.1656(2)	0.0551(5)	6.2(1.2)	0.339(65)
2.149(25)	0.334(14)	0.1144(51)	2.18(18)	0.249(24)
2.149(25)	0.334(14)	0.1144(51)	2.57(45)	0.294(53)
2.131(25)	0.2256(40)	0.0765(16)	5.84(25)	0.447(21)
2.131(25)	0.2256(40)	0.0765(16)	5.76(92)	0.441(71)
2.163(27)	0.2239(9)	0.0771(10)	4.64(37)	0.357(29)
2.163(27)	0.2239(9)	0.0771(10)	4.16(93)	0.320(72)
2.212(26)	0.310(15)	0.1090(54)	2.05(11)	0.224(16)
2.212(26)	0.282(37)	0.099(13)	2.25(31)	0.224(42)
2.194(27)	0.2205(10)	0.0770(10)	5.32(33)	0.410(26)
2.194(27)	0.2205(10)	0.0770(10)	4.12(60)	0.317(46)
2.226(25)	0.2383(12)	0.0844(10)	3.26(33)	0.275(28)
2.241(26)	0.1639(5)	0.0585(69)	8.90(66)	0.520(39)
2.241(26)	0.1639(5)	0.0585(69)	6.4(2.0)	0.38(12)

Table A.8 *The results of our numerical simulations are reported in this table for $N_5 = 6$. When more than one value is shown, they come from different fitting ranges in the plateaux of the primary observables. The spread of the values is used to estimate a systematic error that is then reported in the plots.*

Appendix B

Gluonic lattice spectroscopy

In this appendix we present the construction of glueball operators and we review the general methodology for extracting glueball masses. The standard variational procedure and the construction of operators in irreducible representations of the cubic lattice group is well known [184, 185], but we want to describe the details of the algorithms used to perform the calculations included in this thesis.

The author has been working on improving glueball masses calculations since the original work of Ref. [71], which allowed the computation of the glueball spectrum in the $N \to \infty$ of Yang–Mills theories at finite lattice spacing (see Appendix C for a brief description of the results). The gluonic results described in Chapter 2 and Chapter 3 are obtained thanks to the improved glueball spectroscopy developed in Ref. [71].

Additional applications of this framework include a study of heavy glueballs in $N_f = 2+1$ lattice QCD on fine lattices [73], targeting exotic channels to improve a possible future experimental discovery of glueballs [132]. Another important contribution made possible by the setup described in this Appendix is the study of the scaling properties in the spectrum of a SU(2) pure gauge theory with mixed fundamental and adjoint plaquette action. A detailed analysis of the spectrum which allows the identification of critical exponents is described in Ref. [186] and preliminary results were included in Ref. [139].

B.1 Euclidean correlators and effective masses

We start by describing how to extract the mass of propagating particles in a pure gauge theory. In the continuum Minkowskian space–time, we look at the poles in the 2–point function of gauge fields; in the Euclidean lattice regularised theory, the spectrum can be otherwise extracted from the large–time decay rate of the 2–point functions of the lattice gauge fields (i.e. the link variables).
In terms of the statistical system corresponding to the Euclidean lattice gauge theory, the mass of the lowest state of the spectrum (the ground state), above the vacuum of the theory, can be viewed as the largest correlation length.

Following the statistical mechanics correspondence, we can interpret the correlation function in a physical appealing way by using the transfer matrix formalism [187]. The lattice four–dimensional gauge theory can be viewed as a three–dimensional quantum mechanical system with a Hilbert space $\mathcal{H}$ of physical states, a Hamilton operator $\hat{H}$ and linear operators $\hat{\Phi}$ corresponding to the Euclidean functionals Φ. The Euclidean functionals correspond themselves to fields in the gauge theory. The transfer matrix $\hat{T}$ can be defined explicitly as an operator acting on $\mathcal{H}$, and it is related to the partition function of the system by

$$\mathcal{Z} \;=\; \mathrm{Tr}\; \hat{T}^{L_t} \;. \tag{B.1}$$

In the previous formula, L_t is the size of the temporal direction of the lattice, and the trace is over all the states of $\mathcal{H}$. From the above relation, the Hamiltonian is defined through

$$\hat{T} \;=\; e^{-a\hat{H}} \;. \tag{B.2}$$

The transfer matrix evolves the states defined on one time–slice of the lattice to states on a subsequent time–slice. Thus the 2–point function of an operator $\hat{\Phi}(t)$ localised on a time–slice t, reads

$$C_{\Phi\Phi}(t) \;\equiv\; \left\langle \hat{\Phi}^\dagger(t)\hat{\Phi}(0) \right\rangle \;=\; \langle 0|\, \hat{\Phi}^\dagger(0)\hat{T}^t\hat{\Phi}(0)\,|0\rangle \;=\; \langle 0|\, \hat{\Phi}^\dagger(0)e^{-t\hat{H}}\hat{\Phi}(0)\,|0\rangle \;. \tag{B.3}$$

Inserting a complete set of energy eigenstates $\hat{H}\,|n\rangle = E_n\,|n\rangle$, we get

$$C_{\Phi\Phi}(t) \;=\; \sum_n \langle 0|\, \hat{\Phi}^\dagger(0)\,|n\rangle\,\langle n|\,\hat{\Phi}(0)\,|0\rangle\, e^{-E_n t} \;=\; \sum_n |\,\langle n|\,\hat{\Phi}\,|0\rangle\,|^2 e^{-E_n t} \;. \tag{B.4}$$

The interpretation is particularly simple: the operator $\hat{\Phi}(0)$ "creates" states from

the vacuum $|0\rangle$, which have a projection $c_n = \langle n| \hat{\Phi} |0\rangle$ on $|n\rangle$ at time $t = 0$, and $\hat{\Phi}^\dagger(t)$ "annihilates" them at time t.

The basic principle of lattice spectroscopy measurements is that the sum on the right hand side of Eq. (B.4) is dominated by the state with the smallest energy when t is large and if the overlap coefficient $|c_n|^2$ does not vanish. Then, the eigenvalues of the Hamiltonian of the system can be calculated from the $t \to \infty$ limit of suitable correlators $C_{\Phi\Phi}(t)$. This correlators is referred to simply as $C(t)$ in the following.

To extract the mass spectrum, we restrict ourselves to consider zero–momentum operators $\hat{\Phi}_{\vec{p}=0}$. This is done for simplicity reasons and due to a good signal in numerical simulations for this kind of operators. When dealing with lattice systems having periodic boundary conditions, discrete translational invariance is satisfied and the operators can always be chosen to have definite momentum: in Fourier transform, $\hat{\Phi}_{\vec{p}=0}(t) = \sum_x \hat{\Phi}_x(t)$. Moreover, close to the continuum limit where continuum symmetries are restored, the continuum relativistic dispersion relation $E^2 = m^2 + |\vec{p}|^2$ is approximately valid on the lattice and the zero–momentum correlators give us the mass spectrum following Eq. (B.4).

In general, physical states are characterised by quantum numbers dictated by the symmetry group of the theory. For example, in the continuum, glueballs are classified as irreducible representations of the Lorentz symmetry group and they are eigenstates of discrete symmetry transformations such as parity and charge conjugation. Zero–momentum glueball states are labelled with spin J, parity P and charge conjugation C [15]. Therefore, the mass m of a J^{PC} state can be calculated from the correlation function of operators capable of creating from the vacuum a state with the same quantum numbers.

In our lattice approach, the pure gauge theory has a symmetry group which is only a subgroup of the continuum one. The continuum SO(3) rotation invariance is not shared by the discretised system: only rotations in unit of $\pi/2$ are allowed. Moreover, only discrete translations are allowed as well, so momentum is conserved in discrete steps $p = 2\pi L/n$, where L is the spatial extent of the cubic lattice and $n \in \mathbb{Z}$.

This implies that zero–momentum glueball states on a simple cubic lattice are characterised by irreducible representations of the cubic group O, combined with parity P and charge conjugation C: we label these states with R^{PC}, or simply R. Now, provided that we can write operators with the right symmetry properties,

and that we can measure the asymptotic behaviour of their correlators, it is possible to extract the mass spectrum. The first mass estimate is given by the effective mass (we work in units of the lattice spacing in the following):

$$m_{\text{eff}} \;=\; -\ln \frac{\left\langle \hat{\Phi}^{\dagger}(1)\hat{\Phi}(0) \right\rangle}{\left\langle \hat{\Phi}^{\dagger}(0)\hat{\Phi}(0) \right\rangle} \;. \tag{B.5}$$

Since it involves the correlator $C(1)$ at such a short temporal distance, this quantity overestimates the real mass, which sets the exponential decay rate at large time separations. It can, however, be a good estimate if, even at $t = 1$, $\left\langle \hat{\Phi}^{\dagger}(t)\hat{\Phi}(0) \right\rangle$ can be written as a single exponential. This assertion is certainly false because heavier excited states usually propagate as well.

We can improve our previous mass estimate by considering effective masses at different temporal distances, to see whether or not, from a certain time t_{min}, $C(t)$ starts to behave like a single exponential. Using the definition

$$m_{\text{eff}}(t) \;=\; -\ln \frac{C(t)}{C(t-1)} \;, \tag{B.6}$$

we try to identify a plateaux $t \geq t_{min}$ where the effective mass $m_{\text{eff}}(t)$ is the same as $m_{\text{eff}}(t_{min})$ within the errors. If such a plateaux is found, then the exponential decay of the correlators is governed by a single scale, which is the plateaux mass $m_{eff}(t_{min})$.

The correlators $C(t) \;=\; \left\langle \hat{\Phi}^{\dagger}(t)\hat{\Phi}(0) \right\rangle$ are evaluated as vacuum expectation values of product of Euclidean functionals at different times, using numerical simulations. This numerical approach implies that, for every time separation t, $C(t)$ is measured with a statistical error. The error is mainly independent of t, but the correlator decreases exponentially with increasing time. Therefore, the ratio between signal and statistical noise decreases exponentially fast and the small t points of the correlator have the smallest relative errors. Hence, the effective mass is best determined at small times.

On the other hand, far away from the asymptotic $t \to \infty$ regime, the correlator Eq. (B.4) is a sum of exponentials. At small temporal distances excited states contribute as well in the exponential decay. The conclusion is that, at small t the relative statistical error on the correlator is small, but the effective mass has large systematic errors.

The simple solution to this impasse is to make $C(t)$ behave like a single exponential from the smallest possible time, by removing contributions of excited states. In general, we can have a single exponential decay if the sum on the energy eigenstates is dominated by a single one of them; this happen, for example, if the normalised overlap coefficient of one state is of order 1.

Let us say that we are interested in the mass of the state $|1\rangle$. Then, if

$$|c_1|^2 \;=\; |\,\langle 1|\,\hat{\Phi}\,|0\rangle\,|^2 \;\approx\; O(1)\;, \tag{B.7}$$

and we have normalised the coefficients such that

$$\sum_n |c_n|^2 \;=\; 1\;, \tag{B.8}$$

the correlator reads

$$C(t) \;=\; \sum_n |c_n|^2 e^{-m_n t} \;\approx\; |c_1|^2 e^{-m_1 t} \quad \forall t\;. \tag{B.9}$$

The systematic error in the effective masses is drastically reduced. There are several ways to improve the overlap on the state of interest and then find a good estimate of its mass. We are going to describe two methods in the following: the first is related to the construction of operators which are good approximations of the physical wave–function of the desired state. The second is a variational method which try to minimise the $m_{\rm eff}(t)$ over a range of basis operators and it is also capable of extracting excited states masses.

B.2 Operators with a physical size

As we shall see in more details in the following, glueball operators $\hat{\Phi}$ are gauge–invariant combinations of link variables $U_{x,\mu}$. Such operators can be constructed starting from products of link variables around spatial Wilson loops. Making use only of spatial links supports the transfer matrix interpretation of the two point function.

Now we describe how to obtain operators that are good approximations of glueballs wave–functions, in order to enhance the coefficient $|\,\langle n|\,\hat{\Phi}\,|0\rangle\,|^2$. If we construct $\hat{\Phi}$ using the 4–links plaquette, for example, we are using a highly local

operator, whereas a physical glueball wave–functional has a typical extended scale. When the lattice spacing decreases, the plaquette operator starts being dominated by ultraviolet fluctuations and overlaps more or less equally on all the physical states. To better approximate glueball wave–functions, even at small lattice spacing, we construct operators that are smooth at the physical scale of glueball states (cfr. Fig. B.1).

There are two well–developed algorithms to obtain such operators on the lattice. They are smearing [188] and blocking [189]. Let us briefly review how these iterative techniques work. Since we are going to use only spatial paths, the indices in the following link variables run from 1 to 3.

The smearing algorithm replaces the links pertaining to a path, used to construct an operator, with the sum over the five shortest paths connecting the sites at the extrema of the original link. This substitution allows to "fatten" the links extending the physical size of the resulting operator. The first step of the algorithm consists in evaluating the staples and then summing them to the original link. For a SU(N) gauge theory this produces a link matrix which is no more unitary (it is proportional to a unitary matrix only in the SU(2) case). The second step consists in assigning this matrix to the original link, after a projection back to the SU(N) gauge group. This smearing procedure produces SU(N) matrices on the links of the lattice. It can also introduce a parameter p_a to weight the sum of the staples relatively to the original link, which determines how rapidly the lattice gauge field spreads outwards as the procedure is iterated. If p_a is small with respect to 1, operators constructed using smeared links will extend, with a fine resolution, over all important length scales.

The first smearing step can be further improved in order to make it more symmetric about the axis of the basic link. To the four staples we can also add 16 diagonal staples connecting next–to–nearest neighbours on the lattice. A new parameter p_d is introduced to weight these diagonal staples in the smearing sum. The parameters p_a and p_d are chosen such that the operator constructed using smeared links is a good approximation of the glueball wave–function.

The whole procedure can be iterated as follows. Define $\tilde{U}_i^s(x)$ to be the $N \times N$

matrix after s iteration smearing iteration. Each iteration can be written as

$$\begin{aligned}\tilde{U}_i^{s+1}(x) \;=\; & U_i^s(x) + p_a \sum_{j\neq i} U_j^s(x) U_i^s(x+\hat{\jmath}) U_j^{s\dagger}(x+\hat{\imath}) \\ & + p_a \sum_{j\neq i} U_j^{s\dagger}(x-\hat{\jmath}) U_i^s(x-\hat{\jmath}) U_j^s(x-\hat{\jmath}+\hat{\imath}) \\ & + p_d \sum_{j\neq i} \sum_{k\neq i,j} U_j^s(x) U_k^s(x+\hat{\jmath}) U_i^s(x+\hat{\jmath}+\hat{k}) \sum_{j'\neq i} \sum_{k'\neq i,j'} U_{j'}^{s\dagger}(x+\hat{\imath}+\hat{k}) U_{k'}^{s\dagger}(x+\hat{\imath}) \\ & + p_d \text{ [rotated terms]} \quad ,\end{aligned} \tag{B.10}$$

starting from

$$\tilde{U}_i^{s=0}(x) \;=\; U_i(x) \; . \tag{B.11}$$

The new SU(N) link matrix $U_i^{s+1}(x)$ is then obtained with a unitarization procedure represented by

$$U_i^{s+1}(x) \;=\; \mathcal{U}\Big\{\tilde{U}_i^{s+1}(x)\Big\} \; . \tag{B.12}$$

In Eq. (B.10), the rotated terms refer to three further terms similar to the previous one representing the diagonal staples, but rotated around the i–axis of the original link by multiples of $\pi/2$. In Fig. B.2 we show a pictorial representation of Eq. (B.10).

The blocking algorithm is different because the resulting matrices live on "super–links" joining sites that are 2^b lattice spacing apart, where b is the number of blocking iterations (called blocking level). After each iteration, the original link's length is doubled and elongated staples are added. This implies that blocking is faster than smearing in increasing the size of an operator, but the resolution of the scale probed is rather crude. This can be a problem, because blocked operators constructed using super–links can be too large or too small with respect to the typical size of the physical glueball state of interest.

The iterative blocking procedure is as follow:

$$\begin{aligned}\tilde{U}_i^{b+1}(x) \;=\; & U_i^b(x) U_i^b(x+2^b\hat{\imath}) \\ & + p_b \sum_{j\neq i} U_j^b(x) U_i^b(x+2^b\hat{\jmath}) U_i^b(x+2^b\hat{\jmath}+2^b\hat{\imath}) U_j^{b\dagger}(x+2^{b+1}\hat{\imath}) \\ & + p_b \sum_{j\neq i} U_j^{b\dagger}(x-2^b\hat{\jmath}) U_i^b(x-2^b\hat{\jmath}) U_i^b(x-2^b\hat{\jmath}+2^b\hat{\imath}) U_j^b(x-2^b\hat{\jmath}+2^{b+1}\hat{\imath}) \; ,\end{aligned} \tag{B.13}$$

where we set

$$\tilde{U}_i^{b=0}(x) \;=\; U_i(x)\;. \tag{B.14}$$

The blocked matrices are then projected back to SU(N) following Eq (B.12). The new parameter p_b which weight the sum of elongates staples is typically chosen to be $O(1)$ so that the width of the blocked link grows together with its length. The paths added in the blocking algorithm are shown in Fig. B.3.

An improved blocking algorithm that we use in our studies of gluonic observables is defined in Ref. [69]. The improved blocking has both the rapid increasing rate of the blocking above and the fine resolution of the smearing;. In fact, it consists in multiplying together two smeared links at smearing level s

$$\begin{aligned} U_i^{b+1}(x) \;&=\; U_i^{b,s}(x) U_i^{b,s}(x+2^b\hat{\imath}) \\ U_i^{b,s}(x) \;&=\; \mathrm{Smear}^s\Big\{U_i^b(x)\Big\}\;. \end{aligned} \tag{B.15}$$

Here Smear^s denotes the smearing procedure iterated at level s and generalised to blocked links $U_i^b(x)$. The difference between Eq (B.15) and the original blocking in Eq (B.13) is that the former includes more paths at intermediate length scales and the probability to obtain a good overlap is greater.

The above procedure has two parameters, p_a and p_d, which have to be tuned in order to optimise the overlap. The links resulting from the previous procedure are used to create the operator $\hat{\Phi}$, which can be considered to be smooth on physical scales.

B.3 Effective mass minimisation

Another way to find good overlaps for physical glueball states works very well with the algorithms described in the previous section. The main idea is to choose a whole basis $\big\{\Phi_\alpha\big\}_{\alpha=1,\ldots,N_o}$ of operators and to find the one that minimise the effective mass. To use this method, we simultaneously measure correlators between Φ_α coming from differently shaped closed loops $\mathcal{C}$. Moreover, we insert in the variational basis, operators with different blocking levels b. The variational method described below finds the linear combination of basis operators which best approximate the wave–function of the state we are interested in.

Imagine we start with a certain number N_o of basis operators. These are of

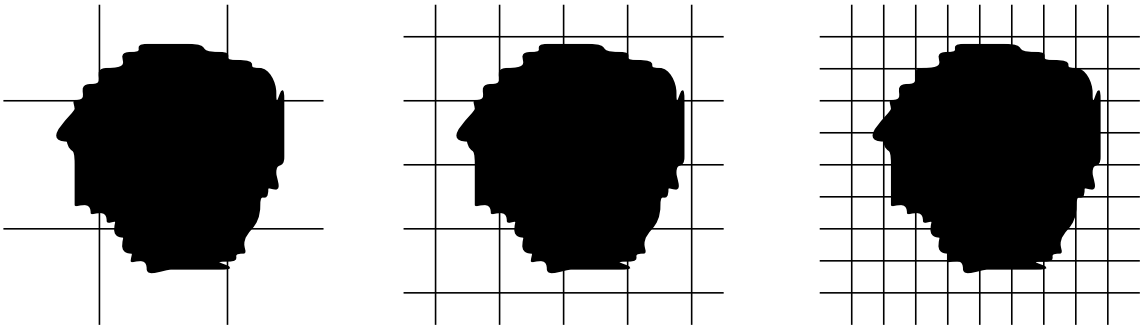

Figure B.1 *When the lattice spacing shrinks, operators constructed only from local path shrink as well and they are no more a good approximation of the glueball wave–functional, which always remains of the same physical extension.*

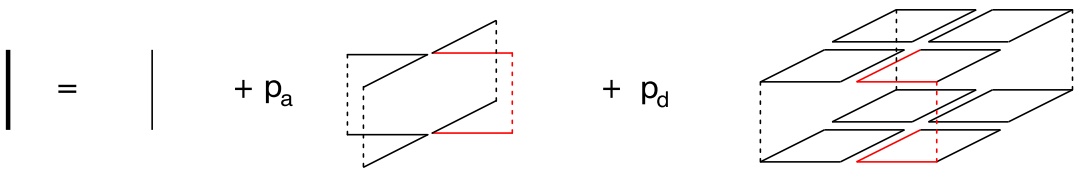

Figure B.2 *In the smearing algorithm, a smeared lattice link (on the left) is obtained adding to the original link the parallel transported nearest neighbour links weighted by the parameter p_a, and the next–to–nearest neighbour links parallel transported along all possible paths on the elementary cube weighted by another parameter p_d. In red we highlight a normal staple and a particular diagonal staple; all other diagonal staples are constructed following the lines in the picture.*

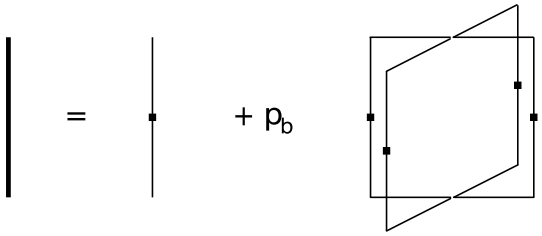

Figure B.3 *Pictorial representation of a blocked super–link as a sum of elongated staples. These staples are parallel transported nearest neighbour links which go from the site x to the site $x + 2^{b+1}\hat{\imath}$*

different shapes and sizes, but they all have the same symmetry quantum numbers of the glueball state we want to study. Call these operators $\Phi_\alpha^{(R)}$, where α labels the operator and R the quantum numbers. Since we deal with a single symmetry channel in the following, we drop the superscript (R).

We measure the $N_o \times N_o$ correlation matrix for every time separation t

$$\tilde{C}_{\alpha\beta}(t) \;=\; \sum_{\tau} \langle 0|\, \Phi_\alpha^\dagger(t+\tau)\Phi_\beta(\tau)\,|0\rangle \;\; . \tag{B.16}$$

We define our correlated operators to be always vacuum subtracted

$$\Phi_\alpha(t) \;=\; \mathcal{O}_\alpha(t) - \langle \mathcal{O}_\alpha(t)\rangle \;\; . \tag{B.17}$$

The aim is to find an appropriate linear combination

$$\hat{\Phi}(t) \;=\; \sum_\alpha v_\alpha \Phi_\alpha(t) \;, \tag{B.18}$$

such that its correlator gives us the best estimation of the mass of the lowest lying state with quantum numbers R. Of course, between different estimates of the mass, the best one in a variational sense, is the lowest one. The coefficients v_α are chosen to minimize the effective mass

$$m_{\rm eff}(\bar{t}) \;=\; -\frac{1}{\bar{t}} \ln \frac{\sum_{\alpha\beta} v_\alpha v_\beta \tilde{C}_{\alpha\beta}(\bar{t})}{\sum_{\alpha\beta} v_\alpha v_\beta \tilde{C}_{\alpha\beta}(0)} \;, \tag{B.19}$$

where we usually choose $\bar{t} = 1$ in lattice units because it gives the best statistical signal. It is easy to show that the effective mass above is exactly the effective mass one would obtain from $\left\langle \hat{\Phi}^\dagger(t)\hat{\Phi}(0)\right\rangle$.

This minimisation is usually turned into a *generalised eigenvalue problem* [190] in order to solve for the coefficients v_α. If we denote $\vec{v}$ a column vector whose elements are the coefficients v_α, then the optimal values for v_α are obtained when $\vec{v}$ is an eigenvector of $\tilde{C}(\bar{t})$. The problem is to numerically solve the following eigenvalue equation

$$\tilde{C}(\bar{t}) \cdot \vec{v} \;=\; \lambda(\bar{t})\vec{v} \;, \tag{B.20}$$

where the eigenvalues are

$$\lambda(\bar{t}) \;=\; e^{-m_{\rm eff}(\bar{t})\bar{t}}\tilde{C}(0) \;. \tag{B.21}$$

One way to proceed is to diagonalise the matrix $\tilde{C}^{-1}(0)\tilde{C}(\bar{t})$ for $\bar{t} = 1$. To each eigenvector $\vec{v}^i$ corresponds an effective mass. The eigenvector corresponding to the lowest effective mass $m^0_{\rm eff}$ yields the coefficients v^0_α for the operator $\hat{\Phi}^0$ which best overlaps on the lowest–lying glueball state with quantum numbers R. Higher–mass eigenvectors can be used to construct operators with good overlap onto excited states.

We usually consider the 5 lowest effective masses (or equivalently the 5 eigenvectors corresponding to the 5 highest eigenvalues). The operators constructed following Eq. (B.18) are correlated in the matrix

$$C_{ij}(t) \;=\; \langle 0|\, \hat{\Phi}^\dagger_i(t)\hat{\Phi}_j(0)\,|0\rangle \;\; . \tag{B.22}$$

The diagonal correlator $C_{ii}(t)$ contains informations about the mass of the $i^{\rm th}$ state of the spectrum in the channel R.

On a finite lattice with periodic boundary conditions, the correlator has also contributions from propagation backward in time. When the correlation distance (in time) is large, these contributions cannot be neglected.Therefore we fit the correlator with

$$C_{ii}(t) \;=\; A\big[e^{-mt} + e^{-m(L_t-t)}\big] \;, \tag{B.23}$$

where various regions $[t_{min}, \ldots, t_{max}]$ are fitted and the best χ^2 fit is chosen. Clearly, the multiplicative constant A is also fitted and it corresponds to the overlap $|c_n|^2$ in Eq (B.7) and Eq (B.9).

B.4 Constructing glueball operators

We have shown how to extract the spectrum of a lattice gauge theory for correlators of certain operators. Now we are going to explain how this operators are chosen and what properties they should have in order to create glueball states from the vacuum of the theory. We begin reviewing the symmetry group of a simple cubic lattice and then we show how to explicitly construct glueball operators.

B.4.1 Cubic group rotations

Zero–momentum glueball states on a simple cubic lattice fall into the irreducible representations of the rotations of the cube, combined with parity transformations and charge conjugation. If we take an operator, which is a gauge–invariant product of link variables around a closed contour, we can say that it creates a glueball state with the same symmetries of the closed contour. We will make this point clearer in the following section, describing how to create closed paths that transform under the irreducible representations of the cubic group. First we describe these irreducible representations and their relations with the representations of the continuum rotation group.

The cubic group O is the symmetry group of a cubic polyhedron and it is also called the *octahedral point group*. It contains only pure rotations: each element can be written as a rotation around a uniquely defined axis. The rotations are discrete. If the cube is brought into coincidence with itself after a rotation through an angle $\varphi = 2\pi/n$ (n integer), we say that the rotation axis in a *n–fold* axis. If $n = 1$, we have coincidence after rotations through 2π, which is the identity transformation denoted by E. All other rotation through $2\pi/n$ are denote by C_n, and successive rotations by C_n^2, C_n^3, etc...

There are four 3–fold axis (space diagonals), three 4–fold axis (joining centers of opposite faces), and six 2–fold axis (joining midpoints of opposite edges) in the cube. This is sketched in Fig. B.4. In the group there are 24 elements which are further divided in 5 different equivalence classes. Two elements a and b of a group G are equivalent if $b = gaa^{-1}$ for a $g \in G$, and are in the same equivalence class also called *conjugacy class*.

O is divided into conjugacy classes

$$O: \qquad E; \quad C_2(6); \quad C_3, C_3^2(8); \quad C_4, C_4^3(6); \quad C_4^2(3); \tag{B.24}$$

where we show the number of elements in each class. The number of conjugacy classes is equal to the number of irreducible representations and therefore the cubic group O has 5 irreducible representations. They are called A_1, A_2, E, T_1 and T_2. Moreover the dimension of these representations satisfies the following relation

$$\sum_\mu n_\mu^2 \;=\; \dim(G)\;, \tag{B.25}$$

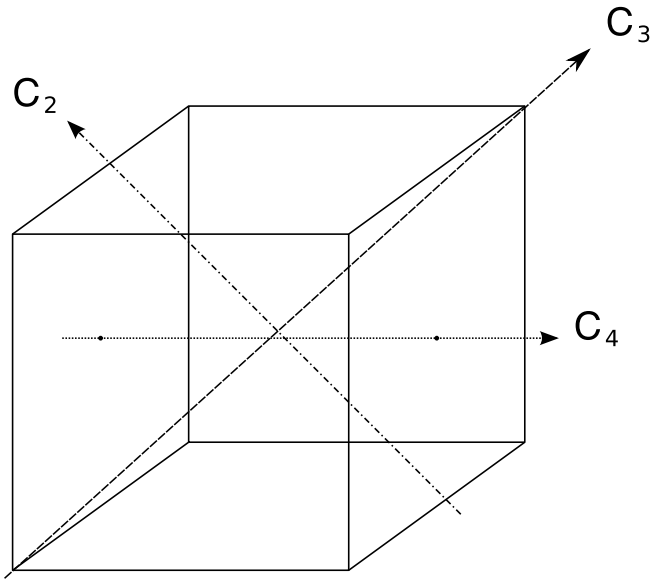

Figure B.4 *Symmetry axis of the cube.*

where $dim(G)$ is the order of the finite group G and n_μ is the dimension of each irreducible representation μ (the sum runs over all μ's). This gives us the dimensions of the irreducible representations: 1, 1, 2, 3, 3 respectively for A_1, A_2, E, T_1 and T_2. The usual way to represent the relation between the conjugacy classes and the irreducible representations is the table of characters shown in Tab. B.1.

	E	$C_2(6)$	$C_3(8)$	$C_4(6)$	$C_4^2(3)$
A_1	1	1	1	1	1
A_2	1	-1	1	-1	1
E	2	0	-1	0	2
T_1	3	-1	0	1	-1
T_2	3	1	0	-1	-1

Table B.1 *Character table of the cubic group O. The character of a conjugacy class is invariant inside the class because it is the trace of the matrix associated to the class elements in each representation.*

Glueball states on the lattice transform under irreducible representations of O, but continuum glueball states must be irreducible representations of SO(3). The aim is to obtain the continuum spectrum making the continuum limit of the discrete one. Therefore we need to know how the irreducible representations of SO(3) are decomposed in terms of those of O. We are interested in single–valued representations of the continuum rotation group, identified by an integer number J, the spin of the particle. Each representation J has a degeneracy of $2J + 1$

(its dimension). On the lattice this degeneracy is split into terms belonging to irreducible representations of O: for example, the spin 2 representation has 5 polarisations in the continuum which split into the E and T_2 (respectively 2 and 3 dimensional) irreducible representations. The irreducible representations of spin J in SO(3) restricted to O are called *subduced representations* $J \downarrow O$ and are reducible in O. The decomposition of the subduced representations $J \downarrow O$ is shown in Tab. B.2.

J	A_1	A_2	E	T_1	T_2
0	1	0	0	0	0
1	0	0	0	1	0
2	0	0	1	0	1
3	0	1	0	1	1
4	1	0	1	1	1

Table B.2 *Subduced representations $J \downarrow O$ of the cubic group up to $J = 4$. In the table we give the multiplicities with which the irreducible representations of O can be found in the subduced representation for each J.*

It is possible to reconstruct the continuum spectrum from the masses extracted on the lattice by matching the patterns of degeneracies observed in each level. For example, if the same mass (within the errors) is present in the irreducible representations A_2, T_1 and T_2, then it corresponds to the mass of a spin $J = 3$ particle in the continuum.

So far, we have neglected parity and charge conjugation transformations. However it is easy to include them in the discussion above. Including parity means adding reflections to the cubic point group. This is easily done by taking the direct product of O with $\mathcal{C}_i$, the group of order 2 containing the identity and the inversion with respect to the origin of the axis. The full group is then $O_h = O \times \mathcal{C}_i$: it contains 48 elements, which are combinations of pure rotations and reflections, divided in 10 classes. The group $\mathcal{C}_i$ has 2 irreducible representations which we can identify with the parity eigenvalues $P = \pm 1$. The irreducible representations of O_h are obtained directly from those of O using the character table in Tab. B.1: there are 10 irreducible representations, labelled by $A_1^{\pm}$, $A_2^{\pm}$, $E^{\pm}$, $T_1^{\pm}$ and $T_2^{\pm}$.

Adding charge conjugation in the same way brings us to a total of 20 irreducible representations of the group O_h^C (or O^{PC}). In each of these channels we can extract the mass of the lowest–lying state, usually denoted as R^{PC}, where $R \in$

$\{A_1, A_2, E, T_1, T_2\}$, $P \in \{+1, -1\}$ and $C \in \{+1, -1\}$.

B.4.2 Operators for glueball states

The single–trace operator that we use to project onto glueball states is simply defined as

$$\mathcal{O}(t) \;=\; \phi(t) \;, \tag{B.26}$$

where $\phi(t)$ is a zero-momentum operator given by the wall average over the temporal slice t:

$$\phi(t) \;=\; \frac{1}{L_s^3} \sum_x \phi(x,t) \qquad \phi(x,t) = \mathrm{Tr} \prod_{(i;\hat{\mu})\in\mathcal{C}} U_\mu(i) \;, \tag{B.27}$$

where L_s is the spatial size of the lattice and $\mathcal{C}$ a closed spatial Wilson loop.

In the following, we denote our operators simply as paths $\mathcal{P}$ because that is the relevant structure to understand their symmetry properties. Let us follow the notation in [184], where a path $\mathcal{P}$ of length L is represented by a L–tuple

$$(\hat{f}_1, \hat{f}_2, \ldots, \hat{f}_L) \;, \tag{B.28}$$

with the constraint given by the fact that the path is closed $\sum_{i=1}^{L} \hat{f}_i = 0$.

The vectors $\hat{f}_i$ are $\pm\hat{e}_j$, the unit vectors corresponding to the spacelike coordinates of the lattice. Given a path $\mathcal{P}$, it is independent of the point where it starts, as long as the orientation is preserved; hence we can construct equivalence classes in which paths are equivalent if we make a ciclic permutation of the $\hat{f}_i$. The equivalence class of $(\hat{f}_1, \hat{f}_2, \ldots, \hat{f}_L)$ is denoted by $[\hat{f}_1, \hat{f}_2, \ldots, \hat{f}_L]$.

Obtaining the operator with the desired charge conjugation C symmetry is easy in this case, because on link variables the conjugation operation is equivalent to reverse the orientation of the link :

$$C\,[\hat{f}_1, \hat{f}_2, \ldots, \hat{f}_L] \;=\; [-\hat{f}_L, -\hat{f}_{L-1}, \ldots, -\hat{f}_1] \;. \tag{B.29}$$

A path with defined charge $C = \pm 1$ is defined by the combination

$$[\hat{f}_1, \hat{f}_2, \ldots, \hat{f}_L]_\pm \;=\; \frac{[\hat{f}_1, \hat{f}_2, \ldots, \hat{f}_L] \pm [-\hat{f}_L, -\hat{f}_{L-1}, \ldots, -\hat{f}_1]}{2} \;. \tag{B.30}$$

This amounts in taking only the real part of the trace in Eq. (B.27) for a $C = +1$ operator and only the imaginary part for a $C = -1$ operator. Therefore, we just need to find oriented paths which transforms under the 10 irreducible representations of O_h.

The parity operation applied on a path reverts every link $\hat{f}_i$, because it is equivalent to an inversion with respect to the starting point of the path. Thus we can write

$$P\,[\hat{f}_1, \hat{f}_2, \ldots, \hat{f}_L] \;=\; [-\hat{f}_1, -\hat{f}_2, \ldots, -\hat{f}_L]\;, \tag{B.31}$$

and paths with defined parity $P = \pm 1$ are

$$[\hat{f}_1, \hat{f}_2, \ldots, \hat{f}_L]^{\pm} \;=\; \frac{[\hat{f}_1, \hat{f}_2, \ldots, \hat{f}_L] \pm [-\hat{f}_1, -\hat{f}_2, \ldots, -\hat{f}_L]}{2}\;. \tag{B.32}$$

Our aim is to find paths which transforms in the 5 irreducible representations of O (A_1, A_2, E, T_1, T_2).

Let us define how a given element of the symmetry group O, i.e. a rotation $\mathcal{R}$, acts on a given path. Since the path is a collection of elementary spacelike unit vectors, the operation of rotation on the path is defined by the action on each of the vectors:

$$M_{\mathcal{R}}(\mathcal{P}) \;=\; [\mathcal{R}(\hat{f}_1), \mathcal{R}(\hat{f}_2), \ldots, \mathcal{R}(\hat{f}_L)]\;, \tag{B.33}$$

where $\mathcal{R}$ on the right hand side of the equation stands for an operator in a 3 dimensional vector representation (we use the same symbol for the operator and for its representation), whereas on the left had side we have the same operator in an arbitrary representation M.

The standard way to construct a representation of a group, is to choose any function on which the elements of the group can act as operators, and then apply all the operators of the group to this function. If the transformed functions are linearly independent, they form a basis for a representation with dimension equal to the order of the group. In our case, the function is replaced by a path, and the transformed paths are given by Eq. (B.33) for each rotation.

$M_{\mathcal{R}}(\mathcal{P})$ is linearly independent only if the path $\mathcal{P}$ has no symmetries at all under the cubic group. This is the point where we start to construct all the irreducible representations of the cubic group; after that we will be able to construct an orthonormal basis of each representation starting from any path $\mathcal{P}$.

Let us start with the path

$$\mathcal{P}_{base} \;=\; [\hat{e}_1, \hat{e}_2, \hat{e}_3] \;, \tag{B.34}$$

which is not left invariant by any rotation $\mathcal{R}$. The 24 rotated paths $\mathcal{P}_{\mathcal{R}} = M_{\mathcal{R}}(\mathcal{P}_{base})$ are an orthonormal basis for a 24 dimensional representation M_{base}. This representation is fully decomposable and we want to find its irreducible content, in other words, the 5 irreducible representations. $\mathcal{P}_{\mathcal{R}}$ can be expressed as linear combinations of $n \leq 24$ other paths, the basis of a new representation of smaller dimension. The result is that there exists a unitary matrix A which change the initial basis into the new one and transforms the original representation in a new representation which has a $n \times n$ diagonal block in its matrix form (this block corresponds to the new basis of n paths):

$$M' \;=\; A^{-1} M_{base} A \;. \tag{B.35}$$

There is a general method used to decompose a representation of finite dimension and it is based on the Schur lemmas (which is related to the existence of the matrix A). In our case, it consists in turning the original 24×24 matrix representation M_{base} into its Jordan form, with blocks on the main diagonal, using matrices that commutes with M_{base}. In practice, we construct matrices C which commute with M_{base} using sum of matrices in the conjugacy classes of M_{base}, then we try to find a matrix A which diagonalizes them, or better, that turns them into their Jordan form $C_{Jord} = A^{-1} C A$. As a result, M_{base} gets decomposed using Eq. (B.35). We need to stress that with this method we are able to Jordanize matrices of all conjugacy classes at the same time. To find the fully reduced form of M_{base}, we need to iterate this procedure: after 3 iterations using matrices C_i coming from 3 different conjugacy classes, we get a M''' matrix with 5 blocks on its diagonal, corresponding to the invariant subspaces of the 5 irreducible representations of O:

$$M''' \;=\; A_3^{-1} A_2^{-1} A_1^{-1} M_{base} A_1 A_2 A_3 \;, \tag{B.36}$$

where the A_i comes from the 3 Jordanization of matrices C_i.

Using the matrix $\bar{A} = A_1 A_2 A_3$ we can change the original 24–dimensional basis made of $\mathcal{P}_{base}$, in a new set of paths which is subdivided into 5 more subsets forming the basis of each of the invariant subspaces of the irreducible

representations. We take the vectors

$$\mathcal{P}_{irr} \;=\; \bar{A} \cdot \mathcal{P}_{base} \;, \tag{B.37}$$

which are the base paths of the 5 irreducible representations of the cubic group O. Following our method just discussed we are able to reproduce the table given in [191], which prescribes how to create an orthonormal basis of each irreducible representation R starting from an arbitrary path. The table is given by the 24 $\mathcal{P}_{irr}$ vectors, taken as a 24×24 matrix (remember that $\mathcal{P}_{base}$ are 24 vectors in a 24 dimensional space): they form the projection table $Pr(R, \mathcal{R})$.

To conclude this section we show how we can find a set of basic operators in each R^{PC} channel to be used in the variational method described in Sec. B.3. We start from a set of prototypical paths $\mathcal{P}^i$ of different shapes with length varying from 4 lattice spacings up to 10 lattice spacings. Some of them are shown in Fig. B.5.

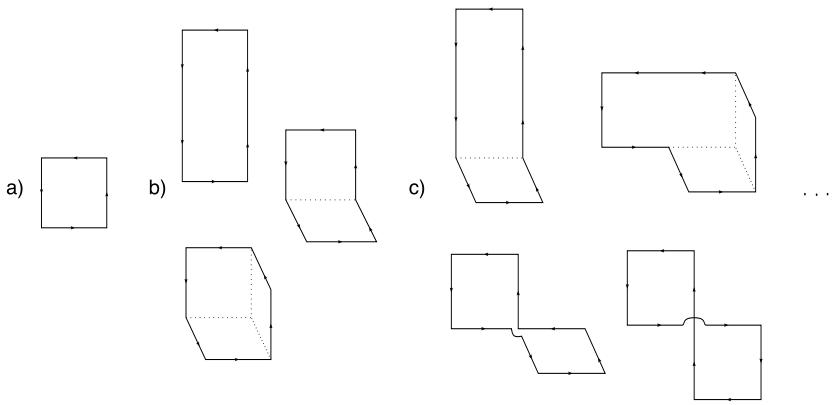

Figure B.5 *Set of basic prototypical path used to construct operators in all the* 20 R^{PC} *symmetry channels. The path in (a) in the only possible one of length* 4*a; in (b) there are the* 3 *possible path of length* 6*a; in (c) we show* 4 *of the* 21 *paths of length* 8*a. Their projections on each symmetry channel is used to construct basis operators for the variational method.*

From each of them, we define a basis for the irreducible representation R using the projection table $Pr(R, \mathcal{R})$ by means of

$$\mathcal{P}^i_R \;=\; \sum_{\mathcal{R}} Pr(R, \mathcal{R}) M_{\mathcal{R}}(\mathcal{P}^i) \;, \tag{B.38}$$

where $\mathcal{P}^i_R$ are linear combinations of rotated paths ($M_{\mathcal{R}}(\mathcal{P}^i)$ is defined in Eq (B.33)), weighted by coefficients in the projection table.

However, the $\mathcal{P}^i_R$ obtained are not linearly independent in general because, for every R, we have in $Pr(R,\mathcal{R})$ a number of $\mathcal{R}$ equal to the square of the dimension of the representation; we then try to identify only a subset of $\mathcal{P}^i_R$ which are actually different from one another and we perform the parity and charge conjugation operations as defined in Eq. (B.32) and Eq. (B.30). This leaves us with a full range of combinations of paths $\mathcal{P}^i_{R^{PC}}$ in each of the R^{PC} channels, from which we can construct operators

$$\Phi^{R^{PC}} \;=\; \sum_{c\in\mathcal{P}^i_{R^{PC}}} \mathrm{Tr}\prod_{l\in c} U(l)\;. \tag{B.39}$$

The sum in the previous expression means that an operator $\phi^{R^{PC}}$ is created from a single combination in $\mathcal{P}^i_{R^{PC}}$, but, since this combination is made up summing paths c with appropriate coefficients, we should sum the traces around the paths c using exactly those coefficients. Therefore we can use a more compact notation

$$\Phi^{(R)}(t) \;=\; \sum_i c_i^{(R)}\mathcal{R}_i(\bar{\mathcal{O}}(t))\;, \tag{B.40}$$

where, for any given gauge–invariant and vacuum subtracted operator $\bar{\mathcal{O}}$ on the lattice, we define a rotation transformation as $\mathcal{R}_i(\bar{\mathcal{O}})$ where the index i labels all the 24 elements of the group O_h^C, and the coefficients c_i are exactly the elements of $Pr(R,\mathcal{R})$ corresponding to the rotation $\mathcal{R}_i$ in the irreps R.

The full procedure described above is implemented in a Mathematica code which is capable of creating the source code to measure any operator in any irreducible representation R^{PC}, starting from a string defining the prototypical path $\mathcal{P}$. This versatility allows the user to forget about the actual implementation of the operators. As a results, more and more operators can be included in the variational analysis without additional effort, limited only by computational resources needed to measure and store the matrix $\tilde{C}_{\alpha\beta}(t)$.

B.4.3 Multi–state operators

At finite volume, the single–particle glueball spectrum receives non–negligible corrections from multi–glueball states. The energy of these states has a definite scaling with the volume of the lattice and they are usually identified by comparing the spectrum of the theory on increasingly large volumes. Moreover, one can

estimate the lowest energy of two–glueball state in the limit where all interactions are neglected:

$$E \approx \sqrt{|\vec{p}|^2 + m_1^2} + \sqrt{|\vec{p}|^2 + m_2^2} \,, \tag{B.41}$$

where glueballs of rest mass m_1 and m_2 with opposite momentum $\vec{p}$ are considered.

Our approach is to explicitly construct gauge–invariant lattice operators with a non–negligible overlap on these scattering states. Hence, by including these multi–state operators in the variational analysis described in previous sections, we expect to identify their presence in the spectrum without the need of a finite–size study.

An operator that projects onto scattering states of two glueballs is a double–trace operator. We take it to be of the form

$$\mathcal{O}(t) = (\phi(t) - \langle\phi(t)\rangle)^2 \,, \tag{B.42}$$

where $\phi(t)$ is a zero–momentum operator defined as in Eq. (B.27).

The operator appearing in the correlator matrix for the scattering states can be written using Eq. (B.40) as

$$\begin{aligned}\Phi^{(R)}(t) &= \sum_i c_i^{(R)} \mathcal{R}_i \Big((\phi(t) - \langle\phi(t)\rangle)^2 \Big) - \sum_i c_i^{(R)} \mathcal{R}_i \Big(\big\langle (\phi(t) - \langle\phi(t)\rangle)^2 \big\rangle \Big) \\ &\equiv \sum_i c_i^{(R)} \mathcal{R}_i \left((\phi(t) - \langle\phi(t)\rangle)^2 \right) - \left(\langle\phi^2(t)\rangle - \langle\phi(t)\rangle^2 \right) \sum_i c_i^{(R)} \,.\end{aligned} \tag{B.43}$$

The last term vanishes for $R \neq A_1^{++}$ due to the symmetries of the coefficients $c_i^{(R)}$, but the local subtraction of $\langle\phi(t)\rangle$ in the first term will appear in all the representations and is crucial in order to obtain the correct two–point function, even though $\langle\phi(t)\rangle$ alone, once appropriately symmetrised, would be different from zero only in the A_1^{++} channel.

B.4.4 Bi–torelon excitations

When the lattice system is closed with periodic boundary conditions, topological excitations wrapping the compact directions with the same quantum numbers of

glueballs appear. In the literature they are referred to as torelons and we have used them to extract the string tension in Sec. 2.4.2 and Sec. 3.5.1.

If not correctly accounted for, these states can affect significantly the measured glueball spectrum. The mass of a torelon state scales linearly with the lattice size L_s and the contribution of these states in the spectrum can be easily identified with a finite volume study. In order to control these spurious contributions, we can include in the variational set operators that best overlap with torelon states, in the same fashion as we did for scattering states.

Torelon excitations transform non–trivially under the centre of the gauge group, and are characterised by their charge under this transformation (n–ality). Since glueballs transform trivially under the centre of the gauge group, they can only couple to states that have zero n–ality, like a pair of torelons winding in opposite directions (bi–torelons).

We define bi–torelons operators from products of two Polyakov loops l_ν winding around opposite directions

$$\mathcal{O}(t) \;=\; \frac{1}{2L_s^2}\sum_{\mu\neq\nu}\sum_{x} l_\nu(x,t)l_\nu^\dagger(x+\hat{\mu}a,t)\;, \tag{B.44}$$

where the sum over μ runs on the spatial directions orthogonal to the one of the loops, and then the operator $\Phi^{(R)}(t)$ can be constructed as in the previous cases by using Eq. (B.40).

By choosing different shapes for the combination $l_\nu(x,t)l_\nu^\dagger(x+\hat{\mu}a,t)$, we can obtain a fairly large variational set in all the 20 symmetry channels R^{PC}. Some of the shapes are pictorially shown in Fig. B.6.

Figure B.6 *Paths used for the construction of operators coupling with bi–torelon states. Periodic boundary conditions apply at the edges represented by the dashed lines.*

Appendix C

The large–N glueball spectrum

This Appendix briefly describes the results of Ref. [71], where the glueball spectrum of a pure SU(N) Yang–Mills theory is extrapolated to $N \to \infty$ at fixed lattice spacing in the scaling limit. It is included as a concrete application of the techniques described in Appendix B. Specifically, we want to underline how contributions from scattering states and bi–torelons are identified thanks to the extended variational basis described in Sec. B.4.

The physics of large–N Yang–Mills theories is very interesting [192–196] and important for topics ranging from confinement in non–Abelian theories to the gauge–gravity correspondence. Many analytical predictions for observables in the $N \to \infty$ limit are available but need to be tested from ab initio non–perturbative calculations provided by lattice simulations.

C.1 Numerical simulations

We measure the glueball spectrum using an entirely conventional setup for the lattice discretisation of the SU(N) Yang–Mills theory. We use the Wilson plaquette action on isotropic and symmetric lattices $N_L^3 \times N_T$

$$S = \beta \sum_{i,\mu>\nu} \left(1 - \frac{1}{N} \mathrm{Re\ Tr\ } (U_{\mu\nu}(i)) \right) \ , \tag{C.1}$$

where $U_{\mu\nu}(i)$ is the parallel transport of the link variables along the elementary lattice plaquette stemming from point i and identified by the positive pair of

directions $(\hat{\mu}, \hat{\nu})$. The lattice gauge coupling constant β is defined as $\beta = 2N/g_0^2$, with g_0 the bare gauge coupling.

The large N limit is taken by simulating the action above for different number of colours $3 \leq N \leq 8$, at fixed lattice spacing a as N varies. The lattice spacing is chosen in the domain where the behaviour of the discretised theory is dominated by the physics in the continuum limit. For example, it correspond to $a \sim 0.12$ fm for the SU(3) theory.

In order to compare quantities at fixed lattice spacing across different SU(N) groups, we set the scale using the deconfinement temperature on a lattice with fixed temporal extent. This choice was successfully used in [197, 198]. We adopt the deconfinement temperature at $N_T = 6$ to fix the lattice spacing to the same value when changing N. The deconfinement temperature as a function of the number of colours has been recently studied in Ref. [138].

N	$\beta_c(N_T = 6)$	β	N_L	N_τ	N_{MC}	$N_{compound}$	N_{width}	N_{bins}	runs
3	5.8941(12)	5.8945	12	10k	100k	200	20	25	20
4	10.7893(23)	10.789	12	10k	100k	200	20	25	20
5	17.1068(30)	17.107	12	10k	100k	200	20	25	20
6	24.8458(33)	24.845	12	10k	100k	200	20	25	20
7	33.9995(37)	33.995	12	10k	65k	250	20	13	40
8	44.4960(30)	44.496	12	10k	100k	250	16	25	20

Table C.1 *Values of the critical couplings for the deconfinement temperature at $N_T = 6$ and parameters of the Monte Carlo simulations on lattices with N_L^4 points for $3 \leq N \leq 8$.*

The parameters used in the simulations are also summarised in Tab. C.1. A typical run has N_τ thermalisation sweeps after which we start measuring the correlators. A Monte Carlo step consists of a compound sweep in which one heat–bath update is followed by 4 over–relaxation sweeps. After the thermalisation process we perform N_{MC} sweeps. We chose to measure every $N_{compound}$ sweeps to reduce autocorrelation between the measures. The $N_{measures}$ measure sweeps are further divided in N_{bins} bins; each bin is an average over N_{width} measures. The total set of measures to be analysed is then $N_{bins} \times$ runs, where each run is independent of all the others.

C.2 Variational analysis

We consider operators that we classify, for definiteness, in three different groups:

G: single–glueball operators described in Sec. B.4.2

S: two–glueball scattering operators defined in Sec. B.4.3

T: bi–torelon operators described in Sec. B.4.4

Operators of these three types are included in the variational analysis (cfr. Sec. B.3) used to extract glueball masses. The number of operators of each type we construct in each symmetry channel R^{PC} is summarised in Tab. C.2 and Tab. C.3.

	$++$	$-+$	$+-$	$--$
A_1	8	2	1	3
A_2	3	1	3	3
E	22	7	7	14
T_1	19	24	48	27
T_2	44	33	33	29

Table C.2 *Number of different operators (G and S) calculated in each of the 20 symmetry channels R^{PC}. This number is to be multiplied by the number of blocking levels N_b to obtain the full variational basis.*

	$++$	$-+$	$+-$	$--$
A_1	2	1	0	0
A_2	1	0	1	1
E	7	3	3	3
T_1	3	3	14	9
T_2	9	9	8	3

Table C.3 *Number of different bi–torelon operators (T) calculated in each of the 20 symmetry channels R^{PC}. This number is to be multiplied by the number of blocking levels N_b to obtain the full variational basis.*

Since a calculation involving scattering states is much more demanding in terms of computer time, we use the results from the computation involving only single–particle and bi–torelon operators to target the channels where mixing with multi–particle states is expected to affect significantly the results. At large N, this is expected to happen for the excited states that are close to twice the energy of the ground state following Eq. (B.41). The channel in which scattering states can

potentially influence the measured spectrum in a relevant way is the A_1^{++}, where we can also extract several excitations. Therefore, we measure the three sets of operators G, S and T in the A_1 irreducible representation of the cubic symmetry group.

When all three types of operators are used, we proceed as follow. We decompose the operators obtained after the variational procedure Eq. (B.18) into their projections onto operators of type G, S and T:

$$\tilde{\Phi} = \alpha_G \Phi_G + \alpha_S \Phi_S + \alpha_T \Phi_T \ , \tag{C.2}$$

where Φ_G, Φ_S and Φ_T are normalised to unity.

This allows us to define how much each single group $X \in \{G, S, T\}$ contributes to the extracted state:

$$\mathrm{mix}_X = \frac{|\alpha_X|^2}{|\alpha_G|^2 + |\alpha_S|^2 + |\alpha_T|^2} \ . \tag{C.3}$$

Then we measure the full correlation matrix Eq. (B.16) and we analyse it in turn removing a selected set of operators, G, S or T. The mass spectrum obtained with different choices of variational basis is illustrated in Fig. C.1 for the A_1^{++} channel in SU(3). In the plot we also report the measured mix_X when it is larger than 50% for any subset other than G.

It is remarkable that, when only S and T operators are used, the lowest–lying state has a mass that is much higher than the mass of the ground state extracted with the full variational basis ($G + S + T$). Moreover, the latter appears always when single–particle operators are included in the calculation. This is an indication that our multi–glueball set of operators project only on scattering states, as it should be.

The scattering state seems to be slightly above the first excited single–glueball excitation. This feature carries over at any value of N. Another feature we notice is that the number of excitations we are able to extract depends on the subset of operators used. This is hardly surprising, given the variational nature of the procedure. Moreover, a scattering state also appear in the A_1^{-+} channel.

We performed an additional check of finite volume effects in the A_1^{++} channel studying SU(3) at $N_L = 18$, with the results illustrated in the right panel of

Fig. C.1. This test shows the expected result that bi–torelons overlap less to the lowest–lying spectrum when the volume is increased. In addition, the computed single–glueball mass spectrum in the A_1^{++} channel is compatible with the one measured for $N_L = 12$. This check indicates that finite–size corrections are negligible for $N_L = 12$.

When scattering operators are not included, we still check the contribution mix_T coming from bi–torelons. It turns out that our large variational set enables us to correctly disentangle single–particle states, which we keep for the large–N extrapolation, from scattering states and bi–torelon excitations. Moreover, the mixing coefficients give a measure of the contamination of the single–particle states from unwanted contributions.

We consider single–glueball states all the states with a projection onto the single–glueball operator sector G of 85% or larger and we disregard states with a projection of 20% or larger onto the T sector. Scattering states are identified as the states in the spectrum with a significant (30% or larger) projection onto the scattering sector that are degenerate in mass with the lowest–lying state in the $S + T$ basis, when the latter has the largest component in the scattering sector.

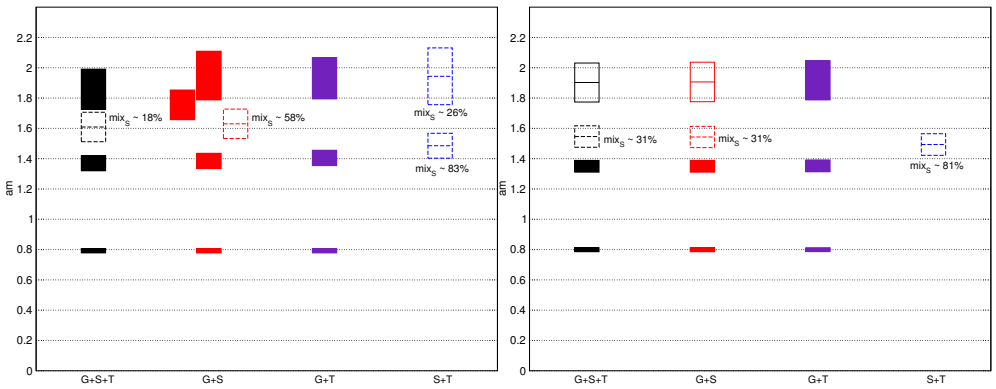

(a) *SU(3)* $N_L = 12$ **(b)** *SU(3)* $N_L = 18$

Figure C.1 *The plots show the* A_1^{++} *spectrum for the SU(3) theory obtained using different variational basis. The unfilled symbols represent masses that cannot be reliably interpreted as pure glueballs due to the high contamination of S and T operators. Bi–torelon contributions decrease with volume as expected.*

C.3 The large–N spectrum

The masses am_G of the extracted spectrum can be extrapolated to the large–N limit using the leading $1/N^2$ correction:

$$am_G(N) = am_G(\infty) + c/N^2 \ , \tag{C.4}$$

where c is a coefficient of order one which depends on the symmetry channel. This type of corrections is expected from general considerations in the planar limit [199, 200] when fermions are absent and Eq. (C.4) has been proven successful already in previous lattice calculations [69, 201].

We perform a similar extrapolation for the states extracted in our study and the results are summarised in Tab. C.4. In the table we also include the extrapolated masses of scattering states identified in the A_1^{++} and A_1^{-+} channels. For the former state, for which we have better control, the extrapolated value of the energy is compatible with twice the mass of the ground state. This agrees with the expectation that particles do not interact at large N. The energy of the A_1^{-+}(S) is slightly smaller than twice the mass of the corresponding ground state. This should probably be ascribed to the lack of control over the extrapolation to the large N limit, which had to rely only on two finite–N values.

Typical extrapolations are shown in Fig. C.2 and Fig. C.3. In the former we show the states which correspond to the continuum scalar and pseudoscalar glueballs (with positive charge), together with two excited states in the scalar channel. Here scattering states are discarded. The fits with Eq. (C.4) do perform very well for values of N down to $N = 3$ for most of the states in the spectrum.

In Fig. C.3, we also highlight the degeneracy between the states in the E^{++} channel and in the T_2^{++} channel. As already mentioned in Tab. B.2, a continuum spin $J = 2$ glueball would appear as a state in these two channels with the same mass. Even though we are not in the continuum limit, our lattice spacing is small enough that this degeneracy is preserved. Not only this is true for the ground state, but also for the first excited state and it is maintained in the $N = \infty$ limit as well.

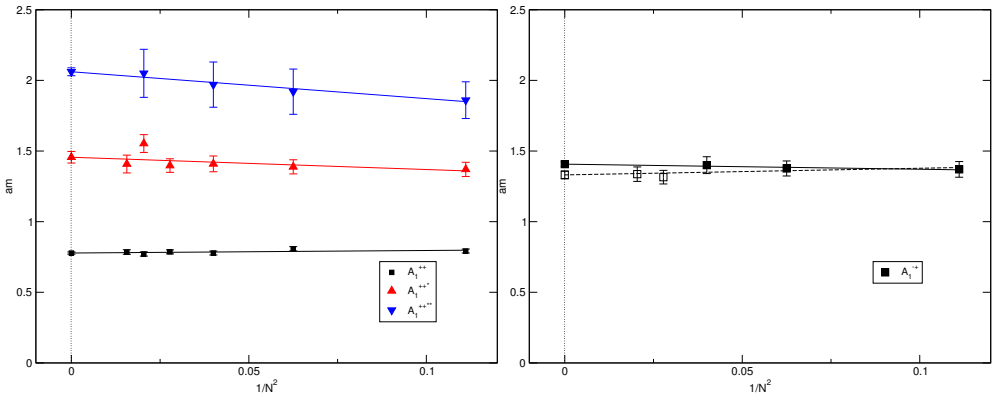

(a) A_1^{++} **(b)** A_1^{-+}

Figure C.2 *Scalar and pseudoscalar glueball masses extrapolated to $N = \infty$. The A_1^{++} channel also include the first two excited states. Less conservative fits (not included in Tab. C.4) are shown with open symbols and dashed lines.*

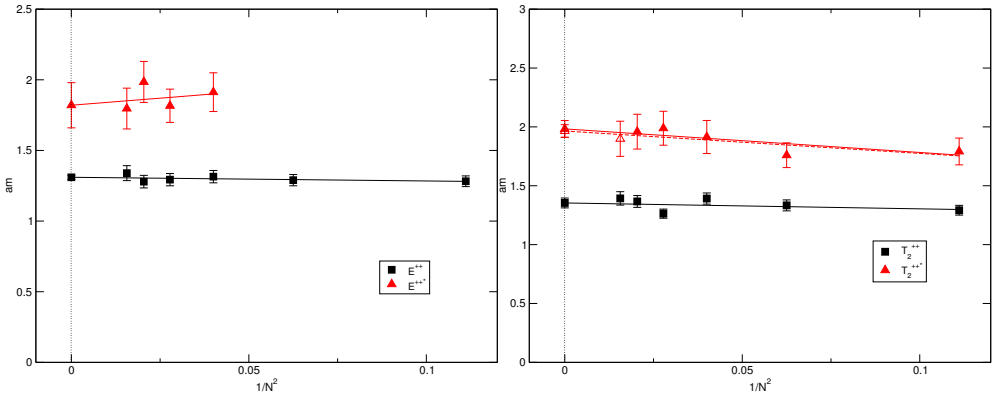

(a) E^{++} **(b)** T_2^{++}

Figure C.3 *Tensor glueball masses extrapolated to $N = \infty$. The masses in both channels are expected to be degenerate in the continuum limit and correspond to a $J = 2$ glueball. Less conservative fits (not included in Tab. C.4) are shown with open symbols and dashed lines.*

SU(∞)				
R^{PC}	$am(\sigma)$	c	range N	$\tilde{\chi}^2$
A_1^{++}	0.778(8)	0.18(0.15)	(3,4,5,6,7,8)	0.66
$A_1^{++\star}$	1.456(41)	-0.87(0.68)	(3,4,5,6,7,8)	1.08
$A_1^{++\star\star}$	2.061(28)	-1.9(0.4)	(3,4,5,7)	0.03
A_1^{++}(S)	1.578(47)	0.71(1.1)	(4,5,6,7)	0.17
A_1^{-+}	1.407(17)	-0.36(0.22)	(3,4,5)	0.04
A_1^{-+}(S)	2.33	3	(4,6)	–
A_2^{+-}	2.61(31)	-9(6)	(4,5,6)	0.29
A_2^{--}	2.25	1.4	(3,4)	–
E^{++}	1.310(15)	-0.26(0.24)	(3,4,5,6,7,8)	0.23
$E^{++\star}$	1.82(16)	2(6)	(5,6,7,8)	0.57
E^{+-}	2.714(86)	-1.2(1.2)	(3,5,6,7,8)	0.03
E^{-+}	1.830(35)	-1.8(0.6)	(3,4,5,6,7,8)	0.20
$E^{-+\star}$	2.589(37)	-1.5(0.6)	(3,5,6,7)	0.01
E^{+-}	2.714(86)	-1.2(1.2)	(3,5,6,7,8)	0.03
E^{--}	2.35(15)	-2(4)	(4,5,6,8)	0.18
T_1^{++}	2.310(80)	-2.5(1.2)	(3,4,5,6,7,8)	0.17
T_1^{+-}	1.659(19)	-0.4(0.3)	(3,4,5,6,7,8)	0.11
$T_1^{+-\star}$	1.840(55)	4(2)	(4,5,6,7,8)	0.11
T_1^{-+}	2.50(14)	-3(3)	(4,5,6,8)	0.06
T_2^{++}	1.354(42)	-0.5(0.7)	(3,4,5,6,7,8)	1.58
$T_2^{++\star}$	1.983(71)	-2(1)	(3,4,5,6,7)	0.38
T_2^{+-}	2.05	0.8	(6,8)	–
T_2^{-+}	1.812(38)	-1.5(0.6)	(3,4,5,6,7,8)	0.23
T_2^{--}	2.327(91)	-0.6(1.5)	(3,6,7,8)	0.15

Table C.4 *Spectrum of the SU(∞) lattice gauge theory. The masses, in units of lattice spacing, are obtained from fits over the range of N shown; also the fitted coefficient c of the $1/N^2$ correction is shown. The fits only include our most reliable glueball masses. The states with (S) are considered, by this study, two–glueball scattering states.*

C.4 Summary and outlook

We have studied numerically on the lattice the glueball spectrum in Yang-Mills SU(N) gauge theories in the large–N limit. Using an automated technique for constructing trial wave–functionals in all possible symmetry channels, we have built a large variational basis that has enabled us to obtain a large number of states, including some excitations. Moreover, the inclusion of functionals that best overlap with scattering and torelon states has allowed us to unambiguously exclude multi–particle states or finite–size artefacts from the spectrum of narrow resonances.

This is a significant advance in our understanding of the large N glueball spectrum from first principles. So far only a single SU(8) lattice calculation was available for the full spectrum [202], while studies of SU(∞) were mainly restricted to the scalar and tensor channel only [69, 201]. Our large–N extrapolation is shown in Fig. C.4 for all the channels in the spectrum.

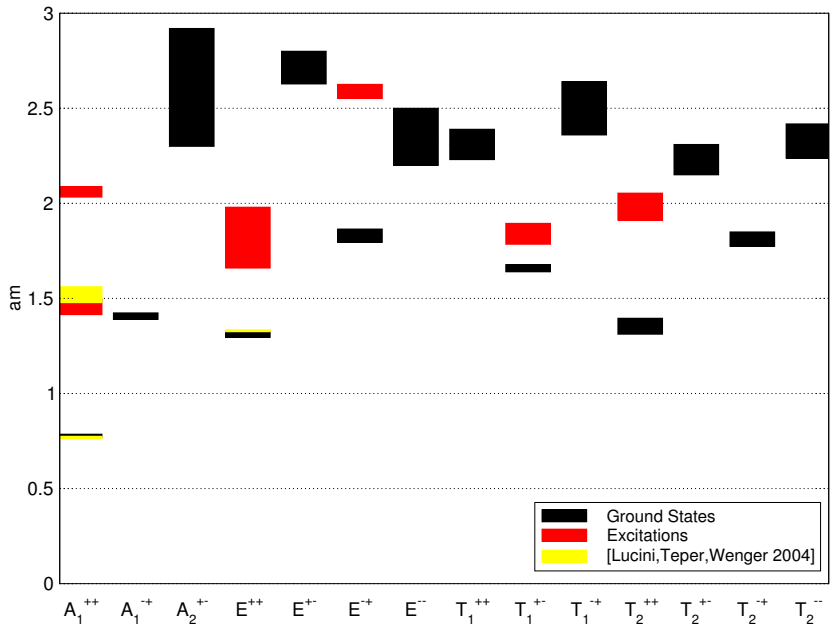

Figure C.4 *The spectrum at $N = \infty$. The yellow boxes represent the large–N extrapolation of masses obtained in Ref. [69].*

We are already pursuing an extension of this work that would allow us to reach the continuum limit in a controlled way. It is well known that the update algorithm we use has a low efficiency and develops slow modes the closer we get to the continuum limit [165]. New developments in this regard have been proposed [166].

Appendix D

Symmetries of lattice fermions: a brief overview

This appendix is not meant to be a detailed description of the different discretisations of Dirac fermions on the lattice. It is intended to complement the description of results given in Chapter 3, where staggered fermions are used in simulations, and Chapter 4 where domain wall fermions are introduced as well.

The following overview is necessarily based on material that can be found on many good lattice textbooks, e.g. Refs. [203–205].

D.1 Naive discretisation of Dirac fermions

The continuum Euclidean action for a single flavour of free Dirac fermion in four dimensions is

$$\mathcal{S}_{\text{cont}} \;=\; \int \mathrm{d}^4x \; \bar{\psi}(x)(\gamma_\mu \partial_\mu + m)\psi(x) \;, \tag{D.1}$$

where the Dirac matrices γ_μ satisfy the Euclidean anti-commutation relation $\{\gamma_\mu, \gamma_\nu\} = 2\delta_{\mu\nu}\mathbb{I}$ (and we can also introduce $\gamma_5 = \gamma_1\gamma_2\gamma_3\gamma_4$). The parameter m is the bare quark mass.

This is discretised on a lattice with lattice spacing a by doing the following replacements:

- $x_\mu \to a n_\mu$ with integer components vector n_μ in a four–dimensional volume

Λ

- $\int \mathrm{d}^4x \to a^4 \sum_{n_\mu \in \Lambda}$
- $\partial_\mu \psi(x) \to \frac{\psi(n+\hat{\mu}) - \psi(n-\hat{\mu})}{2a}$ where we choose the simplest symmetric difference and $\hat{\mu}$ is the versor in the μ direction.

We end up with the naive single–flavour lattice action

$$\mathcal{S}_{\text{latt}} \;=\; a^4 \sum_{n_\mu \in \Lambda} \bar{\psi}(n) \left(\sum_{\mu=1}^{4} \gamma_\mu \frac{\psi(n+\hat{\mu}) - \psi(n-\hat{\mu})}{2a} + m\psi(n) \right) \;. \tag{D.2}$$

It is possible to include gauge interactions in Eq. (D.2) by discretising the continuum covariant derivative D_μ and using link variables $U_\mu(n)$ as lattice gauge fields. Let us skip the details of this derivation and write down the interacting action on the lattice as

$$\mathcal{S}_{\text{latt}}[U] \;=\; a^4 \sum_{n_\mu \in \Lambda} \bar{\psi}(n) \left(\sum_{\mu=1}^{4} \gamma_\mu \frac{U_\mu(n)\psi(n+\hat{\mu}) - U_\mu^\dagger(n)\psi(n-\hat{\mu})}{2a} + m\psi(n) \right) \;. \tag{D.3}$$

It follows that the QCD action for N_f Dirac fermions naively discretised on the lattice is

$$\begin{aligned} \mathcal{S}_{\text{QCD}} \;=\; & a^4 \sum_{f=1}^{N_f} \sum_{n_\mu \in \Lambda} \left(\bar{\psi}^{(f)}(n) \sum_{\mu=1}^{4} \gamma_\mu \frac{U_\mu(n)\psi^{(f)}(n+\hat{\mu}) - U_\mu^\dagger(n)\psi^{(f)}(n-\hat{\mu})}{2a} \right) \\ & + a^4 \sum_{f=1}^{N_f} \sum_{n_\mu \in \Lambda} m^{(f)} \; \bar{\psi}^{(f)}(n)\psi^{(f)}(n) \;, \end{aligned} \tag{D.4}$$

where each flavour f is clearly independent, since weak interactions are not included in the action. We are also neglecting the pure gauge part of the QCD action in Eq. (D.4), but it will not affect the following discussion.

We want to stress the important point that different discretisations are possible as long as they reproduce the continuum Eq. (D.1) in the limit $a \to 0$. For example we will see that higher dimensional terms can be added to the single–flavour action Eq. (D.2), that are suppressed by powers of the cutoff $\Lambda_{\text{UV}} = a^{-1}$, hence are irrelevant towards the continuum limit.

D.1.1 Shift symmetry and the doublers

Let us now explore some of the symmetries of free fermions on the lattice that are relevant for our discussion. For simplicity, we start from Eq. (D.2) which does not include gauge interactions (free field $U_\mu = \mathbb{I}$).

We focus on the spinor structure of the action and we note that it is encoded in the gamma matrices γ_μ, responsible for mixing spinor components. It is possible to show that similar representations of γ_μ exist such that the action is left invariant:

$$V_p(n)\gamma_\mu V_p^{-1}(n \pm \hat{\mu}) \;=\; \gamma_\mu \;, \tag{D.5}$$

where p is the lattice momentum vector at the corners of the Brillouin zone: $p_\mu = \zeta_\mu \pi/a$, and $\zeta_\mu \in \{0, 1\}$. The exact form of $V_p(n)$ is quite complicated

$$V_p(n) \equiv \prod_\rho (\gamma_5 \gamma_\rho)^{\zeta_\rho} exp(in \cdot p) \;, \tag{D.6}$$

but it can be shown that this transformation in momentum space corresponds to a shift in the momenta by p.

Therefore, if we apply the transformation above to the fermion fields

$$\psi(n) \to V_p(n)\psi(n) \;, \tag{D.7}$$

and

$$\bar{\psi}(n) \to \bar{\psi}(n)V_p^{-1}(n) \;, \tag{D.8}$$

we can show that the action is invariant due to the relation in Eq. (D.5). Since there exists a transformation V_p for each of the 16 corners of the Brillouin zone, there are 16 equivalent *tastes* of fermions even if we have started with a single fermion field. In other words, the action Eq. (D.2) does not represent a single particle, but 16 equivalent fermion modes. These modes are also called "doublers" and must be removed somehow, since they are not present in the continuum and are a consequence of the symmetries of the lattice action.

The presence of doublers has very profound implications that can be all traced back to the famous No Go theorem by Nielsen and Ninomiya [206]. The theorem states that doublers will always appear in a lattice discretisation of Eq. (D.1) which respects the usual hermiticity, locality and translational invariance requirements, if chiral symmetry has to be preserved at zero fermion

mass. Moreover, doubler are intimately related to the cancellation of the chiral anomaly on the lattice.

D.1.2 Lifting the doublers

The first proposal carried forward by Wilson to remove the unwanted doublers was the addition of an irrelevant term $\mathcal{O}(a)$ proportional to the Laplacian $\partial_\mu \partial_\mu$. Explicitely, the lattice action with the inclusion of this Wilson term reads

$$\begin{aligned} \mathcal{S}_{\text{Wilson}} \;=\; & a^4 \sum_{n_\mu \in \Lambda} \sum_{\mu=1}^{4} \left(\bar{\psi}(n) \gamma_\mu \frac{1}{2a} (\psi(n+\hat{\mu}) - \psi(n-\hat{\mu})) \right) \\ & - a^4 \sum_{n_\mu \in \Lambda} \sum_{\mu=1}^{4} \left(\bar{\psi}(n) \frac{r}{2a} (\psi(n+\hat{\mu}) - 2\psi(n) + \psi(n-\hat{\mu})) \right) \\ & + a^4 \sum_{n_\mu \in \Lambda} m \bar{\psi}(n) \psi(n) \;, \end{aligned} \tag{D.9}$$

where r is usually set to unity and gauge fields can be added as explained above.

As can be seen by the structure of the added term, the doubling symmetry of the previous section is explicitely broken. As a consequence, all doublers disappear from the spectrum. With this action one can work out the spectrum of the fermionic modes and realise that all but the zero mode remains unchanged: all modes corresponding to a non–zero p are lifted by a mass term $\sim 2r/a$ which separates them from the physical low–energy spectrum when the continuum limit is taken. The No Go theorem is not avoided though. In fact, the Wilson term explicitely breaks chiral symmetry on the lattice, even at zero fermion mass.

D.2 Staggered fermions

In this section we exploit the symmetry introduced in Sec. D.1.1 to partially remove the number of different *tastes* of fermions present in the naive action Eq. (D.2). Moreover, we will see that this particular formulation of fermions also retain a subgroup of chiral symmetry. The first work done on staggered fermions is due to Kogut and Susskind [207]. The main idea is to rearrange the spinor and space–time index of the fermion field $\psi_\alpha(n)$ such that the 16 degrees of freedom we saw emerging in Sec. D.1.1 are distributed in a unit hypercube on the lattice.

Moreover, they can be reduced by making the fermion action spin–diagonal as we describe in the following.

Let us start by defining the following transormation that mixes spin and space–time indices:

$$\Omega(n) \equiv \gamma_1^{n_1}\gamma_2^{n_2}\gamma_3^{n_3}\gamma_4^{n_4} \ , \tag{D.10}$$

where we used the previously defined Euclidean gamma matrices and the component of the lattice coordinate vector n_μ. This so called staggered transorfmation has the property that can eliminate the gamma matrices, since

$$\Omega(n)\gamma_\mu\Omega^\dagger(n+\hat{\mu}) \ = \ (-1)^{n_1+n_2+\cdots+n_{\mu-1}} \ = \ \eta_\mu(n) \ . \tag{D.11}$$

The space–time dependent function $\eta_\mu(n)$ replaces the gamma matrices and it is obviously diagonal in spinor space.

Therefore, by transforming the fields

$$\psi(n) \to \Omega(n)\psi(n) \qquad \bar{\psi}(n) \to \bar{\psi}(n)\Omega^\dagger(n) \ , \tag{D.12}$$

we reduce the action to a spin–diagonal form and we can decide to keep only a single spinor component field $\chi(n)$

$$\mathcal{S}_{\text{stagg}} \ = \ a^4 \sum_{n_\mu\in\Lambda}\sum_{\mu=1}^{4}\eta_\mu(n)\frac{\bar{\chi}(n)\chi(n+\hat{\mu}) - \bar{\chi}(n)\chi(n-\hat{\mu})}{2a} + m\bar{\chi}(n)\chi(n) \ . \tag{D.13}$$

We have reduced the 16 degrees of freedom of the four–component spinor field $\psi(n)$ by a factor of four: this is achieved by a non–trivial change of variables which makes the spinor components of the transformed field interact independently from each other. In other words, we can now interpret the 16 doublers in the one–component staggered action Eq. (D.13) as four tastes of a four–component fermion field $\psi(n)$.

To make this one last step, we need a second change of variables, from the spin–diagonal basis to the so called spin–taste basis. The fermionic degrees of freedom $\chi(n)$ at the corners of a unit hypercube are combined together to form a full Dirac spinor with a taste quantum number

$$\psi_\alpha^{(t)}(h) \equiv q(h)_{\alpha t} = \frac{1}{8}\sum_\zeta \Omega(\zeta)_{\alpha t}\chi(2h+\zeta) \ , \tag{D.14}$$

where h is a vector labelling the hypercube instead of a single site ($n = 2h + \zeta$), t labels the taste and α the Dirac index. We have also explicitely written out the 4×4 stucture of the Ω matrix which mixes spin and taste indices.

Without entering in too much details, suffices to say that the resulting staggered action, written in terms of Dirac fermions $\psi_\alpha^{(t)}(h)$ on a lattice with a lattice spacing $b = 2a$ (due to the hypercubic structure), is

$$\begin{aligned} \mathcal{S}_{\text{stagg}} &= b^4 \sum_{h,t} \left(\sum_\mu \bar{\psi}_\alpha^{(t)}(h)(\gamma_\mu)_{\alpha\beta} \Delta_\mu \psi_\beta^{(t)}(h) + m \bar{\psi}_\alpha^{(t)}(h) \psi_\alpha^{(t)}(h) \right) \\ &\quad + b^4 \sum_h \left(-\frac{b}{2} \sum_{t,t'} \sum_\mu \bar{\psi}_\alpha^{(t)}(h)(\gamma_\mu)_{\alpha\beta} (\xi_5 \xi_\mu)_{t,t'} \Box_\mu \psi_\beta^{(t)}(h) \right) \ . \end{aligned} \tag{D.15}$$

In the equation above we have highlighted the spin and taste structure of each term in the action. Moreover, we have introduced finite derivatives on the blocked lattice with $b = 2a$, namely Δ_μ corresponding to the discretised ∂_μ and $\Box_\mu$ corresponding to the discretised $\partial_\mu \partial_\mu$. The matrices acting in taste space are $\xi_\mu = \gamma_\mu^T$ and $\xi_5 = \gamma_5$.

The term in the second line of Eq. (D.15) is due to the spin–taste transformation in Eq. (D.14) and its space–time structure strongly resembles the one of the Wilson term in Eq. (D.9). We can rewrite the staggered action in a more compact and useful way by hiding the spin–taste structure in a tensor product form, introducing

$$\gamma_\mu \otimes \mathbb{I} = (\gamma_\mu)_{\alpha\beta} (\mathbb{I})_{t,t'} \qquad \gamma_\mu \otimes \xi_5 \xi_\mu = (\gamma_\mu)_{\alpha\beta} (\xi_5 \xi_\mu)_{t,t'} \ , \tag{D.16}$$

where the first matrix of the product acts on the Dirac spin space and the second one on the taste space. We obtain

$$\begin{aligned} \mathcal{S}_{\text{stagg}} &= b^4 \sum_h \left(\sum_\mu \bar{\psi}(h)(\gamma_\mu \otimes \mathbb{I}) \Delta_\mu \psi(h) + m(\mathbb{I} \otimes \mathbb{I}) \bar{\psi}(h) \psi(h) \right) \\ &\quad + b^4 \sum_h \left(-\frac{b}{2} \sum_\mu \bar{\psi}(h)(\gamma_\mu \otimes \xi_5 \xi_\mu) \Box_\mu \psi(h) \right) \ . \end{aligned} \tag{D.17}$$

In Sec. 3.3 we introduced three species of staggered fermions in order to simulate $N_f = 12$ QCD. This is basically done by using a lattice action with three independent pieces of the form Eq. (D.17). Each piece describes four tastes, which

can be interpreted as four independent flavours in the continuum limit, where the taste–breaking term ($\gamma_\mu \otimes \xi_5 \xi_\mu$) vanishes due to its higher dimensionality. Hence the full theory describes 12 flavours of quarks, each with a continuum action as in Eq. (D.1).

The interacting theory ($U_\mu \neq 1$) is more complicated and taste–exchange effects are introduced due to scattering of quarks with highly virtual gluons (with momentum of the cutoff order). By reducing the presence of highly energetic gluons at the cutoff scale, one can reduce taste–breaking effects at fixed lattice spacing. This is the main goal of the improvement program which brought to variant of the staggered action called *asqtad* and *HISQ*. Both have been used in simulations reported in this thesis and imply a different smearing scheme of the gauge fields in the action. We refer the interested reader to the literature: Ref. [149] for the asqtad action and Ref. [121] for the HISQ action.

D.2.1 Remnant of chiral symmetry

One of the main advantages of the staggered formalism with respect to the Wilson treatment of the doubling problem is chiral symmetry. The chiral symmetry of the continuum fermion action at zero mass

$$\psi(n) \to e^{i\theta\gamma_5}\psi(n) \qquad \bar{\psi}(n) \to \bar{\psi}(n)e^{i\theta\gamma_5} \ , \tag{D.18}$$

is broken explicitely by the Wilson term at finite lattice spacing. The dimension five taste–breaking term in the staggered action instead, allows for a remnant of chiral symmetry to be present. Namely, the action in Eq. (D.17) is invariant under

$$\psi(n) \to e^{i\theta\gamma_5\otimes\xi_5}\psi(n) \qquad \bar{\psi}(n) \to \bar{\psi}(n)e^{i\theta\gamma_5\otimes\xi_5} \ . \tag{D.19}$$

This $U(1)_A$ symmetry group may be identified with a subgroup of the $\mathrm{SU}(4)_A$ axial group of the four tastes of staggered fermions. Since it is a remnant of the continuum chiral symmetry, it reduces additive quark mass renormalization which is one of the great disadvantages of Wilson fermions. Moreover, it produces the correct spectrum of chiral Goldstone bosons and it is therefore particularly suitable for the study of light quark physics.

D.3 Domain wall fermions

There is an additional lattice fermion formulation which has good chiral properties and has been used in this thesis. It is due to Kaplan [208] and it is generally referred to as domain wall fermions. It is quite different from the Wilson or staggered fermion formulations in the sense that it deals with five–dimensional Dirac fermions in order to obtain a low–energy four–dimensional theory of chiral fermions on the lattice, which is also free of doublers.

D.3.1 Ginsparg–Wilson relation

Before starting with the description of the domain wall fermion action, we must explain how the No Go theorem [206] is evaded by this lattice fermion formulation.

Chiral symmetry in the continuum (Eq. (D.18)) can be concisely summarised by the anti–commutation of γ_5 with the Dirac operator D

$$D\gamma_5 + \gamma_5 D \;=\; 0 \;, \tag{D.20}$$

and this is the type of relation implicitely assumed in Ref. [206] among the hypotheses of the No Go theorem. By replacing this relation with a different definition of chiral transformations, it is possible to regularise fermions on the lattice in such a way that they have both chiral properties and no doublers.

A modified chiral rotation was firstly introduced by Ginsparg and Wilson [209] who proposed

$$D\gamma_5 + \gamma_5 D \;=\; aD\gamma_5 D \;. \tag{D.21}$$

The anti–commutation relation is altered by a higher–dimensional term which vanishes in the continuum limit $a \to 0$ to recover Eq. (D.20), but at the same time allows for chiral symmetry to be defined at finite lattice spacing a. In fact, the added term only induces a contact term in the anti–commutator of the fermion propagator with γ_5, implying that chiral symmetry is violated only at zero distances.

The chiral trasformations that are allowed on the lattice take the form [210]

$$\psi(n) \to e^{i\theta\gamma_5\left(\mathbb{I}-\frac{a}{2}D\right)}\psi(n) \qquad \bar{\psi}(n) \to \bar{\psi}(n)e^{i\theta\left(\mathbb{I}-\frac{a}{2}D\right)\gamma_5} \;, \tag{D.22}$$

where the introduction of the Dirac operator makes the chiral properties dependent on gauge fields in the interacting case.

Unfortunately, it is difficult to solve the non–linear equation Eq. (D.21) and find a definite form for D. In the next sections we describe a Dirac operator which was obtained independently and then proved to satisfy the Ginsparg–Wilson relation.

D.3.2 Introducing the extra dimension

By considering fermions in five infinite dimensions we can write the continuum Dirac operator

$$D_5(x,s) \;=\; \gamma_\mu \partial_\mu + \gamma_5 \partial_5 - m(s) \;, \tag{D.23}$$

where s is the extra $\hat{5}$ coordinate. The fermion fields would now depend on this extra coordinate as well: $\Psi(x,s)$.

The introduction of a s–dependent mass term with the following properties

$$m(s) \;=\; \theta(s) m_f \;, \tag{D.24}$$

generates a massless solution on the domain wall at $s = 0$, which separates the regions of positive and negative masses. Such a massless solution needs to satisfy the Dirac equation in the remaining four directions, namely $D_5 \Psi = \gamma_\mu \partial_\mu \Psi = 0$, and can be shown to take the form

$$\Psi(x,s)_\pm \;=\; e^{i p_\mu x^\mu} u_\pm \phi(s)_\pm \;. \tag{D.25}$$

Hence they are a combination of a four–dimensional massless chiral fermion $e^{i p_\mu x^\mu} u_\pm$, with $\gamma_5 u_\pm = \pm u_\pm$, and an exponentially decaying function in the extra dimension

$$\phi(s)_\pm \;=\; e^{\mp \int_0^s m(\tau) d\tau} \;, \tag{D.26}$$

which solves the Dirac–like equation

$$\big[\pm \partial_5 + m(s) \big] \phi(s)_\pm \;=\; 0 \;. \tag{D.27}$$

What we have shown so far is that the described set up in Eq. (D.23) gives rise to a single normalised solution $\Psi(x,s)_-$, which describes a chiral fermion travelling along the domain wall at $s = 0$ and bound to it in such a way that it decays

exponentially with increasing distance s from the wall. Although this seems a successfull way of creating a chiral fermion in four dimensions, when the above set up is discretised on a five–dimensional lattice, it is still affected by the presence of doublers which have to be lifted as described in Sec. D.1.2.

D.3.3 The lattice action for domain wall fermions

On a lattice with finite extra dimension of length L_s and periodic boundary conditions we would see two chiral fermions with the form in Eq. (D.25) and opposite chirality; one of them would be bound to the $s = 0$ wall, or boundary, and due to periodic conditions, the second one would appear at $s = L_s - 1$. If we modify the boundary conditions by avoiding connecting the $s = L_s - 1$ site with the $s = L_s = 0$ site, then we reach a configuration where nothing exists for $s < 0$ or $s > L_s - 1$ and the two chiral fermions only overlap in the middle region with exponentially suppressed tails.

The lattice version of the five–dimensional Dirac operator in Eq. (D.23) mirrors the one of the Wilson formalism. On the lattice with sites labelled by pairs (n, s), denoting the coordinate in the four dimensions with n and in the extra dimension with s, we have the free action (setting $a = 1$ and suppressing spin–color indices)

$$\mathcal{S}_{\rm DWF} \;=\; \sum_{n,m\in\Lambda}\sum_{s,r=0}^{L_s-1} \bar{\Psi}(n,s) D_{\rm DWF}(n,s|m,r)\Psi(m,r) \;. \tag{D.28}$$

The discretised domain wall Dirac operator $D_{\rm DWF}(n,s|m,r) = \delta_{s,r} D_{\rm Wilson}(n|m) + \delta_{n,m} D_5(s|r)$ will depend on two mass parameters, M_5 and m_f. The first, M_5, is the mass appearing in the Wilson–type Dirac operator $D_{\rm Wilson}(n|m)$ connecting sites in the four dimensions and diagonal in the extra–dimensional site indices:

$$D_{\rm Wilson}(n|m) \;=\; (4 - M_5)\delta_{n,m} - \frac{1}{2}\sum_{\mu}(\mathbb{I} - \gamma_\mu)\delta_{n+\hat{\mu},m} \;. \tag{D.29}$$

The second, m_f, represents the mass parameter for the four–dimensional fermions on the domain wall and appears in the extra–dimensional term $D_5(s|r)$:

$$\begin{aligned} D_5(s|r) \;&= \delta_{s,r} - (1 - \delta_{s,L_s-1})P_-\delta_{s+1,r} - (1 - \delta_{s,0})P_+\delta_{s-1,r} \\ &\quad + m_f\big(P_-\delta_{s,L_s-1}\delta_{0,r} + P_+\delta_{s,0}\delta_{L_s-1,r}\big) \;, \end{aligned} \tag{D.30}$$

where $P_\pm = (1 \pm \gamma_5)/2$ are the chiral projectors with Dirac structure.

By looking carefully at the expression Eq. (D.30) we can understand that setting $m_f = 0$ is equivalent to fixing the boundary conditions in s for the fermions, due to terms like $(1 - \delta_{s,L_s-1})$ and $(1 - \delta_{s,0})$ preventing hopping between $s = 0$ and $s = L_s - 1$, as already mentioned at the beginning of this section. If m_f is not zero then it parametrizes the interaction between the modes on the two boundaries in such a way that we can define our four–dimensional fermionic fields as

$$\begin{aligned} q(n) &= P_- \Psi(n, 0) + P_+ \Psi(n, L_s - 1) \\ \bar{q}(n) &= \bar{\Psi}(n, L_s - 1) P_- + \bar{\Psi}(n, 0) P_+ \ . \end{aligned} \tag{D.31}$$

These fermionic fields $q(n)$ and $\bar{q}(n)$ are defined in four dimensions and are constructed from opposite chirality fermions living on the two boundaries of the five–dimensional system.

To construct the interacting theory, gauge links $U_\mu(n)$ can be added to the opeator Eq. (D.29) in the usual gauge–covariant way and then replicated equally for all $s = 0, 1, \ldots, L_s - 1$ keeping $U_5(n) = 1$ since the different layers do not interact.

In conclusion, domain wall fermions defined in five dimensions reproduce chiral fermions in four dimensions when $m_f = 0$ and $L_s = \infty$. Chirally–violating effects are suppressed exponentially in L_s and further depends on M_5 which can be optimally tuned to reduce them.

D.3.4 Residual mass and conserved currents

In the effective four–dimensional theory we can define the following Ward–Takahashi identity

$$\Delta_\mu \left\langle \mathcal{A}^a_\mu(n) O(m) \right\rangle \ = \ 2 m_f \left\langle J^a_5(n) O(m) \right\rangle + 2 \left\langle J^a_{5q}(n) O(m) \right\rangle + \text{contactterm} \ , \tag{D.32}$$

where the partially conserved axial current $\mathcal{A}^a_\mu(n)$ of flavour a is constructed from the five–dimensional conserved vector current

$$\begin{aligned} j^a_\mu(n, s) = \frac{1}{2} \Big[& \bar{\Psi}(n + \mu, s)(1 + \gamma_\mu) U^\dagger_\mu(n + \mu) t^a \Psi(n, s) \\ & - \bar{\Psi}(n, s)(1 - \gamma_\mu) U_\mu(n) t^a \Psi(n + \mu, s) \Big] \ , \end{aligned} \tag{D.33}$$

as

$$\mathcal{A}^a_\mu(n) \ = \ \sum_{s=0}^{L_s - 1} \text{sign}(s - L_s/2 + 1/2) j^a_\mu(n, s) \ . \tag{D.34}$$

The four–dimensional currents $J_5^a(n)$ and $J_{5q}^a(n)$ are defined from the fifth component of $j_\mu^a(n)$, $j_5^a(n,s)$. The second term on the RHS of Eq. (D.32) survives in the chiral limit $m_f = 0$ and breaks chiral symmetry. This term contains the mid–point current $J_{5q}^a(n) = j_5^a(n, L_s/2-1)$ which is zero in the $L_s = \infty$ case since the fermions on the boundary do not interact. On the other hand, the first term, proportional to the fermion mass breaks chiral symmetry explicitely and contains the current at the boundary $J_5^a(n) = j_5^a(n, L_s)$. By using Eq. (D.31) and the full expression of $j_5^a(n, L_s)$, we notice that the $J_5^a(n)$ current is just a four–dimensional pseudoscalar current $\bar{q}(n)\gamma_5 t^a q(n)$.

We can combine both terms on the RHS of Eq. (D.32) in an effective mass term $m' = m + m_{\rm res}$ by requiring

$$J_{5q}^a(n) = m_{\rm res} J_5^a(n) \tag{D.35}$$

and therefore use $m_{\rm res}$ to quantify the amount of chiral symmetry breaking in this formulation.

A practical quantity to look at on the lattice is the ratio

$$R(t) = \frac{\sum_{\vec{x},\vec{y}} \left\langle J_{5q}^a(\vec{x},t) J_5^a(\vec{y},0) \right\rangle}{\sum_{\vec{x},\vec{y}} \left\langle J_5^a(\vec{x},t) J_5^a(\vec{y},0) \right\rangle} \ , \tag{D.36}$$

which would equal a constant in some intermediate time region if Eq. (D.35) holds. Such constant value is used to define $m_{\rm res}$. We note that at small t the numerator and denominator of Eq. (D.36) contains excited states contaminations and a plateau to a constant value is only reached for $t > t_{\rm min}$.

D.3.5 Shamir vs. Möbius formulation

Different prescriptions exist to discretise the five–dimensional Dirac operator that enters in Eq. (D.28). Some of them offer the advantage of having small violations to chiral symmetry at a significantly reduced computational cost. In fact, one would like to reach the chiral properties which exist at $L_s = \infty$ for modest values of $L_s \sim O(10)$. In the following we give two examples that have been used in Chapter 4, the Shamir and the Möbius operators.

As we have anticipated, chiral symmetry at finite lattice spacing is achieved in the four–dimensional effective theory because the domain wall Dirac operator

$D_{\mathrm{DWF}}(M_5, m_f)$ at $L_s = \infty$ is shown to be equivalent to the so–called "overlap" Dirac operator $D_{\mathrm{overlap}}(m)$ [211–213]. It is the Ginsparg–Wilson relation Eq. (D.21) satisfied by $D_{\mathrm{overlap}}(m = 0)$ which evades the No Go theorem.

The overlap operator can be written as

$$D_{\mathrm{overlap}}(m) \;=\; \frac{1+m}{2} + \frac{1-m}{2}\gamma_5 \epsilon[H] \;, \tag{D.37}$$

where all indices are suppresses and the sign function $\epsilon(x)$ contains a kernel H which can be simply chosen to be $H = \gamma_5 D_{\mathrm{wilson}}(M_5)$ using the definition in Eq. (D.29).

Different kernels can provide better chiral properties and here we introduce the Shamir kernel [214] $H = \gamma_5 D_{\mathrm{shamir}}(M_5)$ with

$$D_{\mathrm{shamir}}(M_5) \;=\; \frac{a_5 D_{\mathrm{wilson}}(M_5)}{2 + a_5 D_{\mathrm{wilson}}(M_5)} \;, \tag{D.38}$$

and the Möbius kernel [215] $H = \gamma_5 D_{\mathrm{mobius}}(M_5)$

$$D_{\mathrm{mobius}}(M_5) \;=\; \frac{(b_5 + c_5) D_{\mathrm{wilson}}(M_5)}{2 + (b_5 - c_5) D_{\mathrm{wilson}}(M_5)} \equiv \alpha D_{\mathrm{shamir}}(M_5) \;. \tag{D.39}$$

As explained in Ref. [216], the scale factor α in Eq. (D.39) corresponds to getting almost the same chiral symmetry violations of D_{shamir} with L_s by using D_{mobius} at L_s/α. We refer to the original paper for a more detailed explanation of this approximate relation.

Bibliography

[1] Luigi Del Debbio, Richard D. Kenway, Eliana Lambrou, and Enrico Rinaldi. The transition to a layered phase in the anisotropic five-dimensional SU(2) Yang-Mills theory. *Physics Letters B*, 724:133–137, July 2013.

[2] Shinji Ejiri, Jisuke Kubo, and Michika Murata. A study on the nonperturbative existence of Yang-Mills theories with large extra dimensions. *Phys. Rev.*, D62:105025, 2000. doi: 10.1103/PhysRevD.62.105025.

[3] Peter W. Higgs. Broken symmetries, massless particles and gauge fields. *Phys.Lett.*, 12:132–133, 1964. doi: 10.1016/0031-9163(64)91136-9.

[4] F. Englert and R. Brout. Broken Symmetry and the Mass of Gauge Vector Mesons. *Phys.Rev.Lett.*, 13:321–323, 1964. doi: 10.1103/PhysRevLett.13.321.

[5] G.S. Guralnik, C.R. Hagen, and T.W.B. Kibble. Global Conservation Laws and Massless Particles. *Phys.Rev.Lett.*, 13:585–587, 1964. doi: 10.1103/PhysRevLett.13.585.

[6] CMS. Observation of a new boson at a mass of 125 GeV with the CMS experiment at the LHC. *Phys.Lett.*, B716:30–61, 2012. doi: 10.1016/j.physletb.2012.08.021.

[7] ATLAS. Observation of a new particle in the search for the Standard Model Higgs boson with the ATLAS detector at the LHC. *Phys.Lett.*, B716:1–29, 2012. doi: 10.1016/j.physletb.2012.08.020.

[8] C.S. Lim. The Higgs Particle and Higher-Dimensional Theories. 2013.

[9] Christopher T. Hill and Elizabeth H. Simmons. Strong dynamics and electroweak symmetry breaking. *Phys.Rept.*, 381:235–402, 2003. doi: 10.1016/S0370-1573(03)00140-6.

[10] Francesco Sannino. Higgs Discovery: Impact on Composite Dynamics [Thinking Fast and Slow]. 2013.

[11] A. Lenz, U. Nierste, J. Charles, S. Descotes-Genon, H. Lacker, et al. Constraints on new physics in $B - \bar{B}$ mixing in the light of recent LHCb data. *Phys.Rev.*, D86:033008, 2012. doi: 10.1103/PhysRevD.86.033008.

[12] R Aaij et al. First observation of CP violation in the decays of B_s^0 mesons. *Phys.Rev.Lett.*, 110:221601, 2013. doi: 10.1103/PhysRevLett.110.221601.

[13] R Aaij et al. Measurement of the $B_s^0 \to \mu^+\mu^-$ branching fraction and search for $B^0 \to \mu^+\mu^-$ decays at the LHCb experiment. 2013.

[14] John L. Cardy. Scaling and renormalization in statistical physics. 1996.

[15] Wolfgang Ochs. The Status of Glueballs. *J. Phys. G*, 40(4):043001, 2013.

[16] Giuseppe Degrassi, Stefano Di Vita, Joan Elias-Miro, Jose R. Espinosa, Gian F. Giudice, et al. Higgs mass and vacuum stability in the Standard Model at NNLO. *JHEP*, 1208:098, 2012. doi: 10.1007/JHEP08(2012)098.

[17] Nicola Cabibbo. Unitary Symmetry and Leptonic Decays. *Phys.Rev.Lett.*, 10:531–533, 1963. doi: 10.1103/PhysRevLett.10.531.

[18] Makoto Kobayashi and Toshihide Maskawa. CP Violation in the Renormalizable Theory of Weak Interaction. *Prog.Theor.Phys.*, 49:652–657, 1973. doi: 10.1143/PTP.49.652.

[19] Kaustubh Agashe, Gilad Perez, and Amarjit Soni. Flavor structure of warped extra dimension models. *Phys.Rev.*, D71:016002, 2005. doi: 10.1103/PhysRevD.71.016002.

[20] Martin Bauer, Raoul Malm, and Matthias Neubert. A Solution to the Flavor Problem of Warped Extra-Dimension Models. *Phys.Rev.Lett.*, 108: 081603, 2012. doi: 10.1103/PhysRevLett.108.081603.

[21] S.L. Glashow, J. Iliopoulos, and L. Maiani. Weak Interactions with Lepton-Hadron Symmetry. *Phys.Rev.*, D2:1285–1292, 1970. doi: 10.1103/PhysRevD.2.1285.

[22] Ulrich Nierste. B Mixing in the Standard Model and Beyond. 2012.

[23] Theodor Kaluza. On the Problem of Unity in Physics. *Sitzungsber.Preuss.Akad.Wiss.Berlin (Math.Phys.)*, 1921:966–972, 1921.

[24] O. Klein. Quantum Theory and Five-Dimensional Theory of Relativity. (In German and English). *Z.Phys.*, 37:895–906, 1926. doi: 10.1007/BF01397481,10.1007/BF01397481.

[25] Keith R. Dienes, Emilian Dudas, and Tony Gherghetta. Grand unification at intermediate mass scales through extra dimensions. *Nucl. Phys.*, B537: 47–108, 1999. doi: 10.1016/S0550-3213(98)00669-5.

[26] Lisa Randall and Raman Sundrum. A Large mass hierarchy from a small extra dimension. *Phys.Rev.Lett.*, 83:3370–3373, 1999. doi: 10.1103/PhysRevLett.83.3370.

[27] N.S. Manton. A New Six-Dimensional Approach to the Weinberg-Salam Model. *Nucl.Phys.*, B158:141, 1979. doi: 10.1016/0550-3213(79)90192-5.

[28] Yutaka Hosotani. Dynamical Mass Generation by Compact Extra Dimensions. *Phys. Lett.*, B126:309, 1983. doi: 10.1016/0370-2693(83)90170-3.

[29] Yutaka Hosotani. Gauge-Higgs Unification Approach. *AIP Conf.Proc.*, 1467:208–213, 2012. doi: 10.1063/1.4742101.

[30] Ilia Gogoladze, Nobuchika Okada, and Qaisar Shafi. 125 GeV Higgs Boson From Gauge-Higgs Unification: A Snowmass white paper. 2013.

[31] Ilia Gogoladze, Nobuchika Okada, and Qaisar Shafi. Higgs boson mass from gauge-Higgs unification. *Phys.Lett.*, B655:257–260, 2007. doi: 10.1016/j.physletb.2007.08.082.

[32] Hisaki Hatanaka, Takeo Inami, and C. S. Lim. The gauge hierarchy problem and higher dimensional gauge theories. *Mod. Phys. Lett.*, A13:2601–2612, 1998. doi: 10.1142/S021773239800276X.

[33] Hsin-Chia Cheng, Konstantin T. Matchev, and Martin Schmaltz. Radiative corrections to Kaluza-Klein masses. *Phys. Rev.*, D66:036005, 2002. doi: 10.1103/PhysRevD.66.036005.

[34] Luigi Del Debbio, Eoin Kerrane, and Rodolfo Russo. Mass corrections in string theory and lattice field theory. *Phys. Rev.*, D80:025003, 2009. doi: 10.1103/PhysRevD.80.025003.

[35] Leonard Susskind. Dynamics of Spontaneous Symmetry Breaking in the Weinberg-Salam Theory. *Phys.Rev.*, D20:2619–2625, 1979. doi: 10.1103/PhysRevD.20.2619.

[36] Steven Weinberg. Implications of Dynamical Symmetry Breaking: An Addendum. *Phys.Rev.*, D19:1277–1280, 1979. doi: 10.1103/PhysRevD.19.1277.

[37] Edward Farhi and Leonard Susskind. Technicolor. *Phys.Rept.*, 74:277, 1981. doi: 10.1016/0370-1573(81)90173-3.

[38] Savas Dimopoulos and Leonard Susskind. Mass Without Scalars. *Nucl.Phys.*, B155:237–252, 1979. doi: 10.1016/0550-3213(79)90364-X.

[39] Estia Eichten and Kenneth D. Lane. Dynamical Breaking of Weak Interaction Symmetries. *Phys.Lett.*, B90:125–130, 1980. doi: 10.1016/0370-2693(80)90065-9.

[40] Liam Keegan. *Dynamical Electroweak Symmetry Breaking on the Lattice*. PhD thesis, University of Edinburgh, May 2011.

[41] Bob Holdom. Techniodor. *Phys.Lett.*, B150:301, 1985. doi: 10.1016/0370-2693(85)91015-9.

[42] Masako Bando, Ken-iti Matumoto, and Koichi Yamawaki. TECHNIDILATON. *Phys.Lett.*, B178:308, 1986. doi: 10.1016/0370-2693(86)91516-9.

[43] Koichi Yamawaki, Masako Bando, and Ken-iti Matumoto. Scale Invariant Technicolor Model and a Technidilaton. *Phys.Rev.Lett.*, 56:1335, 1986. doi: 10.1103/PhysRevLett.56.1335.

[44] V.A. Miransky and Koichi Yamawaki. Conformal phase transition in gauge theories. *Phys.Rev.*, D55:5051–5066, 1997. doi: 10.1103/PhysRevD.56.3768,10.1103/PhysRevD.55.5051.

[45] Koichi Yamawaki. Composite Avenue beyond the Standard Model - Legacy of Sakata in LHC Era. *Prog.Theor.Phys.Suppl.*, 197:76–91, 2012. doi: 10.1143/PTPS.197.76.

[46] Shinya Matsuzaki and Koichi Yamawaki. Discovering 125 GeV technidilaton at LHC. *Phys.Rev.*, D86:035025, 2012. doi: 10.1103/PhysRevD.86.035025.

[47] Shinya Matsuzaki and Koichi Yamawaki. Holographic techni-dilaton at 125 GeV. *Phys.Rev.*, D86:115004, 2012. doi: 10.1103/PhysRevD.86.115004.

[48] Zoltan Fodor, Kieran Holland, Julius Kuti, Daniel Nogradi, Chris Schroeder, et al. Can the nearly conformal sextet gauge model hide the Higgs impostor? *Phys.Lett.*, B718:657–666, 2012. doi: 10.1016/j.physletb.2012.10.079.

[49] Yasumichi Aoki, Tatsumi Aoyama, Masafumi Kurachi, Toshihide Maskawa, Kei-ichi Nagai, Hiroshi Ohki, Akihiro Shibata, Koichi Yamawaki, and Takeshi Yamazaki. Walking signals in Nf=8 QCD on the lattice. 2013.

[50] Laurent Lellouch. Flavor physics and lattice quantum chromodynamics. pages 629–698, 2011.

[51] HFAG working group. Heavy flavor averaging group, June 2012. URL `http://www.slac.stanford.edu/xorg/hfag/`.

[52] Ulrich Nierste. Flavour and CP Violation. *J.Phys.Conf.Ser.*, 447:012017, 2013. doi: 10.1088/1742-6596/447/1/012017.

[53] FLAG working group. Review of lattice results concerning low energy particle physics, July 2013. URL `http://itpwiki.unibe.ch/flag`.

[54] Luigi Del Debbio and Enrico Rinaldi. Scalar mass corrections from compact extra dimensions on the lattice. *PoS*, LATTICE2011:086, 2011.

[55] Enrico Rinaldi, Luigi Del Debbio, and Alistair Hart. Light scalar spectrum in extra-dimensional gauge theories. *PoS*, LATTICE2012:038, 2012.

[56] Luigi Del Debbio, Alistair Hart, and Enrico Rinaldi. Light scalars in strongly-coupled extra-dimensional theories. *JHEP*, 1207:178, 2012. doi: 10.1007/JHEP07(2012)178.

[57] Shinji Ejiri, Shouji Fujimoto, and Jisuke Kubo. Scaling laws and effective dimension in lattice SU(2) Yang-Mills theory with a compactified extra dimension. *Phys.Rev.*, D66:036002, 2002. doi: 10.1103/PhysRevD.66.036002.

[58] A. Kurkela, Ph. de Forcrand, and M. Panero. Dimensional reduction and the phase diagram of 5d Yang-Mills theory. *PoS*, LAT2009:050, 2009.

[59] Philippe de Forcrand, Aleksi Kurkela, and Marco Panero. The phase diagram of Yang-Mills theory with a compact extra dimension. *JHEP*, 06:050, 2010. doi: 10.1007/JHEP06(2010)050.

[60] Francesco Knechtli, Nikos Irges, and Antonio Rago. Dimensional reduction and confinement from five dimensions. *PoS*, LATTICE2010:059, 2010.

[61] Francesco Knechtli, Magdalena Luz, and Antonio Rago. On the phase structure of five-dimensional SU(2) gauge theories with anisotropic couplings. *Nucl.Phys.*, B856:74–94, 2012. doi: 10.1016/j.nuclphysb.2011.11.001.

[62] S. Chandrasekharan and U. J. Wiese. Quantum link models: A discrete approach to gauge theories. *Nucl. Phys.*, B492:455–474, 1997. doi: 10.1016/S0550-3213(97)00006-0.

[63] R. Brower, S. Chandrasekharan, and U.J. Wiese. QCD as a quantum link model. *Phys.Rev.*, D60:094502, 1999. doi: 10.1103/PhysRevD.60.094502.

[64] Michael Creutz. Confinement and the Critical Dimensionality of Space-Time. *Phys. Rev. Lett.*, 43:553–556, 1979. doi: 10.1103/PhysRevLett.43.553.

[65] M.E.J. Newman and G.T. Barkema. *Monte Carlo Methods in Statistical Physics*. Oxford University Press, 2001.

[66] Benjamin Svetitsky and Laurence G. Yaffe. Critical Behavior at Finite Temperature Confinement Transitions. *Nucl.Phys.*, B210:423, 1982. doi: 10.1016/0550-3213(82)90172-9.

[67] K. Farakos and S. Vrentzos. Exploration of the phase diagram of 5d anisotropic SU(2) gauge theory. *Nucl.Phys.*, B862:633–649, 2012.

[68] P. de Forcrand, G. Schierholz, H. Schneider, and M. Teper. The String and Its Tension in SU(3) Lattice Gauge Theory: Towards Definitive Results. *Phys.Lett.*, B160:137, 1985. doi: 10.1016/0370-2693(85)91480-7.

[69] Biagio Lucini, Michael Teper, and Urs Wenger. Glueballs and k-strings in SU(N) gauge theories: Calculations with improved operators. *JHEP*, 06: 012, 2004.

[70] Nikos Irges and Francesco Knechtli. Lattice Gauge Theory Approach to Spontaneous Symmetry Breaking from an Extra Dimension. *Nucl. Phys.*, B775:283–311, 2007. doi: 10.1016/j.nuclphysb.2007.01.023.

[71] Biagio Lucini, Antonio Rago, and Enrico Rinaldi. Glueball masses in the large N limit. *JHEP*, 1008:119, 2010. doi: 10.1007/JHEP08(2010)119.

[72] Colin J. Morningstar and Mike J. Peardon. The glueball spectrum from an anisotropic lattice study. *Phys. Rev.*, D60:034509, 1999. doi: 10.1103/PhysRevD.60.034509.

[73] E. Gregory, A. Irving, B. Lucini, C. McNeile, A. Rago, Chris M. Richards, and E. Rinaldi. Towards the glueball spectrum from unquenched lattice QCD. *JHEP*, 1210:170, 2012. doi: 10.1007/JHEP10(2012)170.

[74] A.D Kennedy and B.J. Pendleton. Improved heatbath method for Monte Carlo calculations in lattice gauge theories. *Phys.Lett.*, B156:393–399, 1985. doi: 10.1016/0370-2693(85)91632-6.

[75] V.A. Miransky. Dynamics in the conformal window in QCD like theories. *Phys.Rev.*, D59:105003, 1999. doi: 10.1103/PhysRevD.59.105003.

[76] L. Del Debbio, B. Lucini, A. Patella, C. Pica, and A. Rago. Conformal versus confining scenario in SU(2) with adjoint fermions. *Phys.Rev.*, D80: 074507, 2009. doi: 10.1103/PhysRevD.80.074507.

[77] Biagio Lucini. Strongly Interacting Dynamics beyond the Standard Model on a Spacetime Lattice. *Phil.Trans.Roy.Soc.Lond.*, A368:3657–3670, 2010. doi: 10.1098/rsta.2010.0030.

[78] Luigi Del Debbio, Biagio Lucini, Agostino Patella, Claudio Pica, and Antonio Rago. The infrared dynamics of Minimal Walking Technicolor. *Phys.Rev.*, D82:014510, 2010. doi: 10.1103/PhysRevD.82.014510.

[79] Yasumichi Aoki, Tatsumi Aoyama, Masafumi Kurachi, Toshihide Maskawa, Kei-ichi Nagai, Hiroshi Ohki, Enrico Rinaldi, Akihiro Shibata, Koichi Yamawaki, and Takeshi Yamazaki. The scalar spectrum of many-flavour QCD. 2013.

[80] Yasumichi Aoki, Tatsumi Aoyama, Masafumi Kurachi, Toshihide Maskawa, Kei-ichi Nagai, Hiroshi Ohki, Enrico Rinaldi, Akihiro Shibata, Koichi Yamawaki, and Takeshi Yamazaki. Light composite scalar in twelve-flavor QCD on the lattice. 2013.

[81] Luigi Del Debbio and Roman Zwicky. Hyperscaling relations in mass-deformed conformal gauge theories. *Phys.Rev.*, D82:014502, 2010. doi: 10.1103/PhysRevD.82.014502.

[82] Luigi Del Debbio and Roman Zwicky. Scaling relations for the entire spectrum in mass-deformed conformal gauge theories. *Phys.Lett.*, B700: 217–220, 2011. doi: 10.1016/j.physletb.2011.04.059.

[83] Luigi Del Debbio and Roman Zwicky. Conformal scaling and the size of m-hadrons. 2013.

[84] Thomas DeGrand. Finite-size scaling tests for SU(3) lattice gauge theory with color sextet fermions. *Phys.Rev.*, D80:114507, 2009. doi: 10.1103/PhysRevD.80.114507.

[85] Zoltan Fodor, Kieran Holland, Julius Kuti, Daniel Nogradi, and Chris Schroeder. Nearly conformal gauge theories in finite volume. *Phys.Lett.*, B681:353–361, 2009. doi: 10.1016/j.physletb.2009.10.040.

[86] J. Gasser and H. Leutwyler. Chiral Perturbation Theory to One Loop. *Annals Phys.*, 158:142, 1984. doi: 10.1016/0003-4916(84)90242-2.

[87] Martin Luscher, Peter Weisz, and Ulli Wolff. A Numerical method to compute the running coupling in asymptotically free theories. *Nucl.Phys.*, B359:221–243, 1991. doi: 10.1016/0550-3213(91)90298-C.

[88] A. Hasenfratz, P. Hasenfratz, Urs M. Heller, and F. Karsch. Improved Monte Carlo renormalization group methods. *Phys.Lett.*, B140:76, 1984. doi: 10.1016/0370-2693(84)91051-7.

[89] Ari J. Hietanen, Kari Rummukainen, and Kimmo Tuominen. Evolution of the coupling constant in SU(2) lattice gauge theory with two adjoint fermions. *Phys.Rev.*, D80:094504, 2009. doi: 10.1103/PhysRevD.80.094504.

[90] Thomas Appelquist, George T. Fleming, and Ethan T. Neil. Lattice Study of Conformal Behavior in SU(3) Yang-Mills Theories. *Phys.Rev.*, D79: 076010, 2009. doi: 10.1103/PhysRevD.79.076010.

[91] Thomas DeGrand, Yigal Shamir, and Benjamin Svetitsky. Infrared fixed point in SU(2) gauge theory with adjoint fermions. *Phys.Rev.*, D83:074507, 2011. doi: 10.1103/PhysRevD.83.074507.

[92] Francis Bursa, Luigi Del Debbio, Liam Keegan, Claudio Pica, and Thomas Pickup. Mass anomalous dimension in SU(2) with six fundamental fermions. *Phys. Lett.*, B696:374–379, 2011. doi: 10.1016/j.physletb.2010.12.050.

[93] Tuomas Karavirta, Kimmo Tuominen, and Kari Rummukainen. Perturbative Improvement of the Schrodinger Functional for Lattice Strong Dynamics. *Phys.Rev.*, D85:054506, 2012. doi: 10.1103/PhysRevD.85.054506.

[94] Tuomas Karavirta, Jarno Rantaharju, Kari Rummukainen, and Kimmo Tuominen. Determining the conformal window: SU(2) gauge theory with Nf = 4, 6 and 10 fermion flavours. *JHEP*, 1205:003, 2012. doi: 10.1007/JHEP05(2012)003.

[95] M. Hayakawa, K.-I. Ishikawa, Y. Osaki, S. Takeda, S. Uno, et al. Running coupling constant of ten-flavor QCD with the Schródinger functional method. *Phys.Rev.*, D83:074509, 2011. doi: 10.1103/PhysRevD.83.074509.

[96] Anna Hasenfratz. Investigating the critical properties of beyond-QCD theories using Monte Carlo Renormalization Group matching. *Phys. Rev.*, D80:034505, 2009. doi: 10.1103/PhysRevD.80.034505.

[97] Anna Hasenfratz. Conformal or Walking? Monte Carlo renormalization group studies of SU(3) gauge models with fundamental fermions. *Phys. Rev.*, D82:014506, 2010. doi: 10.1103/PhysRevD.82.014506.

[98] Simon Catterall, Luigi Del Debbio, Joel Giedt, and Liam Keegan. MCRG Minimal Walking Technicolor. *Phys.Rev.*, D85:094501, 2012. doi: 10.1103/PhysRevD.85.094501.

[99] Anna Hasenfratz. Infrared fixed point of the 12-fermion SU(3) gauge model based on 2-lattice MCRG matching. *Phys.Rev.Lett.*, 108:061601, 2012. doi: 10.1103/PhysRevLett.108.061601.

[100] Ethan T. Neil. Exploring Models for New Physics on the Lattice. *PoS*, LATTICE2011:009, 2011.

[101] Martin Luscher. Properties and uses of the Wilson flow in lattice QCD. *JHEP*, 1008:071, 2010. doi: 10.1007/JHEP08(2010)071.

[102] Szabolcs Borsanyi, Stephan Durr, Zoltan Fodor, Christian Hoelbling, Sandor D. Katz, et al. High-precision scale setting in lattice QCD. *JHEP*, 1209:010, 2012. doi: 10.1007/JHEP09(2012)010.

[103] Szabolcs Borsanyi, Stephan Durr, Zoltan Fodor, Sandor D. Katz, Stefan Krieg, et al. Anisotropy tuning with the Wilson flow. 2012.

[104] Zoltan Fodor, Kieran Holland, Julius Kuti, Daniel Nogradi, and Chik Him Wong. The Yang-Mills gradient flow in finite volume. *JHEP*, 1211:007, 2012. doi: 10.1007/JHEP11(2012)007.

[105] Luigi Del Debbio, Agostino Patella, and Antonio Rago. Space-time symmetries and the Yang-Mills gradient flow. 2013.

[106] Martin Lüscher. Future applications of the Yang-Mills gradient flow in lattice QCD. 2013.

[107] Dennis D. Dietrich and Francesco Sannino. Conformal window of SU(N) gauge theories with fermions in higher dimensional representations. *Phys.Rev.*, D75:085018, 2007. doi: 10.1103/PhysRevD.75.085018.

[108] Zoltan Fodor, Kieran Holland, Julius Kuti, Daniel Nogradi, Chris Schroeder, et al. Twelve massless flavors and three colors below the conformal window. *Phys.Lett.*, B703:348–358, 2011. doi: 10.1016/j.physletb.2011.07.037.

[109] T. Appelquist, G.T. Fleming, M.F. Lin, E.T. Neil, and D.A. Schaich. Lattice Simulations and Infrared Conformality. *Phys.Rev.*, D84:054501, 2011. doi: 10.1103/PhysRevD.84.054501.

[110] A. Deuzeman, M.P. Lombardo, and E. Pallante. Evidence for a conformal phase in SU(N) gauge theories. *Phys.Rev.*, D82:074503, 2010. doi: 10.1103/PhysRevD.82.074503.

[111] C.-J. David Lin, Kenji Ogawa, Hiroshi Ohki, and Eigo Shintani. Lattice study of infrared behaviour in SU(3) gauge theory with twelve massless flavours. 2012.

[112] Etsuko Itou. Properties of the twisted Polyakov loop coupling and the infrared fixed point in the SU(3) gauge theory. 2012.

[113] Anqi Cheng, Anna Hasenfratz, Gregory Petropoulos, and David Schaich. Scale-dependent mass anomalous dimension from Dirac eigenmodes. 2013.

[114] Anqi Cheng, Anna Hasenfratz, and David Schaich. Novel phase in SU(3) lattice gauge theory with 12 light fermions. *Phys.Rev.*, D85:094509, 2012. doi: 10.1103/PhysRevD.85.094509.

[115] Xiao-Yong Jin and Robert D. Mawhinney. Lattice QCD with 12 Quark Flavors: A Careful Scrutiny. 2013.

[116] Albert Deuzeman, Maria Paola Lombardo, Tiago Nunes da Silva, and Elisabetta Pallante. The bulk transition of QCD with twelve flavors and the role of improvement. *Phys. Lett.*, B720:358–365, 2013. doi: 10.1016/j.physletb.2013.02.030.

[117] Yasumichi Aoki, Tatsumi Aoyama, Masafumi Kurachi, Toshihide Maskawa, Kei-ichi Nagai, Hiroshi Ohki, Akihiro Shibata, Koichi Yamawaki, and Takeshi Yamazaki. Lattice study of conformality in twelve-flavor QCD. *Phys.Rev.*, D86:054506, 2012. doi: 10.1103/PhysRevD.86.054506.

[118] Yasumichi Aoki, Tatsumi Aoyama, Masafumi Kurachi, Toshihide Maskawa, Kei-ichi Nagai, Hiroshi Ohki, Akihiro Shibata, Koichi Yamawaki, and Takeshi Yamazaki. Exploring walking behavior in SU(3) gauge theory with 4 and 8 HISQ quarks. *PoS*, LATTICE2012:035, 2012.

[119] Yasumichi Aoki, Tatsumi Aoyama, Masafumi Kurachi, Toshihide Maskawa, Kei-ichi Nagai, Hiroshi Ohki, Akihiro Shibata, Koichi Yamawaki, and Takeshi Yamazaki. Low energy spectra in many flavor QCD with Nf=12 and 16. *PoS*, LATTICE2012:029, 2012.

[120] *Many flavor QCD with $N_f = 12$ and 16*, 2012.

[121] E. Follana et al. Highly improved staggered quarks on the lattice, with applications to charm physics. *Phys.Rev.*, D75:054502, 2007. doi: 10.1103/PhysRevD.75.054502.

[122] A. Bazavov, T. Bhattacharya, M. Cheng, C. DeTar, H.T. Ding, et al. The chiral and deconfinement aspects of the QCD transition. *Phys.Rev.*, D85: 054503, 2012. doi: 10.1103/PhysRevD.85.054503.

[123] Milc public lattice gauge theory code. URL `http://physics.indiana.edu/~sg/milc.html`.

[124] Martin Hasenbusch. Speeding up the hybrid Monte Carlo algorithm for dynamical fermions. *Phys.Lett.*, B519:177–182, 2001. doi: 10.1016/S0370-2693(01)01102-9.

[125] N. Ishizuka, M. Fukugita, H. Mino, M. Okawa, and A. Ukawa. Operator dependence of hadron masses for Kogut-Susskind quarks on the lattice. *Nucl.Phys.*, B411:875–902, 1994. doi: 10.1016/0550-3213(94)90475-8.

[126] J. Beringer et al. Review of Particle Physics (RPP). *Phys.Rev.*, D86:010001, 2012. doi: 10.1103/PhysRevD.86.010001.

[127] C. McNeile, C. Michael, and K. J. Sharkey. Flavor singlet mesons in qcd. *Phys. Rev. D*, 65:014508, 2001. doi: 10.1103/PhysRevD.65.014508.

[128] Craig McNeile and Christopher Michael. Mixing of scalar glueballs and flavor singlet scalar mesons. *Phys.Rev.*, D63:114503, 2001. doi: 10.1103/PhysRevD.63.114503.

[129] Teiji Kunihiro et al. Scalar mesons in lattice QCD. *Phys.Rev.*, D70:034504, 2004. doi: 10.1103/PhysRevD.70.034504.

[130] A. Hart, C. McNeile, Christopher Michael, and J. Pickavance. A Lattice study of the masses of singlet 0++ mesons. *Phys.Rev.*, D74:114504, 2006. doi: 10.1103/PhysRevD.74.114504.

[131] M.F.M. Lutz et al. Physics Performance Report for PANDA: Strong Interaction Studies with Antiprotons. 2009.

[132] Ulrich Wiedner. Future Prospects for Hadron Physics at PANDA. *Prog.Part.Nucl.Phys.*, 66:477–518, 2011. doi: 10.1016/j.ppnp.2011.04.001.

[133] C. Morningstar, J. Bulava, B. Fahy, J. Foley, Y.C. Jhang, et al. Extended hadron and two-hadron operators of definite momentum for spectrum calculations in lattice QCD. 2013.

[134] Xiao-Yong Jin and Robert D. Mawhinney. Lattice QCD with 12 Degenerate Quark Flavors. *PoS*, LATTICE2011:066, 2011.

[135] L. Venkataraman and G. Kilcup. The eta-prime meson with staggered fermions. *Phys.Rev.D*, 1997.

[136] Eric B. Gregory, Alan C. Irving, Chris M. Richards, and Craig McNeile. Methods for Pseudoscalar Flavour-Singlet Mesons with Staggered Fermions. *Phys.Rev.*, D77:065019, 2008. doi: 10.1103/PhysRevD.77.065019.

[137] C. McNeile, A. Bazavov, C.T.H. Davies, R.J. Dowdall, K. Hornbostel, et al. Direct determination of the strange and light quark condensates from full lattice QCD. 2012.

[138] Biagio Lucini, Antonio Rago, and Enrico Rinaldi. SU(N_c) gauge theories at deconfinement. *Phys.Lett.*, B712:279–283, 2012. doi: 10.1016/j.physletb.2012.04.070.

[139] Enrico Rinaldi, Giuseppe Lacagnina, Biagio Lucini, Agostino Patella, and Antonio Rago. Scaling properties of SU(2) gauge theory with mixed fundamental-adjoint action. *PoS*, LATTICE2012:252, 2012.

[140] A. Hart and M. Teper. On the glueball spectrum in O(a) improved lattice QCD. *Phys.Rev.*, D65:034502, 2002. doi: 10.1103/PhysRevD.65.034502.

[141] Ofer Aharony and Eyal Karzbrun. On the effective action of confining strings. *JHEP*, 0906:012, 2009. doi: 10.1088/1126-6708/2009/06/012.

[142] M. Bona et al. Model-independent constraints on Δ F=2 operators and the scale of new physics. *JHEP*, 0803:049, 2008. doi: 10.1088/1126-6708/2008/03/049.

[143] E. Lunghi and Amarjit Soni. Possible evidence for the breakdown of the CKM-paradigm of CP-violation. *Phys.Lett.*, B697:323–328, 2011. doi: 10.1016/j.physletb.2011.02.016.

[144] C. McNeile, C.T.H. Davies, E. Follana, K. Hornbostel, and G.P. Lepage. High-Precision c and b Masses, and QCD Coupling from Current-Current Correlators in Lattice and Continuum QCD. *Phys.Rev.*, D82:034512, 2010. doi: 10.1103/PhysRevD.82.034512.

[145] C.T.H. Davies, C. McNeile, E. Follana, G.P. Lepage, H. Na, et al. Update: Precision D_s decay constant from full lattice QCD using very fine lattices. *Phys.Rev.*, D82:114504, 2010. doi: 10.1103/PhysRevD.82.114504.

[146] Estia Eichten and Brian Russell Hill. An Effective Field Theory for the Calculation of Matrix Elements Involving Heavy Quarks. *Phys.Lett.*, B234:511, 1990. doi: 10.1016/0370-2693(90)92049-O.

[147] Michele Della Morte, Jochen Heitger, and Rainer Sommer. Towards Precision B-physics from Non-Perturbative Heavy Quark Effective Theory. pages 31–39, 2010.

[148] K. Symanzik. Continuum Limit and Improved Action in Lattice Theories. 1. Principles and phi**4 Theory. *Nucl.Phys.*, B226:187, 1983. doi: 10.1016/0550-3213(83)90468-6.

[149] G. Peter Lepage. Flavor symmetry restoration and Symanzik improvement for staggered quarks. *Phys.Rev.*, D59:074502, 1999. doi: 10.1103/PhysRevD.59.074502.

[150] Roberto Frezzotti, Pietro Antonio Grassi, Stefan Sint, and Peter Weisz. Lattice QCD with a chirally twisted mass term. *JHEP*, 0108:058, 2001.

[151] R. Frezzotti and G.C. Rossi. Chirally improving Wilson fermions. 1. O(a) improvement. *JHEP*, 0408:007, 2004. doi: 10.1088/1126-6708/2004/08/007.

[152] W.E. Caswell and G.P. Lepage. Effective Lagrangians for Bound State Problems in QED, QCD, and Other Field Theories. *Phys.Lett.*, B167:437, 1986. doi: 10.1016/0370-2693(86)91297-9.

[153] B.A. Thacker and G. Peter Lepage. Heavy quark bound states in lattice QCD. *Phys.Rev.*, D43:196–208, 1991. doi: 10.1103/PhysRevD.43.196.

[154] Aida X. El-Khadra, Andreas S. Kronfeld, and Paul B. Mackenzie. Massive fermions in lattice gauge theory. *Phys.Rev.*, D55:3933–3957, 1997. doi: 10.1103/PhysRevD.55.3933.

[155] Norman H. Christ, Min Li, and Huey-Wen Lin. Relativistic Heavy Quark Effective Action. *Phys.Rev.*, D76:074505, 2007. doi: 10.1103/PhysRevD.76.074505.

[156] Jochen Heitger and Rainer Sommer. Nonperturbative heavy quark effective theory. *JHEP*, 0402:022, 2004. doi: 10.1088/1126-6708/2004/02/022.

[157] Benoit Blossier, Michele della Morte, Nicolas Garron, and Rainer Sommer. HQET at order $1/m$: I. Non-perturbative parameters in the quenched approximation. *JHEP*, 1006:002, 2010. doi: 10.1007/JHEP06(2010)002.

[158] B. Blossier et al. A Proposal for B-physics on current lattices. *JHEP*, 1004:049, 2010. doi: 10.1007/JHEP04(2010)049.

[159] P. Dimopoulos et al. Lattice QCD determination of mb, fB and fBs with twisted mass Wilson fermions. *JHEP*, 1201:046, 2012. doi: 10.1007/JHEP01(2012)046.

[160] N. Carrasco, M. Ciuchini, P. Dimopoulos, R. Frezzotti, V. Gimenez, et al. B-physics from Nf=2 tmQCD: the Standard Model and beyond. 2013.

[161] Ikaros I.Y. Bigi, Mikhail A. Shifman, N.G. Uraltsev, and A.I. Vainshtein. The Pole mass of the heavy quark. Perturbation theory and beyond. *Phys.Rev.*, D50:2234–2246, 1994. doi: 10.1103/PhysRevD.50.2234.

[162] A. Bazavov, D. Toussaint, C. Bernard, J. Laiho, C. DeTar, et al. Nonperturbative QCD simulations with 2+1 flavors of improved staggered quarks. *Rev.Mod.Phys.*, 82:1349–1417, 2010. doi: 10.1103/RevModPhys.82.1349.

[163] Claude W. Bernard, Tom Burch, Kostas Orginos, Doug Toussaint, Thomas A. DeGrand, et al. The QCD spectrum with three quark flavors. *Phys.Rev.*, D64:054506, 2001. doi: 10.1103/PhysRevD.64.054506.

[164] C. McNeile, C.T.H. Davies, E. Follana, K. Hornbostel, and G.P. Lepage. High-Precision f_{B_s} and HQET from Relativistic Lattice QCD. *Phys.Rev.*, D85:031503, 2012. doi: 10.1103/PhysRevD.85.031503.

[165] Stefan Schaefer, Rainer Sommer, and Francesco Virotta. Investigating the critical slowing down of QCD simulations. *PoS*, LAT2009:032, 2009.

[166] Martin Luscher and Stefan Schaefer. Lattice QCD without topology barriers. *JHEP*, 1107:036, 2011. doi: 10.1007/JHEP07(2011)036.

[167] A. Bazavov et al. Topological susceptibility with the asqtad action. *Phys.Rev.*, D81:114501, 2010. doi: 10.1103/PhysRevD.81.114501.

[168] Krzysztof Cichy, Vincent Drach, Elena Garcia-Ramos, Gregorio Herdoiza, and Karl Jansen. Overlap valence quarks on a twisted mass sea: a case study for mixed action Lattice QCD. *Nucl.Phys.*, B869:131–163, 2013. doi: 10.1016/j.nuclphysb.2012.12.011.

[169] Kostas Orginos and Andre Walker-Loud. Mixed meson masses with domain-wall valence and staggered sea fermions. *Phys.Rev.*, D77:094505, 2008. doi: 10.1103/PhysRevD.77.094505.

[170] T. Blum and A. Soni. Domain wall quarks and kaon weak matrix elements. *Phys.Rev.Lett.*, 79:3595–3598, 1997. doi: 10.1103/PhysRevLett.79.3595.

[171] C. Aubin, Jack Laiho, and Ruth S. Van de Water. The Neutral kaon mixing parameter B(K) from unquenched mixed-action lattice QCD. *Phys.Rev.*, D81:014507, 2010. doi: 10.1103/PhysRevD.81.014507.

[172] Gerhard Buchalla. Heavy quark theory. pages 57–104, 2002.

[173] P.A. Boyle, A. Juttner, C. Kelly, and R.D. Kenway. Use of stochastic sources for the lattice determination of light quark physics. *JHEP*, 0808: 086, 2008. doi: 10.1088/1126-6708/2008/08/086.

[174] Peter A. Boyle. The BAGEL assembler generation library. *Comput.Phys.Commun.*, 180:2739–2748, 2009. doi: 10.1016/j.cpc.2009.08.010.

[175] Karl Jansen and Martin Schmaltz. Critical momenta of lattice chiral fermions. *Phys.Lett.*, B296:374–378, 1992. doi: 10.1016/0370-2693(92)91335-7.

[176] N.H. Christ and G. Liu. Massive domain wall fermions. *Nucl.Phys.Proc.Suppl.*, 129:272–274, 2004. doi: 10.1016/S0920-5632(03)02553-2.

[177] R. Arthur and P.A. Boyle. Step Scaling with off-shell renormalisation. *Phys.Rev.*, D83:114511, 2011. doi: 10.1103/PhysRevD.83.114511.

[178] R. Arthur, P.A. Boyle, N. Garron, C. Kelly, and A.T. Lytle. Opening the Rome-Southampton window for operator mixing matrices. *Phys.Rev.*, D85: 014501, 2012. doi: 10.1103/PhysRevD.85.014501.

[179] R. Arthur et al. Domain Wall QCD with Near-Physical Pions. 2012. doi: 10.1103/PhysRevD.87.094514.

[180] N. Carrasco et al. Neutral meson oscillations in the Standard Model and beyond from Nf=2 Twisted Mass Lattice QCD. *PoS*, LATTICE2012:105, 2012.

[181] C. Albertus, Y. Aoki, P.A. Boyle, N.H. Christ, T.T. Dumitrescu, et al. Neutral B-meson mixing from unquenched lattice QCD with domain-wall light quarks and static b-quarks. *Phys.Rev.*, D82:014505, 2010. doi: 10.1103/PhysRevD.82.014505.

[182] Kouji Kashiwa and Tatsuhiro Misumi. Phase structure and Hosotani mechanism in gauge theories with compact dimensions revisited. *JHEP*, 1305:042, 2013. doi: 10.1007/JHEP05(2013)042.

[183] Nikos Irges and Francesco Knechtli. Non-perturbative definition of five-dimensional gauge theories on the R**4 x S**1/Z(2) orbifold. *Nucl. Phys.*, B719:121–139, 2005. doi: 10.1016/j.nuclphysb.2005.05.002.

[184] B. Berg and A. Billoire. Glueball Spectroscopy in Four-Dimensional SU(3) Lattice Gauge Theory. 1. *Nucl. Phys.*, B221:109, 1983. doi: 10.1016/0550-3213(83)90620-X.

[185] B. Berg and A. Billoire. Glueball spectroscopy in four-dimensional SU(3) Lattice Gauge Theory. 2. *Nucl. Phys.*, B226:405, 1983. doi: 10.1016/0550-3213(83)90199-2.

[186] Biagio Lucini, Agostino Patella, Antonio Rago, and Enrico Rinaldi. Infrared conformality and bulk critical points: SU(2) with heavy adjoint quarks. 2013.

[187] M. Luscher. Selected topics in Lattice Field Theory. 1988. Lectures given at Summer School 'Fields, Strings and Critical Phenomena', Les Houches, France, Jun 28 - Aug 5, 1988.

[188] M. Albanese et al. Glueball Masses and String Tension in Lattice QCD. *Phys. Lett.*, B192:163–169, 1987. doi: 10.1016/0370-2693(87)91160-9.

[189] M. Teper. An Improved Method for Lattice Glueball Calculations. *Phys. Lett.*, B183:345, 1987. doi: 10.1016/0370-2693(87)90976-2.

[190] Benoit Blossier, Michele Della Morte, Georg von Hippel, Tereza Mendes, and Rainer Sommer. On the generalized eigenvalue method for energies and matrix elements in lattice field theory. *JHEP*, 0904:094, 2009. doi: 10.1088/1126-6708/2009/04/094.

[191] Christopher Michael. The glueball spectrum from lattice gauge theory. *Acta Phys. Polon.*, B21:119, 1990.

[192] Sumit R. Das. Some Aspects of Large n Theories. *Rev. Mod. Phys.*, 59:235, 1987. doi: 10.1103/RevModPhys.59.235.

[193] Michael Teper. Large N. *PoS*, LATTICE2008:022, 2008.

[194] Rajamani Narayanan. Continuum reduction in large N gauge theories. 2009.

[195] Michael Teper. Large N and confining flux tubes as strings - a view from the lattice. 2009.

[196] Biagio Lucini and Marco Panero. SU(N) gauge theories at large N. *Phys.Rept.*, 526:93–163, 2013. doi: 10.1016/j.physrep.2013.01.001.

[197] Luigi Del Debbio, Biagio Lucini, Agostino Patella, and Claudio Pica. Quenched mesonic spectrum at large N. *JHEP*, 03:062, 2008. doi: 10.1088/1126-6708/2008/03/062.

[198] Adi Armoni, Biagio Lucini, Agostino Patella, and Claudio Pica. Lattice Study of Planar Equivalence: The Quark Condensate. *Phys. Rev.*, D78: 045019, 2008. doi: 10.1103/PhysRevD.78.045019.

[199] Gerard 't Hooft. A planar diagram theory for strong interactions. *Nucl. Phys.*, B72:461, 1974.

[200] G. 't Hooft. Large N. 2002.

[201] B. Lucini and M. Teper. SU(N) gauge theories in four dimensions: Exploring the approach to N = infinity. *JHEP*, 06:050, 2001.

[202] Harvey B. Meyer and Michael J. Teper. Glueball Regge trajectories and the pomeron: A lattice study. *Phys. Lett.*, B605:344–354, 2005. doi: 10.1016/j.physletb.2004.11.036.

[203] T. DeGrand and C. DeTar. *Lattice Methods for Quantum Chromodynamics*. World Scientific Publishing Company, 2006.

[204] C. Gattringer and Christian B. Lang. *Quantum Chromodynamics on the Lattice: An Introductory Presentation*. Number 788 in Lect. Notes Phys. Springer, 2010.

[205] H. J. Rothe. *Lattice Gauge Theories: An introduction*, volume 82 of *Lecture Notes in Physics*. World Scientific Publishing Company, 4th edition, 2012.

[206] Holger Bech Nielsen and M. Ninomiya. No Go Theorem for Regularizing Chiral Fermions. *Phys.Lett.*, B105:219, 1981. doi: 10.1016/0370-2693(81)91026-1.

[207] John B. Kogut and Leonard Susskind. Hamiltonian Formulation of Wilson's Lattice Gauge Theories. *Phys.Rev.*, D11:395, 1975. doi: 10.1103/PhysRevD.11.395.

[208] David B. Kaplan. A Method for simulating chiral fermions on the lattice. *Phys.Lett.*, B288:342–347, 1992. doi: 10.1016/0370-2693(92)91112-M.

[209] Paul H. Ginsparg and Kenneth G. Wilson. A Remnant of Chiral Symmetry on the Lattice. *Phys.Rev.*, D25:2649, 1982. doi: 10.1103/PhysRevD.25.2649.

[210] Martin Luscher. Exact chiral symmetry on the lattice and the Ginsparg-Wilson relation. *Phys.Lett.*, B428:342–345, 1998. doi: 10.1016/S0370-2693(98)00423-7.

[211] Herbert Neuberger. A Practical implementation of the overlap Dirac operator. *Phys.Rev.Lett.*, 81:4060–4062, 1998. doi: 10.1103/PhysRevLett.81.4060.

[212] Herbert Neuberger. Exactly massless quarks on the lattice. *Phys.Lett.*, B417:141–144, 1998. doi: 10.1016/S0370-2693(97)01368-3.

[213] Herbert Neuberger. More about exactly massless quarks on the lattice. *Phys.Lett.*, B427:353–355, 1998. doi: 10.1016/S0370-2693(98)00355-4.

[214] Vadim Furman and Yigal Shamir. Axial symmetries in lattice QCD with Kaplan fermions. *Nucl.Phys.*, B439:54–78, 1995. doi: 10.1016/0550-3213(95)00031-M.

[215] Richard C. Brower, Hartmut Neff, and Kostas Orginos. Mobius fermions: Improved domain wall chiral fermions. *Nucl.Phys.Proc.Suppl.*, 140:686–688, 2005. doi: 10.1016/j.nuclphysbps.2004.11.180.

[216] Richard C. Brower, Harmut Neff, and Kostas Orginos. The Móbius Domain Wall Fermion Algorithm. 2012.